The Genesis of Sulphides in the Shetland Ophiolite

Thesis

The Genesis of Sulphides in the Shetland Ophiolite

by

Jonathan Maynard, B.Sc.Hons (London)

A dissertation submitted for the degree of
Doctor of Philosophy

Date of submission: 16th September 1993
Date of award: 10th February 1994

September 1993
Department of Earth Sciences,
The Open University

ProQuest LLC.
789 East Eisenhower Parkway
P.O. Box 1346
Ann Arbor, MI 48106 – 1346

Abstract

This thesis describes the sulphide, arsenide and antimonide mineral assemblages and stable isotope geochemistry of each magmatic and alteration lithology of the Shetland ophiolite complex and identifies a new assemblage of Pd and Pt-bearing nickel antimonides.

The assemblages have been characterized as follows. Cumulate rocks typically contain a variety of Ni- Fe- and Cu-bearing opaque phases including relict sulphides, native metals, arsenides and antimonides. The sulphide assemblages show a strong correlation with the host silicate lithology. Dunite pods in harzburgite and cumulate dunites contain the assemblage pentlandite-heazlewoodite-millerite-godlevskite-chalcopyrite-chalcocite-native Cu ± awaruite ± troilite ± orcelite ± breithauptite/Ni- Cu antimonide. Cumulate wehrlites and pyroxenites contain pentlandite-pyrrhotite-pyrite-chalcopyrite-bornite-chalcocite-native copper ± orcellite and maucherite. Gabbros and dolerite dykes contain pyrrhotite-pyrite-marcasite-chalcopyrite ± pentlandite. These assemblages developed by the alteration of precursory magmatic sulphides.

A technique has been developed and used to measure whole-rock $\delta^{34}S$ values to a precision of ±0.5‰. $\delta^{34}S$ measurements suggest an igneous source for sulphur in sulphide-bearing dunite pods (+4.3‰), cumulate dunites (+3.1‰), cumulate pyroxenites (+2.9‰) and gabbros and dolerite dykes (+4.5‰). Talc-carbonate altered rocks (+0.9‰) from close to the basal thrust may have derived a portion of sulphur from the underlying metasediments (-4.2‰). Sub-massive pyrite mineralization from high-level gabbros (+9 to +14‰) requires a contribution of hydrothermal sulphur; this has been corroborated by He isotope analysis. Hydrogen and oxygen isotope analyses have shown that serpentine minerals in dunites have exchanged water with meteoric fluids, whereas pyroxenites and gabbros retain a hydrothermal seawater signature.

A diverse assemblage of PGM are known to be intergrown or intimately associated with the base metal suphides and nickel arsenides in dunite pods in harzburgite and cumulate dunites. A new assemblage of Pd ± Pt-bearing Ni and Ni- Cu antimonides are associated with these PGM and disseminated Ni- Fe-sulphides. The paragenesis of these antimonides is described for a sulphide-bearing dunite pod from the PGE-rich Cliff locality and from a PGE-enriched mineralized horizon in cumulate dunites. At both localities the paragenesis of the antimonides is closely linked to the alteration of the coexisting sulphide assemblage.

Acknowledgements

Many thanks are due to Drs. H.M. Prichard, R.A. Ixer and Professor C.T. Pillinger for setting up this project and for guidance and ideas throughout the course of this work. The help of Drs. I.P. Wright and A.D. Morse in supervising laboratory experiments and commenting on thesis drafts is gratefully acknowledged. Dr. R.A. Lord provided many ideas on aspects of this thesis and the help of Drs. D.S. Stevenson, C. Oppenheimer, S.R. Boyd, I.A. Franchi proved invaluable in writing this thesis. Dr. P. McConville performed laser probe $\delta^{34}S$ measurements and Dr. F. Stuart made He-isotope analyses. Dr. A.G. Tindle and Dr. P. Potts are thanked for help with microprobe analyses and Naiomi Williams operated the SEM. I. Chaplin, K. Chambers and B. Ellis produced many thin sections. J. Watson helped with XRF analysis and R. Quill and E. Parker provided secretarial skills.

TABLE OF CONTENTS

LIST OF FIGURES

LIST OF TABLES

Chapter 1

Sulphides in mafic and ultramafic rocks

1.1 Introduction: The distribution of sulphides in ophiolitic crust

It is generally accepted that ophiolites are fragments of oceanic lithosphere that were formed at ancient constructive plate margins and emplaced onto continental or island arc margins (Gass and Masson-Smith, 1963; Gass and Masson-Smith, 1968; Coleman, 1977). The term "ophiolite" is based on the consensus definition proposed by the participants of the Penrose conference, organized by the Geological Society of America (Anonymous, 1972) and is summarized as follows: ophiolite refers to a distinctive assemblage of mafic to ultramafic rocks, from the stratigraphic base;

(i) an ultramafic complex, consisting of harzburgite, lherzolite and dunite, usually with a metamorphic tectonic fabric (more or less serpentinized).

(ii) a gabbroic complex, ordinarily with cumulus textures commonly containing peridotites and pyroxenites and usually less deformed than the ultramafic complex.

(iii) a mafic sheeted dyke complex.

(iv) a mafic volcanic complex, commonly pillowed.

A consensus model showing the processes responsible for the formation of these rock units is shown in Fig. 1.1.

Ophiolite complexes contain economic base metal deposits in their volcanic sequences that are concentrated as massive sulphides, but there is an absence of significant concentrations of sulphide in the lower cumulate basic and ultramafic parts of these complexes (Naldrett, 1973). This may explain the lack of a systematic study of the sulphide mineralogy and sulphur isotope geochemistry of a complete section of ophiolitic crust. Where sulphides are present in ophiolitic cumulates they usually occur as disseminated Ni-Fe-Cu-sulphides, which form approximately 1-2% of the modal mineralogy by volume. Examples of such occurrences are sparse, but include black dunite lenses in the lower ultramafic cumulates of the Zambales ophiolite, Philippines (Paringit, 1975), and in the cumulate ultramafic rocks of the Leka ophiolite, Norway (Pederson, 1993). A generalized map showing the worldwide distributions of some mineralized ophiolite complexes is shown

in Fig. 1.2. The sulphide assemblages in these complexes vary throughout the ophiolite sequences. The aim of this study, therefore, is to examine the mineralogical and sulphur isotopic variation in a single ophiolite complex (Shetland) by determining the sulphide assemblages and sulphur isotope signature of the different lithologies of an ophiolite complex.

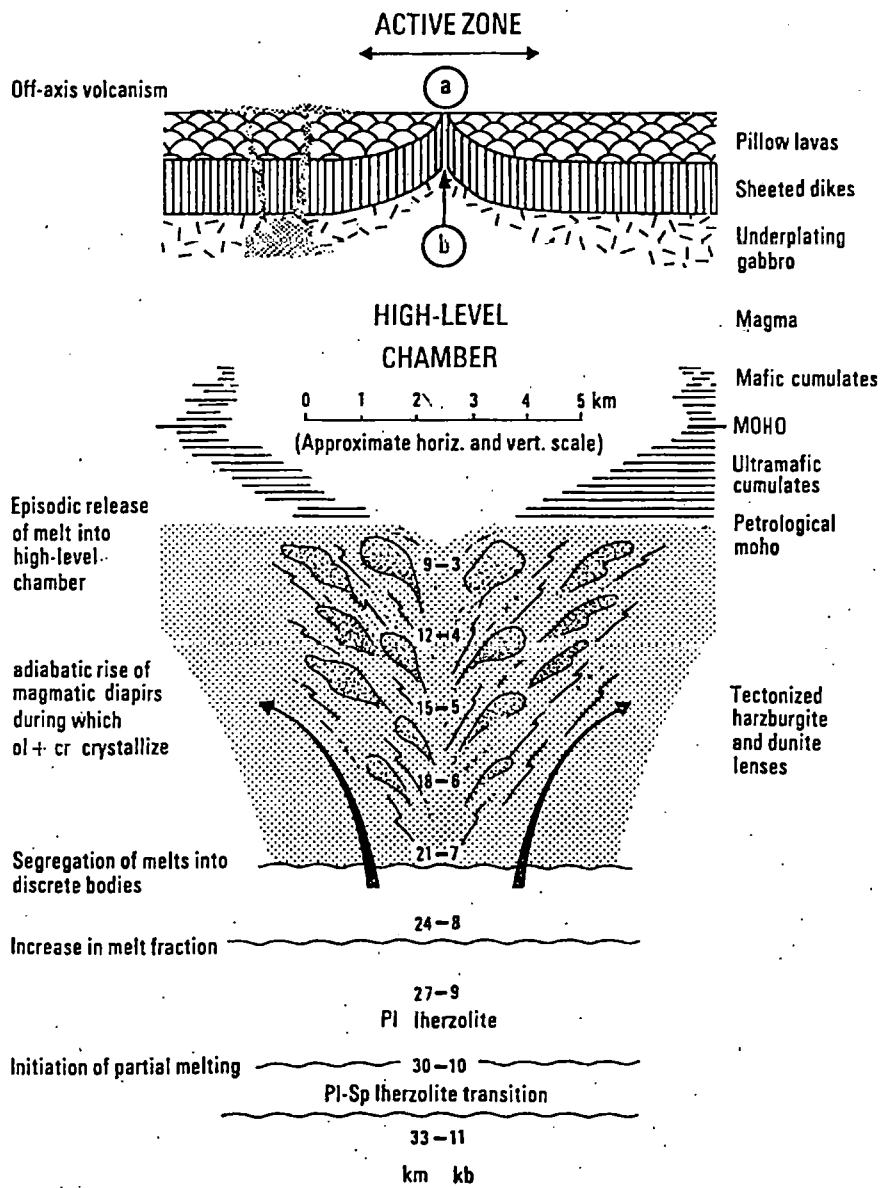

Fig. 1.1. Space form of an ophiolite magma chamber and its relation to the various rock units (Gass, 1980).

The affinity of base-metals with sulphur is well displayed in massive economic Cu-Ni sulphide mineralization, where the sulphides commonly form 100% of the rock, and are composed of dominantly monoclinic pyrrhotite + pentlandite + chalcopyrite + pyrite in order of decreasing abundance (Craig and Kullerud, 1969). These massive Fe-Ni-Cu-sulphide deposits are relatively common in continental layered intrusions, *e.g.* Naldrett *et al.* (1979).

Massive sulphide deposits in ophiolite complexes are almost exclusively hosted in the volcanic sequences, represented by pillow lavas. Examples include the Fe-Cu-Zn bearing Cyprus sulphide deposits situated in the upper part of the Troodos ophiolite complex (Constantinou and Govett, 1973), and the massive sulphide deposits of Lasail, Bayda and Aarja, which are hosted within pillow lava units of the Semail ophiolite in Oman (Coleman *et al.*, 1979; Ixer *et al.*, 1986). These deposits are related to hydrothermal processes operative at mid-ocean ridge spreading centres (Upadhyay and Strong, 1973), unlike much of the base-metal sulphide mineralization hosted in stratiform layered complexes, which formed by magmatic processes (Naldrett, 1973).

Massive sulphide deposits from crustal cumulate ophiolitic rocks and mantle harzburgites are volumetrically very small when compared to the massive Ni- Cu-sulphide deposits of the continental layered intrusions *e.g.*, Noril'sk in Russia (Fig. 1.2). The pyrrhotite, chalcopyrite and pentlandite mineralization hosted by feldspathic cumulates in the Bay-of-Islands ophiolite complex in Newfoundland (Fig. 1.2) is one example of a massive sulphide deposit hosted in ophiolitic cumulates although it has been shown to be hydrothermal in origin (Lydon and Lavigne, 1990). The magmatic pyrrhotite-pentlandite-chalcopyrite-pyrite sulphide assemblage developed in a gabbroic magma chamber, Haylyn Block, Semail ophiolite, Oman (Lachize *et al.*, 1991) only approaches 30% by volume of the rock and is only developed over a restricted (150m) stratigraphic horizon. In the Troodos ophiolite, sulphide deposits located at the transition zone between cumulate ophiolitic rocks and mantle harzburgites have been interpreted as resulting from the complete alteration of a pre-existing magmatic sulphide concentration or, alternatively, result from some other non-magmatic process (Foose *et al.*, 1985). Economou and Naldrett (1984) considered Ni-Fe-Cu-Co sulphides associated with podiform chromite from Eretria, Greece

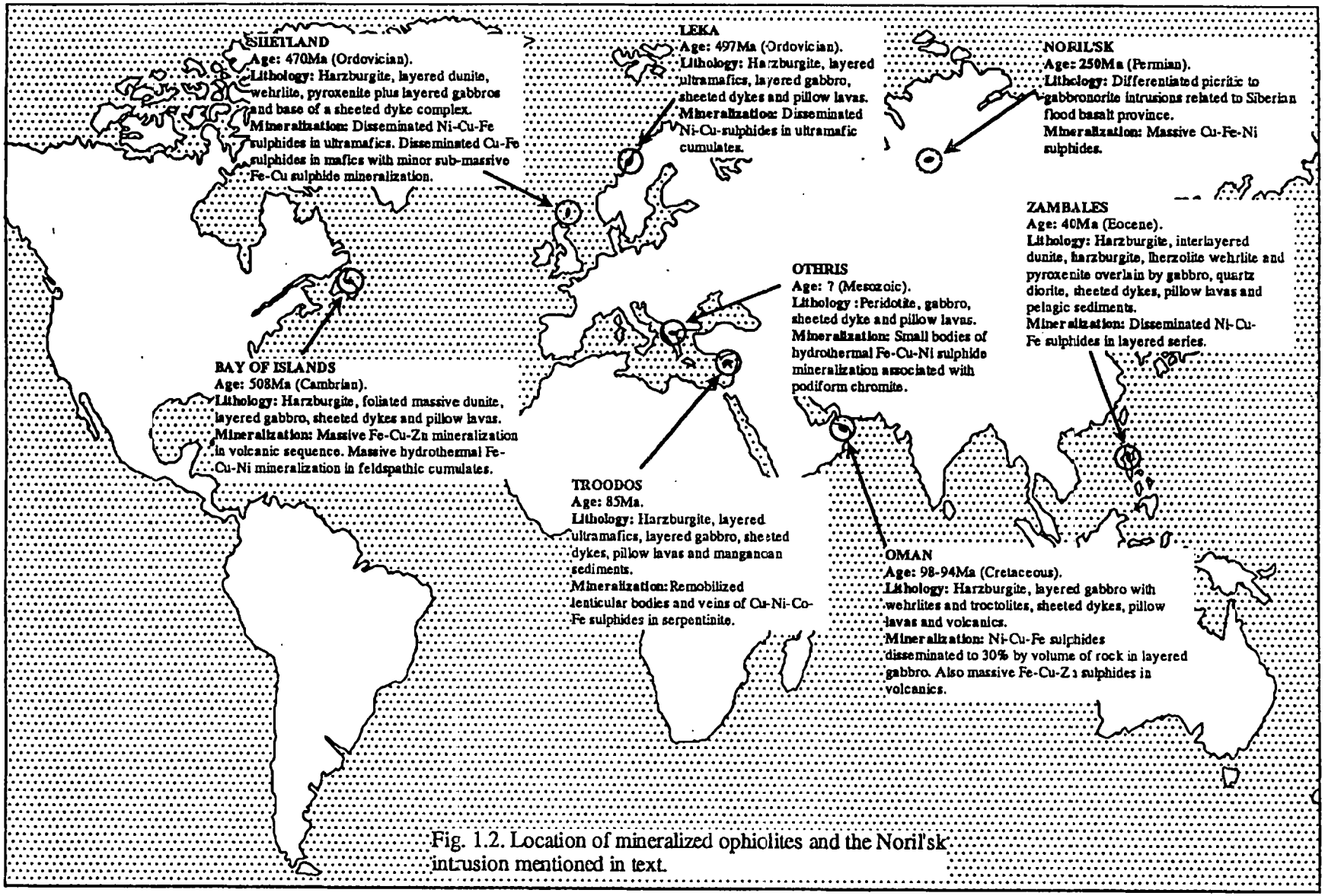

Fig. 1.2. Location of mineralized ophiolites and the Noril'sk intrusion mentioned in text.

to have been formed by hydrothermal fluids related to serpentinization of host rocks, the host rocks themselves perhaps providing the source of metals.

Disseminated Ni-Fe-Cu-sulphides, typically forming approximately 0.5-5% of the host rock by volume are known from the ultramafic cumulates of the Leka ophiolite (Pedersen, 1993) and the Zambales ophiolite (Paringit, 1975).

1.2 The source of sulphur in sulphides from ultramafic and mafic rocks

Since sulphur is frequently the major non-metal in an ore deposit, a study of the sulphur isotope geochemistry of these deposits has proved useful in ascertaining the source of sulphur and hence the ore deposit. Early workers on sulphide deposits ascribed the observed sulphur isotope variations to result from the sulphur being derived from either an igneous or a sedimentary sulphur source (Jensen, 1967). However later studies have shown that such large variations in sulphur isotope ratios are also reproducible by deposition of sulphides from fluids with varying oxidation states (Ohomoto, 1972).

Sulphur isotope ratios are conventionally expressed in delta notation, a concept introduced by Urey (1948). This essentially involves measuring the difference between the sulphur isotope ratio of a sample of unknown isotopic composition and that of a reference material of known sulphur isotope composition. Because terrestrial differences in sulphur isotope ratios are relatively small this difference is expressed in parts per thousand (per mil) given by;

$$\delta^{34}S‰ = (((^{34}S/^{32}S \text{ sample})/(^{34}S/^{32}S \text{ standard}) - 1) \times 1000$$

For sulphur isotope analysis the standard conventionally used is troilite from the Canon Diablo meteorite which has a $^{34}S/^{32}S$ ratio of 0.0450045 (Jensen and Nakai, 1962). In this work all $\delta^{34}S$ values are reported as ‰ variations relative to this standard.

Table 1.1 gives the sulphur contents and isotope compositions of the mantle, crust and seawater and Fig. 1.3 shows the ranges of sulphur isotope values in terrestrial rocks. The sulphur budget in the crust, seawater and upper mantle system is largely dependent upon the sulphur content assumed for the upper mantle because this is the largest reservoir of the system (Chaussidon *et al.*, 1989) (table 1.1). Chaussidon *et al.* (1989) suggest a

$\delta^{34}S$ value of +0.5‰ for the primitive upper mantle, which is slightly different from that of chondritic meteorites (0.2±0.2‰, Thode *et al.*, 1961).

Reservoir	*Total mass* [a] *(g)*	*Sulphur content* [b] *(ppm)*	*Sulphur mass (g)*	*% of total sulphur*		$\delta^{34}S$ *(‰)* [c]
Oceanic crust	5×10^{24}	1000	5×10^{21}	1.5		+1
Seawater	1.4×10^{24}	915	1.28×10^{21}	0.4		+21
Depleted mantle	1×10^{27}	300 *	3×10^{23}	93.2		+0.4
Continental crust	2×10^{25}	780	1.56×10^{22}	4.8		+7
					Mean	+0.8
Ordinary chondrites	-	-	-	-		+0.2 ± 0.2 ‡

Table 1.1. Sulphur contents and isotope compositions of the mantle, crust and seawater, after Chaussidon *et al.*, (1989). The term primitive mantle is the assumed initial source of sulphur held by the depleted upper mantle, oceanic crust, continental crust and seawater.

[a] Data from Heydemann (1969).
[b] Data from Sakai *et al.*, (1984), Holser & Kaplan (1966).
[c] Data from Nielsen (1978), Holser & Kaplan (1966). Mean for MORB from Sakai *et al.*, (1984).
* Upper limits of Chaussidon *et al.*, (1989)
‡ Data from Thode *et al.*, (1961), Kaplan & Hulston (1966).

Basaltic and granitic rocks generally have $\delta^{34}S$ values close to 0‰ (Fig. 1.3). This value reflects the presence of predominantly mantle-derived sulphur in these rocks with $\delta^{34}S$ values of 0±3‰ (Ohomoto, 1986). However, departures from this value may arise as a result of assimilation of crustal sulphur (*e.g.* Mainwaring and Naldrett, 1977; Poulson *et al.*, 1991) and from mantle source heterogeneities (Chaussidon *et al.*, 1987). Sedimentary rocks show a large spread in $\delta^{34}S$ (Fig. 1.3) reflecting contributions of sulphur from bacterial reduction of sulphate, which produces isotopically light sulphur, and sulphur which is isotopically heavy (marine sulphate in limestones). Sulphur is not appreciably fractionated during the precipitation of evaporitic sulphate and hence reflects the sulphur isotopic composition of the body of water from which it formed (Ault and Kulp, 1959). The spread in $\delta^{34}S$ values observed for evaporitic sulphur in Fig. 1.3 is due to changes in the sulphur isotope composition of the world's oceans through geological time. The enrichment of ocean

waters in ^{34}S reflects the contribution of sulphate from rivers, deposition of sulphate and bacterial activity, it is the competition of these three processes which change the $\delta^{34}S$ value of ocean sulphate with time.

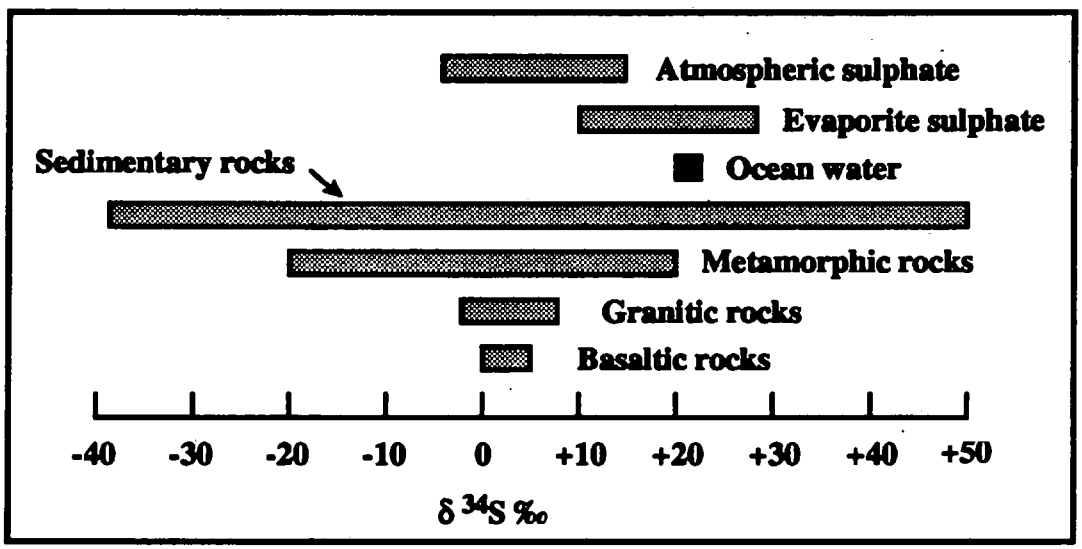

Fig. 1.3. Range of $\delta^{34}S$ values for some terrestrial rocks (Hoefs, 1986). Atmospheric sulphate data fom Holser and Kaplan (1966).

Significant sulphur isotope fractionations may occur in the mantle source region of mafic and ultramafic rocks, and also in crustal magma chambers, resulting in $\delta^{34}S$ values of sulphides outside Ohomoto's 'magmatic range' of 0±3‰. Mantle processes, which can induce such anomalous sulphur isotope values, include contamination with subducted oceanic crust (Ueda and Sakai, 1984) and high temperature isotope fractionation between liquid sulphide and sulphur dissolved in a silicate liquid (Chaussidon *et al.*, 1989). Processes in crustal magma chambers that may result in sulphur isotope variations outside the magmatic range include Rayleigh factionation during the segregation of an immiscible sulphide liquid in crustal magma chambers (Ripley 1983) and assimilation of sulphur from country rocks (Mainwaring and Naldrett, 1977). A third source of sulphur isotope heterogeneity in ophiolitic crust results from hydrothermal processes. These include reduction of seawater sulphate during the suboceanic metamorphism of oceanic crust the resulting enrichment in ^{34}S of sulphides (Shanks *et al.*, 1981; Bowers, 1989). A more detailed review of the processes that fractionate sulphur isotopes in mafic and ultramafic rocks is given in Chapter 6.

Sulphur isotope analyses of sulphides in ultramafic and mafic igneous rocks that have a close spatial association, or are intergrown, with platinum group minerals (hereafter abbreviated to PGM), should therefore help to identify the sources of the sulphur, *i.e.* magmatic, sedimentary/introduced hydrothermal *etc.* that formed the sulphide minerals (Godlevski and Grenenko, 1963; Ripley, 1981; Abrajano and Pasteris, 1989; Lydon and Richardson, 1987). Where the source of sulphur is magmatic, resultant sulphides should have $\delta^{34}S$ values that reflect a magmatic or mantle source (0±3‰, Ohomoto, 1986). However, as discussed above, caution should be exercised in interpreting $\delta^{34}S$ since high-temperature magmatic sulphur isotope fractionation mechanisms can produce sulphides with $\delta^{34}S$ values outside this range, and assimilation of crustal sulphur may produce sulphides with $\delta^{34}S$ values identical to, or outside of the magmatic range.

1.3 The ultramafic and mafic igneous complex of Shetland as an ophiolite

The Shetland ophiolite was chosen for this mineralogical and isotope study because it was known to be sulphur-enriched in the cumulate portion of the ophiolite sequence. The sulphides present are known to be associated with platinum group elements (hereafter abbreviated to PGE) (Prichard *et al.*, 1986).

The dismembered ultrabasic-basic complex of the northeast Shetland Islands (Fig. 1.4), was first described as an ophiolite complex by Garson and Plant (1973) in a study of alpine-type ultramafic rocks of the Scottish Highlands. The lithological association; basal harzburgite tectonite, ultrabasic cumulates, gabbro, and basic dykes (Fig. 1.5) conforms to the lower portion of an ophiolite complex, as defined by the delegates of the Penrose Conference (Anonymous, 1972). The complex is situated on the islands of Unst and Fetlar and the ophiolite sequence is best developed on the northernmost island, Unst, where tectonic disruption has been least severe. Re-mapping of the whole ophiolite was undertaken by Gass *et al.* (1982), in response to a re-appraisal of the chromite mineralization of the complex. Prichard and Lord (1988) presented new geochemical evidence on the basic dykes

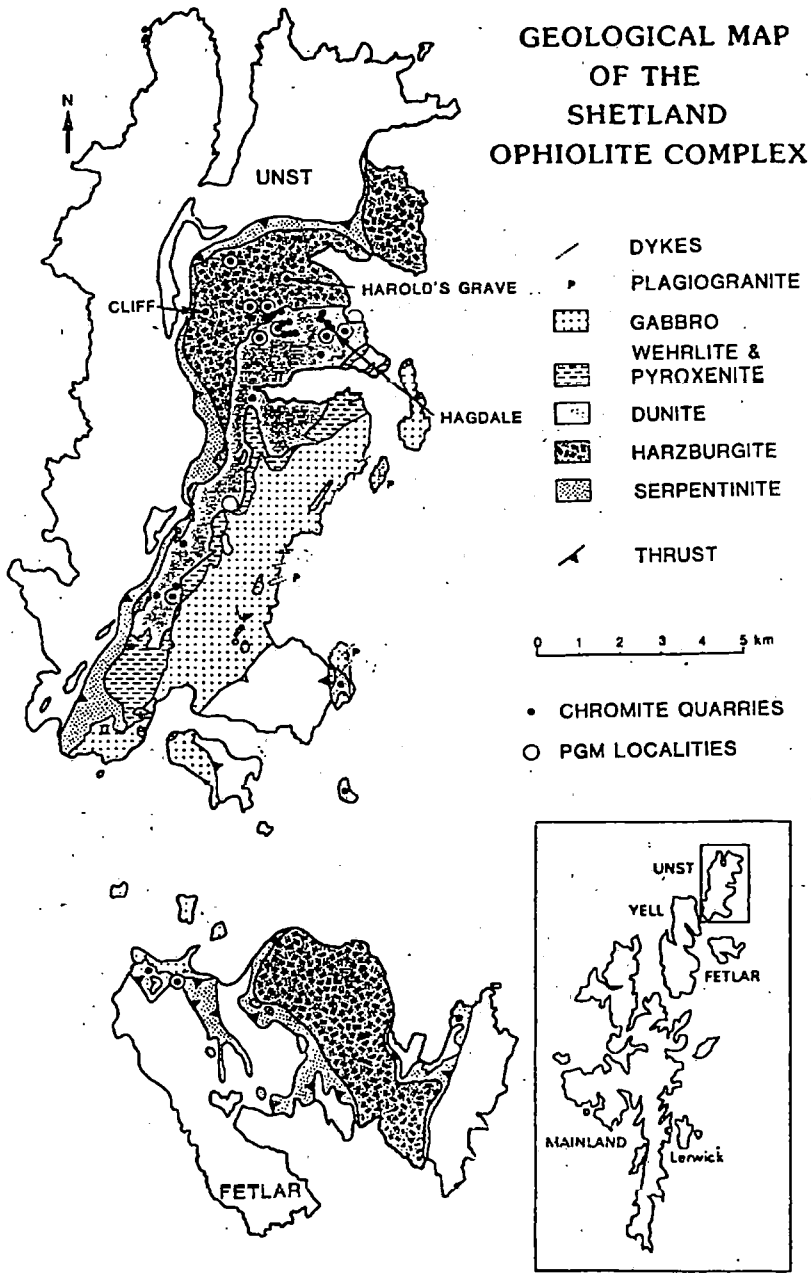

Fig. 1.4. Geological map of the Shetland ophiolite complex. Also shown are the location of disused chromite quarries and localities where PGE have been discovered. Inset map shows the location of Unst and Fetlar in relation to the Shetland Islands. After Prichard and Lord (1988).

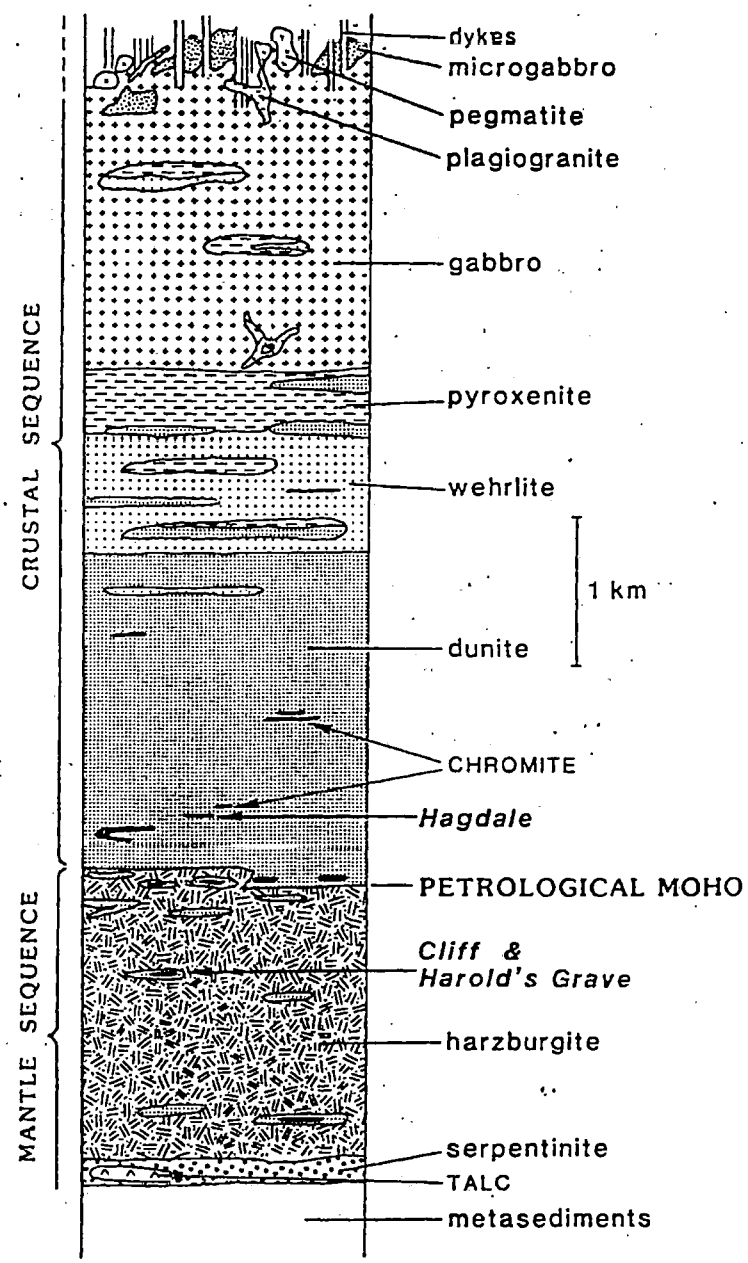

Fig. 1.5 Geological column showing the relationship of the lithologies within the Shetland ophiolite complex. Hagdale, Cliff and Harold's Grave are localities where enrichments of PGE occur. After Prichard and Lord (1988).

and podiform chromite, which confirmed the origin of the complex as part of an ophiolite, and indicated formation in a supra-subduction zone. The olivine compositions reported by Prichard (1985), are forsteritic and range from Fo_{91} for olivine in harzburgite to Fo_{89} for olivine in cumulate dunite. The olivine compositions from the harzburgite are similar to those in equivalent rocks from Troodos (Menzies and Allen, 1974) and Oman (Smewing, 1980). Similarly, the compositions of orthopyroxene determined by Prichard (1985) from the harzburgite unit of Unst, En_{91}-En_{92}, are similar to those from other ophiolitic harzburgites, *e.g.* Troodos and Oman.

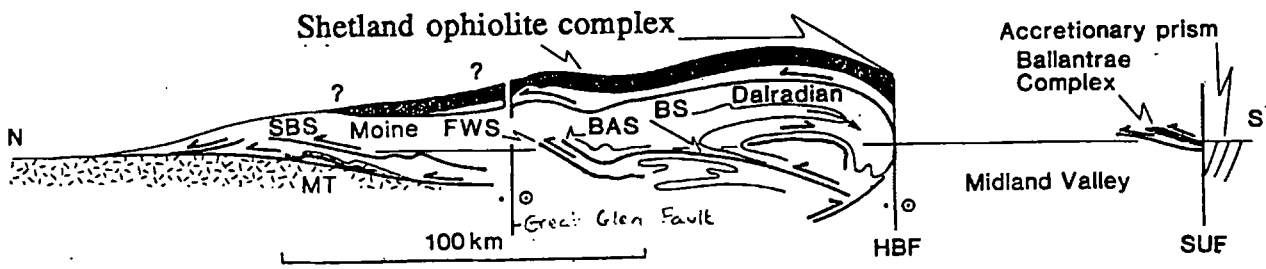

Fig. 1.6. Sketch section showing possible relationship of the Shetland ophiolite complex with the major structural features in the NW and Grampian Highlands of Scotland. BAS, Ballachulish Slide; BS, Boundary Slide; FWS, Fort William Slide; HBF, Highland Boundary Fault; MT, Moin Thrust; SBS, Sgurr Beag Slide; SUF Southern Uplands Fault. After Dewey and Shackelton (1984).

Dewey and Shackelton (1984) suggest that the Shetland ophiolite complex is comparable to other obducted ophiolite complexes such as those in Newfoundland. Furthermore they considered that the Shetland ophiolite formed part of a huge 10-15km thick obducted ophiolite that originally covered most of the Scottish Highlands. The relationship of the Shetland ophiolite to the major structures in the NW and Grampian Highlands of Scotland is shown in Fig. 1.6 (after Dewey and Shackelton, 1984). Age determinations (K-Ar) of amphibole mineral separates from the thermally inverted metamorphic sole of the Shetland ophiolite (Spray, 1988), suggest initiation of obduction of the complex at 479±6 Ma (Fig. 1.7). Final emplacement took place in late Silurian times over a

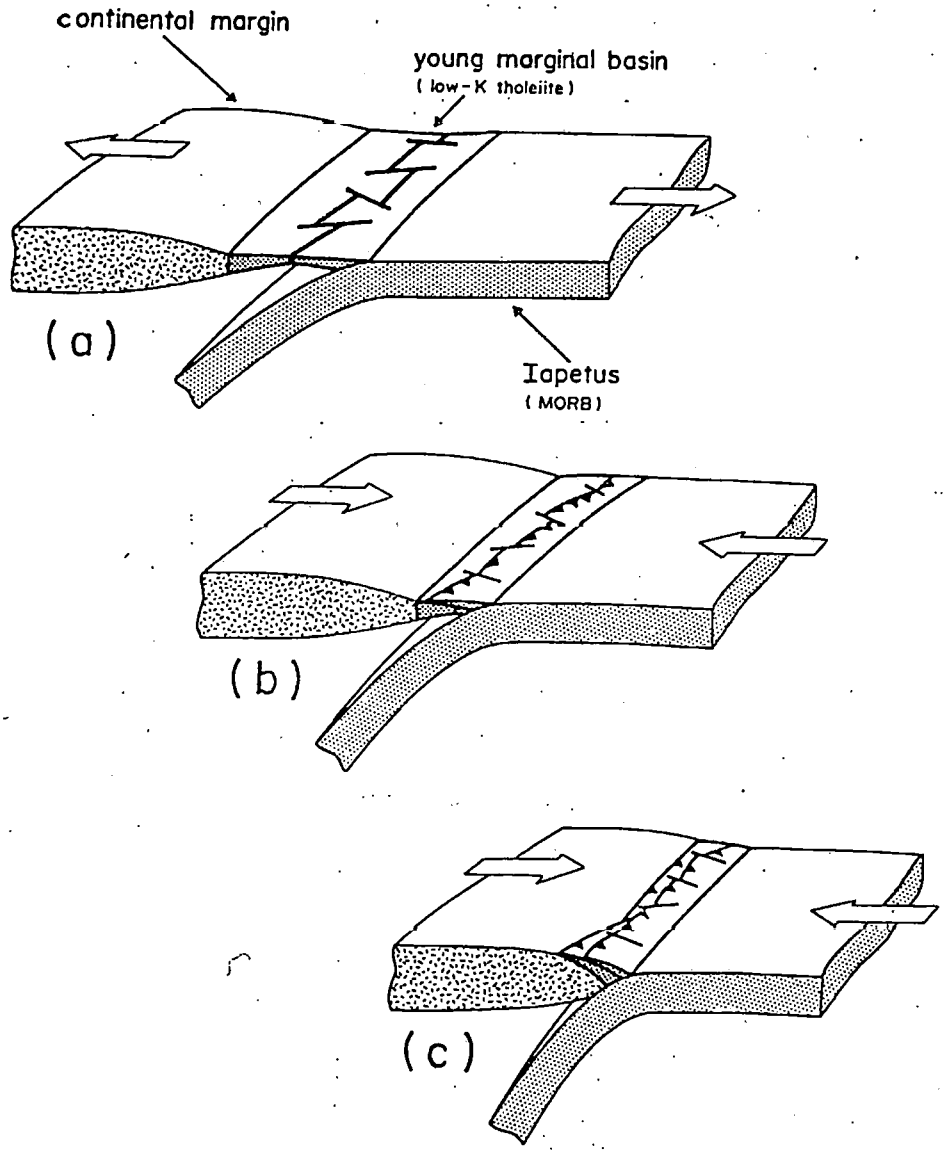

Fig. 1.7. Cartoon representation of Ordovician marginal basin development and subsequent destruction as it may have affected the Shetland Islands oceanic fragment. (a) Generation of a young (pre-arc) marginal ocean basin between a continental margin and Iapetus oceanic lithosphere during subduction (~470Ma). Relative movement between the continental and oceanic plates facilitated an intervening tensional environment. (b) At 479 ± 6Ma the overall plate movements change to compression and the marginal basin is gradually shortened. (c) Continued compression results in the destruction of the marginal basin. Some of it is thrust onto the continental margin as a series of oceanic slices.

polymetamorphic basement, which is thought to contain rocks that are equivalent to the Moine and Dalradian of Scotland (Flinn, 1985). The metamorphic sole was formed during intraoceanic thrusting and destruction of a marginal basin that was located between a continental margin and oceanic lithosphere (Spray, 1988). This oceanic lithosphere floored the Iapetus Ocean which opened sometime in the late Precambrian and gradually closed during the Lower Palaeozoic (Harland and Gayer, 1972). Some amphibolites from the metamorphic sole have chemical signatures which Spray (1988) concluded were derived from a Mid Ocean Ridge Basalt (MORB) protolith that was metamorphosed and transferred to the marginal basin hanging wall during the subduction of Iapetus.

1.4 Sulphides in the Shetland ophiolite

Heddle (1878) first described the occurrence of chromite and sulphides within the ultramafics. In more recent times a diverse assemblage of sulphides has been described from the ultramafic portion of the ophiolite (Brozowski, 1977; Neary *et al.*, 1984; Prichard *et al.*, 1986), but not systematically and only from a limited geographical coverage. Brzozowski (1977) recognized disseminated nickel iron sulphide phases associated with 'ferritchromit' (altered chromite showing Al and Mg-depletion) and magnetite, as interstitial grains within silicate inclusions in chrome spinels from Nikka Vord, Unst (uppermost harzburgite) and Hagdale, Unst (cumulate dunites). The opaque mineral assemblages recognized by Brzozowski (1977) are shown in table 1.2. In addition, copper was found in sulphide phases in the eastern area of Nikka Vord and Hagdale. The nickel mineralization at Hagdale was postulated by Brzozowski (1977) to represent a possible hypogene (magmatic) setting within the chromite deposits, with the replacement of pentlandite by millerite, polydymite and heazlewoodite during serpentinization. The assemblage of millerite, polydymite and magnetite are thought to reflect talc-carbonate alteration (Groves *et al.*, 1974). Brzozowski (1977) found that these sulphide compositions showed an alteration trend of Ni and Co-enrichment related to serpentinization. Supergene alteration of the sulphides to bunsenite (NiO) and zaratite [$NiCO_3 2Ni(OH)_2.4H_2O$] occurred where sulphides were exposed in surface samples.

Mineral assemblages;	*Mineral formulae;*	
pentlandite-heazlewoodite	pentlandite	$[(FeNi)_8S_9]$
pentlandite-millerite--polydymite	heazlewoodite	$[Ni_3S_2]$
millerite-heazlewoodite	millerite	$[(Co_{0.01}Ni_{0.95}Fe_{0.04})S]$
pentlandite-millerite- copper-linnaeite	polydymite	$[Ni_3S_4]$
millerite-maucherite-magnetite	cuprian-linnaeite	$[(Ni_{2.54}Cu_{0.46})S_4]$
pentlandite-chromite	maucherite	$[(Ni(Sb))_3As]$
pentlandite--violarite-polydymite	magnetite	$[Fe_3O_4]$
millerite-polydymite-siegenite	chromite	$[FeCr_2O_4]$
violarite-magnetite-millerite	violarite	$[(NiFe)_3S_4]$
	siegenite	$[(Co_{1.21}Ni_{1.26}Fe_{0.53})_3S_4$

Table 1.2. Opaque mineral assemblages in the ultramafic part of the Shetland ophiolite, Unst, recognized by Brzozowski (1977).

Disseminated Ni-Fe and Cu-bearing sulphides in the ultrabasic portion of the Shetland ophiolite complex have been found enclosing or closely associated with PGMs (Neary *et al.*, 1984; Prichard *et al.*, 1986; Ixer and Prichard, 1989). Gunn *et al.* (1985) described Ni/Fe sulphides (pentlandite), Ni-sulphides (heazlewoodite and godlevskite $[Ni_7S_6]$) and Ni-arsenides (orcelite $[Ni_{5-x}As_2]$ and maucherite) from the PGE-rich Cliff locality. They concluded that the sulphide/arsenide mineralogy was consistent with formation during the serpentinization ($T<500^oC$) of peridotite and that the association and textural relationships of PGM with the nickel sulphides/arsenides indicated that the PGE mineralization was also deposited at similarly low temperatures. Supergene alteration of Ni-arsenides to annabergite $[(Ni,Co)_3(AsO_4)_2.8H_2O)]$ and some pentlandites to uncharacterized Ni-Fe sulphates was also noted.

In the ultramafic cumulates of Unst, Pt and Pd were initially concentrated into the first sulphides, represented by disseminated stratiform sulphide + PGE enrichments, that precipitated from a new input of magma into a crustal magma chamber (Prichard and Lord, 1990). Pt and Pd are now concentrated as discreet PGM that are closely associated with the

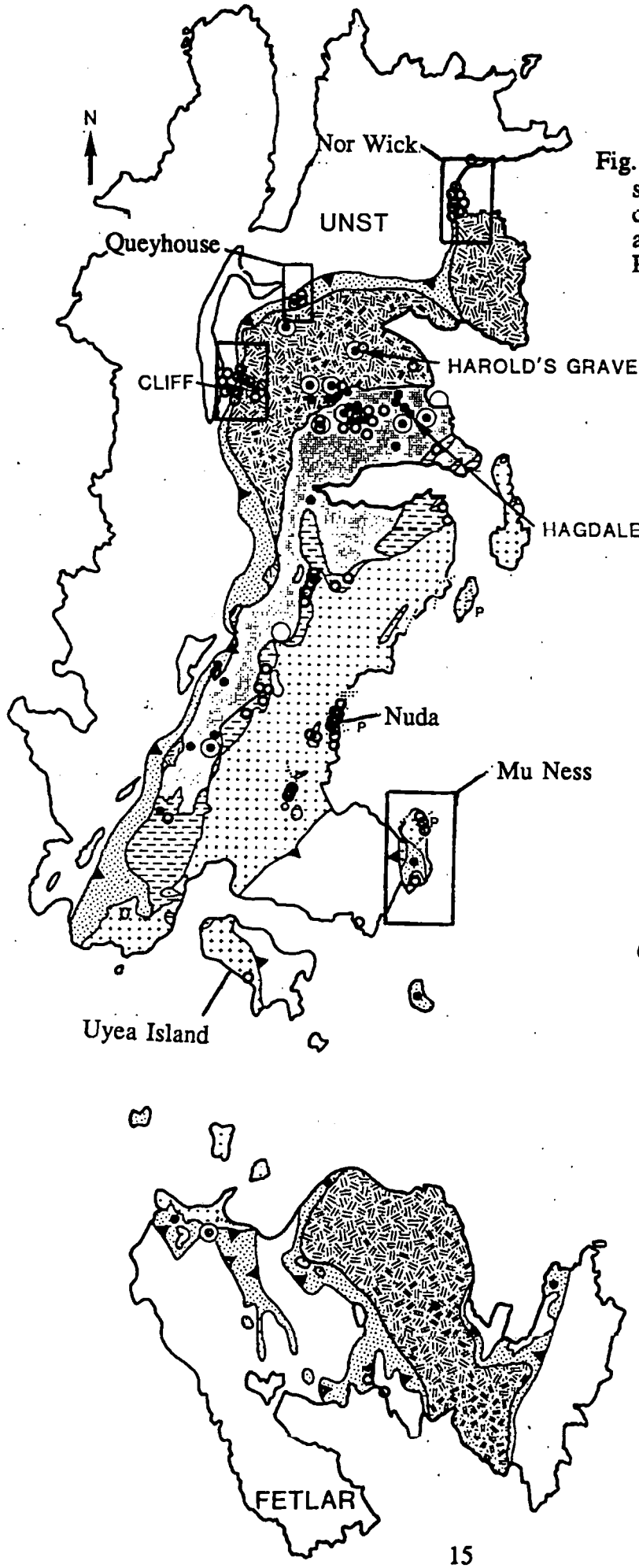

Fig. 1.8. Map of the Shetland ophiolit showing the location of the sample collected during the present study and those collected by Dr. H.M. Prichard and Dr. R.A. Lord.

disseminated, predominantly Ni-bearing sulphides. The paragenesis of these PGM is therefore thought to be intimately linked to the alteration of the associated sulphide phases (Prichard and Lord, 1990). There has been some debate as to the source of PGE in sulphide and PGE-enriched dunites and chromitites subjacent to the basal thrust of the ophiolite, (*i.e.* whether they are magmatic, remobilized or introduced by hydrothermal fluids). Arguments for and against these processes are described in detail by Lord (1991). Gunn *et al.* (1985) suggested that the PGE mineralization at Cliff resulted from hydrothermal processes, whereas Prichard *et al.* (1986) considered it to result from magmatic processes on the basis of textural studies. A third model, suggested by Lord (1991), involved the hydrothermal reworking of a magmatic PGE concentration. The PGE-enriched rocks contain high concentrations of arsenic, which is considered to have been introduced from a fluid that was channelled along the basal thrust (Prichard and Lord, 1989). A possible source of the arsenic in the PGE-rich rocks is the metasediments situated immediately below the basal thrust.

Despite the previous work on the sulphide minerals from the Shetland ophiolite, little was known about the variation in sulphide mineral assemblages throughout the complex, or the details of their alteration. In addition, the Shetland ophiolite complex was of special interest because of the discovery of unusually high grades of the PGE including Pt and Pd. These elements are chalcophile and known to be associated with base-metal sulphide concentrations (see below)

1.5 Thesis organization

1.5.1 Objectives;

1) To describe the sulphide mineralogy and sulphur isotope geochemistry of a suite of igneous and altered lithologies from the Shetland ophiolite complex.

2) To compare the sulphide mineralogy and sulphur isotope geochemistry of other ophiolites and oceanic crust, leading to an understanding of the processes responsible for the siting of mineralization in the Shetland ophiolite.

3) To understand the relationships between the sulphide mineralogy, sulphur isotope geochemistry and the PGE mineralization in the complex.

4) To help constrain the model for PGE mineralization at Cliff.

5) To understand the igneous fractionation of sulphides and sulphur isotopes in the complex.

6) To describe the alteration processes affecting sulphides in the complex.

1.5.2 Sample localities

In order to achieve these objectives, samples were chosen to represent the complete range in lithologies and alteration styles present in the ophiolite. A geological map of the ophiolite of Unst showing the positions of the 45 samples collected and analysed during this study are shown in Fig. 1.8. In addition to these samples, the map shows the location of selected samples taken from over 200 rocks collected by Drs. H.M. Prichard and R.A. Lord during a research program designed to ascertain the distribution of PGE in the ophiolite. A more detailed map of samples collected during this study is given in appendix C.

1.5.3 Techniques

In order to facilitate the objectives outlined above, the following analytical techniques were used:

(1) Reflected light microscopy, to help characterize the sulphide and opaque mineral assemblages.

(2) Electron microprobe and SEM techniques to quantitatively and semi-quantitatively characterize the opaque minerals.

(3) Stable isotope analysis (sulphur, helium, hydrogen and oxygen) to constrain the source of sulphur and igneous fractionation processes (sulphur and helium) and hydrothermal alteration of the silicate lithologies (hydrogen and oxygen).

1.5.4 Structure of the thesis

A general account of the petrology and structure of the Shetland ophiolite complex follows in Chapter 2 to set up a geological framework in which the following mineralogical and stable isotope results are considered. Aspects of the primary and secondary silicate mineralogy are also examined in Chapter 2 to place constraints on the alteration of intergrown opaque mineral phases. Following on from this, Chapter 3 gives a detailed account of the sulphide mineralogy from each of the major silicate lithologies of the ophiolite complex, illustrated with relevant photomicrographs, and also describes the sulphide and

opaque mineral chemistry. Chapter 4 relates the sulphide mineral asemblages established in Chapter 3 to other natural sulphide mineral assemblages and experimental data in order to place constraints on the low temperature, re-equilibration processes. Chapter 5 details the techniques used to elucidate the sulphur isotope geochemistry of the complex and Chapter 6 discusses the stable isotope geochemistry of the sulphide assemblages using sulphur, helium, hydrogen and oxygen isotope analysis. The source and magmatic fractionation of the sulphides are addressed along with the alteration of their host silicate lithologies.

Chapter 2

Petrology, structure, geochemistry and mineralogy

2.1 Introduction

In this chapter a brief description of the petrology and structure of the Shetland ophiolite is followed by an account of the whole-rock geochemistry and silicate mineralogy from each of the major lithologies. Special attention is paid to the secondary silicate mineral assemblages as these provide constraints on the physical and chemical conditions which prevailed during the alteration of sulphides. Silicate minerals were identified by a combination of transmitted light microscopy, X-ray diffraction and wavelength dispersive electron microprobe analysis. Compositions of the silicate minerals were determined solely by wavelength dispersive electron microprobe analysis. The operating and standardization procedures for this technique are given in appendix A.1.

2.2 Petrology and structure of the Shetland ophiolite

The field relations and petrology of the ophiolite have been described in detail by Brzozowski (1977), Gass *et al.* (1982), Prichard (1985) and Lord (1991). A summary of some of the more pertinent features follows.

2.2.1 Ultramafic rocks

The ultramafic portion of the ophiolite comprizes harzburgite, dunite, wehrlite and clinopyroxenite (Prichard, 1985). The harzburgite unit is often extensively serpentinized, but some fresh olivine, orthopyroxene (up to 15%), clinopyroxene (up to 5%) and accessory chrome-spinel is present. Alternating layers of pyroxene and olivine define a mantle foliation which is sub-parallel to the base of the dunite unit. Serpentinized pyroxenite 'dykes' cross-cut the harzburgite at all levels (Lord, 1991). Dunite 'dykes', 5-10cm wide, are concordant with, or cross-cut the phase-zoning at acute angles. Spinel orientations define two foliation directions, the first being gently folded around the second. Both these structural events are considered to be pre-emplacement features as they both die out upwards within the dunites

and are very rarely present in the lowermost gabbros. Lenses of dunite from a few metres to several hundred metres across occur throughout the harzburgite unit. These lenses sometimes contain massive podiform chromite, but in other cases are barren or contain only thin layers enriched in chromite (Prichard and Lord, 1988). The harzburgite is overlain by up to 1600m (Lord, 1991), of massive cumulate dunite with rare dunite veins or dykes. When unaltered, the dunite consists of 1-4mm sized olivine crystals that form 85-95 volume % of the rock, and exhibits an extreme adcumulate texture. Accessory chrome-spinel may constitute up to 15 volume % and minor interstitial sulphides are common (Brzozwski, 1977). Chromite concentrations in the dunite unit range from discontinuous, usually single crystal layers, to laterallly continuous, metre-wide layers of disseminated to massive chromite. Dunite grades stratigraphically upwards, with increasing clinopyroxene content, into wehrlite and pyroxenite and all three lithologies may be interlayered over a distance of 1 to 10's of metres. Cumulate wehrlite and pyroxenite are composed of varying proportions of olivine and clinopyroxene and minor amounts of chrome-spinel and accessory sulphide. Individual clinopyroxene crystals in wehrlites and pyroxenites are usually 2-4mm in size, but a pegmatitic pyroxenite facies from near the contact with the gabbro unit consists of centimetre-sized crystals. Lenses of wehrlite and pyroxenite also occur at higher stratigraphic levels within the gabbro unit. These bodies have wehrlitic bases and grade stratigraphically upwards into pyroxenite.

2.2.2 Mafic rocks

The mafic rocks comprise the gabbro unit, the base of a sheeted dyke complex and co-genetic plagiogranites and amphibole pegmatites. The gabbros are massive to phase-layered pyroxene gabbros which overlie the cumulate pyroxenites. The two rock types may have sharp, tectonic contacts (Flinn, 1970), or display intrusive contacts. Gabbros are extensively altered to a greenschist facies mineral assemblage of albite-epidote-actinolite-chlorite-quartz. The grain size of the gabbro is variable, especially near the top of the unit where both microgabbro and pegmatitic facies are common, along with felsic, late-stage differentiates represented by plagiogranite. The gabbros are cut by basic dykes, plagioclase-hornblende pegmatites, and at higher stratigraphic levels by rare sulphide veins. Basic dykes

intrude the highest levels of the gabbro and in places make up 50% of the exposure. Massive microgabbro from the north of the Mu Ness peninsula (Fig. 1.8) is cut by shears and contains abundant veins of epidote. Hosted within this rock are sporadic pods of pyrite mineralization, one example measuring approximately 1 by 2.5 metres in outcrop.

2.3 Whole rock geochemistry

Major and trace element geochemistry of a range of relatively unaltered to highly altered ultramafic and mafic rocks collected during the present work is consistent with other published whole-rock geochemistry of ultramafic and mafic rocks from this complex *e.g.* Amin (1954), Flinn (1970) and Gass *et al.* (1982).

2.3.1 Geochemistry of partially altered mafic and ultramafic rocks

The major and trace element contents of partially altered rocks are given in table 2.1a-c. Undeformed, serpentinized dunites, including dunite pods, contain approximately 40 wt.% MgO, 8-12 wt.% $Fe_2O_3^t$ (total iron as Fe_2O_3) and usually contain <1 wt.% Al_2O_3. Dunites contain negligible amounts of Ti 0.01 wt.%, Ca 0.24 wt.% and Na 0.92 wt.%. Harzburgite, not analysed during this study, is reported to contain significantly higher levels of Al, Si, and V compared to dunites (Gunn *et al.*, 1985) and this likely reflects the presence of pyroxene in the harzburgites. Cumulate and high-level pyroxenites are characterized by higher calcium, 8-14 wt.% CaO, and aluminium, 2-3 wt.% Al_2O_3, reflecting the presence of cumulus pyroxene. Gabbros contain 6-20 wt.% MgO, 9-12 wt.% $Fe_2O_3^t$, high aluminium (5-20 wt.%), often contain >0.5 wt.% TiO_2 and similar concentrations of CaO to the pyroxenites with 0.5-4 wt.% Na_2O.

2.3.2 Geochemistry of talc-carbonate rock and highly sheared gabbros

Read (1934) identified an episode of stress, or dislocation metamorphism which resulted in the recrystallization of ultramafic rocks to antigorite and talc-carbonate rocks and mafic rocks to tremolite-zoisite schists. Rocks representing this event are most prevalent in the immediate vicinity of the basal thrust and are associated with predominantly harzburgite plus lesser amounts of dunite and chromitite. Some internal zones of intense alteration which

ELEMENT	*Gabbro* *JM1*	*Gabbro* *JM2*	*Gabbro* *JM3*	*Gabbro* *JM4*	*Gabbro* *JM6*	*Amphibole pegmatite* *MNA*	*Mineralized gabbro* *MNG*	*Dolerite dyke* *JM5*	*Dolerite dyke* *JM9*	*Plagiogranite* *JM8*
SiO2	43.16	43.21	46.93	44.79	46.41	46.63	37.62	48.81	47.72	60.73
TiO2	0.62	0.29	0.11	0.18	0.27	0.52	1.05	1.01	1.17	0.29
Al2O3	18.6	19.3	5.53	7.63	17.33	6.36	11.44	15.54	15.67	19.94
Fe2O3	12.36	9.12	11.35	14.83	10.31	19.03	21.75	11.3	11.32	3.42
MnO	0.16	0.12	0.11	0.21	0.19	0.27	0.15	0.17	0.17	0.04
MgO	6.89	8.05	20.24	17.48	8.22	9.93	2.71	8.08	7.46	1.44
CaO	10.52	13.52	9.57	9.13	12.47	12.57	13.5	8.52	10	4.04
Na2O	3.05	2.1	0.68	0.73	2.92	1	0.54	3.65	3.76	9.75
K2O	0.07	0.08	0.05	0.05	0.08	0.06	0.06	0.13	0.24	0.11
P2O5	0.02	0.02	0.02	0.02	0.04	0.03	0.02	0.06	0.12	0.09
S	0.11	0.06	0.02	0.01	0.02	0.16	0.17	0.05	0.05	0.07
LOI	3.75	3.27	5.02	4.19	2.55	3.18	7.31	2.86	2.77	1.31
TOTAL	99.31	98.82	99.55	99.25	100.81	99.65	95.69	100.18	100.45	101.23
Ti	3720	1857	735	1143	1673	3376	6691	4893	5549	1772
Cr	78	247	2858	555	231	908	1012	577	370	45
Mn	1432	1015	1039	1904	1461	2715	2030	1506	1364	263
Ni	13	12	148	64	17	23	25	67	33	11
Cu	64	76	129	90	16	229	197	54	34	109
Zn	85	49	52	84	70	83	47	91	87	9
Ga	18	13	5	8	16	14	21	16	18	15
As	12	27	81	9	6	16	33	4	12	49
Rb	2	2	2	2	2	3	4	3	5	1
Sr	291	386	7	4	202	129	389	154	124	66
Y	5	2	1	2	11	89	17	22	24	8
Zr	11	13	4	4	12	29	45	63	66	42
Nb	2	2.3	2.1	2	2.6	4.1	3	2.2	3.2	1.9
Mo	3	3	3	3	3	3	3	3	3	3
Pb	4	4	4	6	5	8	9	4	4	6
Th	3	3	3	4	3	5	6	3	3	2
U	3	4	3	3	4	5	6	3	3	3

Table 2.1a. Major and trace element wavelength dispersive X-ray fluorescence analysis of rocks from the Gabbro complex.

ELEMENT	*High-level pyroxenite JM20*	*High-level pyroxenite JM21*	*High-level pyroxenite JM22*	*High-level pyroxenite JM23*	*High-level pyroxenite JM44*	*High-level pyroxenite JM45*	*Cumulate pyroxenite JM10*	*Cumulate pyroxenite JM11*	*Cumulate pyroxenite JM12*	*Cumulate pyroxenite JM13*	*Cumulate pyroxenite JM14*
SiO2	43.86		41.8		45.58	41.76	40.52	44.2	48.07	45.44	47.5
TiO2	0.09	n.d.	0.08	n.d.	0.13	0.13	0.01	0.05	0.03	0.05	0.04
Al2O3	2		2.23		2.74	2.38	1.87	2.32	3.63	2.96	2.94
Fe2O3	9.21		9.61		6.92	10.12	9.07	7.35	6.32	7.34	5.73
MnO	0.13		0.14		0.15	0.15	0.15	0.12	0.11	0.12	0.12
MgO	27.72		29.28		21.25	27.02	40.42	26.34	21.17	23.37	21.53
CaO	7.14		7.49		14.51	8.14	0.21	12.35	13.01	14	16.53
Na2O	0.63		0.99		0.7	0.62	0.78	0.65	1	0.67	0.65
K2O	0.03		0.02		0.05	0.03	0.02	0.04	0.05	0.04	0.06
P2O5	0.02		0.02		0.02	0.02	0.02	0.02	0.02	0.02	0.02
S	0.01		0.01		0.01	0.01	0.01	0.01	0.01	0.06	0.01
LOI	8.46		9.58		6.51	7.95	11.32	6.1	5.97	5.1	4.78
TOTAL	99.3		101.25		98.57	98.33	102.78	99.38	100.39	99.17	99.91
Ti	572		524		785	814	143	413	330	357	320
Cr	3046		3503		4199	2477	3362	3706	2923	3519	4125
Mn	1085		1112		1096	1244	1108	841	882	928	884
Ni	601		670		386	593	1450	713	685	1204	532
Cu	13		17		9	96	16	36	257	1328	149
Zn	37		34		37	47	48	33	37	30	27
Ga	6		6		5	5	5	4	5	4	4
As	42		28		67	28	9	4	5	5	5
Rb	2		2		2	2	1	2	2	2	2
Sr	4		4		12	64	1	2	46	5	23
Y	2		1		3	1	1	2	2	2	2
Zr	3		2		2	5	1	2	4	2	3
Nb	2		2.1		2.6	1	1	1.9	2	2.2	1.9
Mo	3		2		3	3	3	3	3	3	3
Pb	4		5		5	4	4	4	9	7	6
Th	3		3		3	3	2	3	3	3	3
U	3		2		3	3	2	3	3	3	3

Table 2.1b. Major and trace element wavelength dispersive X-ray fluorescence analysis of pyroxenites. nd= major element analysis not performed.

ELEMENT	*Wehrlitic dunite JM37*	*Cumulate dunite JM38*	*Cumulate dunite JM39*	*Cumulate dunite JM40*	*Cumulate dunite JM41*	*Transitional dunite JM42*	*Dunite pod JM43*	*Dunite pod JM34*	*Dunite pod JM36*	*Podiform chromitite JM35*	*Podiform chromitite JM33*
SiO2	35.01	35.29	35	35.09	35.59	37.85	35.41		35.84		
TiO2	0.01	0.01	0.01	0.01	0.01	0.01	0.01	n.d.	0.01	n.d.	n.d.
Al2O3	0.83	1.09	0.5	0.78	0.58	0.61	0.49		0.54		
Fe2O3	10.59	12.16	11.96	10.43	10.39	9.47	8.55		7.81		
MnO	0.14	0.16	0.16	0.13	0.14	0.13	0.11		0.09		
MgO	38.34	38.5	41.53	40.94	40.88	39.52	42.49		40.25		
CaO	1.5	0.13	0.17	0.6	0.25	0.11	0.15		0.22		
Na2O	0.7	1.09	1.12	0.95	1.35	0.93	1.01		0.65		
K2O	0.01	0.02	0.01	0.01	0.01	0.01	0.01		0.01		
P2O5	0.02	0.02	0.02	0.02	0.02	0.02	0.02		0.02		
S	0.01	0.01	0.01	0.02	0.01	0.02	0.01		0.02		
LOI	13.04	12.45	10.9	11.3	11.95	12.16	14.02		14.43		
TOTAL	100.2	100.93	100.94	100.28	101.18	100.82	102.28		99.89		
Ti	59	57	55	57	58	56	57	57	54	57	223
Cr	1471	4010	1064	2153	1677	1561	1481	977	2120	1229	163481
Mn	1216	1336	1335	1137	1117	1051	993	885	724	1300	2929
Ni	1605	2193	1577	2347	2070	2838	2816	2845	2543	1658	2031
Cu	23	111	33	394	156	260	71	91	10	17	29
Zn	43	66	60	44	41	44	41	34	37	44	276
Ga	3	6	4	4	3	3	3	3	3	6	10
As	5	10	9	6	10	5	4	7	8	6	418
Rb	1	2	2	2	1	2	1	1	1	2	3
Sr	4	9	2	2	7	3	1	1	5	4	6
Y	1	2	2	2	1	1	1	1	1	2	2
Zr	2	2	1	1	3	2	1	1	2	2	2
Nb	1	1	2	2	1.8	1	1	1	2	2	2
Mo	2	2	3	3	2	2	2	2	3	3	3
Pb	4	5	5	5	3	3	3	3	4	5	8
Th	2	3	3	3	2	2	2	2	2	3	5
U	2	3	3	3	2	2	2	2	2	3	5

Table 2.1c. Major and trace element wavelength dispersive X-ray fluorescence analysis of podiform chromite, dunite and wehrlitic dunite. nd= major element analysis not performed.

ELEMENT	*Serpentinite* *JM25*	*Talc-carbonate rock* *JM31*	*Talc-carbonate rock* *JM32*	*Talc-chlorite schist* *JM16*	*Talc-chlorite schist* *JM17*	*Talc-chlorite schist* *JM19*
SiO2	37.21	38.88		37.69	30.91	55.67
TiO2	0.01	0.01	n.d.	0.01	0.01	0.01
Al2O3	0.61	0.73		9.82	0.4	2.34
Fe2O3	6.62	7.18		10.7	5.94	5.16
MnO	0.09	0.07		0.01	0.1	0.02
MgO	39.59	34.8		29.59	35.25	28.77
CaO	0.56	0.29		0.28	0.34	0.1
Na2O	1.32	0.75		0.68	0.5	0.96
K2O	0.01	0.03		0.14	0.01	0.04
P2O5	0.02	0.02		0.02	0.02	0.02
S	0.02	0.01		0.03	0.01	0.01
LOI	16.15	16.99		11.53	26.41	6.37
TOTAL	102.2	99.76		100.5	99.9	99.47
Ti	55	59	278	150	61	61
Cr	1596	1755	2811	246	3497	739
Mn	782	626	856	52	860	163
Ni	2178	2996	2343	811	2472	1648
Cu	12	8	30	9	11	7
Zn	29	43	35	54	47	68
Ga	6	4	6	21	3	7
As	31	339	55	11	5	3
Rb	1	1	1	11	1	2
Sr	12	7	9	14	2	1
Y	1	1	1	2	1	1
Zr	1	3	6	2	1	1
Nb	2	1	2.1	2	1.8	1.3
Mo	3	2	2	1305	3	311
Pb	4	3	3	5	4	6
Th	2	2	2	3	2	2
U	2	2	2	3	2	2

Table 2.2. Major and trace element wavelength dispersive X-ray fluorescence analysis of serpentinite talc-carbonate rock and talc-chlorite schist. nd= major element analysis not performed.

are found throughout the complex may also be ascribed to this event. The geochemistry of talc-carbonate rocks from close to the basal thrust (Cliff) and talc-schists (Queyhouse talc quarry, Fig. 1.8) are given in table 2.2. A Si-enrichment and concommitant Mg-depletion trend is apparent from harzburgite, to talc-carbonate rock to talc-chlorite schist, if harzburgite is assumed to be the protolith to these rocks. This chemical trend is similar to that described by Gunn *et al.* (1985) and is a common alteration feature at the contact of peridotite and country rock (*e.g* Auclair *et al.*, 1993). An internal shear zone in cumulate pyroxenite, represented by tremolite-serpentine rock has higher Si and lower Mg than surrounding cumulate pyroxenites. Tremolite-zoisite schists along shears in gabbro contain lower Ti, Al, Na and higher Mg and Cr compared to unsheared varieties.

2.3.3 Water and carbon content of altered rocks from the Shetland ophiolite

Serpentinized ultramafic rocks, highly sheared talc-carbonate rocks and sheared gabbros are characterized by high water contents.

Sample	*wt.% H_2O*
dolerite dyke	3.2
amph. pegmatite	1.6
gabbro	1.5
gabbro	4
gabbro	3
gabbro	3.3
pyroxenite	5.3
h.l. pyroxenite	3.4
pyroxenite	5.4
pyroxenite	5.1
pyroxenite	3.3
wehrlite	11
dunite	10.5
dunite	9.7
dunite	10.3
dunite	8.1
transitional dunite	11.1
dunite pod	11.4
podiform chromite	5.8

Table 2.3. Whole-rock water contents of representative lithologies from the Shetland ophiolite complex. The data was obtained by the pyrolysis of whole-rock powders at 1100°C following heating of the sample to 200°C for 2 hours to remove any adsorbed moisture. Abbreviations; amph. pegmatite = amphibole pegmatite, h.l. pyroxenite = high-level pyroxenite.

This feature is ascribed to the presence of hydrous silicate mineral phases within the rock. The amount of water contained within a given sample (table 2.3) was determined during the hydrogen isotope analysis of whole-rock powders (see Chapter 6), and essentially represents structural water liberated by the decomposition of hydrous silicate minerals over a temperature interval between 200 and 1100°C.

Table 2.3 shows that serpentinized dunites contain the most water (up to 11.4 wt.% H_2O, average 10.19 wt.%), reflecting the presence of large quantities of serpentine minerals, whereas pyroxenites and gabbros contain significantly lower concentrations of water, average 3.9 wt.% and 2.5 wt.% respectively, reflecting the presence of a less hydrous mineralogy of predominantly secondary amphibole plus serpentine. Water, released as a by-product of the stepped combustion analysis of sulphur (discussed in detail in Chapter 5) in an altered high-level pyroxenite, is liberated at temperatures >500°C, which is consistent with water released from hydrous silicate minerals. CO_2 liberated from the same sample is released between 600 and 800°C (Fig. 2.1a) and most likely represents carbon from carbonate minerals contained within the sample (see table 2.4).

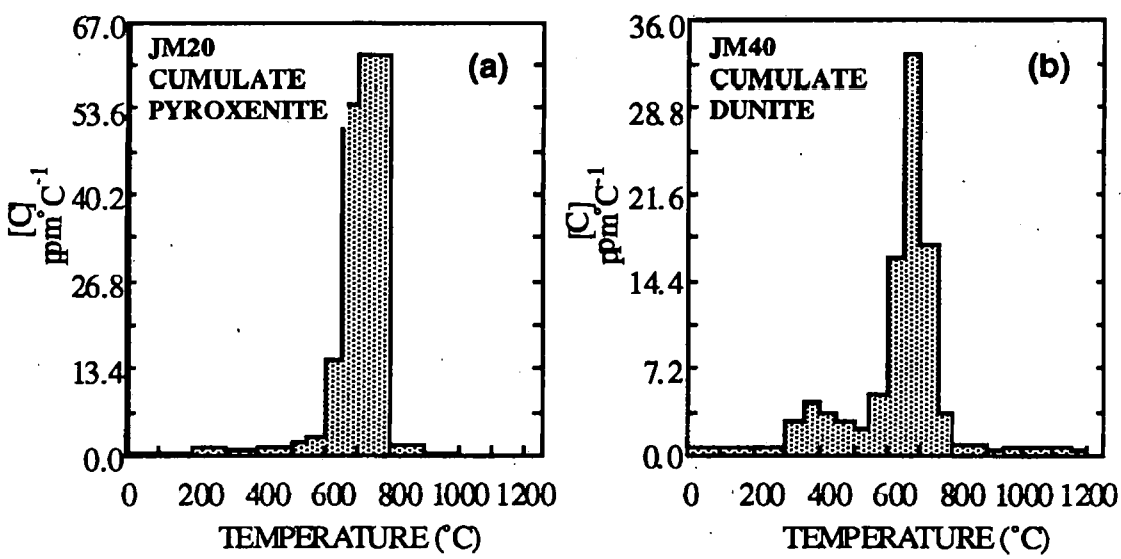

Fig 2.1. Stepped combustion profiles for carbon of two whole-rock powders from the Shetland ophiolite. (a) cumulate pyroxenite showing single carbon release characteristic of carbonate carbon; (b) cumulate dunite showing a small low temperature release, probably from contaminant organics and a larger high temperature release probably from carbonate carbon.

This carbon constitutes 1.03wt% of the altered high-level pyroxenite rock sample. The stepped combustion carbon release profile of a sample of cumulate dunite also suggests the presence of carbonate carbon (Fig. 2.1b) within the sample. The lower temperature release of carbon in this sample is probably derived from contaminant organic material (table 2.4)

Temp(°C)	Component
<200	Surficially-adsorbed gases Loosely bound carbonates
200-500	Organics (indigenous and contaminant)
500-700	Carbonates Elemental carbon
>700	Graphite Diamond Carbide

Table 2.4. Temperature intervals over which different carbon species combust, after Grady *et al.* (1988).

2.4 Primary silicate mineralogy

As discussed above, the Shetland ophiolite complex is extensively altered (*e.g.* Read, 1934) but primary cumulus minerals are preserved within the crustal layered complex and also in the mantle sequence.

2.4.1 Olivine

Olivine and its pseudomorphs constitute about 80 modal % of the harzburgite unit. Olivine in harzburgite exhibits a granular texture and is sometimes enclosed by orthopyroxene. Some olivine grains show strain extinction and twinning (Prichard, 1985). In the cumulate dunite unit olivine and its pseudomorphs constitute 85-95 volume % of the rock.

Olivine analyses determined by wavelength dispersive electron microprobe analysis, are given in table 2.5. Compositions range from $Fo_{92.2}$ (dunite pod in harzburgite) to $Fo_{87.5}$ (cumulate dunite). Olivine in cumulate dunites ranges from $Fo_{87.5}$-$Fo_{91.3}$, and if the dunite sampled from the transitional harzburgite is included then this range is extended to $Fo_{91.9}$.

The NiO content of olivine ranges from 0.45 wt.% (dunite pod in harzburgite) to 0.15 wt.% (cumulate dunite) with an average value of 0.25 wt.%. Olivine from a wehrlitic dunite ranges from $Fo_{88.7}$-$Fo_{89.1}$ and contains 0.21-0.24 wt.% nickel. There appears to be large non-systematic changes in olivine mineral chemistry through the dunite unit, often with abrupt changes to more primitive compositions. More evolved compositions do occur at the higher stratigraphic levels of this unit (in wehrlitic dunite). These observations are consistent with an open-system fractionation model in the crustal cumulate rocks of the ophiolite complex whereby batches of primitive magma mix with an evolving resident magma (Lord, 1991).

2.4.2 Orthopyroxene

Orthopyroxene constitutes up to 12% of the modal mineralogy of the harzburgite unit and usually forms larger crystals which are often more altered than co-existing clinopyroxene crystals (Prichard, 1985). The composition of orthopyroxene from harzburgite, $En_{90.5}$-$En_{91.5}$, is similar to analyses from other harzburgites, *e.g.* Troodos ophiolite, Cyprus and the Semail ophiolite, Oman (Prichard, 1985).

2.4.3 Clinopyroxene

Clinopyroxene forms ~5% of the modal mineralogy of harzburgite in the Shetland ophiolite (Prichard, 1985). Clinopyroxene first appears as a cumulus phase towards the top of the dunite unit which grades into wehrlite and pyroxenite although all three lithologies may be interlayered over a distance of 1 to 20 metres (Prichard, 1985).

Individual clinopyroxene crystals in wehrlites and pyroxenites are generally fresh and usually 2-4mm in size, but a pegmatitic pyroxenite facies from near the contact with the gabbro unit consists of centimetre-sized crystals. Microprobe analysis of clinopyroxenes from wehrlitic dunite, cumulate pyroxenite and high-level pyroxenite are given in table 2.6. They are end-member diopsides with TiO_2 contents ranging from 0.04-0.11 wt.% with Cr_2O_3 from 0.25-1.02 wt.% and contain exsolution lamellae of more Cr-rich clinopyroxene.

	Dun. pod	*Trans dun.*	*Cumulate Dunite*							*Wehr dun*
SiO_2	41.22	40.57	40.35	40.93	41.07	40.64	40.83	40.89	40.81	40.41
TiO_2	0.02	0.02	0.02	0.02	0.02	0.02	0.02	0.02	0.02	0.02
Al_2O_3	0.00	0.00	0.00	0.00	0.00	0.00	0.00	0.00	n.s.	0.00
FeO	8.16	8.68	9.88	9.90	10.93	12.02	9.21	8.57	10.28	10.63
MnO	0.14	0.16	0.17	0.17	0.19	0.16	0.17	0.14	0.14	0.20
MgO	49.80	50.01	48.56	48.78	48.19	47.19	48.95	49.35	48.05	48.00
CaO	0.01	0.1	0.22	0.19	0.11	0.13	0.14	0.20	0.23	0.03
Na_2O	n.s.	n.s.	n.s.	n.s.	n.s.	n.s.	n.s.	n.s.	n.s.	n.s.
Co	n.s.	n.s.	n.s.	n.s.	n.s.	n.s.	0.02	0.03	n.s.	0.00
Cr_2O_3	0.00	0.00	0.00	0.00	0.00	0.00	0.00	0.00	n.s.	0.00
NiO	0.35	0.30	0.24	0.22	0.24	0.18	0.26	0.35	0.24	0.21
Total	99.70	99.84	99.44	100.2	100.8	100.3	99.60	99.55	99.77	99.50
Mg.No.	91.58	91.13	89.76	89.78	88.72	87.50	90.41	91.08	89.28	88.95

Table 2.5. Wavelength dispersive electron microprobe analyses of olivines from the Shetland Ophiolite. Trans. Dunite=Transitional Dunite, n.s.=element not sought.

	Wehrlitic Dunite			*Cumulate Pyroxenite*		*High-level Pyroxenite*	
SiO_2	51.29	52.59	51.31	53.89	53.48	53.69	53.22
TiO_2	0.11	0.09	0.11	0.04	0.06	0.10	0.10
Al_2O_3	4.10	3.07	3.33	1.53	1.76	1.20	1.31
FeO	2.56	2.44	2.76	2.02	2.27	2.78	2.76
MnO	0.11	0.09	0.09	0.09	0.11	0.11	0.11
MgO	16.13	16.2	16.22	17.13	17.07	16.44	16.63
CaO	23.57	23.94	23.3	24.21	23.47	24.30	24.11
Na_2O	0.26	0.19	0.19	0.14	0.17	0.09	0.11
Cr_2O_3	1.02	0.89	0.77	0.68	0.89	0.25	0.37
NiO	0.01	0.03	0.03	0.00	0.00	0.02	0.00
TOTAL	99.16	99.53	98.11	99.73	99.28	98.97	98.72
Oxygens	6	6	6	6	6	6	6
Si	1.888	1.925	1.908	1.963	1.957	1.976	1.965
Ti	0.003	0.002	0.003	0.001	0.002	0.003	0.003
Al	0.178	0.132	0.146	0.066	0.076	0.052	0.057
Fe	0.079	0.075	0.086	0.061	0.069	0.086	0.085
Mn	0.003	0.003	0.003	0.003	0.003	0.003	0.003
Mg	0.885	0.884	0.899	0.930	0.931	0.902	0.915
Ca	0.930	0.939	0.929	0.945	0.920	0.958	0.954
Na	0.019	0.013	0.014	0.010	0.012	0.006	0.008
Cr	0.030	0.026	0.023	0.020	0.026	0.007	0.011
Ni	0.000	0.001	0.001	0.000	0.000	0.001	0.000
TOTAL	4.014	4.000	4.011	3.998	3.996	3.995	4.002

Table 2.6. Wavelength dispersive electron microprobe analyses of clinopyroxenes from the Shetland ophiolite.

2.5 Secondary silicate mineralogy

All lithologies from the Shetland ophiolite show varying degrees of alteration. This alteration is represented by the serpentinization and talc-carbonate alteration of harzburgite, dunite, wehrlite and pyroxenite (Read, 1934) and the conversion of the gabbro complex to a greenschist facies mineral assemblage (Prichard, 1985).

2.5.1 Secondary mineralogy of the ultramafics; previous work

Read (1934) recognized a basal zone of antigorite serpentinite which he related to a period of stress metamorphism. This zone of antigorite sepentinite subjacent to the basal thrust, "was of metamorphic origin and was produced during the translation of the ultrabasic body upwards towards the west. At the sole, talc-schists were formed; in the interior of the ultrabasic body, incipient thrusting gave rise to the talcose layers striking parallel with the main thrust-front, whereas similar talcose belts running at right angles to it are presumably due to tears in the moving mass" (Read, 1934). Amin (1954), noting that the antigorite content of peridotite increased towards the interior of zones of dislocation, suggested that "stress alone was not responsible for the formation of antigorite, but that the mineral was produced by migrating fluids whose passage was facilitated by shearing". Gunn *et al.* (1985) recognized five stages of alteration in serpentinized dunites. The earliest phase of their alteration sequence involves the static hydration of olivine to produce serpentine, followed by the recrystallization of this serpentine to form coarser crystals. Carbonate veining was thought to post-date or to be synchronous with this recrystallization event. Serpentine veins that cross-cut carbonate veins represent a later stage of alteration whereas talc-carbonate rocks, related to shear zones, represent the latest alteration event.

2.5.1.1 X-ray diffraction identification of serpentine and carbonate minerals

The whole-rock X-ray diffraction patterns of a representative suite of eight ultramafic rocks from the ophiolite, are given in appendix B.1, and indicate the presence of serpentine minerals in all but one sample. A summary of the mineralogy of these samples inferred from these XRD traces is shown in table 2.7.

Lithology	*Serpentine polymorph*	*Other minerals*
talc-carbonate schist, basal thrust, Cliff, MR244	antigorite	talc, magnesite, dolomite, chlorite
serpentine vein, basal thrust, Fetlar, JM25	antigorite	none detected
'green serpentinite', Cliff GRA	chrysotile	high-Mg chlorite (type Ia or Ib), pyroaurite-sjorgrenite
dunite pod, Cliff, JM36	antigorite	magnetite, chlorite, trace amphibole, pyroaurite-sjorgrenite?
cumulate dunite, N. Baltasound, JM40	lizardite	magnetite, forsterite
cumulate dunite, N. Baltasound, JM41	lizardite	forsterite, magnetite
cumulate pyroxenite, Mid-Unst, JM14	antigorite	augite, amphibole minor chlorite, magnetite and calcite
high-level pyroxenite, Vord Hill, JM44	none detected	diopside, amphibole, kaolinite, calcite and magnetite.

Table 2.7. Serpentine minerals identified in whole-rock powders by X-ray diffraction analysis.

Antigorite

Antigorite serpentine has been identified in ultramafic rocks that are spatially associated with the basal thrust and also in cumulate pyroxenite. In talc-carbonate rock, which sometimes displays a good foliation, antigorite is intergrown with talc, magnesite, dolomite and quartz or forms cm thick cross-cutting veins. Antigorite forms a massive, bladed matt texture with minor relict olivine and disseminated chrome-spinel in dunite pods from the Cliff locality and occurs intergrown with carbonate and chlorite, interstitial to clinopyroxene and amphibole in cumulate pyroxenite.

Chrysotile

From the whole-rock powder XRD analysis of green serpentinite interstitial to chrome-spinel at the margin of a podiform chromite body, Cliff, the peak intensity ratios suggest the presence of chrysotile serpentine.

Lizardite

This polymorph was identified by XRD in two undeformed serpentinized cumulate dunites. It forms mesh and 'hour-glass' textures replacing olivine and is intergrown with minor amounts of chlorite, carbonate and pentlandite.

Talc

Talc-carbonate rock sampled within ~20m of the basal thrust has a calculated modal mineralogy of talc 45%, magnesite 21%, dolomite 3%, antigorite, 12% and quartz, 19%. At the basal thrust quartz may constitute over 50% of the modal mineralogy. Talc forms mat-like masses in thin section intergrown with antigorite, magnesite, dolomite and chlorite. Talc was characterized by XRD in sample MR244 (appendix B.1).

Chlorite

Chlorite is commonly intergrown with serpentine and talc. It occurs as haloes to chrome-spinels and is also sometimes intergrown with nickel-iron sulphides in dunites. Mg-rich chlorite identified by XRD is intergrown with chrome-spinel in podiform chromitite at Cliff.

Pyroaurite-sjorgrenite group; $[Mg_6Fe_2^{3+}(CO_3)(OH)_{16}.4H_2O]$

A green serpentinite from the Cliff locality, and a serpentinized cumulate pyroxenite from mid-Unst contain a nickel-carbonate of the pyroaurite-sjorgrenite group. This mineral was identified from peaks at 7.76Å and 3.898Å on whole-rock powder XRD traces (appendix B.1).

2.5.1.2 Microprobe analysis of secondary minerals

Serpentine

Wavelength dispersive electron microprobe analysis of antigorite and lizardite serpentines are given in table 2.8. Antigorite analysed from the Shetland ophiolite complex is characterized by higher SiO_2, lower MgO and lower structural water contents compared to lizardite in rocks from the complex. Antigorite from talc-carbonate rocks from the basal thrust and from a high-level pyroxenite contains 4.95-7.01wt.% iron 1.14-1.44 wt.% aluminium and traces of chrome (0.11-0.22 wt.%) and nickel, (0.06-0.14 wt.%). Lizardite from a sample of cumulate dunite and wehrlitic dunite contains between 3.12 and 5.52wt% FeO, 0-3.47 wt.% Al_2O_3, and traces of calcium, (0.07-0.11 wt.%) and nickel, (0-0.26 wt.%).

	Lizardite, Wehrlitic Dunite		*Lizardite, Transitional Dunite*		*Antigorite Talc-carbonate rock*	*Antigorite High-level Pyroxenite*
SiO_2	37.62	35.07	36.64	34.56	42.82	43.09
TiO_2	0.02	0.02	0.02	0.00	0.02	0.04
Al_2O_3	3.47	1.18	0.07	0.00	1.14	1.44
FeO	3.12	5.34	3.85	5.52	7.01	4.95
MnO	0.06	0.09	0.06	0.11	0.05	0.11
MgO	37.84	39.36	40.55	41.08	36.34	35.22
CaO	0.07	0.11	0.11	0.10	0.01	0.92
Na_2O	0.03	0.02	0.03	0.00	0.02	0.00
Cl	0.05	0.06	0.04	0.05	0.00	0.00
Cr_2O_3	0.02	0.00	0.00	0.00	0.22	0.11
NiO	0.02	0.09	0.02	0.26	0.14	0.06
Total	82.32	81.34	81.39	81.68	87.81	85.98

Table 2.8. Wavelength dispersive electron microprobe analyses of serpentines from the Shetland ophiolite.

Talc

Microprobe analyses of talc from the basal thrust (sample MR244) (table 2.9) indicate significant amounts of iron, 2.16-3.08 wt.% FeO and traces of nickel, 0.17-0.29 wt.% NiO.

	Talc, Talc-cabonate rock			
SiO_2	60.86	61.61	60.60	62.39
TiO_2	0.02	0.02	0.02	0.02
Al_2O_3	0.00	0.04	0.09	0.02
FeO	3.08	2.45	2.70	2.16
MnO	0.02	0.02	0.02	0.02
MgO	29.28	29.67	29.32	29.06
Na_2O	0.00	0.00	0.01	0.00
CaO	0.04	0.03	0.01	0.01
Cr_2O_3	0.00	0.02	0.03	0.00
NiO	0.29	0.18	0.21	0.17
Total	93.59	94.04	93.01	93.85

Table 2.9. Wavelength dispersive electron microprobe analyses of talc from the Shetland ophiolite.

Magnesite and dolomite

Calcite is a common component of altered gabbros in Shetland, whereas magnesite is the predominant carbonate mineral in talc-carbonate rocks along with small amounts of dolomite. The iron carbonate siderite occurs in highly altered talc schists from the basal thrust (Neary and Prichard, 1985). Magnesite contains inclusions of pyrrhotite in talc-

carbonate rocks from the basal thrust, Cliff and 0-50μ rhombs of magnesite are intergrown with cm wide veins of antigorite plus minor fine-grained magnetite which cross-cut talc-carbonate rocks. Partially serpentinized cumulate dunites contain traces of carbonate intergrown with chlorite and pentlandite. Altered high-level pyroxenites often contain veinlets of pink-brown carbonate traversed by fine needles of amphibole.

	Magnesite, Talc-carbonate rock						**Dolomite, Talc-carbonate rock**	
SiO_2	0.05	0.05	0.05	0.05	0.05	0.05	0.05	0.05
TiO_2	0.02	0.02	0.02	0.02	0.00	0.02	0.02	0.02
Al_2O_3	0.00	0.00	0.00	0.00	0.00	0.00	0.00	0.00
FeO	9.04	8.88	9.20	8.92	8.52	8.71	2.33	2.24
MnO	0.39	0.42	0.25	0.57	0.23	0.25	0.13	0.11
MgO	40.18	40.56	40.59	40.24	41.06	40.99	19.39	19.50
CaO	0.20	0.15	0.14	0.25	0.15	0.15	28.72	28.81
Na_2O	0.02	0.00	0.02	0.00	0.00	0.00	0.00	0.00
K_2O	0.00	0.00	0.00	0.00	0.00	0.00	0.00	0.00
Cl	0.00	0.00	0.00	0.00	0.00	0.00	0.00	0.00
Cr_2O_3	0.00	0.00	0.00	0.00	0.00	0.00	0.00	0.00
NiO	0.02	0.00	0.02	0.02	0.02	0.02	0.00	0.00
ZnO	0.00	0.02	0.00	0.00	0.00	0.02	0.00	0.00
Total	49.92	50.10	50.29	50.07	50.03	50.21	50.64	50.73
Oxygens	6	6	6	6	6	6	6	6
Si	0.005	0.005	0.005	0.005	0.004	0.004	0.005	0.005
Ti	0.001	0.001	0.001	0.001	0.000	0.001	0.001	0.001
Al	0.000	0.000	0.000	0.000	0.000	0.000	0.000	0.000
Fe	0.666	0.650	0.672	0.655	0.621	0.634	0.189	0.181
Mn	0.029	0.031	0.018	0.043	0.017	0.018	0.011	0.009
Mg	5.272	5.292	5.283	5.266	5.338	5.321	2.803	2.811
Ca	0.018	0.014	0.013	0.024	0.014	0.014	2.984	2.986
Na	0.003	0.000	0.003	0.000	0.000	0.000	0.000	0.000
K	0.000	0.000	0.000	0.000	0.000	0.000	0.000	0.000
Cl	0.000	0.000	0.000	0.000	0.000	0.000	0.000	0.000
Cr	0.000	0.000	0.000	0.000	0.000	0.000	0.000	0.000
Ni	0.001	0.000	0.001	0.001	0.001	0.001	0.000	0.000
Zn	0.000	0.001	0.000	0.000	0.000	0.000	0.000	0.000
Total	5.995	5.994	5.995	5.994	5.996	5.994	5.994	5.994

Table 2.10. Wavelength dispersive electron microprobe analyses of carbonate minerals from the Shetland ophiolite.

Electron microprobe analysis of magnesite indicates 8.52-9.20 wt.% FeO, 0.23-0.57 wt.% NiO, with minor amounts of manganese 0.14-0.25 wt.% substituting for magnesium (table 2.10). Dolomite contains ~2.3 wt.% FeO and 0.11-0.13 wt.% MnO (table 2.10).

2.5.2 Secondary mineralogy of the gabbro unit

2.5.2.1 Amphibole

The majority of the amphibole in the gabbro unit is actinolite formed by the replacement of clinopyroxene, (Read, 1934; Prichard, 1985). Highly sheared lithologies contain bladed tremolite (Read, 1934).

	Actinolite, amphibole pegmatite	Actinolite, mineralized gabbro		Magnesio-hornblende, gabbro	Tremolite, high-level pyroxenite
SiO_2	55.16	55.21	50.58	50.62	58.68
TiO_2	0.02	0.06	0.31	0.39	0.04
Al_2O_3	0.90	1.46	6.38	5.53	0.04
FeO	10.96	13.52	12.78	11.92	1.86
MnO	0.36	1.17	0.36	0.28	0.11
MgO	16.55	15.51	14.23	15.75	22.76
CaO	13.24	12.84	11.83	11.25	13.45
NaO	0.07	0.17	0.93	1.05	0.00
K_2O	0.01	0.01	0.05	0.02	0.00
Cr_2O_3	0.00	0.00	0.02	0.00	0.00
NiO	0.00	0.00	0.00	0.00	0.02
ZnO	0.00	0.00	0.00	0.00	0.00
TOTAL	97.27	99.95	97.47	96.81	96.97
Oxygens	23	23	23	23	23
Si	7.912	7.818	7.329	7.352	8.057
Ti	0.002	0.006	0.034	0.042	0.004
Al	0.153	0.244	1.090	0.947	0.006
Fe	1.315	1.601	1.549	1.448	0.214
Mn	0.044	0.140	0.044	0.034	0.013
Mg	3.540	3.274	3.073	3.409	4.659
Ca	2.035	1.948	1.836	1.750	1.979
Na	0.019	0.047	0.261	0.296	0.003
K	0.002	0.002	0.009	0.004	0.000
Cr	0.000	0.000	0.002	0.000	0.000
Ni	0.000	0.000	0.000	0.000	0.002
Zn	0.000	0.000	0.000	0.000	0.000
TOTAL	15.020	15.079	15.225	15.283	14.937

Table 2.11. Wavelength dispersive electron microprobe analyses of amphiboles from the Shetland ophiolite.

However, pale-brown amphiboles do occur in pegmatites where the amphibole shows no sign of pseudomorphing pyroxene (Prichard, 1985). Representative amphibole microprobe analyses obtained during this study are shown in table 2.11. All the microprobe analyses obtained during this study are plotted on a $Mg/(Mg+Fe^{2+})$ *vs.* Si amphibole classification diagram (Fig. 2.2) constructed after Leake (1978). The majority of amphiboles from the

gabbro unit have low total alkalis (Na+K)<0.5 and Ti<0.5 and are actinolite or actinolitic hornblende. Four green amphibole analyses, all from the gabbro unit, which include the two analyses of Prichard (1985) conform to magnesio-hornblende. Tremolite occurs in a sheared gabbro, and in sheared high-level pyroxenite.

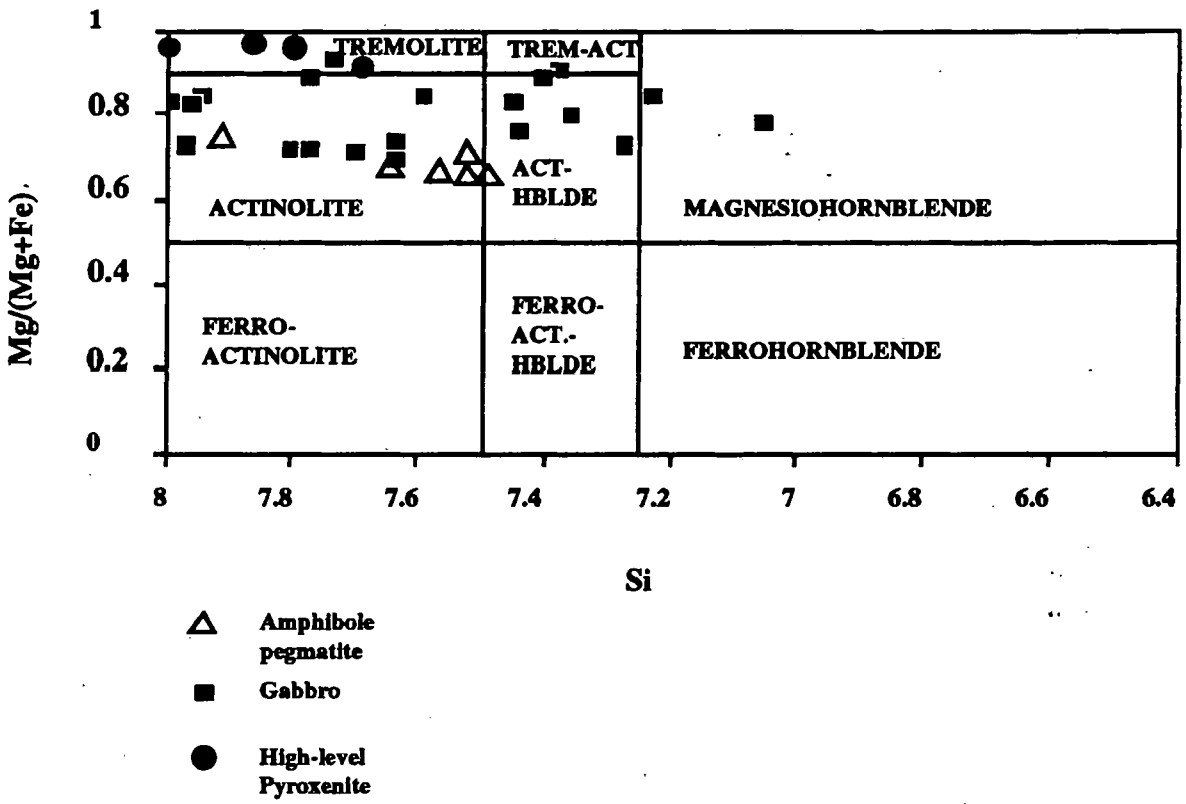

Fig 2.2. Mineral chemistry of amphiboles from the Shetland ophiolite, classifiec after Leake (1978).

2.5.2.2 Epidote

Epidote is ubiquitous in the gabbro unit and is very abundant in high-level gabbros from Mu Ness. It occurs as fine-grained matrix disseminations and as larger euhdral crystals often as veinlets intergrown with quartz and iron-sulphides. Epidotes analysed from two localities in the gabbro unit (table 2.12) have an Fe/(Fe+Al) value of 0.22-0.38 and contain trace TiO_2 (0.06-0.17 wt.%).

	Epidote, gabbro						*Epidote, mineralized gabbro*	
SiO_2	39.93	39.81	39.94	39.93	39.71	39.96	37.92	38.15
TiO_2	0.07	0.07	0.07	0.06	0.06	0.13	0.17	0.07
Al_2O_3	27.36	26.51	27.58	27.66	27.53	27.81	23.01	24.94
Fe_2O_3	7.73	8.49	7.08	7.20	7.55	7.26	14.25	11.72
MnO	0.09	0.08	0.06	0.09	0.05	0.17	0.08	0.12
MgO	0.00	0.00	0.00	0.00	0.00	0.02	0.02	0.00
CaO	20.41	16.46	18.04	19.05	18.01	22.32	23.71	24.05
Na_2O	0.00	0.02	0.02	0.02	0.00	0.02	0.00	0.00
K_2O	0.00	0.00	0.00	0.00	0.00	0.00	0.00	0.00
TOTAL	95.59	91.44	92.79	94.01	92.91	97.69	99.16	99.05

Table 2.12. Wavelength dispersive electron microprobe analyses of epidotes from the Shetland ophiolite.

	Chlorite, gabbro	*Chlorite, mineralized gabbro*		*Biotite, dolerite dyke*
SiO_2	27.49	25.87	26.09	35.04
TiO_2	0.05	0.05	0.07	1.17
Al_2O_3	21.3	20.46	20.37	15.96
Fe_2O_3	19.69	25.93	25.87	15.78
MnO	0.38	0.41	0.38	0.20
MgO	19.81	17.14	17.2	11.25
CaO	0.04	0.03	0.03	0.03
Na_2O	0.00	0.02	0.02	0.09
K_2O	0.00	0.00	0.00	8.80
TOTAL	88.76	89.91	90.03	88.32

Table 2.13. Wavelength dispersive electron microprobe analyses of chlorites and biotite from the Shetland ophiolite.

2.5.2.3 Plagioclase Feldspar

Plagioclase feldspar from the gabbro unit is intergrown with actinolite-chlorite-quartz-epidote and is albitic (An_5). This composition is typical of plagioclase feldspar in greenschist facies rocks.

2.5.2.4 Chlorite and biotite

Table 2.13 gives typical analyses of chlorites and a biotite from the gabbro unit. Biotite, intergrown with actinolite, occurs in a dolerite dyke which cuts high-level gabbro.

2.9 Discussion and conclusions

The Shetland ophiolite displays a primary lithological sequence of harzburgite containing dunite pods overlain by a layered sequence of dunite, wehrlite, pyroxenite and gabbro. These lithologies are extensively altered and, from a compilation of the studies of Read (1934); Gass *et al.* (1982); Gunn *et al.* (1985) and Flinn (1985), a paragenesis for the secondary silicate mineralogy is given in table 2.14.

Event.	*Feature(s).*	*Mineralogy.*
1. Formation of composite ultrabasic and basic rocks.	Mantle foliation. Layering in crustal cumulates.	Chr/Ol/Opx/Cpx/Pl/Amph/Sulph /Mt.
2. Serpentinization; early static hydration of olivine	Massive mesh texture serpentine.	Lizardite, magnetite.
3. Stress metamorphism	Internal dislocations with foliated serpentine strain-slip cleavage.	Basal zone of antigorite-talc-carbonate-quartz rocks Carbonate(magnesite/calcite/dolomite) veining and quartz. Kammererite, pyroaurite and zaratite at Cliff. Tremolite-serpentine in cumulate pyroxenite. Zoisite-tremolite schists in gabbro.
4. Regional greenschist facies metamorphism.	Widespread static recrystallization including retrograde metamorphism of metamorphic sole.	Magnesian-chlorite±carbonate rims to chrome-spinel. Chlorite, (biotite and actinolite) in gabbros.
5. Cataclastic regional metamorphism. Flinn, (1985).		Replacement of biotite by chlorite.

Table 2.14. Simplified structural and metamorphic history of the Shetland ophiolite with associated silicate mineral parageneses, (after Read 1934; Gass *et al.*, 1982; Gunn 1985; Flinn 1985).

Of the three serpentine polymorphs; lizardite, chrysotile and antigorite, identified in the Shetland ophiolite, lizardite is considered to be the earliest polymorph to have crystallized. Lizardite occurs in relatively undeformed dunites away from the basal thrust and internal shear zones and formed by the hydration of primary olivine. This is in agreement with previous studies on the process of serpentinization in ophiolites which suggest that lizardite forms during early stages of serpentinization followed by chrysotile, whereas antigorite is confined to sheared surfaces (Prichard, 1979). The identification of antigorite and talc at the basal thrust of the ophiolite, and antigorite in a sheared high-level pyroxenite body is consistent with those observations of Read (1934), namely that antigorite and talc are spatially associated with zones of dislocation metamorphism within the ophiolite and clearly post-date the formation of lizardite. The work of Wenner and Taylor (1973) suggests

that continental antigorite forms at higher temperatures (220-460°C) than chrysotile-lizardite (85-115°C), and Maltman (1978) and Prichard (1979), both describe the conversion of lizardite to antigorite with increasing deformation. The presence of some CO_2 in the fluid phase during alteration (<5 mole%) may facilitate the transformation of lizardite to antigorite (Donaldson, 1981) and it is noted that in Unst, antigorite is often intergrown with the carbonates magnesite and dolomite.

The tentative identification of chrysotile intergrown with a mineral of the pyroaurite group [$Mg_6Fe_2^{3+}(CO_3)(OH)_{16}.4H_2O$] from the Cliff locality is supported by the work of Gunn *et al.* (1985) who describe chrysotile intergrown with a member of the pyroaurite group, which they identified as probably reevesite [$Ni_{38}Fe_6(CO_3)_3.12H_2O$]. They also describe zaratite, [$Ni_3(CO_3)(OH_4).4H_2O$] in late cross-cutting veins. Donaldson (1981) considered pyroaurite to form either in response to small quantities of CO_2 in the serpentinizing fluid or to the alteration of brucite. Pyroaurite and zaratite therefore formed at a late stage in the alteration at Cliff, probably from CO_2-bearing fluids which may be related to the formation of the talc-carbonate rocks at the basal thrust. The presence of carbonate carbon in deformed high-level pyroxenite and undeformed lizardite serpentinite from the cumulate dunite unit (section 2.3.3) suggests that a CO_2-bearing fluid may have infiltrated the majority of the ophiolite sequence.

The mafic rocks of the ophiolite contain the mineral assemblage actinolite-albite-epidote-quartz-chlorite(sphene/apatite) which is a characteristic greenschist facies mineral assemblage. This assemblage could be a product of oceanic crust greenschist metamorphism (Prichard, 1985) or may have been formed during a later regional greenschist metamorphic event (Read (1934). This regional greenschist metamorphism is manifested by the development of Mg-chlorite rims on disseminated chrome-spinel in the ultramafics and the retrograde metamorphism of aureole rocks at the basal thrust. The sulphides intergrown with this silicate assemblage will therefore have undergone a greenschist facies metamorphic event and may therefore have significantly re-equilibrated at low temperatures (see Chapter 5). Constraints on the alteration of the mafic and ultramafic rocks from the ophiolite from a consideration of their stable isotope signatures is discussed in Chapter 6.

Chapter 3

Mineralogy and mineral chemistry of opaque minerals

3.1 Introduction

In this chapter the sulphide, arsenide and opaque oxide mineralogy is described for each major silicate lithology of the ophiolite, sample localities are shown in Fig. 1.8. Ni-antimonides will be considered separately because of their complex mineralogy. The microscopic textural associations and composition of the different opaque minerals has been established by the use of reflected light microscopy, quantitative wavelength dispersive electron microprobe and scanning electron microscopy techniques. In describing textural relations of the sulphides, arsenides, antimonides, native metals and alloys, the term percent total sulphide (p.t.s.) (after Abrajano and Pasteris, 1989), will often be used to indicate the modal proportion of a given sulphide phase normalized to 100% sulphides. The data described in this chapter will be compared with published experimental phase equilibria relations and thermochemical data of Fe, Ni and Cu sulphides and native metals and alloys in Chapter 4 to place constraints on the physio-chemical conditions of formation of the different opaque mineral assemblages from the complex. Following from this, an opaque mineral paragenesis will be presented for the mineralization in the complex. Mineral paragenesis is here used to describe the formation of different opaque mineral assemblages in time succession.

3.2 Sulphide mineralogy of the mafic portion of the ophiolite

An Fe and Cu-Fe sulphide assemblage is ubiquitous. The most common sulphide is pyrrhotite, followed by pyrite, chalcopyrite, marcasite and cobaltpentlandite. No arsenides, sulpharsenides or antimonides have been found. Fine-grained disseminations of magnetite are common.

3.2.1 Gabbros, basic dykes and plagiogranite

Disseminated sulphides make up <1 modal percent of the silicate + sulphide mineralogy. The most prevalent sulphide is pyrrhotite which commonly forms 50-80 p.t.s. as 100-300μ solitary blebs interstitial to amphibole, epidote and albite, and along veinlets formed from these minerals, or is intergrown with euhedral crystals of pyrite, or anhedral chalcopyrite (Fig. 3.1). Pyrrhotite forms 2-15μ inclusions in albite in veins of plagiogranite. Pyrrhotite often forms elongate grains which lie parallel with the long-axis of fibrous actinolite in sheared lithologies. A sheared gabbro from close to a serpentinite shear zone contains disseminated pyrrhotite which is replaced by pyrite and forms cores to pyrite which is intergrown with chalcopyrite and euhedral cream-white Co-pentlandite (Fig. 3.2). 10-30μ white inclusions of marcasite sometimes occur in pyrrhotite as do 30-60μ euhedral crystals of pyrite. Pyrrhotite forms 20-50μ inclusions in green actinolite. Pyrite typically forms 10-30 p.t.s., but may reach >80 p.t.s. where it occurs as veinlets intergrown with actinolite in highly sheared lithologies and is clearly metamorphic in origin and alters to 'limonite' (Fig. 3.3). Pyrite is also developed along cleavage planes in actinolite or occurs as 10-20μ rounded inclusions in actinolite and albite in a plagiogranite sample. This plagiogranite also contains accessory sphene, pyrrhotite, which is replaced by pyrite (which alters to 'limonite') and marcasite. Chalcopyrite alters to blue, blaubleibender covelline and also to 'limonite' (Ixer, *pers. comm.*). Solitary, large (up to 2mm), spongy euhedral crystals of pyrite commonly replace fibrous amphibole and quartz. Pyrite commonly alters to marcasite. Chalcopyrite usually forms 0-30 p.t.s. but in one recorded instance (southern Mu Ness peninsula), forms 80 p.t.s. and is intergrown with pale pink pyrite. When present, chalcopyrite (5-40μ) is usually intergrown with pyrrhotite or pyrrhotite-pyrite±cobaltpentlandite. Sulphides are often intergrown with minor amounts of magnetite which alters to 'limonite' in sheared and oxidized lithologies.

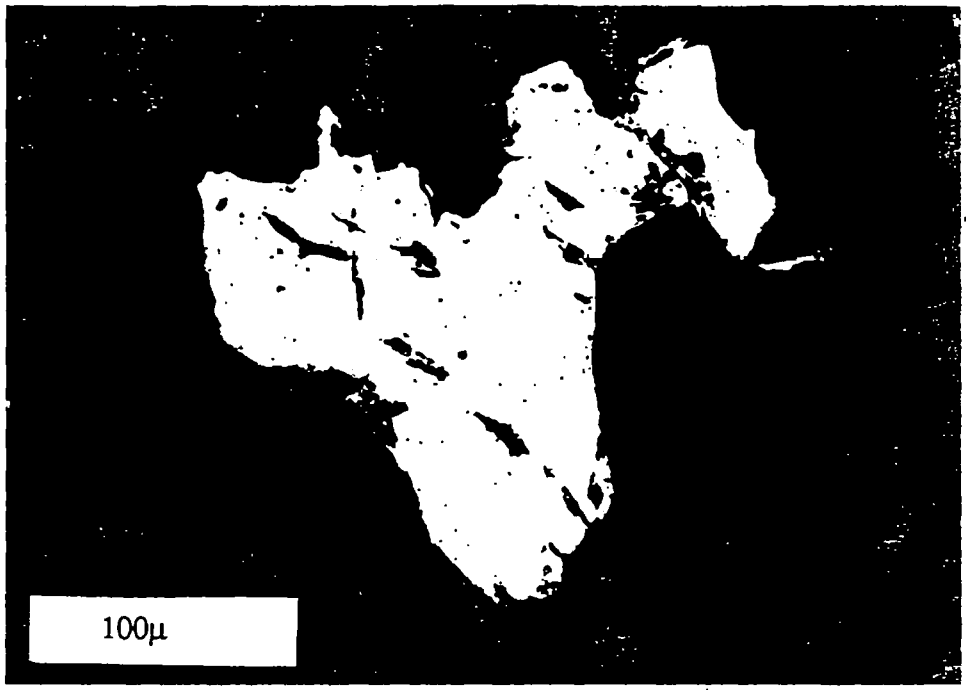

Fig. 3.1. Pyrrhotite intergrown with chalcopyrite in metagabbro, Nuda.

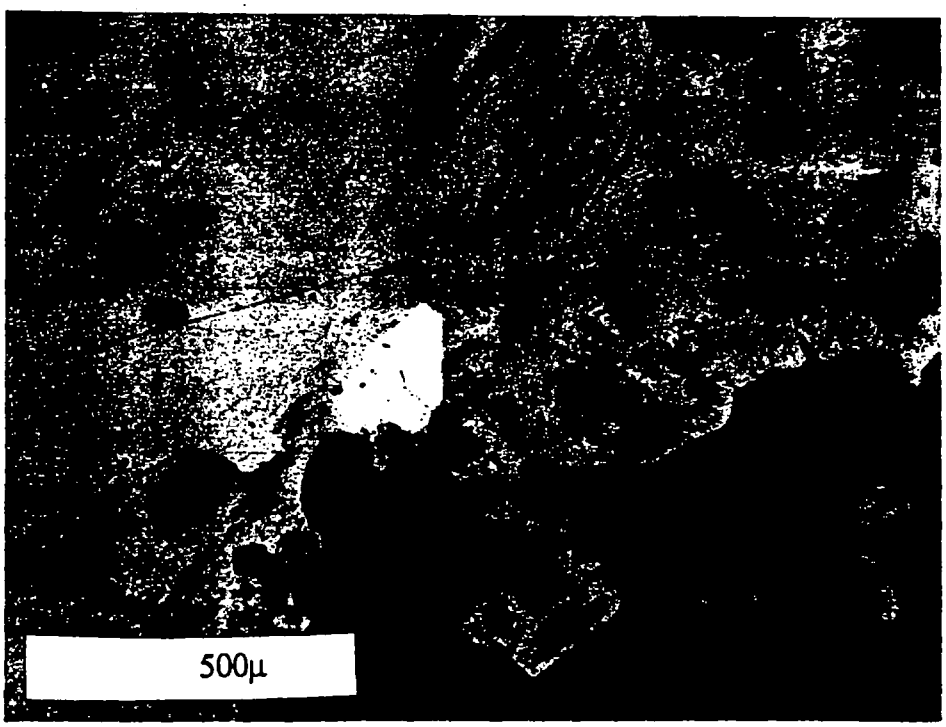

Fig. 3.2. Cobalt-pentlandite (white) intergrown with pyrrhotite altering to marcasite. (partially crossed polars).

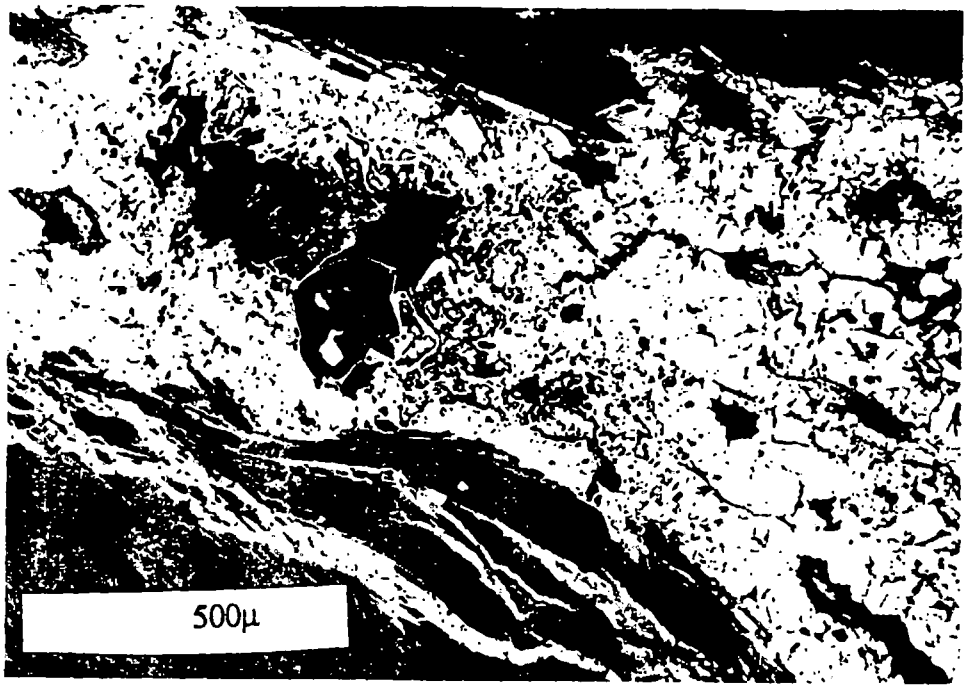

Fig. 3.3. Pyrite altering to 'limonite' hosted in altered gabbro (anthophyllite-chlorite schist), Nuda.

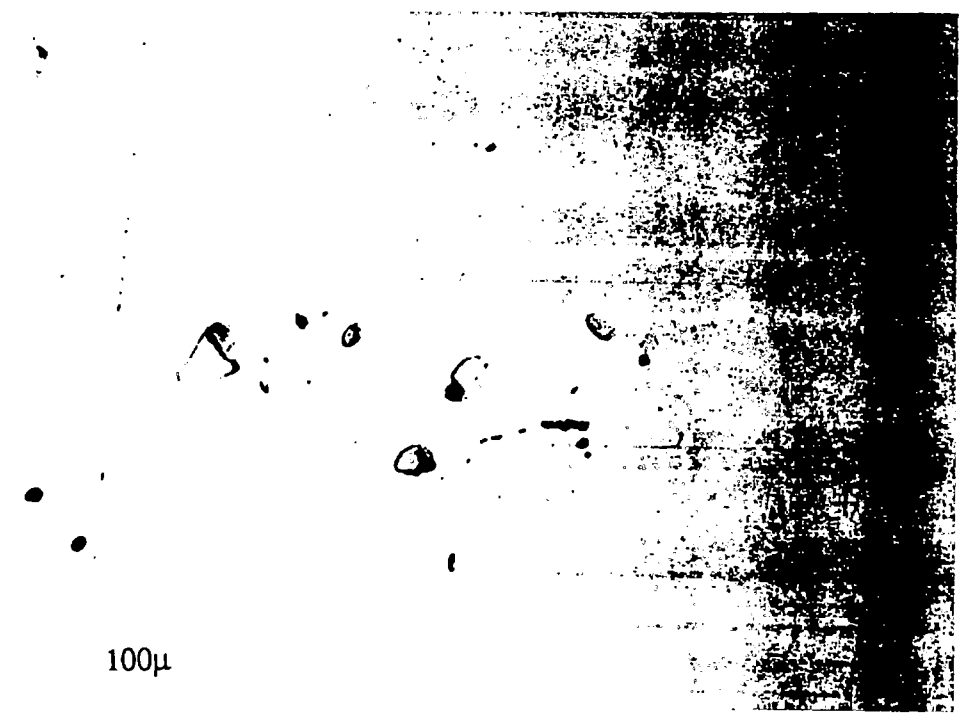

Fig. 3.4. Chalcopyrite (centre) intergrown with pyrite, sub-massive pyrite mineralization hosted in gabbro, Mu Ness.

3.2.2 Amphibole pegmatite, plagiogranite and microgabbro, North Mu Ness peninsula

Sub-massive to disseminated pyrite mineralization occurs as sporadic elongate, rusty-weathering pods, hosted within epidotized microgabbro and also in an amphibole pegmatite from high level gabbro exposed at the north end of the Mu Ness peninsula. In the mineralized pods from this locality, pyrite forms 10-50% of the rock by volume and is intergrown with a fine grained matrix of epidote, quartz and chlorite and minor actinolite. Pyrite also forms along veinlets of quartz and chlorite. Pyrite is anhedral to subhedral and is intergrown with minor chalcopyrite. In the amphibole pegmatite, euhedral to subhedral, coarse-grained pyrite (up to 1.5mm) is intergrown with actinolite. Small intergrowths of chalcopyrite similar to those observed in the mineralized pod are present (Fig. 3.4). Disseminated 20μ-1mm sized pyrite, altering to 5-20μ rims of 'limonite', with a similar euhedral morphology to that observed in the amphibole pegmatite also occurs within plagiogranite from Mu Ness, intergrown with albite, epidote and quartz apatite and sphene (Ixer, *pers. comm.*), and euhedral crystals of magnetite. Pyrite also occurs in anastomosing veinlets of epidote with minor chlorite and quartz.

3.3 Sulphide mineralogy of the ultramafic portion of the ophiolite

Lithologies considered include; (i) wehrlite and pyroxenite enclosed within gabbro, (high-level wehrlites and pyroxenites), (ii) cumulate pyroxenites and wehrlites, (iii) cumulate dunite, including dunite from the transition zone between harzburgite and cumulate dunite, (iv) dunite and chromitite pods enclosed in harzburgite and (v) harzburgite and talc-carbonate rocks from near the basal thrust of the ophiolite.

3.3.1 High-level wehrlite and pyroxenite

Disseminated sulphides make up <1 modal percent of the silicate and sulphide mineralogy. Pyrite is the most common sulphide, forming up to 70 p.t.s , often as large solitary 500-800μ crystals intergrown with antigorite, tremolite and diopside, and associated with small amounts of magnetite (Fig. 3.5). Pyrite occurs as large, ~400μ, spongy or dendritic aggregates,

associated with solitary crystals of Ni-arsenide (niccolite), sulpharsenide (cobaltite), and small composite pyrrhotite-pentlandite grains about chromite altering to 'ferritchromit' (Fig. 3.6). Cobaltite is common in this pyroxenite body, often forming up to 5 p.t.s., and occurs as solitary, euhedral, 10-40μ crystals in the silicate matrix (Fig. 3.7). Pyrrhotite and pentlandite are often intergrown as 100-300μ aggregates and have closely associated 'satellite' crystals of cobaltite intergrown with pink niccolite. Pentlandite forms 10-40 p.t.s., may be intergrown with pyrrhotite and chalcopyrite, and alters to violarite. Magnetite, chrome-spinel, and some ilmenite are common. Magnetite forms up to 30 p.t.s., and constitutes up to 35% of the rock by volume in highly altered lithologies. Ilmenite is also commonly developed in these altered lithologies, forming ≤5 p.t.s. Magnetite occurs as anastomosing veinlets or forms dusty inclusions in matrix serpentine, it is also commonly developed along relict clinopyroxene cleavage planes. Magnetite and pentlandite sometimes form symplectite-like intergrowths. Disseminated chrome-spinel forms approximately 2-5 p.t.s., is up to 500μ in size with altered rims of 'ferritchromit'.

3.3.2 Cumulate wehrlite and pyroxenite

Disseminated pentlandite forms 30-60 p.t.s. Pentlandite alters to heazlewoodite, millerite and godlevskite (Fig. 3.8), and also to supergene violarite. Pentlandite is intergrown with pyrrhotite and chalcopyrite±magnetite, pyrite and bornite in 1-300μ aggregates which often occur interstitially and partially intergrown with pyroxene (Fig. 3.9). Pentlandite and magnetite is developed along altered cleavage planes in clinopyroxene (Fig. 3.10). Pyrrhotite may form up to 60 p.t.s.and is intergrown with pentlandite-pyrite-chalcopyrite. Pyrrhotite alters along (0001) to fine grained, poorly crystalline, pyrite and marcasite (Fig. 3.11). Bornite alters to chalcopyrite which occurs as patches and lamellae in pentlandite (Fig. 3.12), and sometimes as 2-10μ inclusions in clinopyroxene. Bornite also occurs as 5-30μ composite bornite-chalcocite crystals about a pentlandite-bornite-chalcopyrite aggregate. There is often a zonal sequence of alteration of chalcopyrite->bornite->digenite->covellite->native Cu developed within single grains in serpentine interstitial to pyroxene crystals (R. Ixer, *pers. comm.*). Chalcopyrite also alters to 'limonite'. In the most sheared and serpentinized pyroxenites, a Ni-arsenide assemblage of Sb-rich maucherite and orcelite and composite orcelite-pentlandite grains occur. Maucherite occurs

as solitary crystals in chlorite-serpentine rims to pentlandite-chalcopyrite aggregates or is intergrown with pentlandite and orcelite. PGM are associated with aggregates of base-metal sulphides, and are predominantly Pt-arsenides and Pd-antimonides (Prichard *et al.*, 1994). For example, PdSb and PtAs (probably sperrylite) grains as 2-10μ crystals occur in a chalcopyrite-bornite-pyrrhotite-magnetite aggregate, or are closely associated with this aggregate, but enclosed within the silicate matrix. $PtAs_2$ occurs along the boundary of clinopyroxene and chlorite (Prichard *et al.*, 1994). Another association is palladium sulphide, Pd-Pb alloys±Pt, Au, associated with pentlandite found in an unaltered clinopyroxene crystal. Developed along serpentinized cleavage planes within this crystal, are Pd-arsenides, antimonides, tellurides and sperrylite associated with heazlewoodite and magnetite (Prichard *et al.*, 1994). Chrome spinel is ubiquitous, forming 4-5 modal%, rimmed by 'ferritchromit' or magnetite. Magnetite occurs as chains or veinlets in a serpentinized matrix, is intergrown with, and sometimes encloses, pentlandite (Fig. 3.13), or is concentrated along veins of fibrous serpentine. Magnetite encloses sub-rounded grains of pentlandite and pyrrhotite.

3.3.3 Wehrlitic dunite, cumulate dunite and transitional harzburgite

Wehrlitic dunite from the Keen of Hamar, which consists of lizardite, some fresh olivine and 10-20% diopside, contains pentlandite-heazlewoodite and native copper; a similar sulphide assemblage to the underlying dunite cumulates. In cumulate dunite, sulphide and spinels form 100μ-2mm sized intergrowths that are disseminated throughout the silicate matrix together with solitary chrome-spinel. These intergrowths commonly display cuspate boundaries with the silicate matrix which may be a relict intercumulus texture (Fig. 3.14). The two most abundant sulphide phases are pentlandite and heazlewoodite. Pentlandite is more prevalent in samples where there is >10-20% relict olivine and forms up to 80 p.t.s., whereas heazlewoodite is predominant in highly serpentinized dunites with <10% olivine, and forms 70-80 p.t.s. Pentlandite from olivine-rich serpentinized dunites commonly occurs as blocky aggregates, with

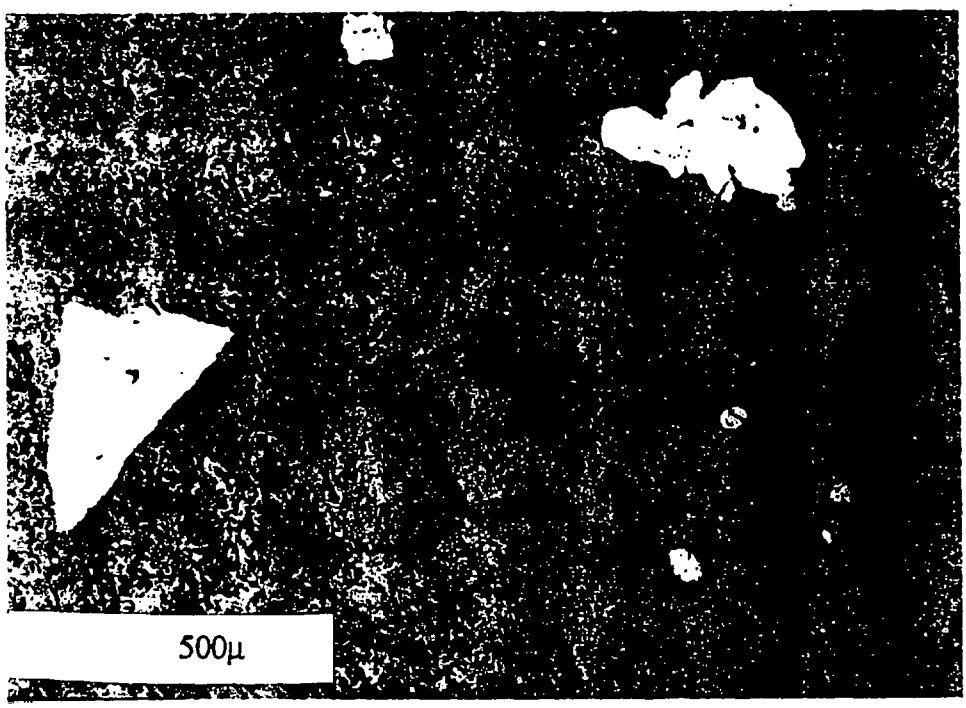

Fig. 3.5. Pyrite (left and top right) and magnetite (top and bottom right) in high-level pyroxenite.

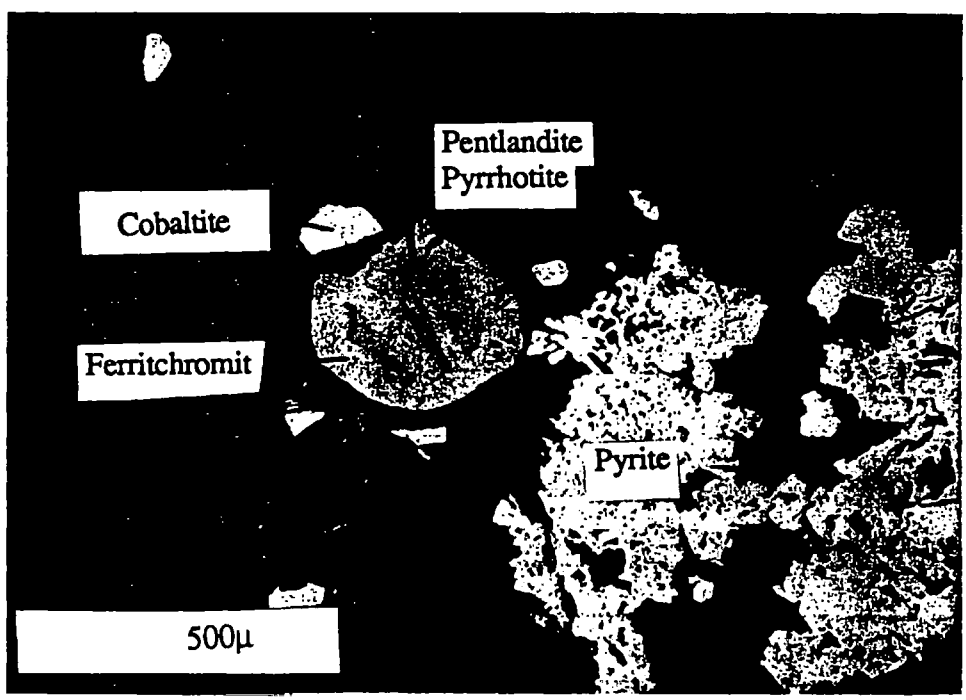

Fig. 3.6. Cluster of composite pyrrhotite-pentlandite and a cobaltite grain associated with chromite altering to 'ferrichromit' at the margin of a spongy pyrite grain, high-level pyroxenite.

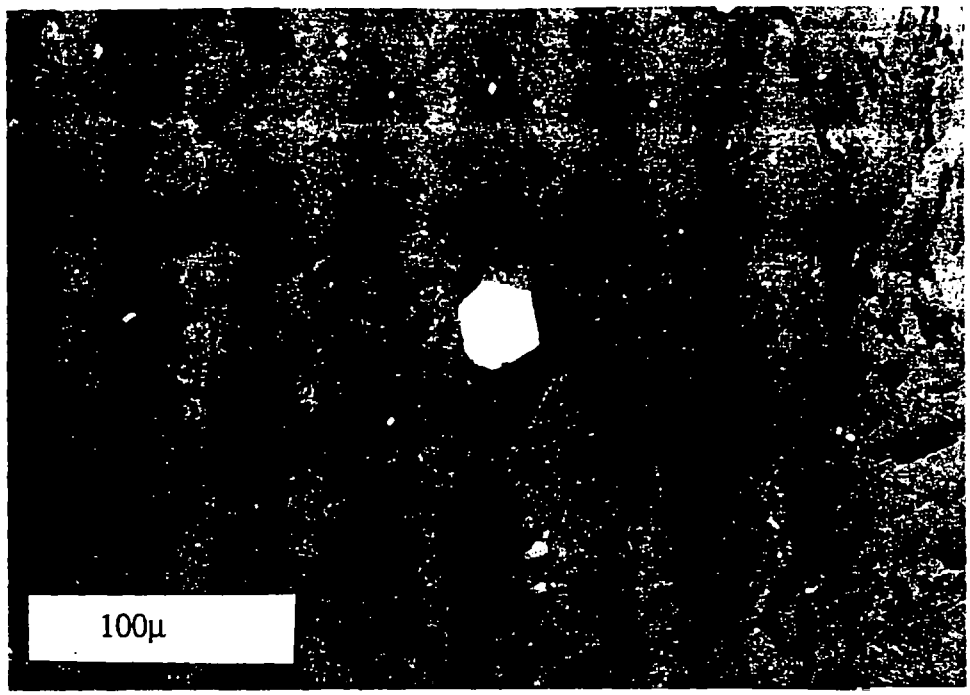

Fig. 3.7. Euhedral cobaltite (centre) intergrown with serpentine, high-level pyroxenite.

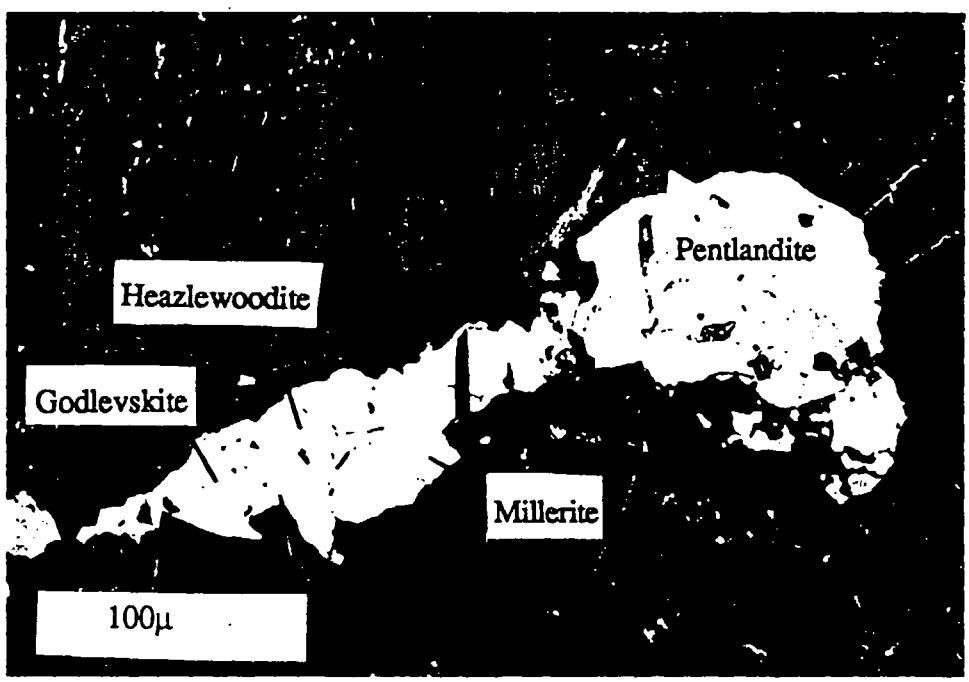

Fig. 3.8. Pentlandite, altering to heazlewoodite, millerite and godlevskite, intergrown with magnetite, cumulate pyroxenite.

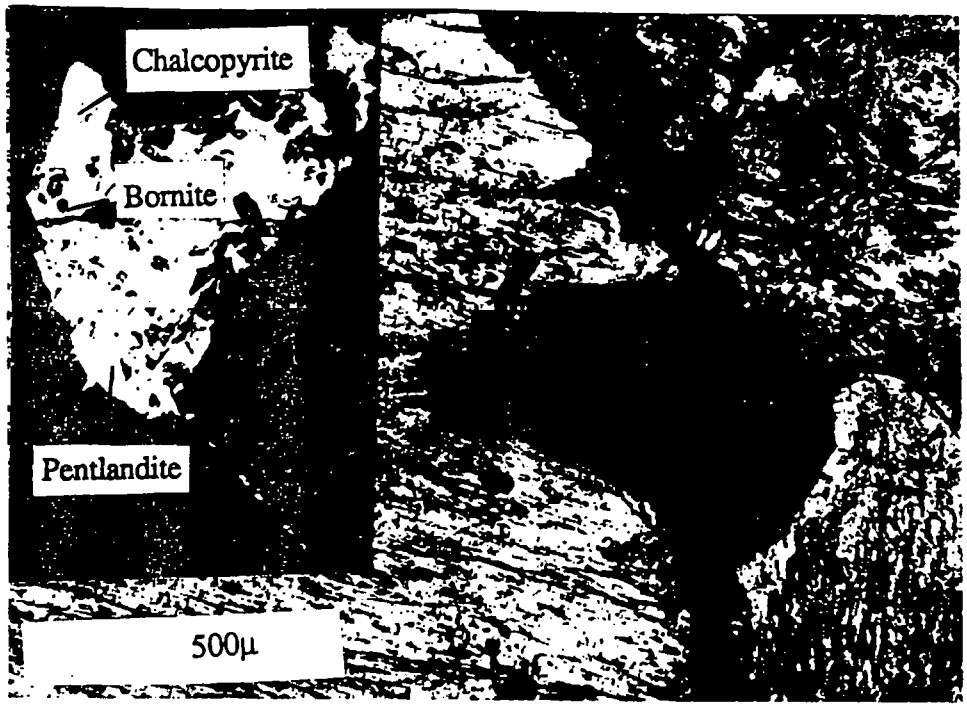

Fig. 3.9. Sulphide-magnetite intergrowth (opaque, centre) interstitial to clinopyroxene (brown, orange, grey and blue interference colours). Inset shows reflected light detail of the opaque intergrowth which comprises pentlandite, magnetite, chalcopyrite and bornite. Cumulate pyroxenite.

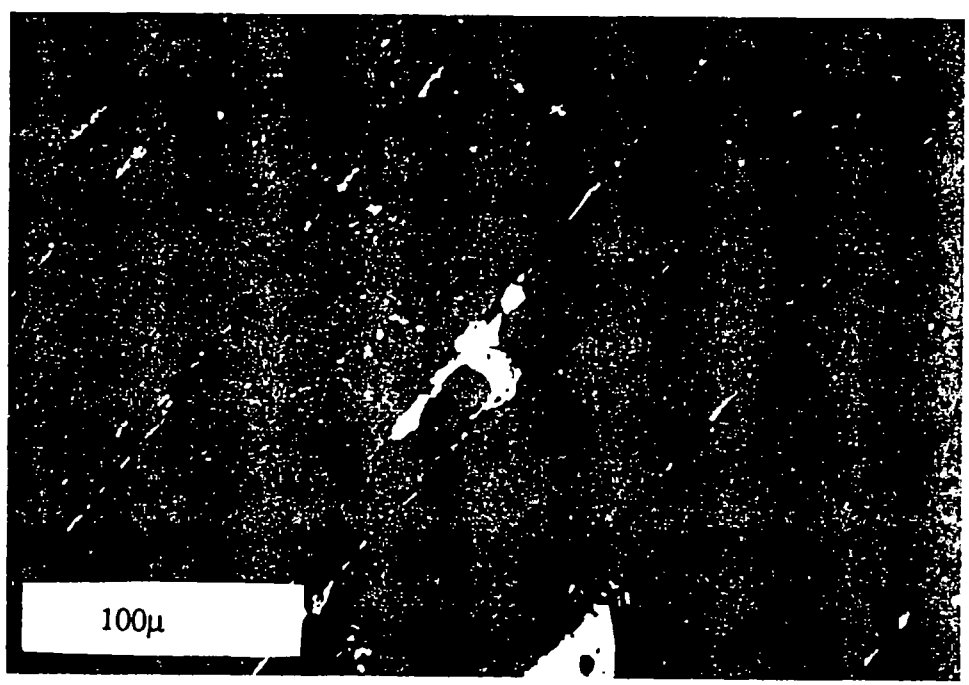

Fig. 3.10. Pentlandite (centre), actinolite (dark grey, centre left) and magnetite (light grey, centre left) along altered cleavage planes in clinopyroxene, cumulate pyroxenite.

Fig. 3.11. Pentlandite (centre left) intergrown with chalcopyrite (yellow, top left) which is altering to blue chalcocite. Pyrrhotite has been completely replaced by a low reflectance mixture of pyrite and marcasite (centre right). Cumulate pyroxenite.

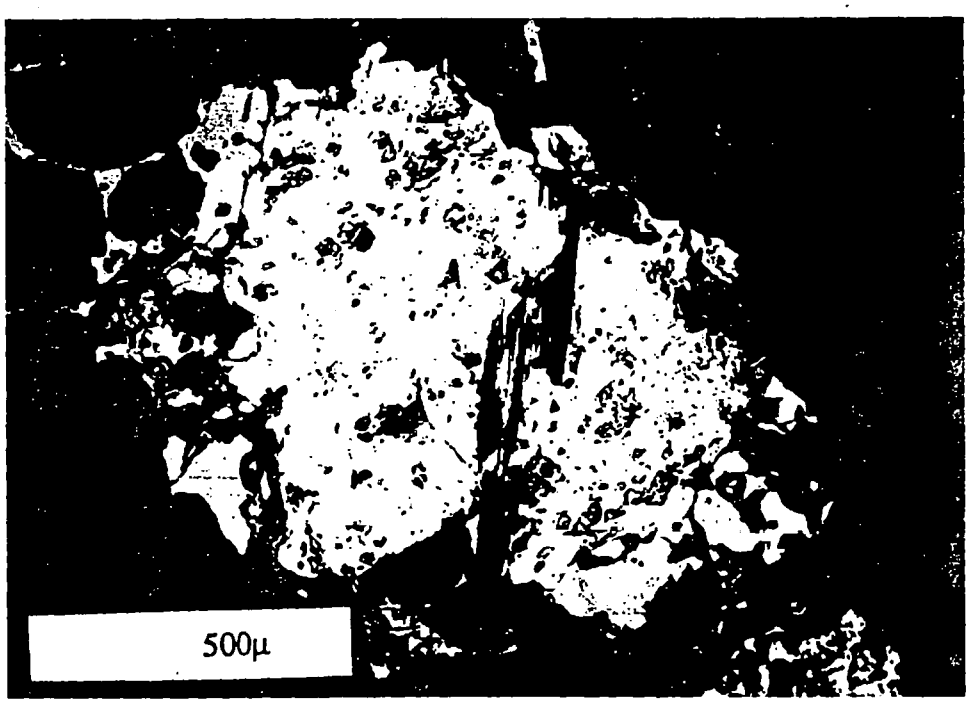

Fig. 3.12. Pentlandite (cream-yellow) intergrown with magnetite (light-grey, top left and bottom right). Bornite is intergrown with the pentlandite (purple-brown, centre) and chalcopyrite (yellow, centre left). Cumulate pyroxenite.

Fig. 3.13. Pentlandite (cream yellow, centre) altering to heazlewoodite (white, centre left) intergrown with chalcopyrite (orange yellow) and magnetite (grey, left and right) which contains inclusions of pentlandite. Cumulate pyroxenite.

well developed cracks along octahedral cleavage planes (Fig. 3.14). In almost completely serpentinized dunites, *i.e.* containing <10% olivine, pentlandite is replaced by large amounts of heazlewoodite (Fig. 3.15). Pentlandite either alters directly to awaruite (Fig. 3.16), or to heazlewoodite (Fig. 3.15). Pentlandite is intergrown with magnetite-awaruite-native Cu (Fig. 3.16), heazlewoodite-magnetite-Ni-Fe alloy, pentlandite-pyrrhotite (rare)-native Cu-magnetite. Pentlandite forms small inclusions in 'ferritchromit' at the boundary between 'ferritchromit' and chrome-spinel, or within cracks in disseminated chrome-spinel crystals. Pentlandite also occurs as 5-10μ solitary grains in the serpentinized matrix. Heazlewoodite often alters to a feathery intergrowth of anisotropic Ni-Fe alloy and silicate (Fig. 3.17). Inclusions of breithauptite and Cu and Pd-bearing Ni-antimonide are intergrown with heazlewoodite-awaruite-pentlandite (Fig. 3.18). Pyrrhotite has been found in one instance, where it is intergrown with pentlandite and magnetite (Fig. 3.19). Cu-Fe sulphides form <5 p.t.s. and often comprise chalcopyrite and chalcocite which occur as 5-30μ rounded inclusions in magnetite (Fig. 3.20). Two optically different Ni-Fe alloys have been identified in different associations. (i) Isotropic Ni-Fe alloys form up to 20 p.t.s., replace pentlandite and sometimes form rims to native Cu, (Fig. 3.16) (ii) Anisotropic Ni-Fe alloy intergrown with silicate which replaces heazlewoodite (Fig. 3.17). Type (ii) alloy is sometimes intergrown with 20-50μ composite Ni-Cu antimonide inclusions, (see section 3.5.3.1). Isotropic Ni-Fe alloy which is not intergrown with silicate, forms along 10-60μ wide cracks in pentlandite (Fig. 3.21), and in one instance has been found intergrown with Pt and Pd-bearing nickel antimonide and orcelite (see section 3.5.3.2). The mineralogy and mineral chemistry of the different Ni, and Ni-Cu antimonide minerals is discussed in detail in section 3.5. Native Cu forms 2-10 p.t.s.and occurs as (i) veinlets in serpentine up to 0.5cm long and 20-60μ wide, (ii) as fine slivers intergrown with serpentine about the margins of magnetite-heazlewoodite-pentlandite aggregates, (iii) intergrown with pentlandite magnetite and Ni-Fe alloy (Fig. 3.16), (iv) as symplectite-like intergrowths with pentlandite and native Cu, (v) as a rim to a Cu-bearing Ni-antimonide (see section 3.5.3.3). Chrome-spinel in the cumulate dunite unit occurs as (i) layers of massive chromite up to 5cm thick (Gass *et al.*, 1982), which are discontinuous, to layers one chromite crystal thick and <10cm long (Gass *et al.*, 1982).

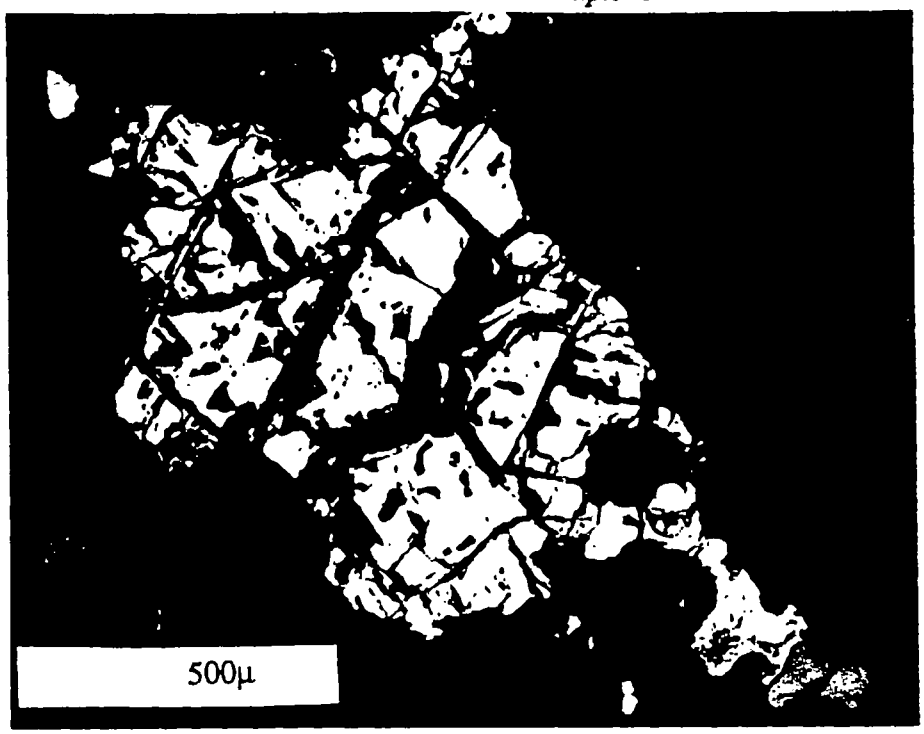

Fig. 3.14. Pentlandite (blocky, centre) showing a cuspate boundary with lizardite matrix (dark grey). Minor native copper and awaruite are intergrown with magnetite (bottom right). Cumulate dunite.

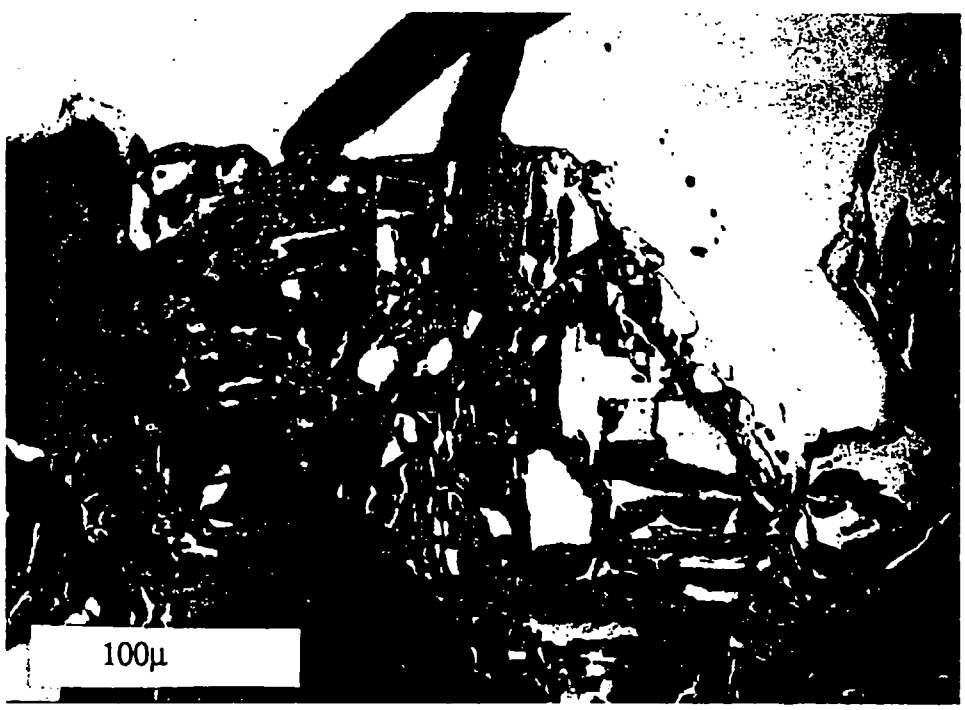

Fig. 3.15. Islands of pentlandite (cream brown, centre and bottom) replaced by heazlewoodite (yellow white, top) intergrown with magnetite (grey brown, bottom and left). Cumulate dunite.

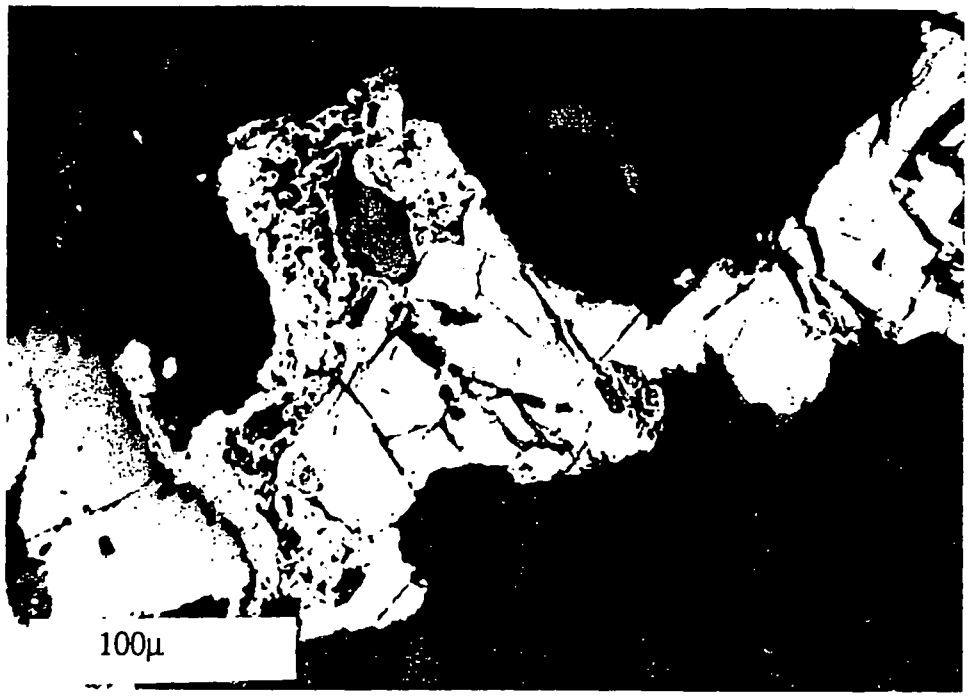

Fig. 3.16. Blocky pentlandite (centre and top right) altering to vermiform Ni-Fe alloy (awaruite) (centre left and top left) intergrown with native copper (pink, bottom left) and magnetite (grey, bottom left and centre top). Cumulate dunite.

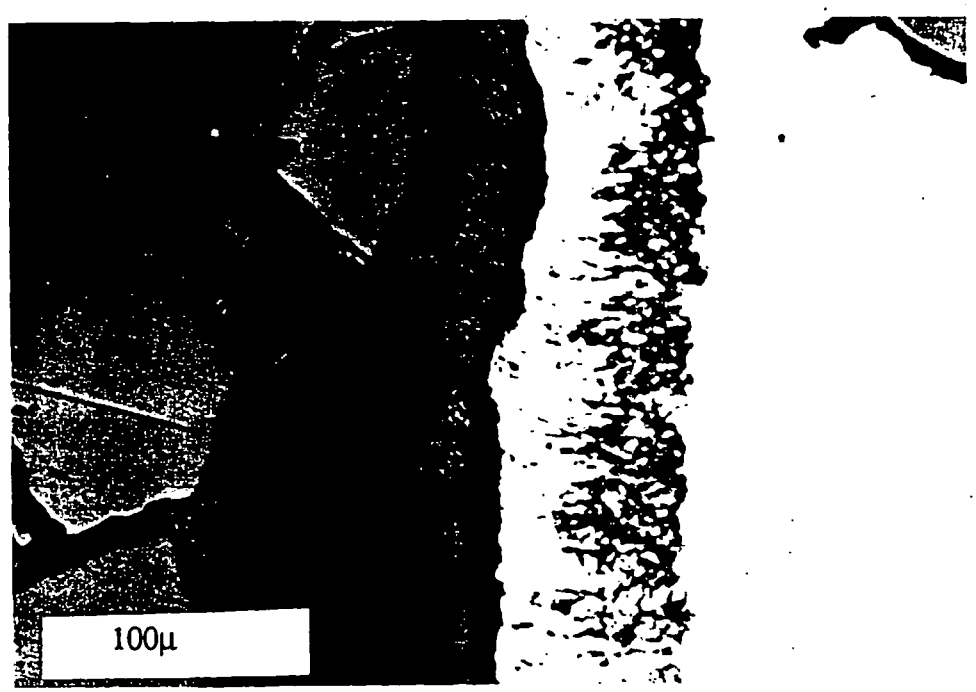

Fig. 3.17. Heazlewoodite (right) altering to a feathery intergrowth of awaruite and silicate (centre right). Magnetite (grey, right) and native copper (orange, next to magnetite) are intergrown with altered silicate. Cumulate dunite.

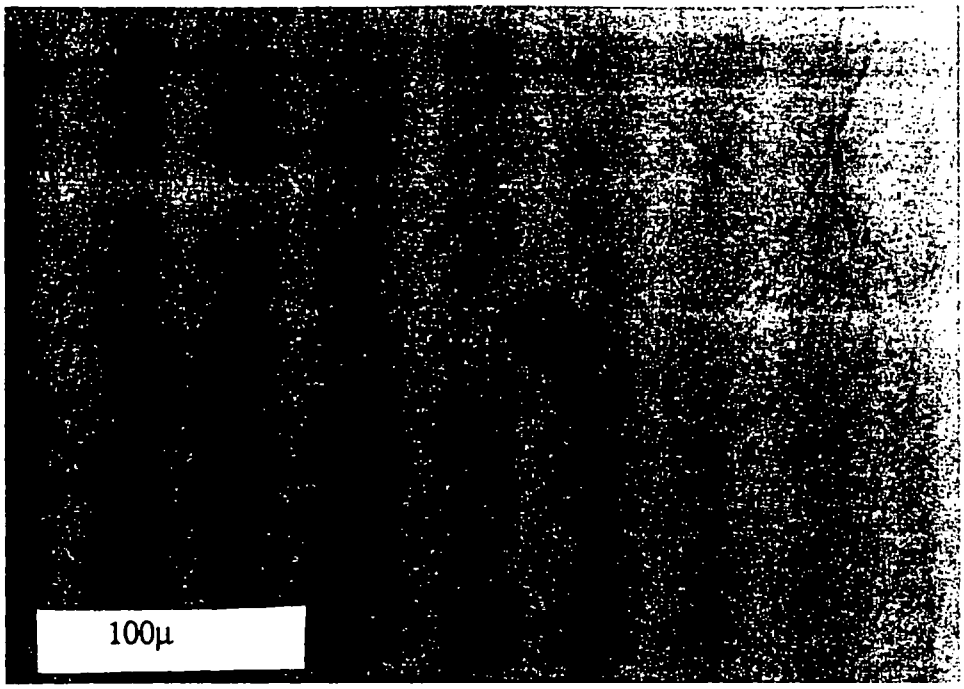

Fig. 3.18. Rounded inclusions of breithauptite (pink, centre) in heazlewoodite. Cumulate dunite.

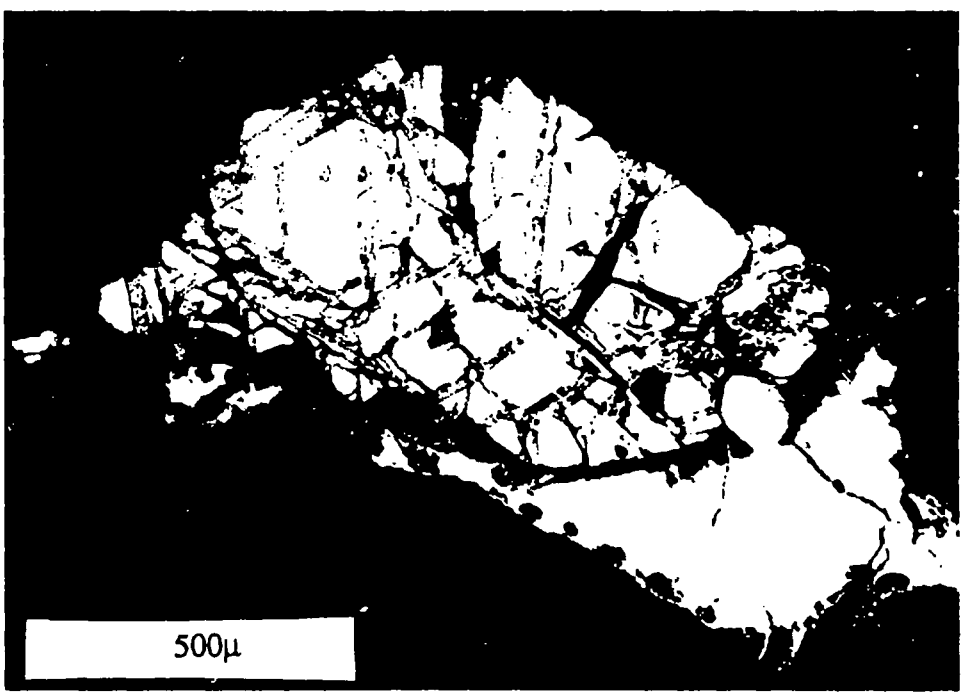

Fig. 3.19. Troilite (bottom right) intergrown with blocky pentlandite (centre top) which is intergrown with magnetite. Cumulate dunite.

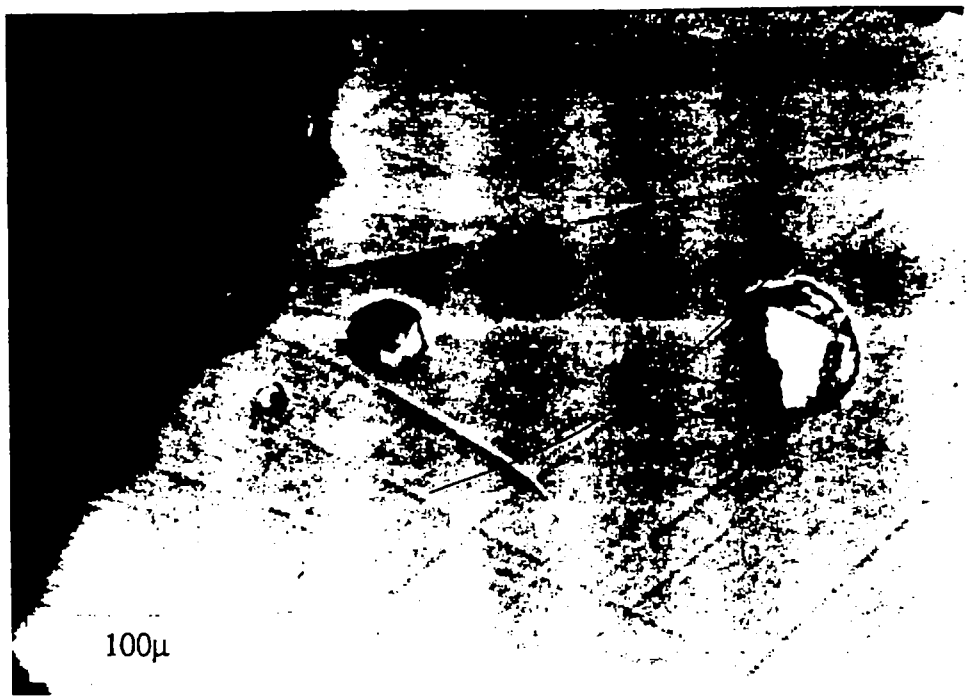

Fig. 3.20. Composite rounded inclusions of chalcopyrite (yellow) and chalcocite (blue) enclosed in magnetite (grey). Cumulate dunite.

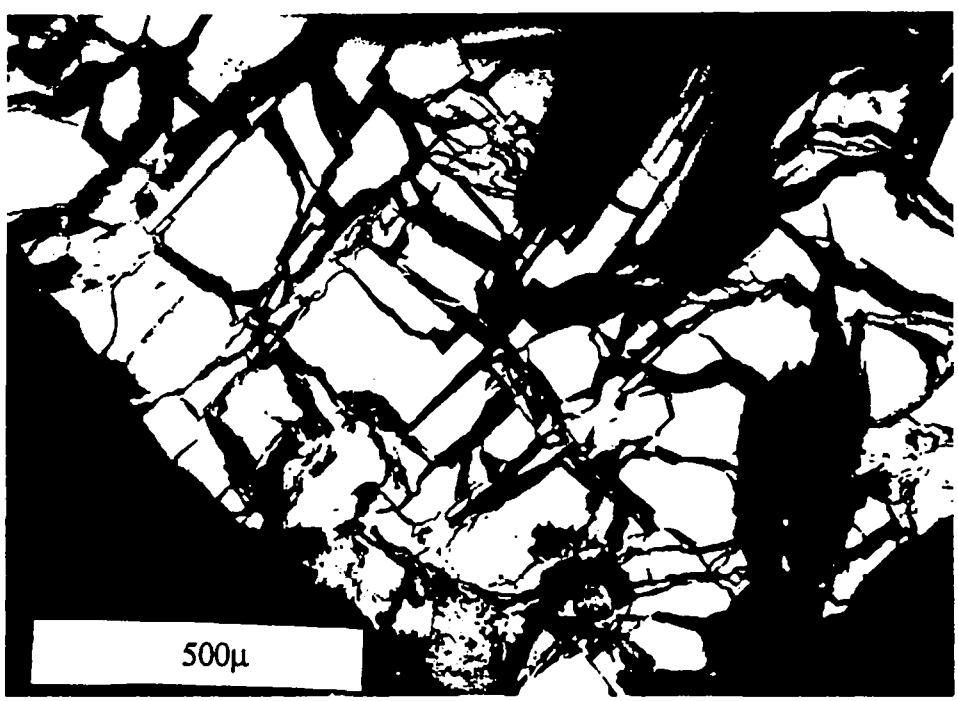

Fig. 3.21. Characteristic fractured, blocky pentlandite with magnetite (grey, centre left) and awaruite (white, centre left) along internal fractures. Magnetite is also intergrown with native copper (centre bottom). Cumulate dunite.

Fig. 3.22. Blocky pentlandite (centre left) replaced by heazlewoodite (centre and bottom left) intergrown with magnetite (mid-grey) and chrome-spinel (centre right). Cumulate dunite.

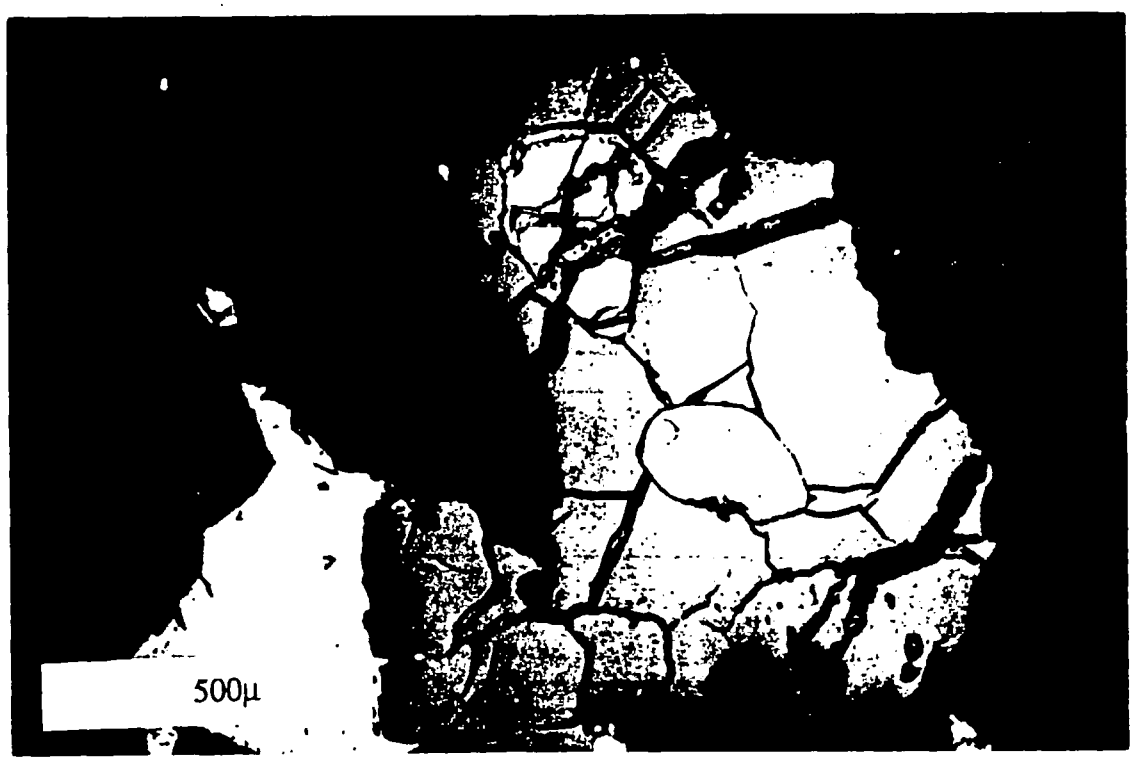

Fig. 3.23. Magnetite (grey) intergrown with rounded heazlewoodite (centre right) and pentlandite (centre top). Cumulate dunite.

Concentrations of chromite may approach 100% in massive ore or may be as low as 10%. (ii) Disseminated 1-2mm, sub-euhedral chrome-spinel in which spinel typically forms 2-15% of the modal mineralogy. Chrome-spinel commonly alters to light grey (in oil immersion) 'ferritchromit', often displaying salt and pepper texture and is often rimmed by carbonate and chlorite. Chromite also occurs in sulphide/oxide aggregates of pentlandite-heazlewoodite-magnetite-chromite (Fig. 3.22). Matrix and vein magnetite constitutes ~2-3% of the bulk sulphide/silicate assemblage and forms 10-70% of the modal sulphide/opaque oxide mineralogy. Magnetite forms rims to chromite and is commonly found intergrown with heazlewoodite and pentlandite in magnetite-spinel-sulphide aggregates up to 2mm in size. Chains of magnetite often occur intergrown with serpentine, an extra thickness of vein magnetite may delineate former olivine crystal grain boundaries (Dr. H. M. Prichard, *pers. comm.*). Magnetite also forms along cross-cutting veinlets of serpentine along with minor carbonate. Magnetite-sulphide intergrowths display several textures: (i) Magnetite is intergrown with rounded heazlewoodite and pentlandite (Fig. 3.23). (ii) Rounded magnetite is intergrown with pentlandite and heazlewoodite. (iii) Magnetite commonly forms along fractures in pentlandite (Fig. 3.21). In detail magnetite may be intergrown with native Cu and vermiform Ni-Fe alloy (Fig. 3.16). In these instances the magnetite displays caries texture suggesting replacement (Fig. 3.24). In the material from the NB borehole, Cu and Pd-bearing breithauptite occur within magnetite. The Ni-arsenide, orcelite occurs as 10-100μ inclusions in magnetite, intergrown with native Cu-altered magnetite-pentlandite, in a fracture in pentlandite where it is has breithauptite and Ni-Cu antimonides about its margin, and enclosed in silicate partially surrounded by a thin rim of native Cu at the margin of a magnetite crystal. Composite orcelite/Ni-Cu (Pd) antimonide has been found enclosed within silicate close to a larger heazlewoodite-pentlandite grain. One ~350μ square, porous crystal of maucherite was found enclosed within serpentine in a shear zone in dunite (Fig. 3.25).

3.3.4 Dunite pods within harzburgite

A similar opaque mineralogy to the cumulate dunite, wehrlitic dunite and transitional harzburgite is developed. Sparse disseminated sulphides of, pentlandite ~90 p.t.s., Ni-Fe alloy

~10 p.t.s., occur intergrown with magnetite. Disseminated chrome-spinel and 'ferritchromit' forms 2-5% by volume of the opaque oxide and sulphide plus silicate mineralogy.

3.3.5 Dunite pods within harzburgite with 4ppm ΣPt+Pd concentrations, Cliff

Chrome-spinel is ubiquitous and often associated with sulphide aggregates. Magnetite is intergrown with heazlewoodite, pentlandite and encloses small (30μ) Cu-Fe sulphides, Cu-sulphide and Ni-Fe sulphides. Heazlewoodite forms 50-70 p.t.s., is intergrown with, and replaces pentlandite. Heazlewoodite alters to millerite and sometimes to godlevskite (Fig. 3.26). Minor chalcocite (Cu_2S) borders heazlewoodite along with sparse native Cu. Ni-arsenides and antimonides are common. The Ni-arsenide orcelite, containing trace Sb and Cu, is enclosed within heazlewoodite and is sometimes concentrated around the margins of heazlewoodite where it is closely associated with Ni-antimonide grains, or occurs as solitary grains closely associated with Ni-sulphide aggregates. The Ni-antimonide breithauptite occurs as 4-40μ inclusions within heazlewoodite or at the boundary between heazlewoodite and pentlandite. Breithauptite contains minor Cu, Pd and As and sometimes occurs as composite grains with a different Ni-antimonide which is richer in Cu. This 'Cu-rich' breithauptite has also been found on its own at the margins of heazlewoodite.

3.3.6 Podiform chromitite, Cliff

A Ni-arsenide assemblage of niccolite closely associated with maucherite occurs as anhedral crystals interstitial to, and along cracks in chrome-spinel and 'ferritchromit' in a serpentinised matrix (Fig. 3.27) Niccolite is yellowish-white to yellow in colour and strongly anisotropic and forms anhedral, 10-300μ crystals often completely surrounded by a 2-15μ rim of a blue-grey phase which is moderately anisotropic. Maucherite forms grains of 5-50μ, is yellowish white in oil and anisotropism where observed is weak.

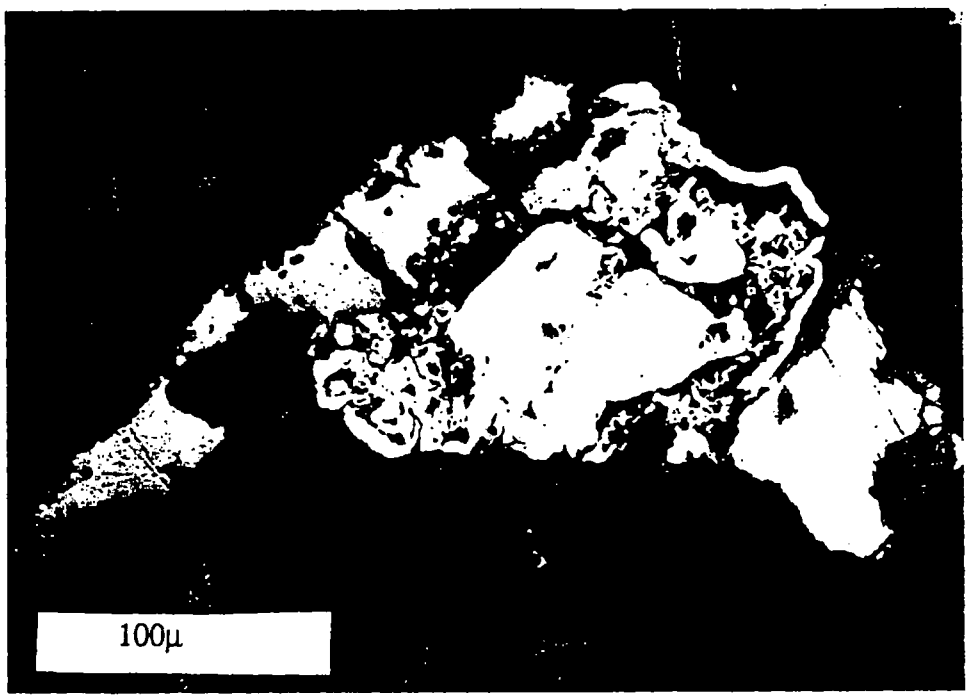

Fig. 3.24. Magnetite (mid-grey, centre left) showing caries texture, intergrown with native copper (orange, right), pentlandite (cream brown, centre) and vermiform awaruite (white, centre). Cumulate dunite.

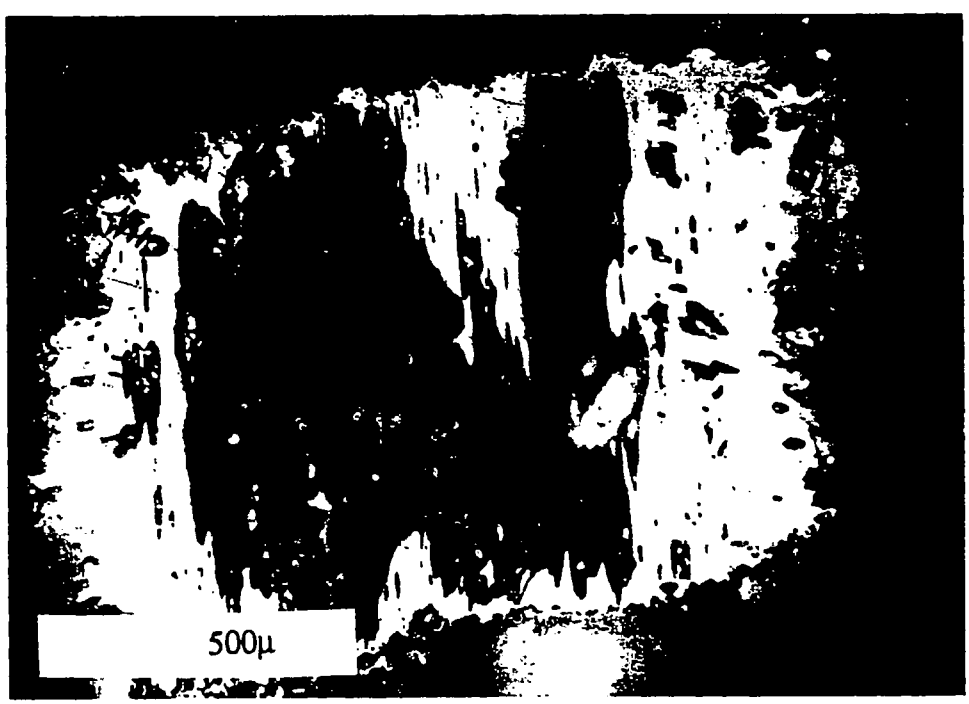

Fig. 3.25. Maucherite enclosed in serpentine. Sheared cumulate dunite.

Fig. 3.26. Godlevskite lamellae (brown, centre and top left) replacing heazlewoodite. Dunite pod, Cliff.

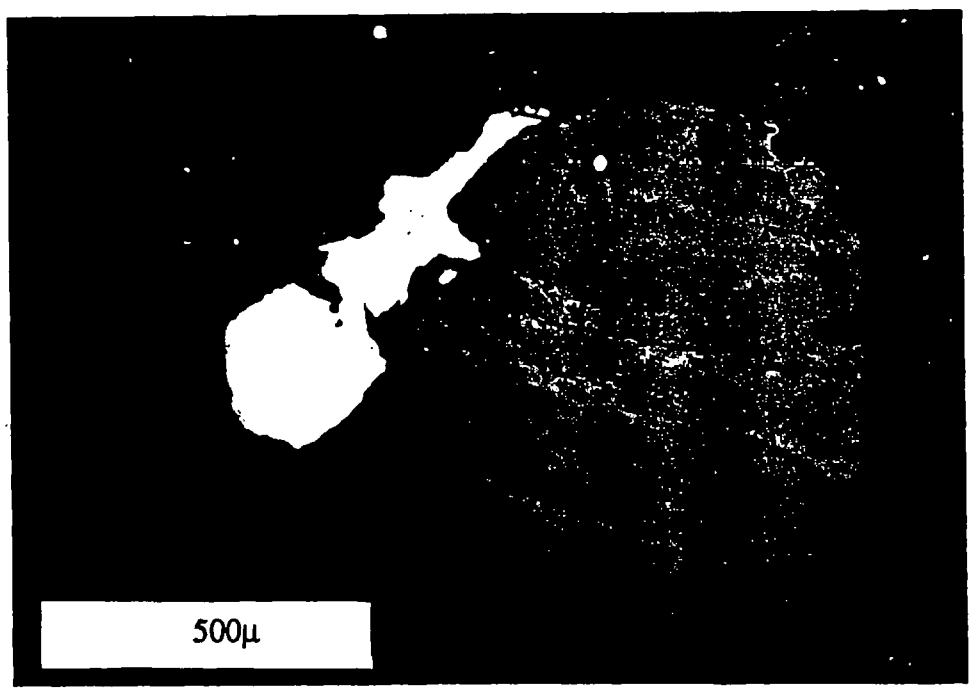

Fig. 3.27. Rounded chrome-spinel (centre) altering along internal cracks to light grey 'ferritchromit' intergrown with niccolite (white, top left). Podiform chromitite, Cliff.

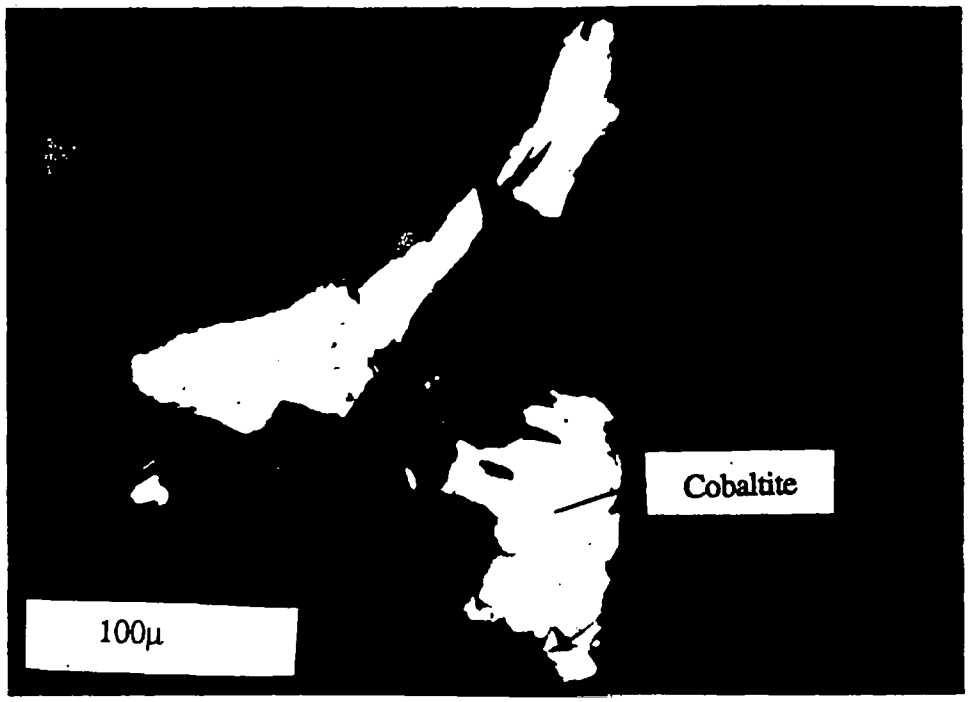

Fig. 3.28. Cobaltite (white, centre bottom) intergrown with pyrrhotite and pentlandite (centre left). Talc-carbonate rock, basal thrust.

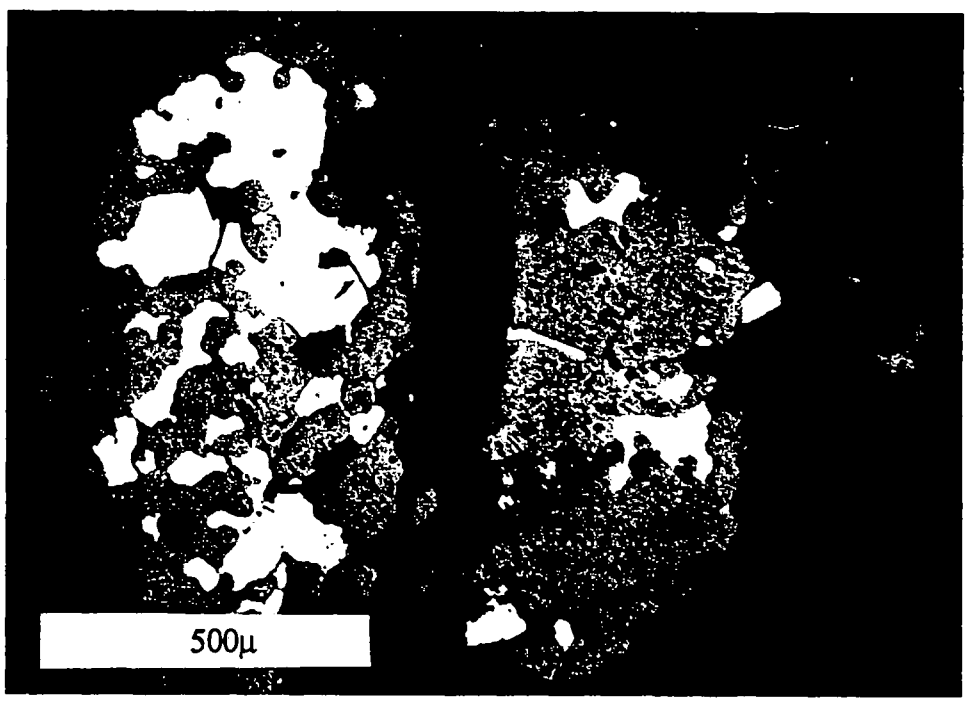

Fig. 3.29. Caries texture 'ferritchromit' (grey, centre left and centre right) replaced by pyrrhotite (cream yellow). Talc-carbonate rock, basal thrust.

3.3.7 Serpentinites from the basal thrust.

Disseminated 1-200μ sized solitary sulphide grains and composite sulphide aggregates are intergrown with secondary silicates. Pyrrhotite occurs as discrete grains (1-40μ) within carbonate grains, encloses magnetite, and is commonly intergrown with pentlandite. Pentlandite forms flames within pyrrhotite or occurs as small blocks about the margins of pyrrhotite. Pyrrhotite alters to 'limonite' and fine mixtures of marcasite and pyrite along cleavage planes. Pentlandite alters to poorly crystalline violarite and 'limonite'. Chalcopyrite is present as discrete grains or more often as intergrown pyrrhotite-chalcopyrite, chalcopyrite-pentlandite, chalcopyrite-pentlandite-pyrrhotite, or chalcopyrite-pyrrhotite-mackinawite (FeS). Cobaltite, which is PGE-rich in its core, is found with pentlandite or is intergrown with pyrrhotite and chalcopyrite in pentlandite (Fig. 3.28). Niccolite is associated with magnetite where it has altered rims of orcelite/rammelsbergite. It is associated with minor amounts of cobaltite and is present as euhedral inclusions in carbonate. Minor amounts of mackinawite are associated with pyrrhotite and pentlandite and minor amounts of valleriite are associated with pentlandite. Chrome-spinel alters to 'ferritchromit' and is often intimately intergrown with pyrrhotite and pentlandite (Fig. 3.29).

3.4 Opaque mineral chemistry

Since the mafic part of the ophiolite complex consists of an Fe-Cu sulphide assemblage which differs from the Ni-Fe sulphide assemblage in the ultramafic sequence, the mineral chemistry of the opaques within the mafic part of the ophiolite will be considered separately from the opaque mineral chemistry of the ultramafic portion. Within the mafic and ultramafic portion of the ophiolite, the sulphide mineral chemistry generally shows no significant variation with lithology and so will be considered by cation. Due to the complex mineralogy and mineral chemistry of the Ni-antimonide minerals these are considered separately in section 3.5. Quantitative determination of the compositions of the different opaque minerals was undertaken using a Cambridge Instruments M9 wavelength dispersive electron microprobe. Some of the analyses obtained at the outset of this study were performed on a Geoscan energy dispersive

electron microprobe. The analytical proceedure for each of these techniques is described in appendices A.1 and A.2. Table 3.1 lists the elements sought in the different sulphide and arsenide and antimonide minerals along with an estimate of the limits of determination for each element.

Element	*Limit of determination (wt%), 6 σ*
Pt	0.37
Pd	0.06
Ag	0.02
As	0.37
Sb	0.04
Co	0.09
Cu	0.13 (0.5)
Fe	0.15 (0.5)
Ni	0.12 (0.35)
S	0.02 (0.2)

Table 3.1. Typical limits of determination for the different elements sought in sulphide, arsenide and antimonide minerals from the Shetland ophiolite by wavelength dispersive electron microprobe analysis. Numbers in brackets are the limits of determination of the elements by energy dispersive electron microprobe analysis. The limit of determination is the smallest signal (in terms of wt.% element) that can be quantitatively measured by the microprobe. The limit of determination is derived from the formula; $6\sqrt{2R_{unk}t_{unk}[C_{std}/S_{std}t_{std}]}$ where R_{unk} = background counts on unknown, t_{unk} = count time (seconds) on unknown, C_{std} = concentration of element in standard, S_{std} = counts - background counts on standard and t_{std} = count time (seconds) on standard (Potts, 1987).

The compositions of all analysed Fe and Ni-bearing sulphides are shown on a triangular diagram in Fig. 3.30. Cu-bearing sulphides are displayed on a triangular diagram in Fig. 3.31

3.4.1 Sulphide mineral chemistry of the mafic portion of the ophiolite

Pyrrhotite has an average S content of 52.75 ± 0.3 at.% and ranges from hexagonal to monoclinic pyrrhotite (Fig. 3.32) with trace amounts of Ni (0-0.38 wt.%) and Co (0-0.21 wt.%). The average composition pyrrhotites from the mafic and ultramafic portions of the ophiolite are given in table 3.2. The average composition of chalcopyrites are given in table 3.3. Formulae range from $[Cu_{0.97}Fe_{1.01}S_2]$-$[Cu_{1.11}Fe_{0.98}S_2]$, (average atomic Cu/Fe ratio 0.98 ± 0.03 at.%). No Cu was detected in pyrrhotite and no Ni was detected in chalcopyrite.

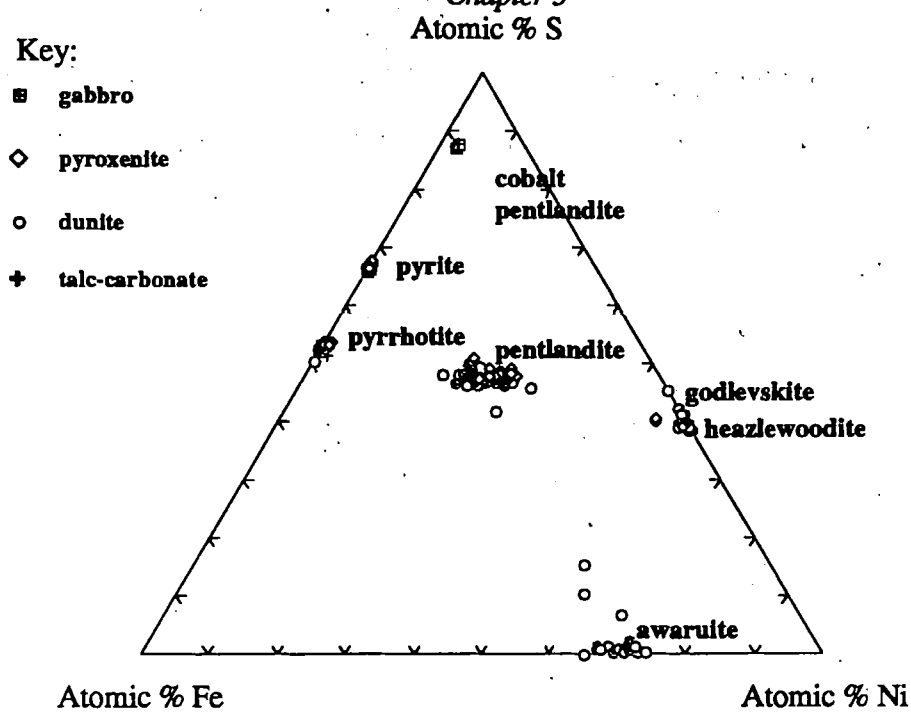

		gabbro	pyroxenite	dunite	talc-carbonate
n	pyrite	15	15	-	-
n	pyrrhotite	15	9	1	9
n	pentlandite	-	34	93	7
n	cobaltian pentlandite	2	-	-	-
n	heazlewoodite	-	5	36	-
n	godlevskite	-	-	1	-
n	awaruite	-	-	25	-

Fig. 3.30. Ternary plot showing the compositions of the different Fe and Ni-bearing sulphides analysed.

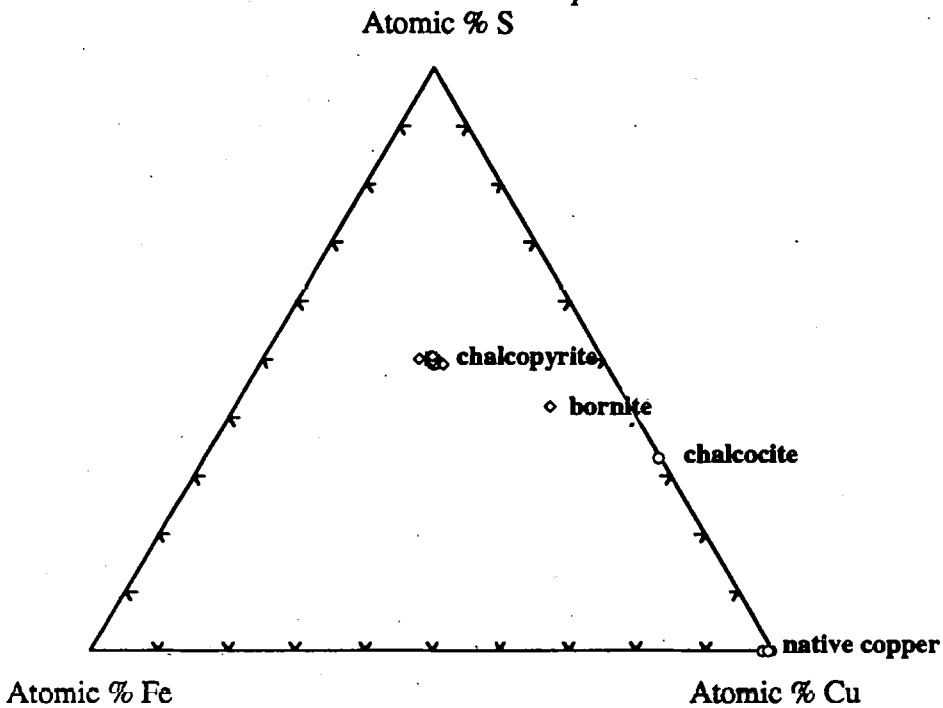

		gabbro	pyroxenite	dunite	talc-carbonate
n	**chalcopyrite**	7	10	-	1
n	**bornite**	-	1	-	-
n	**chalcocite**	-	-	1	-
n	**native copper**	-	-	7	-

Fig. 3.31. Ternary plot showing the compositions of the different Cu-bearing sulphides analysed. Key as for Fig. 3.30.

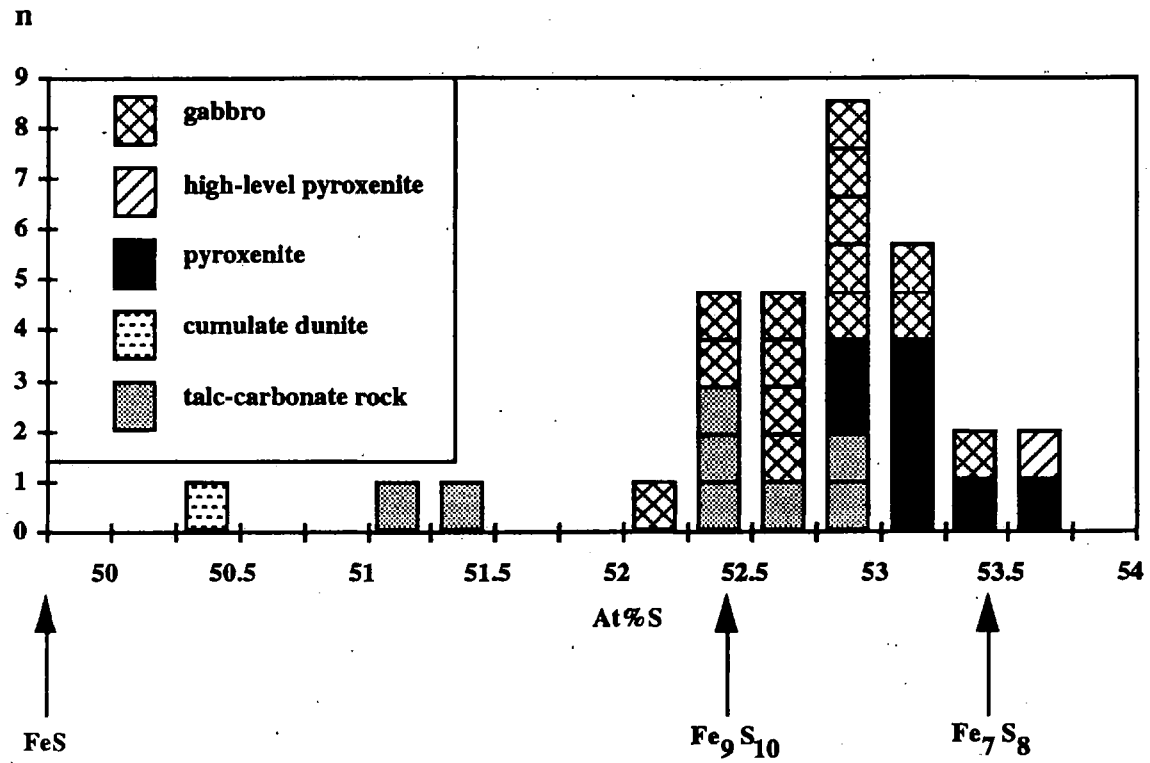

Fig. 3.32. Composition, in terms of atomic percent S, of pyrrhotites from the Shetland ophiolite.

Element	*Fe*	*Ni*	*Co*	*S*	*Cu*	*As*	*Sb*	*Ag*	*Pd*	*Pt*	*Total*
Average	60.06	0.19	0.07	38.58	0.06	0.03	0.00	0.01	0.02	0.04	99.05
Standard deviation (1σ)	0.81	0.43	0.07	0.77	0.10	0.06	0.00	0.01	0.02	0.06	0.71

Table 3.2. Average of all microprobe analyses (in wt.%) of pyrrhotites from the Shetland ophiolite including standard deviations.

Element	*Fe*	*Ni*	*Co*	*S*	*Cu*	*As*	*Sb*	*Ag*	*Pd*	*Pt*	*Total*
Average	30.22	0.00	0.03	34.25	34.11	0.03	0.00	0.01	0.03	0.00	98.68
Standard deviation (1σ)	0.76	0.01	0.04	0.48	1.05	0.07	0.00	0.01	0.02	0.00	0.69

Table 3.3. Average of all microprobe analyses (in wt.%) of Cu-Fe sulphides from the Shetland ophiolite including standard deviations.

Pyrite contains traces of Co (0-0.25 wt.%). Concentrations of Ni and As were below the detection limit of the microprobe in pyrite. The average composition of pyrite grains is given in table 3.4.

Element	*Fe*	*Ni*	*Co*	*S*	*Cu*	*As*	*Sb*	*Ag*	*Pd*	*Pt*	*Total*
Average	45.97	0.07	0.27	53.01	0.02	0.09	0.00	0.00	0.01	0.01	99.44
Standard deviation (1σ)	1.02	0.13	0.40	0.53	0.10	0.18	0.00	0.00	0.01	0.02	0.96

Table 3.4. Average of all microprobe analyses (in wt.%) of pyrites from the Shetland ophiolite including standard deviations.

A white isotropic euhedral sulphide intergrown with pyrrhotite and marcasite contains up to 48.39 at.% Co with 5.55 at.% Fe and 1.25 at.% Ni. The optical properties of this phase are consistent with those for cobaltian pentlandite reported by Ramdohr (1969). The calculated formula of $[(Fe_{0.95}Ni_{0.21}Co_{7.92})_{9.08}S_8]$ would suggest that it is a cobaltian pentlandite. However, this falls outside the range of compositions of natural pentlandites whose Co contents range from 0.1 at.% to 42.47 at.% (Vasjoki *et al.*, 1974).

3.4.2 Opaque mineral chemistry of the ultramafic portion of the ophiolite

The mineral chemistry of Ni and Ni-Fe sulphides, Ni-Fe alloys, Ni-arsenides and sulpharsenides and Ni-Fe alloys and Cu and Cu-Fe and Fe sulphides from ultramafic rocks from the ophiolite complex are discussed below along with spinel mineral chemistry.

3.4.2.1 Ni and Ni-Fe sulphides

Pentlandite

The range of compositions of pentlandite from ultramafic rocks is shown on a ternary plot in Fig. 3.33. The average composition of these pentlandites is given in table 3.5. The total range in composition is from 19.60 at.% to 34.04 at.% Ni, excluding 5 analyses which range from 34.6-49.7 at.% Ni, in which pentlandite is intimately intergrown with, and is altering to, either heazlewoodite or Ni-Fe alloy and therefore shows gross disequilibrium.

Element	*Fe*	*Ni*	*Co*	*S*	*Cu*	*As*	*Sb*	*Ag*	*Pd*	*Pt*	*Total*
Average	31.88	32.91	1.33	32.73	0.14	0.04	0.00	0.01	0.02	0.02	99.09
Standard deviation (1σ)	3.38	3.06	0.89	0.76	0.71	0.06	0.03	0.01	0.02	0.04	0.70

Table 3.5. Average of all microprobe analyses (in wt.%) of pentlandites from the Shetland ophiolite including standard deviations.

Large intra- and intergrain differences in pentlandite chemistry occur within an individual thin section. Intergrain pentlandite analyses from a cumulate dunite sample range from 24.95-34.04 at.% Ni (Fe/Ni 1.08-0.57). The most Ni-rich pentlandites occur in Ni-rich, heazlewoodite-dominated sulphide assemblages, heazlewoodite-pentlandite±awaruite, godlevskite, millerite. The most Fe-rich pentlandite analysed (31.20 at.% Fe) occurs in the rare assemblage pentlandite-troilite-native Cu.

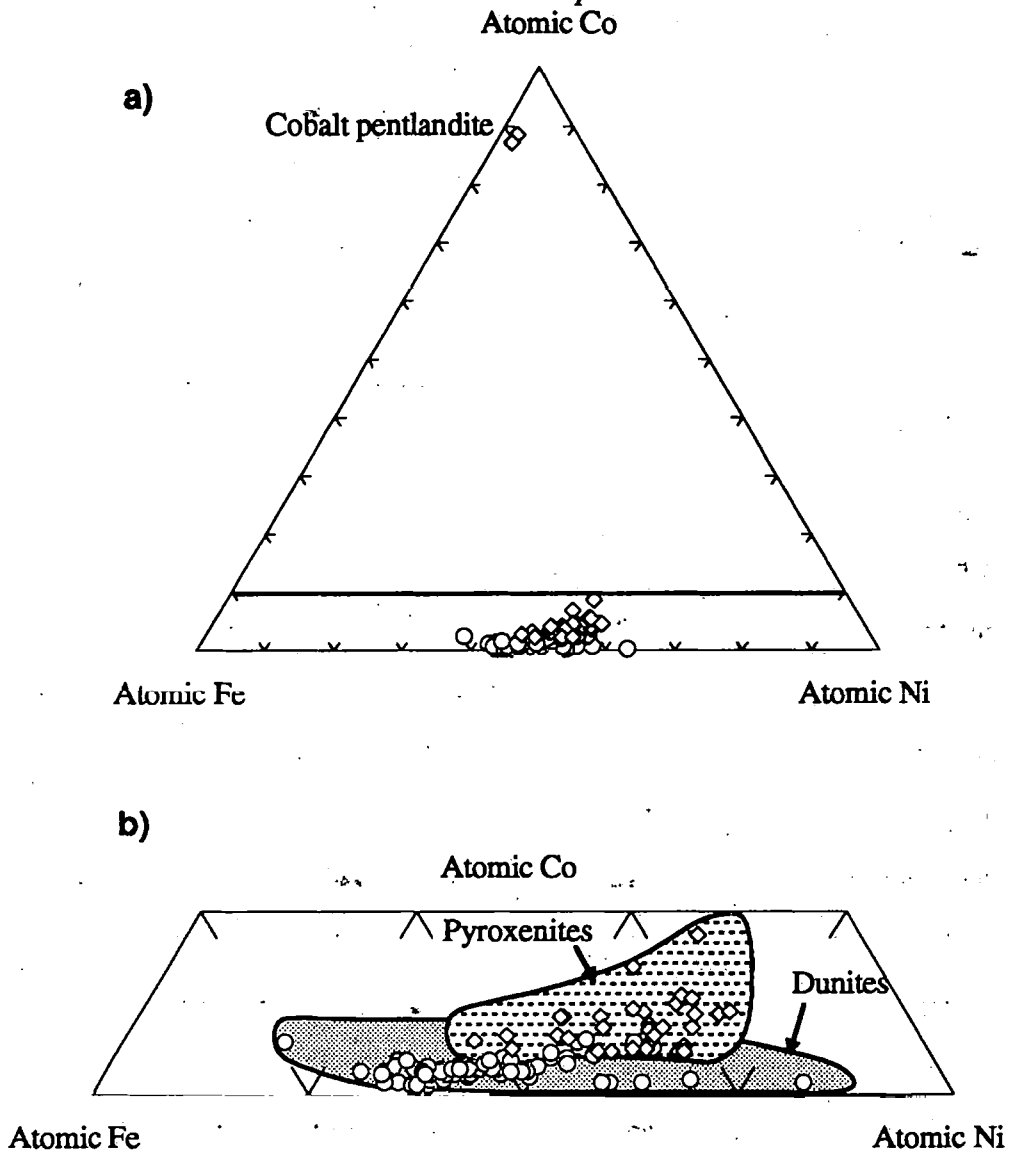

Fig.3.33. a) Ternary plot showing composition of analysed pentlandites from the Shetland ophiolite. b) enlarged portion of a) showing compositions of pyroxenite and dunite-hosted pentlandites.

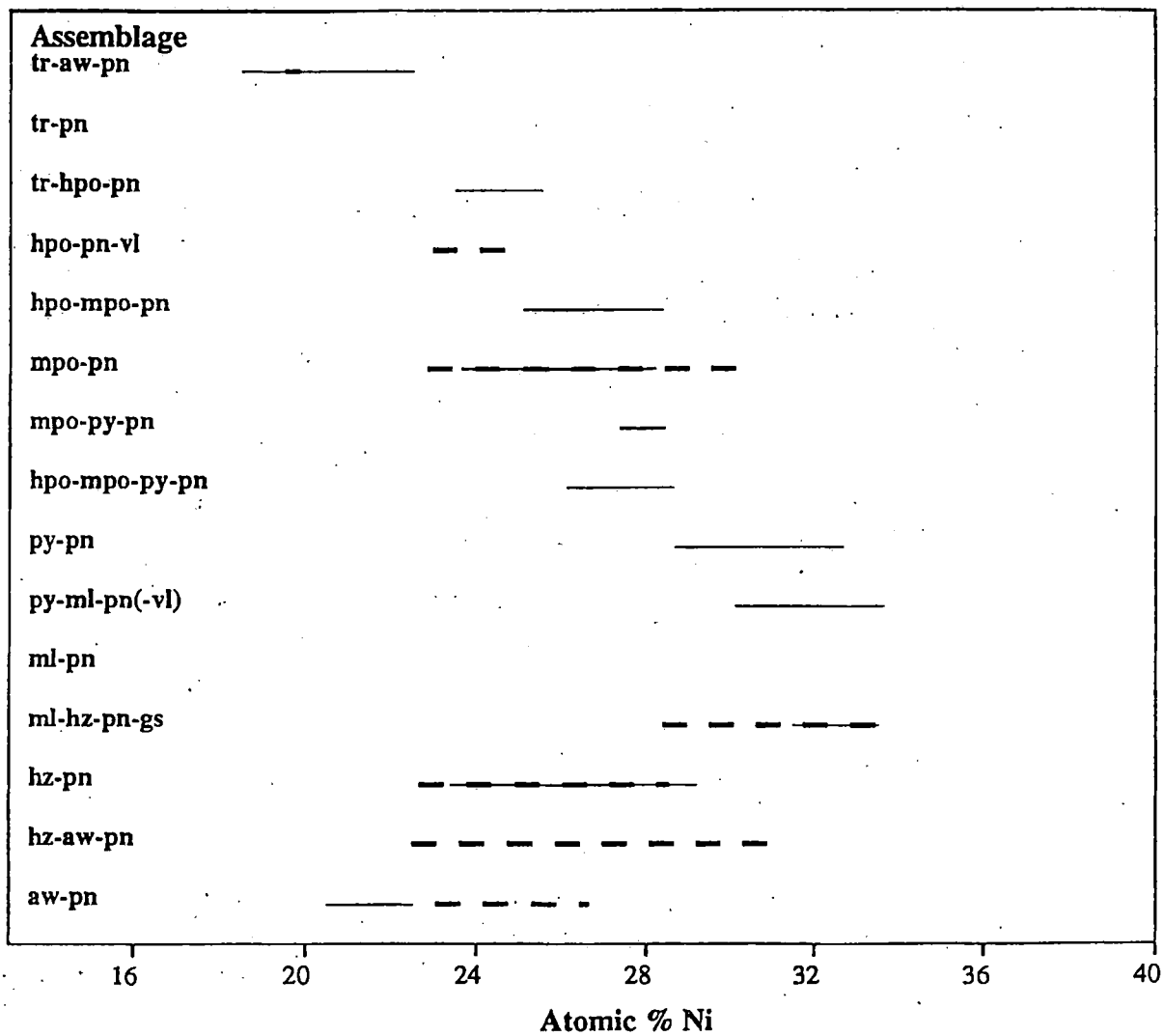

Fig. 3.34. Compositional range of natural pentlandites, solid lines (after Misra and Fleet, 1973), with superimposed compositions of pentlandites from the Shetland ophiolite, dashed lines. Abbreviations as follows; py = pyrite, hpo = hexagonal pyrrhotite, mpo = monoclinic pyrrhotite, tr = troilite, pn = pentlandite, py = pyrite, vl = violarite, hz = heazlewoodite, ml = millerite, gs = godlevskite, aw = awaruite.

The Co content of all analysed pentlandites vary from 0.16-5.85 at.% (excluding cobalt pentlandite from the gabbro). The average Co content of pyroxenite-hosted pentlandite is 1.96 ± 0.75 at.%, higher than the average Co content of dunite hosted pentlandite 0.72 ± 0.27 at.% (Fig. 3.33). The range of pentlandite compositions from the Shetland ophiolite is comparable with the total range of natural pentlandite compositions reported by Misra and Fleet (1973) (18 to 34 at.% Ni) and is similar to the range of pentlandite compositions reported by Abrajano and Pasteris (1989) of 17-32 at.% from the basal cumulate section of the Acoje massif, Zambales ophiolite. The observation that the most Ni-rich pentlandite occurs in the most Ni-rich sulphide assemblage documented in this study (pentlandite-heazlewoodite-millerite-godlevskite) whereas the most Ni-poor pentlandite occurs in the assemblage pentlandite-troilite, is in agreement with Graterol and Naldrett (1971), Harris and Nickel (1972) and Misra and Fleet (1973). They noted that the Ni content of pentlandite increased with increase in the nickel content of the bulk sulphide assemblage, the Ni-poor limit of pentlandite (20 at.% Ni) was defined by the limiting composition of pentlandite in the natural assemblage troilite-pentlandite (Misra and Fleet, 1973). The variation in the Ni content of pentlandite from the dunites and pyroxenites is superimposed upon the ranges of Ni contents of pentlandites from different Fe, Ni sulphide assemblages of Misra and Fleet (1973) (Fig. 3.34). The chemistry of pentlandite from the heazlewoodite-awaruite-pentlandite assemblage and hexagonal pyrrhotite-pentlandite-violarite was not recognized on Misra and Fleet's diagram, but the assemblage heazlewoodite-awaruite-pentlandite is common in cumulate dunites and hexagonal pyrrhotite-pentlandite-violarite occurs in talc-carbonate rock from near the basal thrust on Unst. There is a general agreement between the ranges of Ni-content of pentlandites of this study (bold dashed lines) and those of Misra and Fleet (1973) (thin continuous lines). Lorand (1989) noted increased Fe/Ni ratios in pentlandite in a paragenetically late interstitial sulphide assemblage of pentlandite-troilite-chalcopyrite-mackinawite (Fe/Ni 0.6-1.7), compared to pentlandite in sulphide inclusions in major silicate phases (Fe/Ni 0.7-1.2) from spinel-peridotites from Ariege, N.E. Pyrenees. This was thought to be caused by equilibration of the interstitial sulphides with serpentinizing fluids under lower fS_2 conditions whereas sulphides included in silicates were effectively armoured from such

fluids. Lachize *et al.* (1991) noted that the Co content of pentlandite from a 150m thick disseminated sulphide-rich zone in the gabbroic magma chamber, Wadi Haymiliyah, Semail ophiolite, Oman, increased regularly from the lowermost olivine gabbro (1 wt.% Co) to two-pyroxene gabbro (~7 wt.% Co). This increase in Co content was noted to be negatively correlated with the abundance of blocky pentlandite which decreased progressively in parallel with the disappearance of olivine in the stratigraphically higher two-pyroxene gabbros. A similar trend in Co-enrichment is apparent for the pentlandites analysed in this study. More primitive olivine-rich lithologies host pentlandite-dominated sulphide assemblages containing pentlandites with lower Co-contents than more evolved pentlandite-poor sulphide assemblages in the pyroxenites with Co-enriched pentlandite. Cobalt was detected in Unst chrome-spinels by beta-autoradiography by Potts (1984). Lord (1991) noted correlations between Co and the amounts of modal chrome-spinel, olivine and sulphide in whole-rock analyses of a suite of representative rock types from the ophiolite. This suggested substitution of Co into chrome-spinel olivine and sulphide. In a very simple model, the differences in the Co contents of dunite hosted and pyroxenite hosted pentlandite could therefore be explained by partitioning of Co between chrome-spinel, olivine and pentlandite. In the dunite unit, pentlandite with lower Co content occurs because Co in the melt partitioned into olivine and chrome-spinel as well as pentlandite, whereas in the pyroxenite unit, where there is a paucity of the phases olivine and chrome-spinel, more Co partitioned into pentlandite resulting in pentlandite with significantly higher Co compared to pentlandite from the dunite unit. The variations in the Co contents of pentlandites from the Shetland ophiolite are also consistent with those of Vasjoki *et al.* (1974), namely that cobaltian pentlandite occurs in pyroxenite-hosted sulphide assemblages where chalcopyrite is relatively abundant (forming approximately 10-50 p.t.s.), whereas pentlandites with lower Co-contents occur in mineralized dunites (1-2 volume % sulphide) where chalcopyrite is scarce.

Minor element contents of pentlandites

Pentlandites were routinely analysed for PGE (Pd, Pt) because of the high reported grades of PGE reported from the Shetland ophiolite (up to 100ppm from a chromite rich dunite lens in harzburgite, Cliff (Prichard and Tarkian, 1988)). These high PGE grades are linked to a

well documented and diverse Pt-group and precious metal mineralogy from the complex, (*e.g.* Prichard *et al.*, 1994). The Ag content of pentlandite was also investigated, as argentian pentlandites are well known and Ag alloys are sometimes found in PGE-rich lithologies (Prichard *et al.*, 1994).

Ru-bearing pentlandite containing as much as 11.86 wt.% Ru has been described from two localities in Unst (Prichard and Tarkian, 1988). Cu (0-0.63 wt.%) and As (0-0.34 wt.%) were detected in some pentlandites. It is not clear whether there is true solution of these elements in pentlandite, or whether sub-micron grains of native Cu, Cu sulphide or Ni-arsenide contribute to these analyses. No PGE were detected in pentlandite during the present study.

Of the nine metal atoms in the pentlandite formula (eight in tetrahedral sites and one in the octahedral site), only the octahedral site can be occupied by PGE (Knop *et al.*, 1970). In their experiments (Makovicky *et al.*, 1986), found no Pt in pentlandite (within their analytical uncertainty of 0.05 %), but complete solid solution of Ru, Rh and Pd towards PGE-free pentlandite. Up to 2% Pd in apparent solid solution in natural pentlandite was reported from the Bushveld (Kinloch, 1982), although he noted that this value was anomalously high and "not the norm" for pentlandite from this locality. The possibility that PGE may be present in solid solution in pentlandite at levels below the detection limit of the M9 microprobe cannot be discounted.

Heazlewoodite and godlevskite.

Heazlewoodite analysed in this study ranges from $[Ni_{2.71}S_2]$ to $[(Ni_{3.18}Fe_{0.02})_{3.2}(As_{0.01}S_2)_{2.01}]$.

Element	*Fe*	*Ni*	*Co*	*S*	*Cu*	*As*	*Sb*	*Ag*	*Pd*	*Pt*	*Total*
Average	0.51	72.17	0.03	26.67	0.08	0.11	0.01	0.01	0.03	0.01	99.63
Standard deviation (1σ)	1.15	1.39	0.09	0.80	0.09	0.11	0.05	0.01	0.03	0.03	1.05

Table 3.6. Average of all microprobe analyses (in wt.%) of heazlewoodites from the Shetland ophiolite including standard deviations.

This is close to the 3:2 metal:sulphur ratio of natural heazlewoodite reported by Graterol and Naldrett (1971), which is in agreement with data from synthetic studies in the Ni-S system (Kullerud and Yund, 1962). Trace amounts of Fe ranging from 0 to 5.14 wt.% (average 0.53 wt.%) and arsenic 0-0.47 wt.%, is common in heazlewoodite. Cu contents range from 0-0.59 wt.%. The average composition of heazlewoodite grains is given in table 3.6. Godlevskite was found as 10-15μ wide parallel lamellae replacing heazlewoodite. It contains traces of Fe (0.1 wt.%) and has a formula of $[(Ni_{7.16}Fe_{0.01})_{7.17}(As_{0.01}S_6)_{6.01}]$.

3.4.2.2 Ni-Fe alloy and native metals

Both analyses of isotropic and 'anisotropic' alloys, when plotted on a triangular Ni-Fe-S diagram, are close to the Ni_3Fe stoichiometry of awaruite (Fig. 3.35). The average composition of the isotropic Ni-Fe alloys is shown in table 3.7. and the average composition of 'anisotropic' Ni-Fe alloys is given in table 3.8.

Element	*Fe*	*Ni*	*Co*	*S*	*Cu*	*As*	*Sb*	*Ag*	*Pd*	*Pt*	*Total*
Average	25.00	63.67	0.14	1.53	0.96	0.01	0.00	0.01	0.03	0.01	91.37
Standard deviation (1σ)	1.99	6.26	0.17	2.65	1.06	0.04	0.00	0.01	0.02	0.04	6.04

Table 3.7. Average of all microprobe analyses (in wt.%) of isotropic Ni-Fe alloys from the Shetland ophiolite including standard deviations.

The low totals are due to their often intimate intergrowth with altered silicate. The only known anisotropic Ni-Fe alloy is tetrataenite which has the formula NiFe. The observed anisotropism in the 'feathery' Ni-Fe alloy is likely due to the strong internal reflections exhibited by the intergrown serpentine.

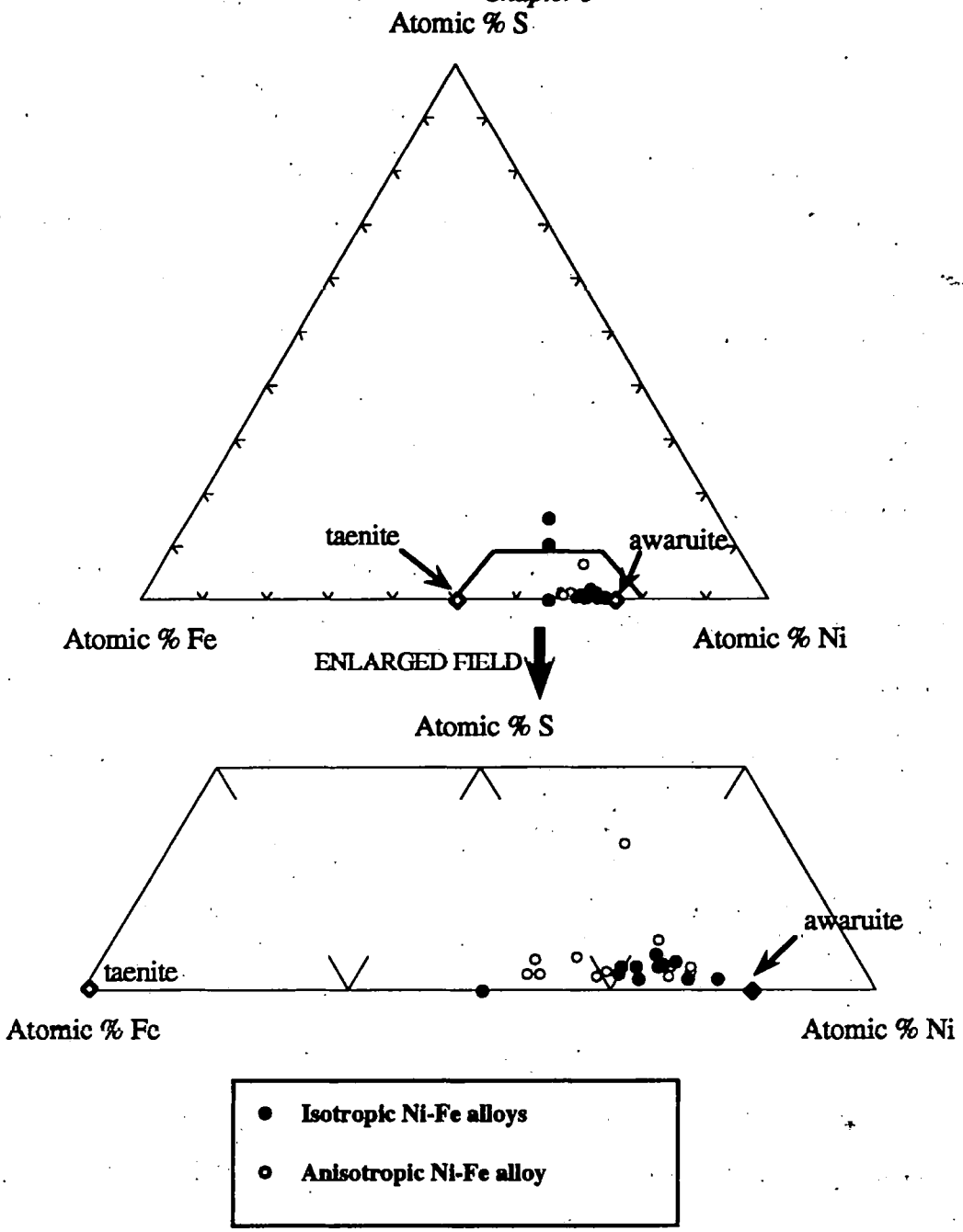

Fig. 3.35. Ternary plot of microprobe analyses of isotropic and anisotropic Ni, Fe alloys from the Shetland ophiolite.

Element	Fe	Ni	Co	S	Cu	As	Sb	Ag	Pd	Pt	Total
Average	24.89	62.27	0.07	0.75	0.35	0.06	0.00	0.01	0.02	0.01	88.44
Standard deviation (1σ)	2.57	4.61	0.05	0.79	0.11	0.07	0.00	0.01	0.02	0.03	5.62

Table 3.8. Average of all microprobe analyses (in wt.%) of 'anisotropic' Ni-Fe alloys from the Shetland ophiolite including standard deviations.

Appreciable sulphur (up to 3 wt.%) occurs in this phase suggesting that awaruite may have been formed by desulphidation of precursor Fe-Ni sulphide, which is also supported by textural evidence. Traces of copper (0.2-2.61 wt.%) are omnipresent in awaruite although the higher values may incorporate a partial analysis of native copper. Cobalt, typically 0.1 wt.% also occurs in awaruite. Some Fe-Ni alloy rims to sulphide are also zoned to higher Cu values. The average composition of native Cu grains is given in table 3.9. Native Cu contains 0-2.8 wt.% Fe and traces of Ni (0-0.53 wt.%).

Element	Fe	Ni	Co	S	Cu	As	Sb	Ag	Pd	Pt	Total
Average	0.80	0.31	0.01	0.05	100.2	0.04	0.00	0.01	0.02	0.00	101.40
Standard deviation (1σ)	0.44	0.50	0.02	0.05	1.28	0.05	0.00	0.01	0.02	0.00	0.86

Table 3.9. Average of all microprobe analyses (in wt.%) of native Cu from the Shetland ophiolite including standard deviations.

3.4.2.3 Nickel arsenides and sulpharsenides

The nickel arsenides orcelite, maucherite, niccolite and the sulpharsenide cobaltite have been analysed. Their mineral chemistry is shown on a ternary Ni-As-Co diagram in Fig. 3.36.

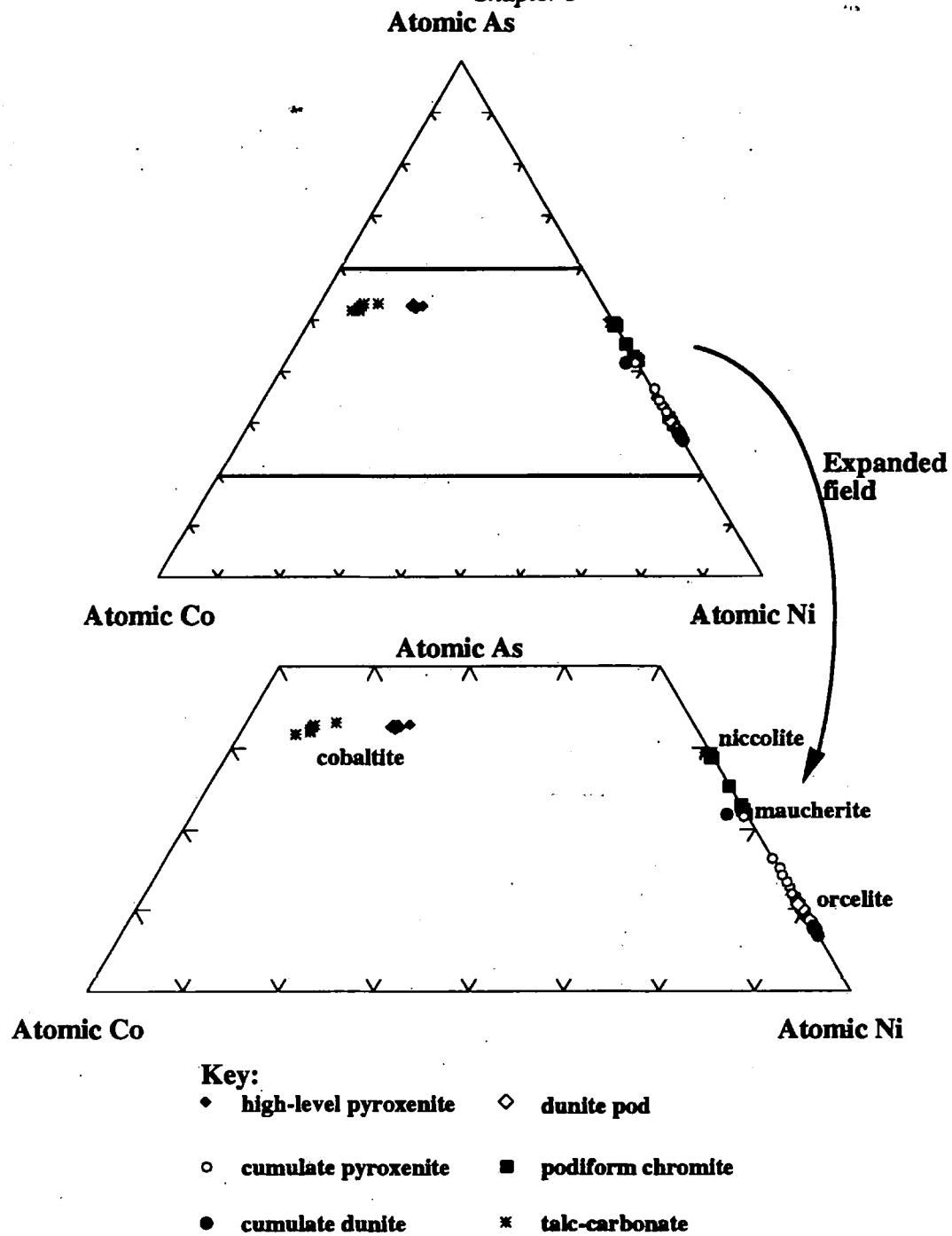

Fig. 3.36. Ternary plot showing composition of analysed Ni-arsenides and sulpharsenides.

Orcelite

Orcelite grains analysed in this study show a wide range of composition, from $[(Ni_{4.30}Cu_{0.02})_{4.32}(As_2Sb_{0.08}S_{0.20})_{2.28}]$ to $[(Ni_{5.44}Fe_{0.18}Cu_{0.02})_{5.66}(As_2Sb_{0.04}S_{0.18})_{2.22}]$ with traces of $Fe_{(0.06-2.19)}$, $S_{(0.08-1.49)}$, $Cu_{(0.48-2.40)}$ and $Sb_{(0.31-2.18)}$. The average composition of orcelite grains is given in table 3.10.

Element	*Fe*	*Ni*	*Co*	*S*	*Cu*	*As*	*Sb*	*Ag*	*Pd*	*Pt*	*Total*
Average	0.61	62.68	0.01	0.39	0.34	34.92	1.06	0.01	0.04	0.01	100.05
Standard deviation (1σ)	0.73	2.94	0.02	0.38	0.28	3.08	0.57	0.01	0.03	0.03	0.94

Table 3.10. Average of all microprobe analyses (in wt.%) of orcelites from the Shetland ophiolite including standard deviations.

Orcelite is known to show significant departures from the ideal formula of $[Ni_{5-x}As_2]$ (Lorand and Pinet, 1984). They describe orcelites from different serpentinized localities associated with a pentlandite-heazlewoodite-awaruite-native Cu-magnetite±maucherite opaque mineral assemblage which range from $[M_{4.20}As_2]$ to $[M_{5.50}As_2]$ (where M=Ni and small amounts of Fe, Co and Cu). This variation is significantly smaller than that observed in the present study. Orcelites from mineralized dunite at Cliff are more As-rich and Ni-poor $[(Ni,Fe,S,Cu)_{4.34}(SbAsS)_{2.28}]$ to $[(Ni,Fe,S,Cu)_{5.04}(SbAsS)_{2.04}]$ compared to orcelites from mineralized cumulate dunite $[(Ni,Fe,S,Cu)_{5.26}(SbAsS)_{2.06}]$ to $[(Ni,Fe,S,Cu)_{5.66}(SbAsS)_{2.20}]$ (Fig. 3.36). Gunn *et al.* (1985) report orcelites from the Cliff locality Unst with a range of mineral formulae from $[Ni_{4.00}As_2]$ to $[Ni_{5.00}As_2]$ with minor amounts of Fe, S and Sb, these formulae are in agreement with those calculated from data obtained during the present study. Arsenide analyses from a sample of cumulate pyroxenite yield compositions intermediate between orcelite $[Ni_{5-x}As_2]$ and maucherite $[Ni_{11}As_8]$ (Fig. 3.36).

Maucherite

Three samples one from each of the lithologies cumulate pyroxenite, sheared cumulate dunite and podiform chromite have calculated mineral formulae of $[(Ni_{10.96}Fe_{0.24}Co_{0.08})_{11.28}$

$(As_8Sb_{0.08}S_{0.16})_{8.24}$] to [$(Ni_{11.12}$ $Fe_{0.24}Co_{0.08}Cu_{0.08})_{11.52}$ $(As_8Sb_{0.08}S_{0.16})_{8.24}$], which approaches the formula of maucherite [$Ni_{11}As_8$]. These analyses contain the following ranges of trace element contents (wt.%); Fe (0.27-1.28), S (0.18-0.74), Cu (0.08-2.40) Sb (0.21-0.59) Co (0-1.86). The average composition of maucherite grains is given in table 3.11.

Element	*Fe*	*Ni*	*Co*	*S*	*Cu*	*As*	*Sb*	*Ag*	*Pd*	*Pt*	*Total*
Average	0.79	49.85	0.38	0.48	0.94	47.00	0.21	0.01	0.01	0.01	99.67
Standard deviation (1σ)	0.41	0.89	0.68	0.21	0.99	0.76	0.30	0.02	0.02	0.02	1.41

Table 3.11. Average of all microprobe analyses (in wt.%) of maucherites from the Shetland ophiolite including standard deviations.

Niccolite

Niccolite compositions vary from [$(Ni_{1.02}Cu_{0.01})_{1.03}$ $(As\ S_{0.04})_{1.04}$] to [$(Ni_{1.01}Fe_{0.06}Cu_{0.01})_{1.08}$ $(As\ S_{0.08})_{1.08}$] with the following ranges of trace element contents; Fe (0-2.32), S (0.54-1.86), Cu (0.51-0.78). The average composition of niccolite grains is given in table 3.12.

Element	*Fe*	*Ni*	*Co*	*S*	*Cu*	*As*	*Sb*	*Ag*	*Pd*	*Pt*	*Total*
Average	0.51	44.10	0.06	0.91	0.42	54.83	0.00	0.00	0.00	0.00	100.83
Standard deviation (1σ)	0.90	0.75	0.16	0.48	0.35	0.68	0.00	0.00	0.00	0.00	0.72

Table 3.12. Average of all microprobe analyses (in wt.%) of niccolites from the Shetland ophiolite including standard deviations.

Cobaltite

Cobaltite grains analysed in this study range in composition from [$(Ni_{0.14}Fe_{0.07}Co_{0.76})_{0.97}As\ S_{0.97}$] for solitary, euhedral grains in altered high-level pyroxenite to [$(Ni_{0.33}Fe_{0.21}Co_{0.56})_{1.10}As\ S_{1.09}$] for cobaltite intergrown with pentlandite from talc-carbonate rocks from close to the basal thrust. The average composition of cobaltite grains is given in table 3.13.

Element	Fe	Ni	Co	S	Cu	As	Sb	Ag	Pd	Pt	Total
Average	3.47	8.18	24.30	19.43	0.00	45.90	0.00	0.01	0.06	0.02	101.33
Standard deviation (1σ)	1.26	3.00	3.76	0.42	0.00	0.94	0.00	0.01	0.08	0.05	0.91

Table 3.13. Average of all microprobe analyses (in wt.%) of cobaltites from the Shetland ophiolite including standard deviations.

No compositional zoning was detected in the cobaltite grains although a cobaltite grain from the basal thrust has a Rh and Pt-rich core (R. Ixer, *pers. comm.*).

Discussion.

The occurence of nickel arsenides in ultramafic rocks is well documented. Orcelite, maucherite, niccolite and cobaltite have been described from numerous different serpentinite bodies. For example orcelite has been found as inclusions in pentlandite in serpentine of New Caledonia (Ramdohr, 1969), and in partially serpentinized peridotite where it is intergrown with pentlandite (Ronda, Spain) or heazlewoodite (Pindos, Greece) (Lorand and Pinet, 1984). Lorand and Pinet (1984), consider that orcelite crystallized between 400-450°C during serpentinization where it replaces a primary niccolite-maucherite assemblage. Chromite-Ni arsenide ores with pyroxenes and cordierite gangue occur in the Ronda and Beni Bousera lherzolite massifs (Oen, 1973; Gervilla and Leblanc, 1990). A nickel arsenide assemblage of niccolite, loellingite and pararammelsbergite as intergranular, intrafractural and as inclusions within chromite, orthopyroxene and cordierite were postulated to be of magmatic origin, having crystallized from an immiscible arsenide-sulphide liquid. The arsenic could have been derived from disseminated orcelite, niccolite and maucherite grains in the mantle magmatic mineral assemblages of the Beni-Bousera peridotite (Lorand, 1983). The arsenide minerals maucherite, niccolite, loellingite [$FeAs_2$], oregonite [Ni_2FeAs_2], cobaltite, and cobaltite which comprise part of a Cu-Ni-Fe sulphide mineralization hosted in Shattered Serpentinite from the Troodos ophiolite complex (Panayiotou , 1986), are thought to have been formed during serpentinization, although niccolite was considered to be primary. The arsenide assemblage from Unst of orcelite-maucherite-niccolite-cobaltite is therefore typical of that found in serpentinized peridotites. Every orcelite grain analysed in this study contains traces of Sb and this mineral is commonly

intergrown with Ni-Cu antimonide minerals (section 3.5.3.1), suggesting a close paragenetic relationship between orcelite and the Ni-Cu antimonides.

3.4.2.4 Fe-Cu and Cu-Fe sulphides

Pyrrhotite from cumulate dunite approximates troilite pyrrhotite in composition (Fig. 3.32). Pyrrhotite from cumulate and high-level pyroxenite ranges from hexagonal to monoclinic pyrrhotite, (average S content 53.19 ± 0.35 at.%). Pyrrhotite from talc-carbonate rock is close to hexagonal pyrrhotite, (average S content of 52.20 ± 0.62 at.%) (Fig. 3.32). Large spongy and euhedral pyrites from pyroxenite bodies hosted in gabbro contain 0-0.95 wt.% arsenic, 0-0.5 wt.% nickel and 0.05-1.06 wt.% cobalt. Pyrite intergrown with pyrrhotite and chalcopyrite from cumulate pyroxenites contains 0-0.8 wt.% Ni and 0-0.5 wt.% As. Chalcopyrite has an average Cu:Fe ratio of 0.998 ± 0.06. No trace metals were detected in chalcopyrite. Bornite intergrown with pentlandite and chalcopyrite shows 1.17 wt.% nickel, although this may arise from excitation of pentlandite. Chalcocite contains trace iron, 0.46 wt.%.

3.4.2.5 Spinel and magnetite

Chromite

The major element chemistry of massive chromite from the Shetland ophiolite has been well established (Gass *et al.*, 1982) and varies between Cr_2O_3 38-60 wt.%, Al_2O_3 8-30 wt.%, Fe_2O_3 0.5-5 wt.%, FeO 8-16 wt.%, MgO 8-16 wt.%, with disseminated chrome-spinel containing higher $Mg/(Mg+Fe^{2+})$ and lower $Fe^{3+}/(Cr+Al+Fe^{3+})$, TiO_2 and NiO. Unst chromite analyses show the wide variations in $Cr/(Cr+Al)$ and $Mg/(Mg+Fe^{2+})$ and low Ti or Fe^{3+} contents typical of podiform chromitites (Prichard and Neary, 1981). Lord (1991), ascribed the higher observed Ti content of chromite from the crustal sequence compared to the mantle sequence to magmatic processes. These differences were postulated to be brought about by, for example, changes in oxygen fugacity as batches of magma entered the main magma chamber and mixed with resident melt.

	MR45 pyrox.	H.L. core	MR45 pyrox.	H.L. rim	JM21 pyrox.	H.L. core	JM21 pyrox.	H.L. rim	*JM21 pyrox.	H.L.
Mg		5.97		0.49		7.60		0.87		0.25
Al		26.43		0.35		27.49		5.32		0.20
Ti		0.31		1.45		n.s.		n.s.		n.s.
Si		0.11		0.36		0.08		0.10		0.16
S		0.00		0.00		0.04		0.04		0.05
Cr		29.99		21.91		30.08		25.17		25.27
Mn		0.97		1.45		0.80		1.70		1.48
Fe		38.15		72.95		35.1		66.06		71.97
Co		n.s.		n.s.		0.04		0.08		0.06
Ni		0.03		0.04		0.06		0.04		0.07
Cu		n.s.		n.s.		0.01		0.00		0.06
As		n.s.		n.s.		0.06		0.00		0.15
Zn		0.56		0.23		n.s.		n.s.		n.s.
Total		102.52		99.23		101.36		99.38		99.72

Table 3.14. Core-rim analyses of disseminated chrome-spinels from two samples of altered high-level pyroxenite.

The mineral chemistry of fresh disseminated chrome-spinel was determined over a 140cm thick section of mineralized NB-2 drillcore from the basal cumulate dunite unit, north of Baltasound (Prichard and Lord, 1990). Microprobe analyses of these chrome-spinels are given in appendix B.2. It was anticipated that systematic changes in the chrome-spinel chemistry would be observed above this interval as the layer evolved by fractional crystallization. This is discussed in conjunction with the sulphur isotope geochemistry of this core material in Chapter 6.

Core-rim analyses of disseminated spinel grains from two bodies of high-level wehrlite and pyroxenite show that chrome-spinels alter to 'ferrichromit' (table 3.14). Al, Cr and Zn show depletions in the rims compared to the cores of the spinel grains whereas Ti and Fe show the opposite trend. Further alteration of chrome-spinel is represented by analysis *JM21 (table 3.14) from a grain which displays the morphology of surrounding disseminated altered spinels, but consists of essentially Cr and Fe with only trace Al (0.2 wt.%) and is a true 'ferritchromit'. 'Ferritchromit' intergrown with magnetite-pentlandite-awaruite-native Cu from cumulate dunite contains trace Ni (0.31 wt.%) and Co.

Magnetite

Magnetite intergrown with heazlewoodite-pentlandite-millerite-godlevskite-orcelite-breithauptite aggregates from a dunite pod, Cliff, contains 1.29 to 4.89 wt.% nickel. Traces of Co (0.11-0.17 wt %) also occur in magnetite in this paragenesis. Magnetite intergrown with heazlewoodite-pentlandite-awaruite from the cumulate dunite unit contains 0.3-0.51wt.% Ni and similar concentrations (0.46-0.47 wt.%) occur in associated vein magnetite intergrown with serpentine, in magnetite developed along cracks in pentlandite (0.44-0.46 wt.% Ni, 0.15-0.17 wt.% Co) and in magnetite rims to 'ferritchromit' (0.57 wt.% Ni, 0.12 wt.% Co), in the assemblage pentlandite-awaruite-native Cu. Vein magnetite along altered cleavages of clinopyroxene in high-level pyroxenite contains 0.09-2.66 wt.% Cr and low <0.08 wt.% Ni and Co. The average composition of magnetite grains is given in table 3.15.

Element	*Fe*	*Ni*	*Co*	*S*	*Cr*	*Mn*	*Mg*	*Al*	*Ti*	*Si*	*Total*
Average	95.49	1.51	0.10	0.10	0.31	0.06	1.24	0.00	0.01	0.49	99.31
Standard deviation (1σ)	1.88	1.52	0.07	0.32	0.62	0.03	0.76	0.01	0.02	0.80	0.91

Table 3.15. Average of all microprobe analyses (in wt.%) of magnetites from the Shetland ophiolite including standard deviations.

3.5 Nickel antimonides

3.5.1 Introduction

The Ni antimonide breithauptite (NiSb), was first described from the Shetland ophiolite by Prichard and Tarkian (1988), in a mineralogical description of PGM from two PGE and chromite-rich dunite lenses in harzburgite. Ixer and Prichard (1989) presented a paragenesis for Pt and Pd antimonides and breithauptite from the Cliff locality. Associated Pd antimonides, mertieite or stibiopalladinite, and genkinite, $(Pt, Pd)_4Sb_3$(+Ni, Rh), Rh-Sb-S, Ir-Sb-S and Rh-Ni-Sb phases were also noted as inclusions in As-rich phases such as irarsite and sperrylite. Ni antimonides and Pd antimonides also occur in the cumulate dunite unit where they are associated with disseminated Ni-Fe sulphides and chrome-spinel which form discontinuous layers, often ~1m thick (Prichard and Lord, 1990).

During the examination of polished thin sections prepared from the NB core material from the cumulate dunite unit, several different Ni antimonides were observed in association with different sulphide, alloy, opaque oxide and silicate phases. These antimonides typically constitute <1p.t.s. An optical and microprobe study of antimonides from the crustal dunite sequence was therefore undertaken in order to establish a paragenesis which could then be compared to the Cliff antimonide paragenesis. Quantitative electron microprobe analysis of antimonides from both of these localities was undertaken to establish the mineral chemistry of discreet antimonide phases. The composition of nickel antimonides was established by a combination of qualitative SEM and quantitative electron microprobe analysis. Mineral formulae were calculated as $[M_x S_y]$ where M=Ni,Fe,Cu,Pt,Pd,Co,Ag and S=S,Sb,As.

3.5.2 Mineralogy of nickel antimonides

3.5.2.1 Reddish-pink highly anisotropic breithauptite

There are broadly two different associations of breithauptite:

(a) As highly anisotropic round to sub-rounded inclusions in Ni-Fe sulphide aggregates

These occur in the cumulate dunite unit and in a dunite pod in harzburgite, Cliff.

(i) Cumulate dunite unit

Breithauptite (NiSb) occurs as 1-10μ, and rarely ~40μ diameter, spherical inclusions either enclosed within heazlewoodite (Fig. 3.18) or pentlandite, or at the boundary of heazlewoodite and Ni-Fe alloy (Fig. 3.37). Polarization colours vary from grey-white to deep red. Breithauptite in heazlewoodite and pentlandite from the cumulate dunite unit contains no detectable Cu or Pd but a small amount of Fe and S were detected on the SEM, although excitation of the host pentlandite matrix could well be responsible for the observed peaks.

(ii) Dunite pod in harzburgite, Cliff

Breithauptite is intergrown with heazlewoodite and pentlandite (Fig. 3.38) or enclosed within pentlandite. An analysis of the breithauptite grain shown in (Fig. 3.38) from the Cliff locality is given in table 3.16.

Fe	Ni	Co	S	Cu	As	Sb	Ag	Pd	Pt	Total
0.09	31.22	0.02	0.07	0.10	0.31	68.01	0.01	0.47	0.00	100.3

Formula; $[(Ni_{0.95}Pd_{0.01})_{0.96}(Sb\ As_{0.01})_{1.01}]$

Table 3.16 Microprobe analysis (in wt.%) of breithauptite.

Traces of Pd were detected. However, these may arise from the thin Cu-Pd enriched lamellae observed in this grain.

(b) As intergrowths with Cu-rich antimonide

Breithauptite, intergrown with lavender-coloured isotropic antimonide, often forming a lamellar structure, has been found as anhedral, or rounded, 5-75μ grains in both core material from the cumulate dunite unit and also in a sulphide-bearing dunite pod in harzburgite from the Cliff locality. These composite antimonides are enclosed within heazlewoodite, heazlewoodite/pentlandite, awaruite/heazlewoodite, awaruite, or occur partially intergrown with altered silicate.

(i) Cumulate dunite unit

Five composite antimonide grains were analysed from two polished thin sections by a combination of qualitative element mapping and spot analysis on the SEM and quantitative WD probe analysis. Photomicrographs of these grains are shown in Fig. 3.39-3.43 which show that they are often sub-rounded grains and in Fig. 3.41, are composed of an aggregate of sub-rounded grains of of anisotropic, pink-red breithauptite with lavender-coloured isotropic lamellae. Fig. 3.39 and Fig. 3.40 show two composite antimonides enclosed within a grain of

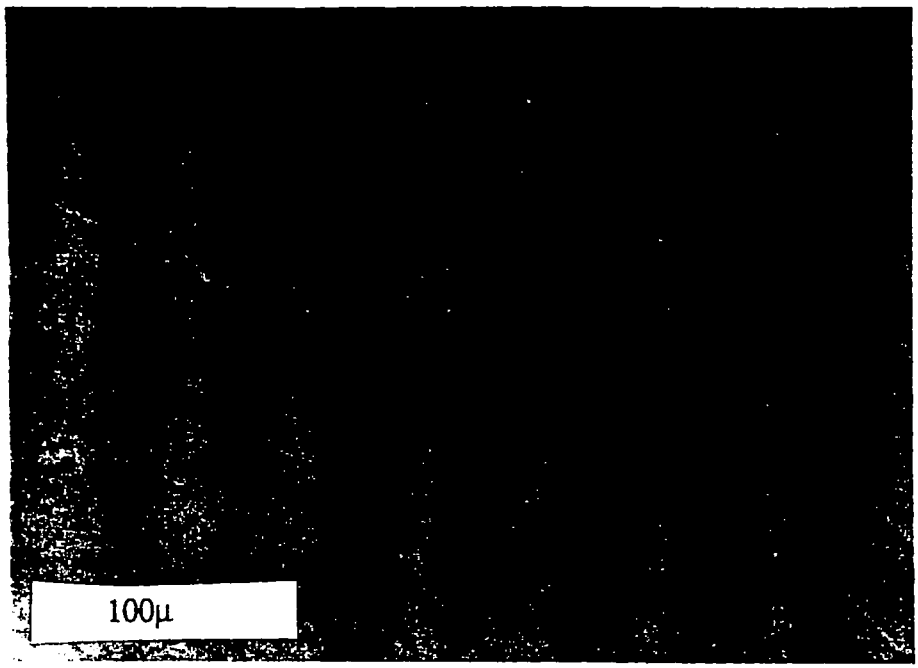

Fig. 3.37. Breithauptite (pink, centre), intergrown with heazlewoodite (bottom), altering to awaruite (porous, yellow grey, top). Cumulate dunite.

Fig. 3.38. Breithauptite (pink, centre containing fine lamellae of lavender antimonide), intergrown with pentlandite (left) and heazlewoodite.(right). Dunite pod, Cliff.

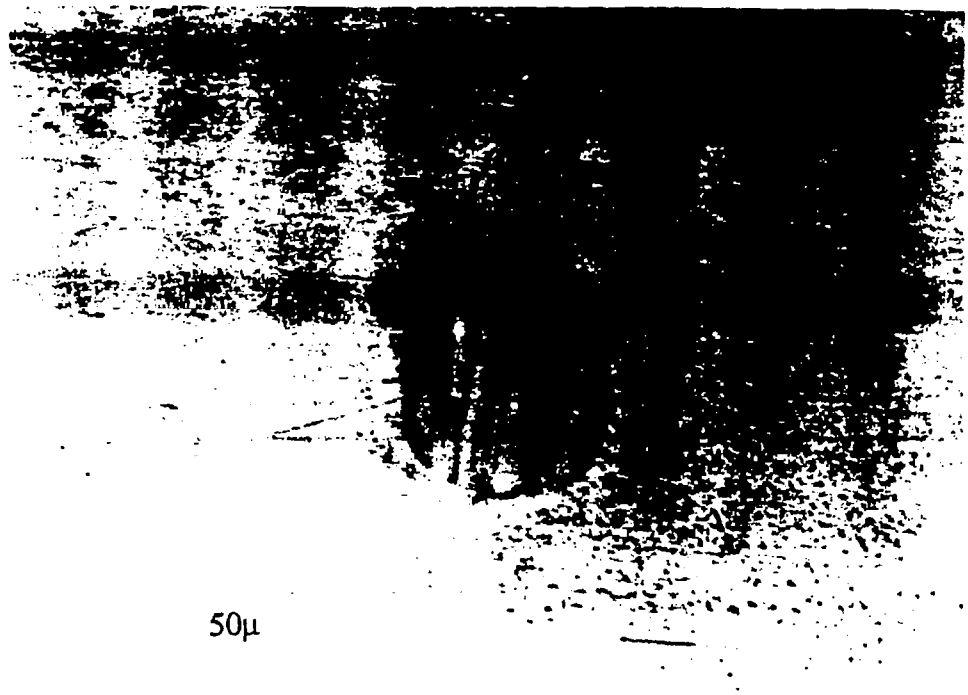

Fig. 3.39. Spherical composite Ni-Cu antimonide grain (centre) composed of anisotropic breithauptite lamellae (pink) and isotropic Cu-rich Ni-antimonide (lavender). This grain is intergrown with heazlewoodite (left), porous heazlewoodite (top and right) and pentlandite (cream-brown, on margin of antimonide grain). Cumulate dunite.

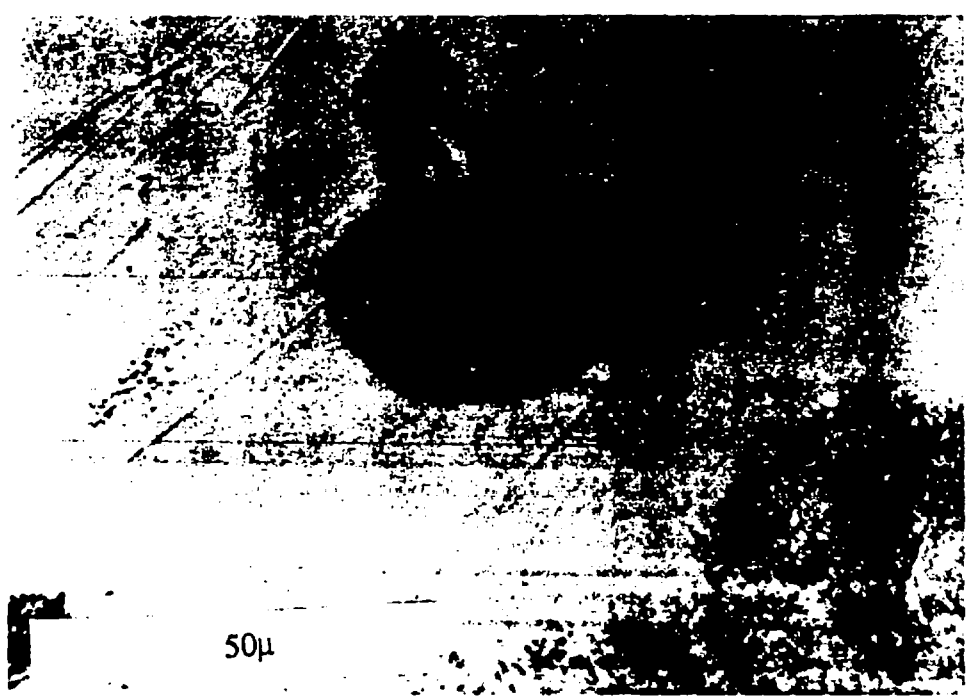

Fig. 3.40. Similar composite antimonide grain to Fig. 3.39, enclosed in heazlewoodite (cream-yellow) altering to awaruite (bottom) and intergrown with pentlandite (cream-brown, centre top and centre right) which has inclusions of awaruite (white, centre top). Cumulate dunite.

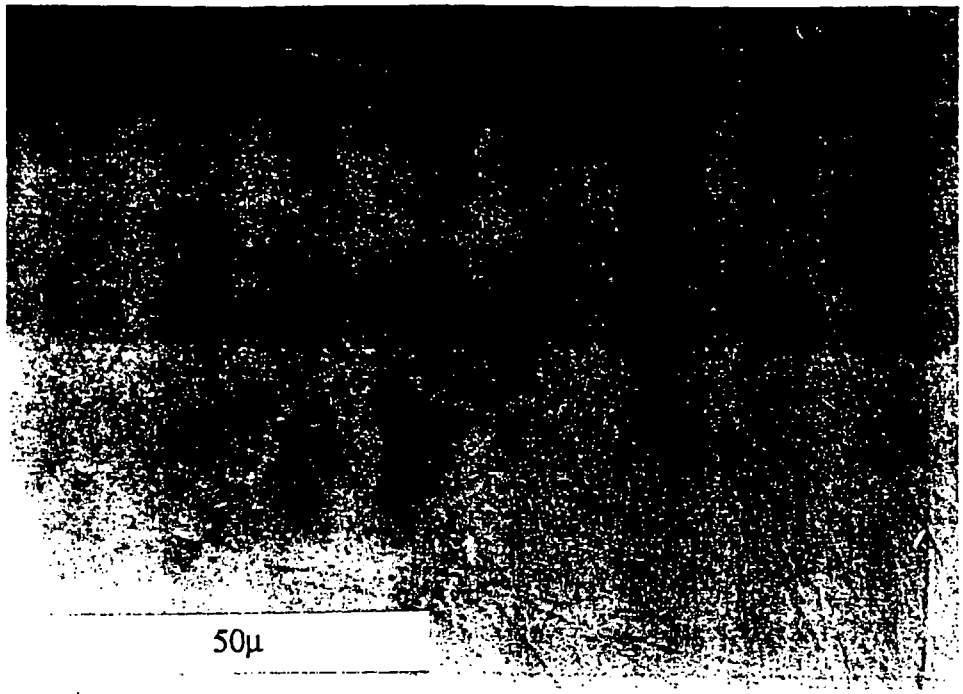

Fig. 3.41. Spherical composite Ni-Cu antimonide grain (centre) of anisotropic breithauptite (pink) and isotropic Cu-rich Ni-antimonide (lavender), intergrown with porous awaruite (centre and top) and heazlewoodite (bottom). Cumulate dunite.

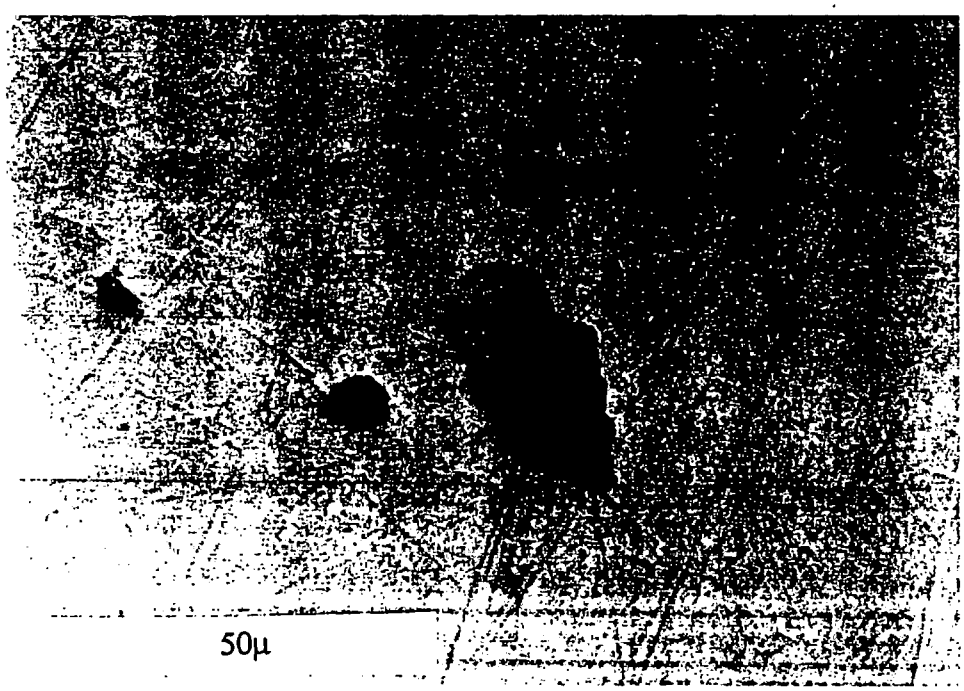

Fig. 3.42. Two-phase Ni-Cu antimonide (centre), intergrown with native copper (orange, centre), enclosed in heazlewoodite. Cumulate dunite.

Fig. 3.43. Elongate aggregate of two-phase breithauptite/Ni-Cu antimonide grains (centre) intergrown with heazlewoodite (bottom), awaruite (centre left and centre right) and pentlandite (top left). Cumulate dunite.

heazlewoodite, which is altering to awaruite. Both of these antimonide grains have discontinuous rims of pentlandite and one grain (Fig. 3.40), has fine inclusions of awaruite within the pentlandite rim. The antimonide grains shown in Fig. 3.41 and Fig. 3.43 are intergrown with awaruite and heazlewoodite whereas the grain in Fig. 3.42 is intergrown with heazlewoodite. Qualitative SEM element mapping of the area in the immediate vicinity of, and including the antimonide grain shown in Fig. 3.40 in terms of Mg, Al, Ni, Cu, Fe, Sb and S, shows the distribution of these elements between different mineral phases of the mapped area (Fig. 3.44). The heazlewoodite grain, delineated by the maps for Ni and S, is altering to awaruite [Ni_3Fe], which is picked out by the map for Fe, and occurs adjacent to a grain of magnetite, which is also clearly shown by the map for Fe. The map for Sb shows the antimonide as an inclusion within heazlewoodite. Furthermore the map for Cu suggests that this antimonide is Cu-bearing. The pentlandite which partially surrounds the antimonide inclusion is clearly picked out by the map for Fe. Fig. 3.45 shows an SEM map, in terms of Cu, S, Sb and Ni, for the composite antimonide grain shown in Fig. 3.39. This map clearly shows that the different coloured lamellae of this grain are compositionally distinct. This is best illustrated by the map for Cu which shows that the lavender-coloured isotropic lamellae are Cu-rich compared to the lighter, anisotropic (breithauptite) lamellae. The fine intergrowths of the composite antimonides meant that quantitative electron microprobe analysis of individual lamellae was not possible since the resolution of the M9 microprobe is ~5μ whereas the lamellae are typically 1-3u wide. However qualitative SEM analysis of individual lamellae of the antimonide grain shown in Fig. 3.39 was possible and the results are shown in table 3.17. The calculated formula of the peach-pink lamellae (table 3.17, Br.1), approaches the 1:1 Ni:Sb ratio of breithauptite.

	Fe	*Ni*	*Co*	*S*	*Cu*	*As*	*Sb*	*Ag*	*Pd*	*Pt*	*Total*
Br. 1	0.07	35.03	0.00	0.00	1.63	n.s.	62.98	n.s.	0.29	0.00	100
Formula; $[(Ni_{1.15}Cu_{0.05}Pd_{0.01})1.21Sb]$											
la. 1	0.09	39.96	0.00	0.00	9.08	n.s.	50.69	n.s.	0.18	0.00	100
Formula; $[(Ni_{1.63}Cu_{0.34})1.97Sb]$											

Table 3.17. Qualitative SEM analysis (in wt.%) of the individual lamellae of the composite antimonide shown in Fig. 3.39.

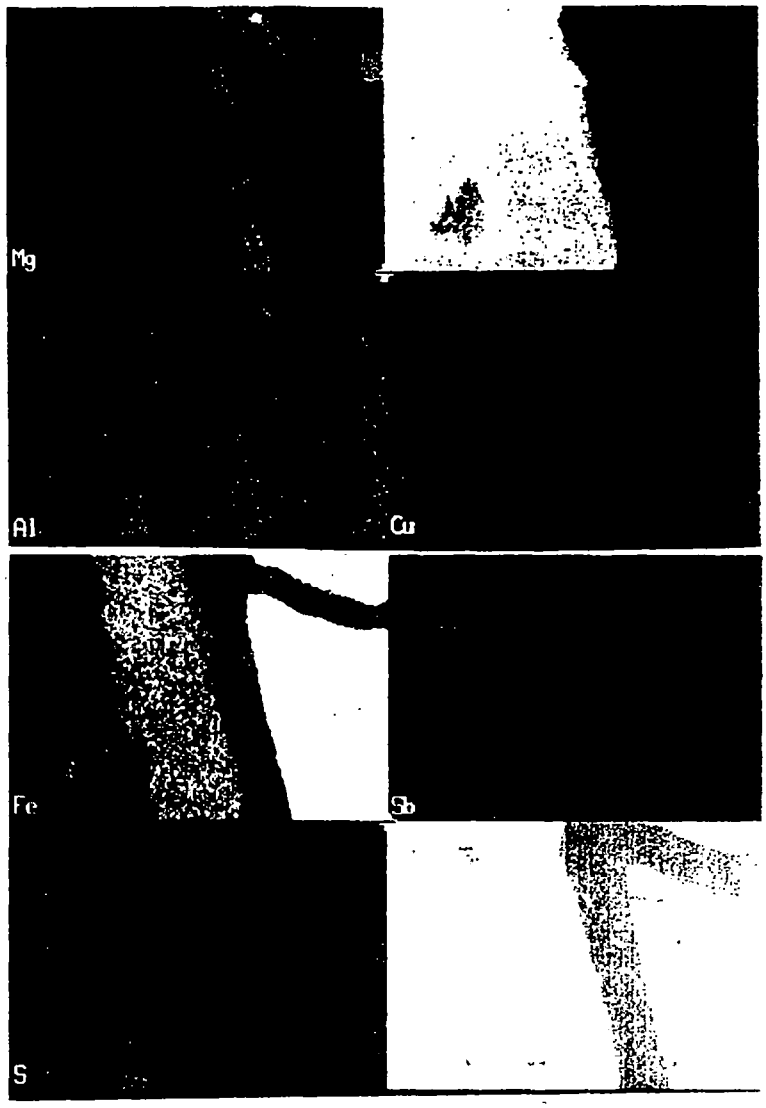

Fig. 3.44. SEM X-ray map showing the distribution of Mg, Al, Ni, Cu, Fe, S, and Sb in the immediate vicinity of a Ni, Cu antimonide grain (see text for discussion)

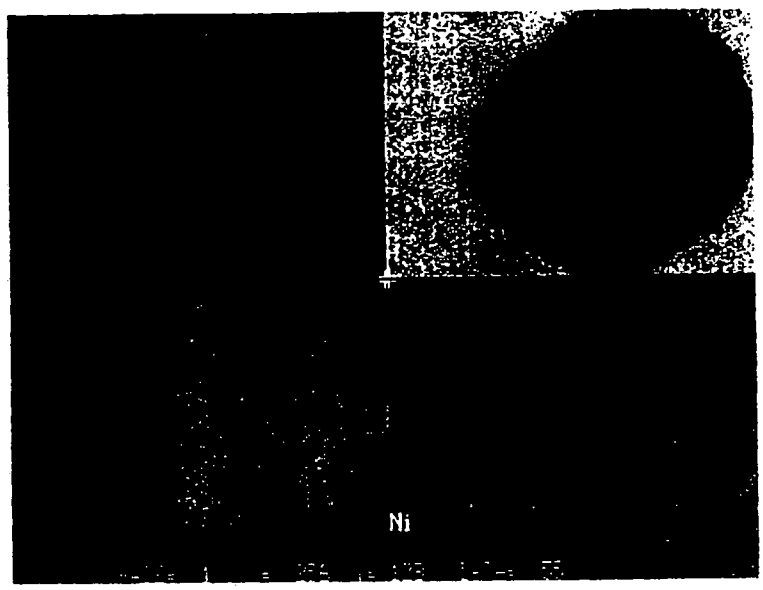

Fig. 3.45. SEM X-ray map showing the distribution of Cu, Sb, S and Ni in the composite antimonide grain shown in Fig. 3.39. See text for discussion.

The composition of the lavender lamellae (table 3.17, la. 1) is Ni and Cu-rich (9.08 wt.% Cu) compared to the intergrown breithauptite. The 1.63 wt.% Cu measured in the breithauptite may arise from excitation of the Cu-rich lamellae. Traces of Pd occur in both the breithauptite (0.29 wt.%) and the Ni-Cu antimonide lamellae (0.18 wt.%). Qualitative SEM analysis of the pink and lavender coloured intergrowths shown in Fig. 3.41 are given in table 3.18.

	Fe	*Ni*	*Co*	*S*	*Cu*	*As*	*Sb*	*Ag*	*Pd*	*Pt*	*Total*
Br. 2	1.73	32.41	0.00	0.00	0.86	n.s.	64.79	n.s.	0.20	0.00	99.99
Formula;	$[(Ni_{1.06}Fe_{0.06}Cu_{0.01})1.13Sb]$										
la. 2	3.19	48.15	0.00	0.06	6.32	n.s.	42.27	n.s.	0.00	0.00	99.99
Formula;	$[(Ni_{2.36}Fe_{0.17}Cu_{0.29})2.82Sb]$										

Table 3.18. Qualitative SEM analysis (in wt.%) of the individual lamellae of the composite antimonide shown in Fig. 3.41.

Analysis of the anisotropic peach-pink portion of the antimonide grain (table 3.18, Br.2) approaches the 1:1 Ni:Sb ratio of breithauptite, whereas the analysis of the lavender portion of the antimonide grain (table 3.18, la. 2) again reveals substantial (6.32 wt.%) Cu and has a mineral formula of $[(Ni, Cu)_{2.82}Sb]$. Traces of Pd occur in the breithauptite analysis (0.20 wt.%). An elongate aggregate, 15μ long, composed of two-phase grains of identical optical properties to that described above is developed along the boundary of heazlewoodite and awaruite (Fig.3.42). Qualitative SEM analyses reveal that the dark, lavender-coloured lamellae contain more Cu and also trace Pd compared to the breithauptite lamellae. Another grain with similar optical properties occurs adjacent to a native Cu inclusion within heazlewoodite which is altering to awaruite (Fig. 3.42). Bulk quantitative analysis of the composite breithauptite/Ni-Cu antimonide grains shown in Fig. 3.39 and Fig. 3.40 are given in table 3.19.

	Fe	Ni	Co	S	Cu	As	Sb	Ag	Pd	Pt	Total
Bk 1	0.18	42.01	0.01	2.56	4.12	0.21	50.13	0.03	0.26	0.00	99.51
Formula;	$[(Ni_{1.74}Fe_{0.01}Cu_{0.16}Pd_{0.01})2.14\ (Sb\ As_{0.01})1.01]$										
Bk 2	0.66	47.61	0.05	0.10	6.16	0.00	46.56	0.03	0.23	0.00	101.4
Formula;	$[(Ni_{2.12}Fe_{0.03}Cu_{0.25}Pd_{0.01})2.41Sb]$										

Table 3.19. Bulk microprobe analysis (in wt.%) of the composite antimonides shown in Figs. 3.39 and 3.40.

Traces of Pd occurs in both grains (0.23-0.26 wt.%) which are similar concentrations to those indicated by the qualitative SEM analysis (table 3.17). In both composite antimonide grains, breithauptite lamellae are subordinate to the Ni-Cu antimonide lamellae which make up 65-80 percent of the grains from visual inspection. The grain with the largest percentage of dark, lavender lamellae (Fig. 3.40), contains the most Cu and Ni, but Pd contents remain uniformly low (0.23-0.25 wt.%) between the two grains.

Soft-pink coloured, anhedral, anisotropic breithauptite occurs intergrown with grey-lavender antimonide at the margin of an orcelite crystal. The grey-lavender antimonide is in contact with altered silicate whereas the breithauptite is partially intergrown with orcelite. A composite analysis of breithauptite/grey-lavender antimonide is given in table 3.20, Br 1 along with the analysis of the grey-lavender antimonide (table 3.20, Gl 1).

	Fe	Ni	Co	S	Cu	As	Sb	Ag	Pd	Pt	Total
Br 1	0.94	36.57	0.01	0.12	8.56	0.12	52.87	n.s.	1.56	0.15	100.9
Formula;	$[(Ni_{1.44}Fe_{0.04}Cu_{0.31}Pd_{0.03})1.82Sb]$										
Gl 1	1.16	37.17	0.04	0.15	12.92	0.30	47.42	n.s.	2.03	0.00	101.2
Formula;	$[(Ni_{1.63}Fe_{0.05}Cu_{0.52}Pd_{0.05})2.25(Sb\ As_{0.01})1.01]$										

Table 3.20. Microprobe analysis (in wt.%) of composite breithauptite/grey-lavender antimonide.

The grey-lavender phase (table 3.20, Gl 1) contains higher Cu (12.92 wt.%) compared to the composite analyses of breithauptite/grey-lavender antimonide (table 3.20, Br 1) which contains 8.56 wt.% Cu. The Pd concentration is lower (1.56 wt.% Pd) for the 'breithauptite-rich' analysis (table 3.20, Br 1) than for the Cu-rich, grey-lavender antimonide analysis (table 3.20, Gl 1) (2.03 wt.% Pd).

Two anhedral grains of pink-red anisotropic breithauptite, 20-40μ, with fine, 1-3u, lamellae of highly anisotropic lavender-grey antimonide occur intergrown with magnetite and serpentine at the margin of a heazlewoodite-pentlandite-awaruite-magnetite aggregate. Quantitative electron microprobe analysis of breithauptite and host anisotropic lamellae are given in table 3.21 and table 3.22.

	Fe	*Ni*	*Co*	*S*	*Cu*	*As*	*Sb*	*Ag*	*Pd*	*Pt*	*Total*
Br. 1	1.42	29.69	0.01	0.14	0.47	0.42	65.74	n.s.	1.88	0.57	100.3
Formula;	$[(Ni_{0.94}Fe_{0.05}Cu_{0.01}Pd_{0.03}Pt_{0.01})_{1.04}(Sb\ As_{0.01}S_{0.01})_{1.02}]$										
la. 2	3.70	28.55	0.01	0.01	4.05	0.23	58.30	n.s.	5.67	0.46	101.0
Formula;	$[(Ni_{1.02}Fe_{0.14}Cu_{0.13}Pd_{0.11}Pt_{0.01})_{1.41}(Sb\ As_{0.01})_{1.01}]$										

Table 3.21. Microprobe analysis (in wt.%) of composite breithauptite/grey-anisotropic antimonide.

	Fe	*Ni*	*Co*	*S*	*Cu*	*As*	*Sb*	*Ag*	*Pd*	*Pt*	*Total*
Br. 1	0.89	29.93	0.01	0.14	0.21	0.31	67.73	n.s.	2.40	0.70	102.3
Formula;	$[(Ni_{0.92}Fe_{0.03}Cu_{0.01}Pd_{0.04}Pt_{0.01})_{1.01}(Sb\ As_{0.01}S_{0.01})_{1.02}]$										
la. 2	3.51	7.96	0.02	0.16	13.53	0.00	32.82	n.s.	38.19	0.06	96.25
Formula;	$[(Ni_{0.50}Fe_{0.23}Cu_{0.80}Pd_{1.33})_{2.86}(Sb\ S_{0.02})_{1.02}]$										

Table 3.22. Microprobe analysis (in wt.%) of composite breithauptite/grey-anisotropic antimonide.

The breithauptite analyses (table 3.21, Br. 1) and table 3.22, Br. 1, contain significant amounts of Pd (1.88-2.40 wt.%), Pt (0.57-0.70 wt.%), and As (0.31-0.42 wt.%). The grey anisotropic lamellae (table 3.21, la. 2 and table 3.22, la. 2) are both Cu (4.05-13.53 wt.%) and Fe-rich (3.51-3.70 wt.%) compared to host breithauptite (table 3.21, Br. 1 and table 3.22, Br. 1). The grey anisotropic lamellae are also richer in Pd (5.67-38.19 wt.%), but contain less Pt (0.06-0.46 wt.%) than host breithauptite.

A composite ~10μ grain of pink-red anisotropic breithauptite intergrown with a ~2μ by 4μ soft-yellow phase is hosted within magnetite and serpentine. The yellow phase may be stibiopalladinite (rich yellow-white in reflected light oil immersion). An analysis of the breithauptite is given in table 3.23.

	Fe	Ni	Co	S	Cu	As	Sb	Ag	Pd	Pt	Total
Br. 1	2.70	25.24	0.01	0.14	0.09	0.00	62.60	n.s.	4.61	4.48	99.9
Formula; $[(Ni_{0.84}Fe_{0.09}S_{0.01}Pd_{0.08}Pt_{0.05})_{1.07}(Sb\ S_{0.01})_{1.01}]$											

Table 3.23. Microprobe analysis (in wt.%) of breithauptite intergrown with soft-yellow coloured antimonide.

The breithauptite of this intergrowth (table 3.23) is Fe, Pd and Pt-rich and could reflect a contribution from the yellow phase (which was too small to analyse quantitatively) with which it is intergrown.

(ii) Dunite pod in harzburgite, Cliff

Composite breithauptite/lavender antimonides from the Cliff locality are shown in Fig. 3.46, Fig. 3.47 and Fig. 3.48. All three antimonides are marginal to sulphide/magnetite aggregates situated at the contact between heazlewoodite/pentlandite and altered silicate. Fig. 3.47 and Fig. 3.48 show that these antimonides are also often closely associated with the pink-brown nickel arsenide orcelite. Considering Fig. 3.46, it appears that within the antimonide grain, the lavender lamellae are more prevalent towards the boundary between the altered silicate and heazlewoodite/pentlandite. Analyses of the antimonide grain shown in Fig. 3.46 are given in table 3.24.

	Fe	Ni	Co	S	Cu	As	Sb	Ag	Pd	Pt	Total
Br. 1	0.09	32.02	0.01	0.08	1.00	0.39	66.63	0.03	0.41	0.00	100.7
Formula; $[(Ni_{1.00}Cu_{0.03}Pd_{0.01})_{1.04}(Sb\ As_{0.01})_{1.01}]$											
la. 2	0.11	35.25	0.02	0.07	6.62	0.50	58.44	0.03	0.32	0.00	101.4
Formula; $[(Ni_{1.25}Cu_{0.22}Pd_{0.01})_{1.48}(Sb\ As_{0.01})_{1.01}]$											

Table 3.24. Microprobe analysis (in wt.%) of breithauptite intergrown with lavender-coloured antimonide shown in Fig. 3.46.

Analysis Br. 1 (table 3.24) is of that area of the antimonide grain which contains few lamellae of lavender antimonide, whereas analysis La.2 (table 3.24) is of that area of the grain that comprises more closely spaced lavender lamellae. The analysis Br. 1 reveals traces of Fe, As and Pd and 1 wt.% Cu and has a calculated formulae close to breithauptite (NiSb). Analysis La. 2 shows higher amounts of Cu (6.62 wt.%) Fe and As, and lower Pd.

3.5.2.2 Isotropic, Cu-rich, lavender-mauve to pink-grey nickel antimonide

These lath shaped-anhedral antimonides vary in size from 10-30μ and often contain minor irregular patches of a pink-cream anisotropic phase. Texturally, these antimonides have been found intergrown with heazlewoodite and awaruite (Fig. 3.49), at the interface between awaruite and altered silicate (Fig. 3.50), intergrown with pentlandite, awaruite and orcelite (Fig. 3.51), amongst a symplectite-like intergrowth of native Cu and Ni-Fe sulphide at the margin of a pentlandite/magnetite grain, intergrown with a Hg, Ag amalgam (Prichard and Lord, 1990), and intergrown with orcelite/serpentine partially enclosed in pentlandite.

The four isotropic lavender-mauve to pink-grey antimonides which were probed are chemically quite similar (table 3.25). They are all Cu-rich, 11.31-13.18 wt.% Cu, contain Fe, 1.1-2.72 wt.%, and trace Pd, 0.15-1.02 wt.%.

	Fe	*Ni*	*Co*	*S*	*Cu*	*As*	*Sb*	*Ag*	*Pd*	*Pt*	*Total*
a	1.1	40.99	0.07	0.09	11.31	0.01	46.49	0.03	0.15	0.00	100.2
Formula;	$[(Ni_{1.83}Fe_{0.05}Cu_{0.47})2.35Sb]$										
b	2.75	40.09	0.03	0.08	11.73	0.04	45.67	0.05	0.69	0.09	101.2
Formula;	$[(Ni_{1.82}Fe_{0.13}Cu_{0.49}Pd_{0.02})2.46(Sb\ S_{0.01})1.01]$										
c	0.15	41.18	0.05	0.10	11.78	0.30	47.05	0.01	0.93	0.00	101.6
Formula;	$[(Ni_{1.82}Fe_{0.01}Cu_{0.48}Pd_{0.02})2.33(Sb\ As_{0.01})1.01]$										
d	1.46	41.81	0.05	0.21	13.18	3.08	38.06	0.09	1.02	1.69	100.7
Formula;	$[(Ni_{2.28}Fe_{0.08}Cu_{0.66}Pd_{0.03}Pt_{0.03})3.09(Sb\ As_{0.13}S_{0.02})1.15]$										

Table 3.25. Microprobe analyses (in wt.%) of four different lavender-mauve antimonide grains.

Analysis of the antimonide intergrown with orcelite (Fig. 3.51) (table 3.25, analysis d) shows 3.08 wt.% As and low (38.06 wt %) Sb, which probably results from a partial contribution to this analysis from the adjacent orcelite grain.

3.5.2.3 Ni-rich antimonide

Isotropic pink-brown, Ni-rich antimonide has been found in two different associations. The first is as a replacement of a lamellar intergrowth of breithauptite and lavender-coloured antimonide (Fig. 3.52), or lavender antimonide (Fig. 3.53). These grains of composite

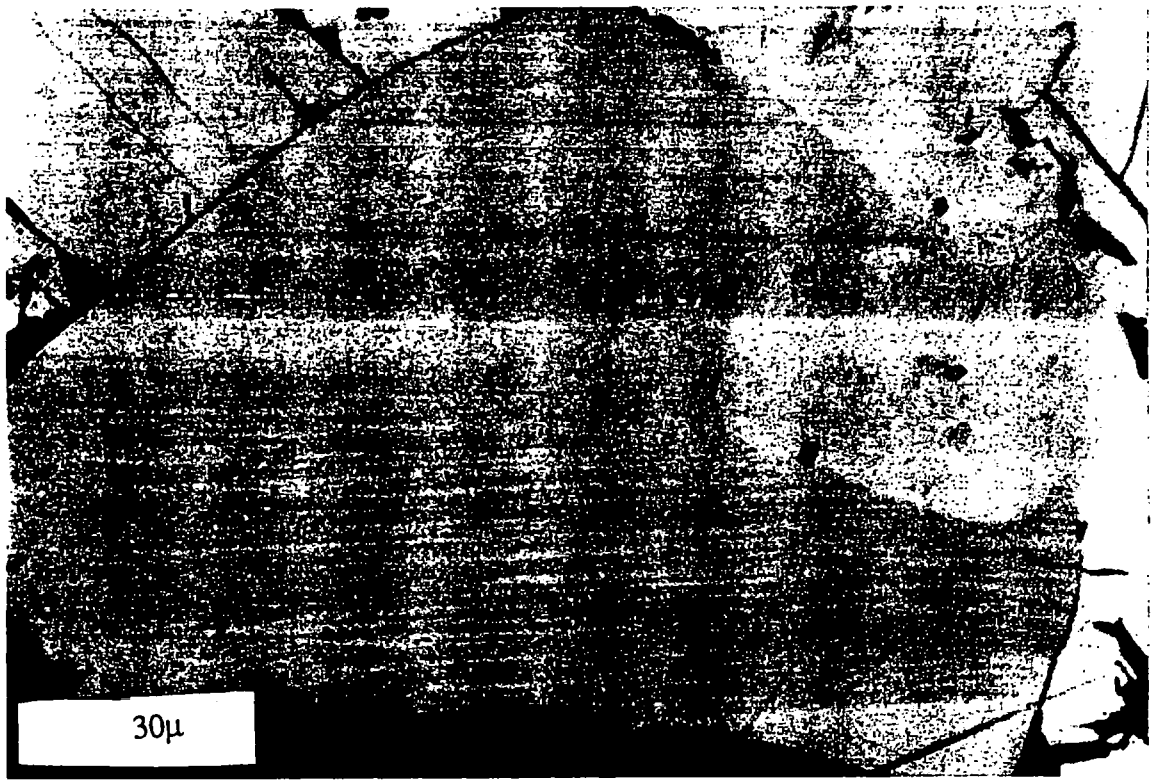

Fig. 3.46. Composite Ni-Cu antimonide grain (centre) comprising a lamellar intergrowth of breithauptite (pink) and Ni-Cu antimonide (deep pink, centre bottom) intergrown with pentlandite (top left), heazlewoodite (top right) and altered silicate (bottom). Dunite pod, Cliff.

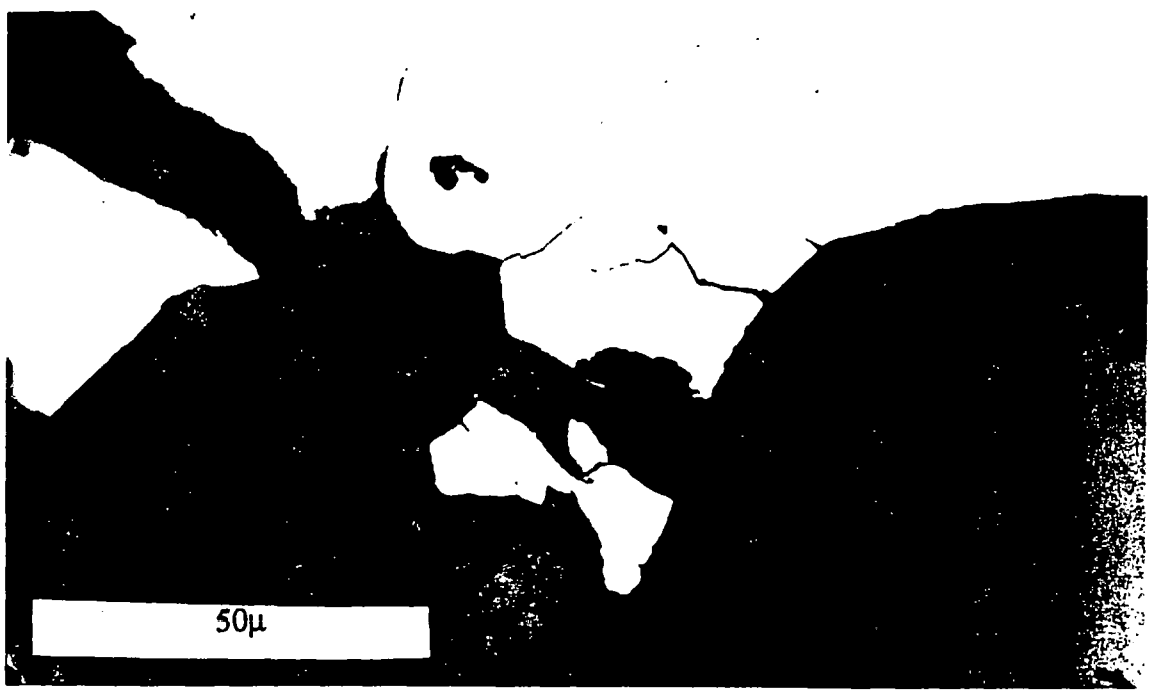

Fig. 3.47. Composite Ni-Cu antimonide grain (centre), comprising a lamellar intergrowth of breithauptite (pink) and Ni-Cu antimonide (deep pink) intergrown with heazlewoodite (top and top left), orcelite (brown, centre top), magnetite (grey, bottom left and bottom right) and altered silicate (centre left). Cumulate dunite.

Fig. 3.48. Composite Ni-Cu antimonide grain (centre left) comprising a lamellar intergrowth of breithauptite (pink) and Ni-Cu antimonide (deep pink) intergrown with heazlewoodite (cream white, right), orcelite (brown, centre) and altered silicate (left). Dunite pod, Cliff.

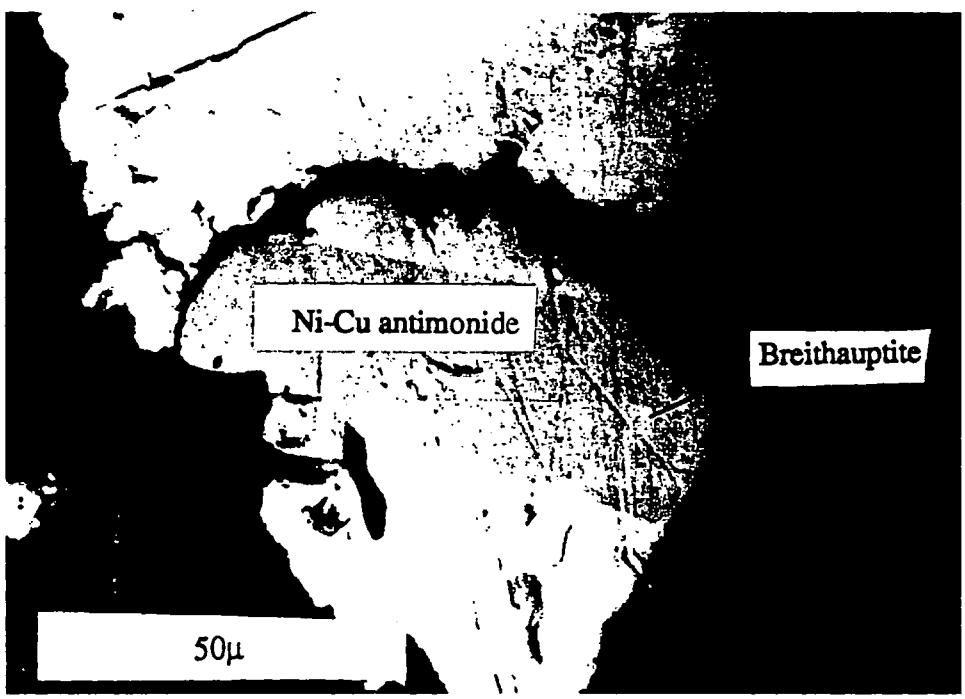

Fig. 3.49. Lath-shaped Ni-Cu antimonide (mauve-brown, centre) intergrown with minor breithauptite (right) enclosed in heazlewoodite (top left) altering to awaruite (top right). Magnetite (dark grey, bottom right and bottom left) is intergrown with heazlewoodite and native copper (orange, bottom left). Cumulate dunite.

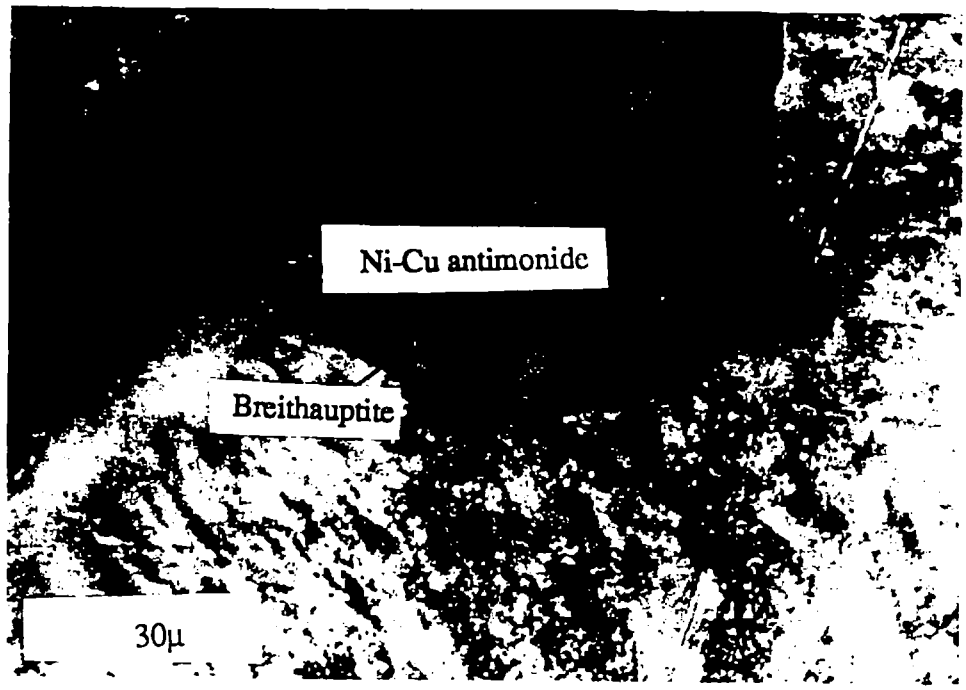

Fig. 3.50. Isotropic Ni-Cu antimonide grain (centre) containing minor breithauptite at the interface between awaruite (blue grey interference colours, bottom) and altered silicate top. Partially crossed polars. Cumulate dunite.

Fig. 3.51. Isotropic Ni-Cu antimonide (pink, centre) intergrown with orcelite (pink brown centre right), awaruite (white, top right) and pentlandite (brown, top and left. Cumulate dunite.

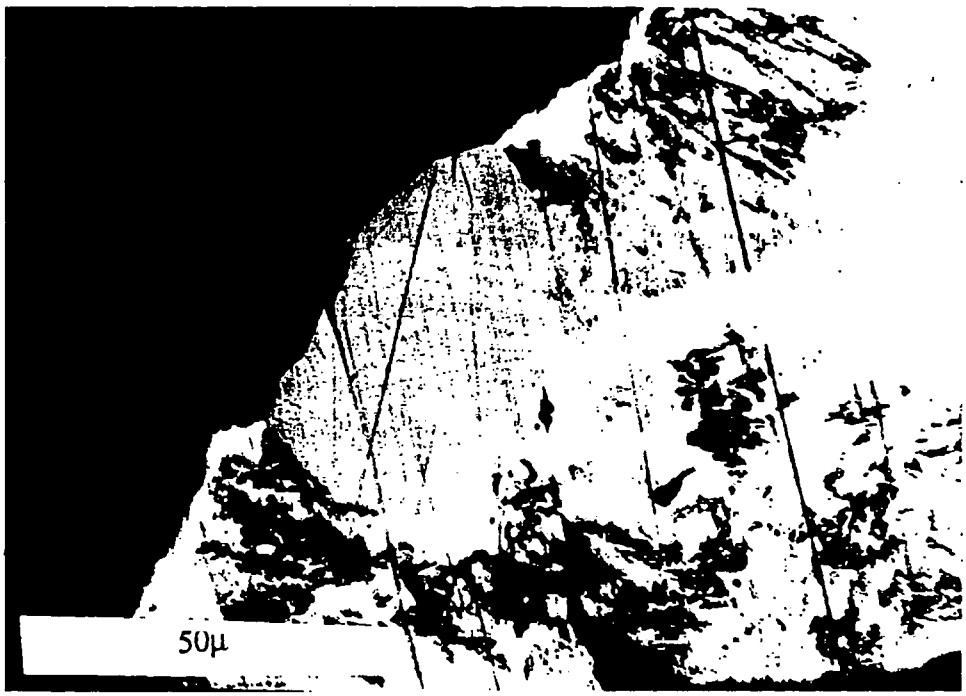

Fig. 3.52. Composite Ni-Cu antimonide grain (centre) of anisotropic breithauptite lamellae (pink) and isotropic Cu-rich Ni-antimonide (lavender). The margin of this grain has altered to an isotropic pink-brown Ni-rich antimonide (centre left intergrown with silicate, right). This grain is intergrown with awaruite (top right and bottom) and heazlewoodite (right). Cumulate dunite.

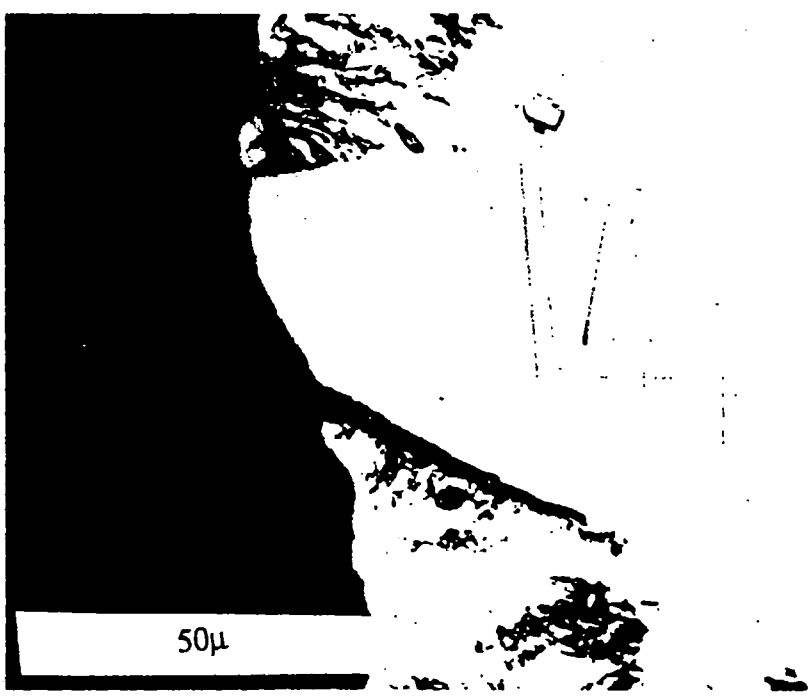

Fig. 3.53. Composite antimonide grain (centre) composed of an intergrowth of Ni-rich antimonide (peach-pink, centre left) and Cu-rich antimonide (centre). The grain is intergrown with heazlewoodite (left), awaruite (centre bottom and top left) and altered silicate (left). Cumulate dunite.

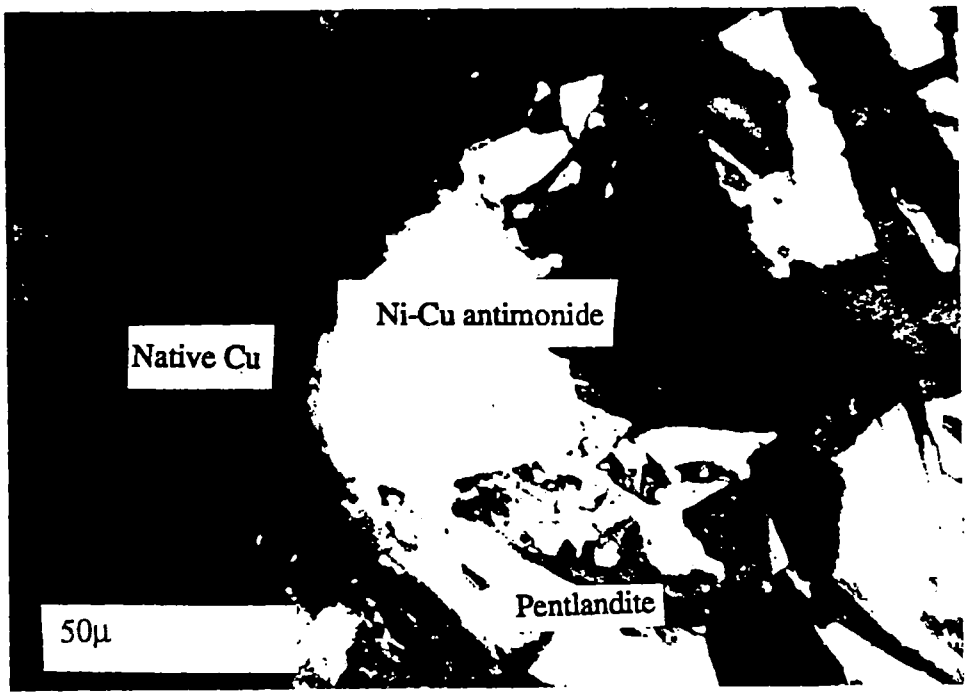

Fig. 3.54. Isotropic anhedral pink-brown Ni-Cu antimonide (centre left) with native copper rim (pink, centre left) intergrown with pentlandite (centre bottom, top left) and altered silicate (left). Cumulate dunite.

antimonide are situated at the boundary between a heazlewoodite-awaruite grain and silicate. The outermost margins of both grains are partially intergrown with altered silicate and consist of a pink-brown isotropic phase. One of these grains which is 40μ in size (Fig. 3.52), displays a lamellar intergrowth of breithauptite and lavender-coloured antimonide. Table 3.26, analysis PB. 1 is a quantitative microprobe analysis of the pink-brown isotropic overgrowth/replacement shown in Fig. 3.52. It contains trace Fe, Pd and 4.5 wt.% Cu. Analysis lv. 1, table 3.26, is of the lamellar mixture of breithauptite and lavender antimonide shown in Fig. 3.52.

	Fe	*Ni*	*Co*	*S*	*Cu*	*As*	*Sb*	*Ag*	*Pd*	*Pt*	*Total*
PB. 1	0.53	54.15	0.01	0.07	4.57	0.05	40.61	0.03	0.10	0.12	100.2
Formula;	$[(Ni_{2.78}Fe_{0.03}Cu_{0.22})3.03(Sb\ S_{0.01})1.01]$										
lv. 1	0.19	40.03	0.06	0.08	6.87	0.00	53.37	0.01	0.08	0.03	100.7
Formula;	$[(Ni_{1.56}Fe_{0.01}Cu_{0.25})1.82(Sb\ S_{0.01})1.01]$										

Table 3.26. Microprobe analyses (in wt.%) of the composite antimonide grain shown in Fig. 3.52.

The other grain, 75μ in size (Fig. 3.53), consists of a patchy intergrowth of pink-brown antimonide and lilac-lavender antimonide. The patchy intergrowth of lilac-lavender antimonide and pink-brown isotropic antimonide of Fig. 3.53 may represent a true patchy intergrowth of two phases or it could be produced from cutting the thin section sub-parallel to the plane of a lamellar structure as displayed by the antimonide in Fig. 3.52. The compositions of the pink-brown isotropic phase and the lavender isotropic phase shown in Fig. 3.53 are given in table 3.27. The pink-brown isotropic antimonide analysis PB. 2 (table 3.27) is nickel-rich with 1.39 wt.% Cu and traces of Pd, (0.12 wt.%). Analysis of the coexisting isotropic lavender phase, analysis lv. 2 (table 3.27) shows it to be Cu-rich and Ni-poor compared to the intergrown pink-brown antimonide, analysis PB. 2 (table 3.27).

	Fe	Ni	Co	S	Cu	As	Sb	Ag	Pd	Pt	Total
PB. 2	0.07	54.88	0.02	0.08	1.39	0.03	43.82	0.03	0.12	0.04	100.5
Formula; $[(Ni_{2.58}Cu_{0.06})2.64(Sb\ S_{0.01})1.01]$											
lv. 2	0.27	44.11	0.05	0.12	8.00	0.00	47.95	0.02	0.10	0.00	100.6
Formula; $[(Ni_{1.91}Fe_{0.01}Cu_{0.32})2.24(Sb\ S_{0.01})1.01]$											

Table 3.27. Microprobe analyses (in wt.%) of the composite antimonide grain shown in Fig. 3.53.

The second occurence of this group of Ni-rich antimonides is as an isotropic, 30μ by 50μ, anhedral rounded grain, with a rim of native Cu, situated at the margin of pentlandite and altered silicate (Fig. 3.54). This grain is a Ni-rich antimonide containing 1.96 wt.% Cu and 0.14 wt.% Pd, table 3.28.

Fe	Ni	Co	S	Cu	As	Sb	Ag	Pd	Pt	Total
0.13	54.39	0.03	0.09	1.96	0.06	44.05	0.02	0.14	0.05	100.9
Formula; $[(Ni_{2.56}Fe_{0.01}Cu_{0.09})2.66(Sb\ S_{0.01})1.01]$										

Table 3.28. Microprobe analyses (in wt.%) of the Ni-rich antimonide grain shown in Fig. 3.54.

3.5.3 Paragenesis of nickel antimonides

It is noted that the mineral formulae of Ni-Cu antimonides is similar to the $Pd_{5+x}Sb_{2-x}$ stibiopalladinite formula of Gunn *et al.* (1985) who also note that there is consistently 4 wt.% Cu contained within this phase. The mineral chemistry of the different antimonides described above is represented as a triangular plot in terms of Ni-Cu and Sb in Fig. 3.55. From Fig. 3.55, three compositionally distinct antimonide groups may be identified. The first is breithauptite, analyses of which fall close to the ideal 1:1 Ni:Sb ratio. The second is a group of Cu-rich antimonides that contain in excess of 10 wt.% Cu and correspond to the isotropic lavender antimonides described above. A third compositionally distinct group of antimonides corresponds to the isotropic pink-brown antimonides which replace lamellar intergrowths of breithauptite and Cu-rich antimonide and also the single solitary grain of isotropic pink-brown antimonide which has a native Cu rim. Included in this plot are the bulk analyses of lamellar intergrowths of breithauptite and Ni-Cu antimonide. These latter analyses often plot, as expected, intermediate between the fields for breithauptite and Cu-rich antimonide. For comparison qualitative SEM analyses of the individual lamellae of two composite antimonide

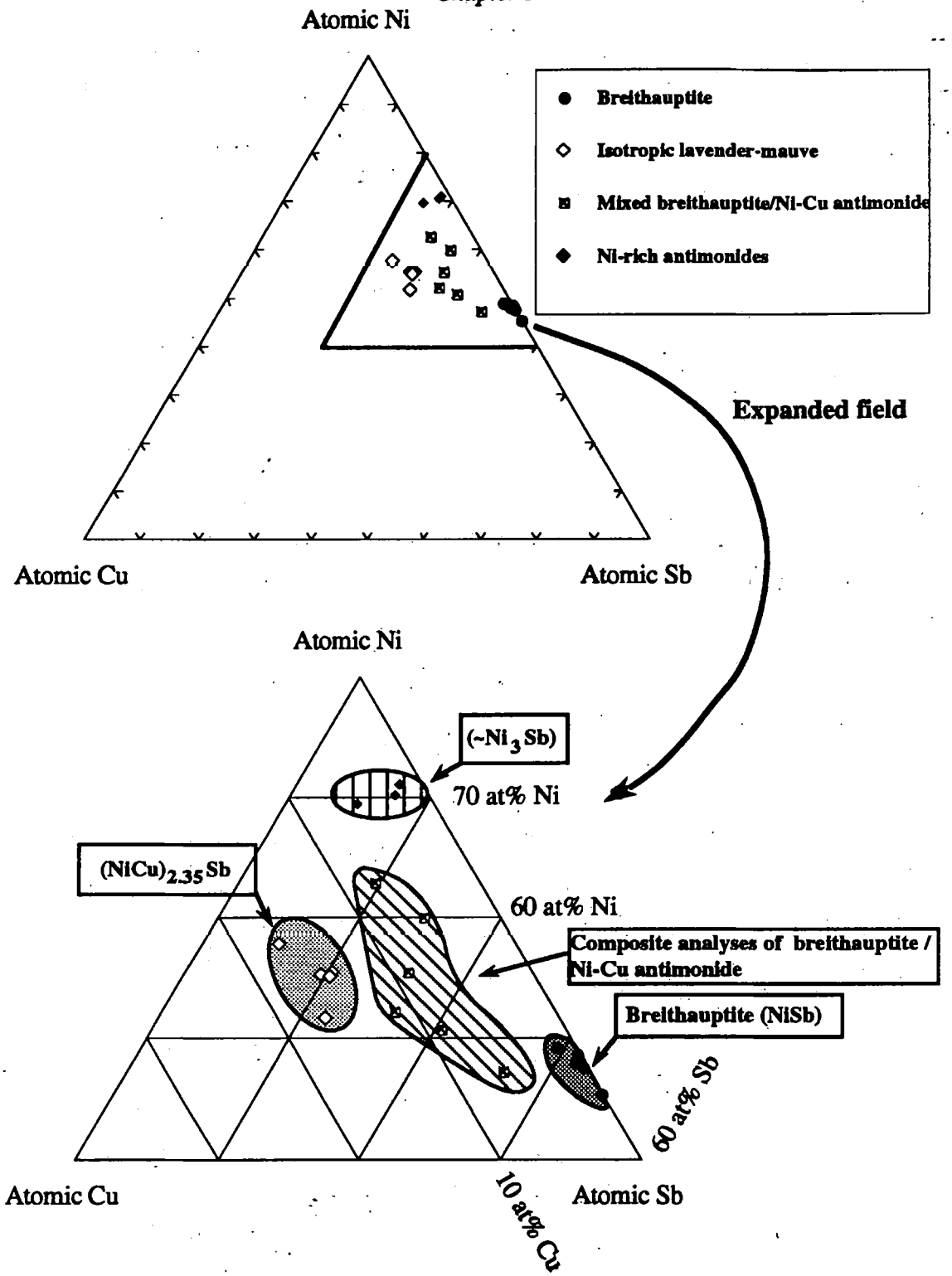

Fig. 3.55. Triangular plot in terms of atomic % Ni, Cu and Sb showing the compositions of the different antimonide minerals analysed.

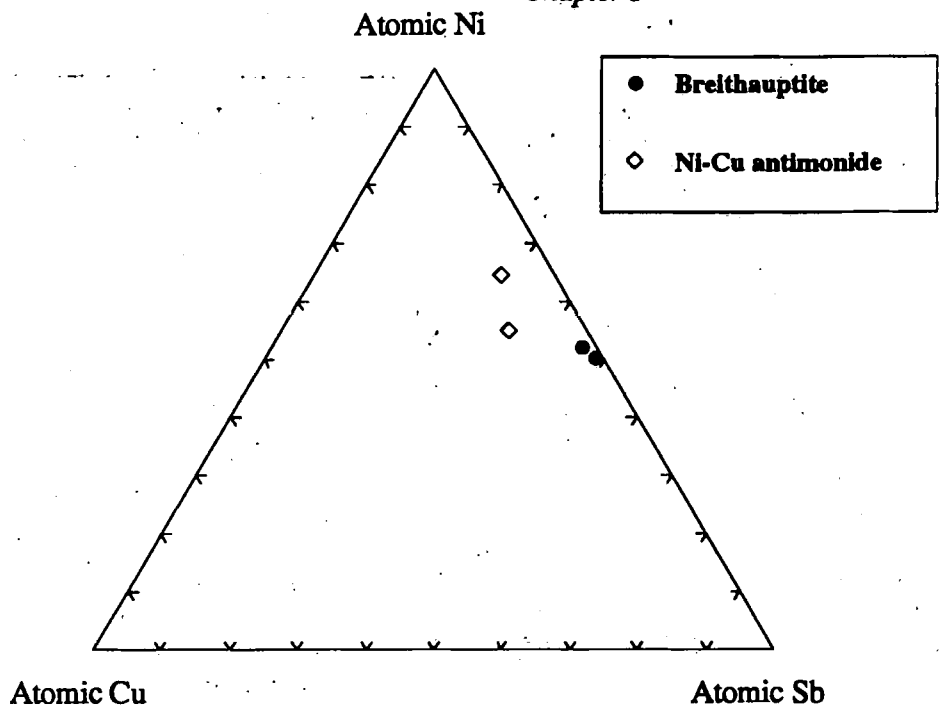

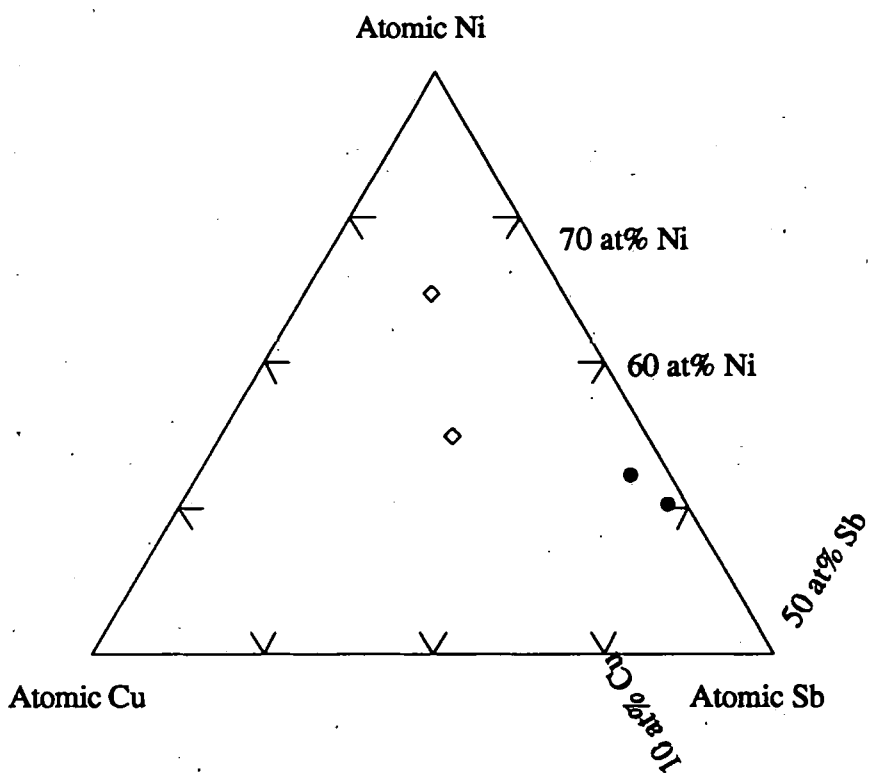

Fig. 3.56 The compositions of individual antimonide lamellae shown in Fig. 3.39 and Fig. 3.43 as determined by qualitative SEM analysis.

grains (see table 3.17 and table 3.18) are also displayed as a triangular plot in terms of Ni, Cu and Sb in Fig. 3.56. A schematic diagram showing the textural relations of the different antimonides is given in Fig. 3.57. The lamellar intergrowths of breithauptite and Ni-Cu antimonide could arise from;

(1) Replacement of breithauptite by Ni-Cu antimonide, producing lamellar breithauptite/Ni-Cu antimonide intergrowths. Such a replacement may have occurred parallel to the (0001) cleavage of breithauptite, during which Cu and Ni ± Fe ± Pd ± As are identified as mobile elements which were introduced.

(2) Exsolution from a precursor Ni-Cu (Fe) antimonide. The mixed antimonides are often enclosed within awaruite rims to heazlewoodite and are therefore possibly intimately linked to the formation of heazlewoodite and awaruite, the latter being stable at temperatures <300°C (see Chapter 4), implying that exsolution occurred at low temperatures. Small amounts of pentlandite ± awaruite, partially surrounding mixed antimonides enclosed within heazlewoodite (*e.g.* Fig. 3.39) may be intimately linked to the formation of these antimonides (expelled surplus cations?) since they have not been observed about breithauptite enclosed within heazlewoodite or pentlandite. The pentlandite could alternatively be relict sulphide which did not react to form heazlewoodite.

If the lamellar intergrowths of breithauptite and Ni-Cu antimonide formed by a replacement mechanism, then rounded breithauptite enclosed within pentlandite, heazlewoodite and heazlewoodite/awaruite may be the earliest antimonide in the paragenesis. The relatively large, subhedral to euhedral, isotropic lavender-mauve to grey-pink high-Cu antimonides are thought to be late in the antimonide paragenesis as they occur about the margins of Ni-Fe sulphide/magnetite grains at heazlewoodite/awaruite, awaruite/silicate junctions and within a symplectite-like intergrowth of native Cu and pentlandite or at the margin of orcelite. Their mineral chemistry is comparable to the lamellar intergrowths of lavender Ni-Cu antimonides that are hosted within breithauptite grains and may represent complete alteration of breithauptite to Ni-Cu antimonide. Furthermore, they contain patches of light peach-pink anisotropic antimonide that may be relict breithauptite.

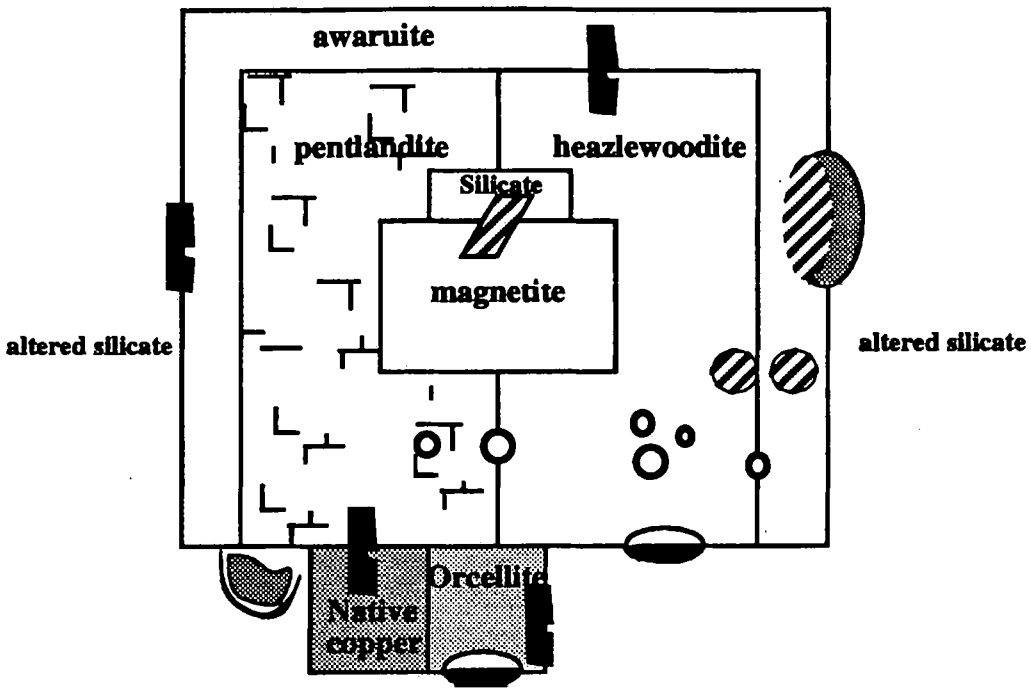

Key to shading:

- Breithauptite
- Ni-Cu antimonide
- Intergrowth of breithauptite and Ni-Cu antimonide
- Ni-rich antimonide

Fig. 3.57. Schematic diagram showing the textural relations of the different antimonide minerals.

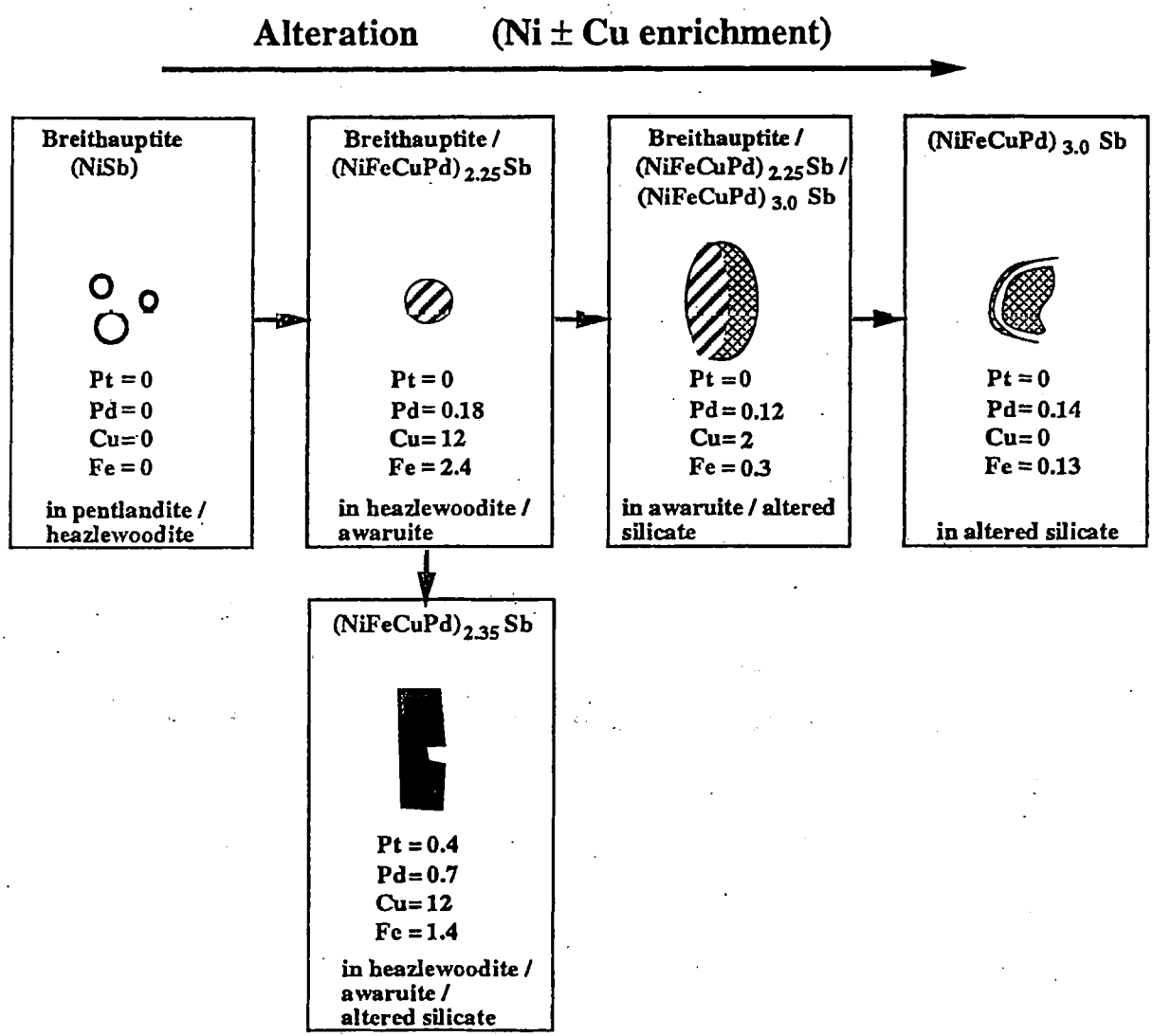

Fig. 3.58. Schematic diagram showing possible pathway for alteration of nickel antimonide minerals.

Lamellar breithauptite/Ni-Cu antimonide intergrowths are replaced by pink-brown isotropic, Ni-rich, Cu-bearing antimonide, which has also been found as a solitary grain intergrown with native Cu and altered silicate. This antimonide is homogenous, has a low Cu content and a partial rim of native Cu, which could be low temperature exsolution, and is thought to be the paragenetically latest antimonide in the proposed replacement/alteration sequence. There appears to be a trend to higher Ni and Cu contents in antimonides in this paragenetic sequence (Fig. 3.58) with late-stage antimonides showing signs of Cu-loss.

The antimonide mineralogy from both dunite pods in harzburgite, Cliff, and cumulate dunites are very similar. Notable differences include the absence of Ni-rich antimonides intergrown with awaruite at Cliff. All analysed breithauptites from Cliff contain trace Pd and As whereas rounded breithauptites in the cumulate dunite unit are barren of these elements.

Nickel antimonides and arsenides often show a close spatial association with Ni and Ni-Fe sulphides and alloys. They are therefore considered to be intimately linked to the formation of base-metal sulphide mineralization. Since Sb is a chalcophile element it may be anticipated that it will form minerals in close spatial association with base-metal sulphides. Sub-rounded inclusions of breithauptite occur both enclosed within pentlandite and heazlewoodite, whereas breithauptite intergrown with Ni-Cu antimonide commonly forms only at the margin of heazlewoodite grains intergrown with awaruite or altered silicate (Fig. 3.57). The Ni and Cu-enrichment trend from breithauptite to Ni-Cu antimonide is therefore considered to parallel the Ni-enrichment involved in the replacement of pentlandite by heazlewoodite and Ni-Fe alloy. The intergrowth of Ni-Cu antimonides with Sb-bearing orcelite suggests that these two minerals are paragenetically similar. Orcelite from the Cliff locality was considered to have crystallized at temperatures <500°C (Gunn *et al.*, 1985) and therefore a similarly low temperature of crystallization is inferred for the Ni-Cu antimonides.

The origin of Sb, *i.e.*, whether it is of primary magmatic origin or whether it has been introduced later was addressed by Lord (1991) using whole-rock INAA on different lithologies and alteration styles from the ophiolite around Baltasound on Unst. It was found that Sb and As showed a predominantly igneous distribution in the complex but highly anomalous levels of Sb in association with sheared and highly altered lithologies suggested concentration by secondary

processes. Certain antimonides of this study are seen to contain trace to major amounts of Pd and occasionally traces of Pt, (*e.g.* table 3.21) It is proposed that Pd (and Pt) concentrations in some later antimonides are related to the alteration of earlier sulphide minerals during which these two PGE were released from an early sulphide phase and incorporated into these later antimonides.

3.6 Summary and conclusions

The sulphide mineralogy of the Shetland ophiolite varies with the host silicate lithology. The ultramafic sequence contains a disseminated Ni-Fe-sulphide dominated assemblage. This is overlain by a disseminated to sub-massive Fe, and Cu-Fe sulphide mafic sequence.

The mafic sequence carries an assemblage of pyrrhotite-pyrite-marcasite-chalcopyrite±pentlandite-'limonite'-blaubleibender covelline-magnetite intergrown with a greenschist facies silicate mineral assemblage (Chapter 2). Sulphides are commonly oxidized to 'limonite' and remobilization of sulphur is evident in highly sheared lithologies where secondary veins of pyrite are common. Hydrothermal veins and pods of predominantly pyrite with minor 'limonite'-chalcopyrite-magnetite occur on the Mu Ness peninsula. Altered high-level pyroxenites carry an assemblage of pentlandite-monoclinic pyrrhotite-pyrite-chalcopyrite-violarite-niccolite-cobaltite-magnetite-'ferritchromit'-ilmenite, that is dominated by large spongy pyrites that replace silicate minerals. Ni-arsenide minerals are also common. Cumulate pyroxenites contain two main sulphide assemblages. Fresh pyroxenites, contain a pentlandite-pyrrhotite-chalcopyrite-bornite-magnetite-chrome spinel-'ferritchromit' assemblage. Pentlandite-chalcopyrite-bornite-magnetite aggregates which occur interstitial to pyroxene crystals are reminiscent of the texture commonly ascribed to the crystallization of sulphides and oxide minerals from an immiscible sulphide/oxide liquid at magmatic temperatures. Altered pyroxenites contain a different assemblage of pentlandite- monoclinic pyrrhotite-pyrite-marcasite-chalcopyrite-heazlewoodite-millerite-godlevskite-chalcocite-bornite-digenite-covellite-minor native Cu±orcelite±maucherite intergrown with serpentine and chlorite which replace clinopyroxene. Wehrlitic dunite and cumulate dunites with substantial (>10%) relict olivine carry a pentlandite-troilite-native Cu-magnetite-chromite-'ferritchromit' or pentlandite-awaruite-native

Cu-magnetite-chromite-'ferritchromit' assemblage. In more serpentinized lithologies the assemblages pentlandite-heazlewoodite-awaruite-native Cu-orcelite-Ni-Cu antimonide and pentlandite-heazlewoodite-millerite-awaruite-chalcopyrite-chalcocite-native Cu-orcelite-breithauptite-Ni-Cu antimonide are recognized. Podiform chromitite from the Cliff locality in the close vicinity of the basal thrust contains a Ni-arsenide assemblage of niccolite-maucherite. At the basal thrust talc-carbonate altered rocks contain pentlandite-hexagonal/monoclinic pyrrhotite-pyrite-marcasite-chalcopyrite-violarite-mackinawite-valleriite-niccolite-orcelite-rammelsbergite-cobaltite-magnetite-'ferritchromit'.

Quantitative microprobe data for the sulphide, arsenide and antimonide minerals have been obtained. Pyrrhotites range from monoclinic to troilite varieties. Cu-Fe and Cu-sulphides are represented by chalcopyrite, bornite and chalcocite. Pentlandite shows a wide range in mineral chemistry which is consistent with the range of natural pentlandite compositions. The most Ni-rich pentlandites occur in the Ni-rich sulphide assemblage pentlandite-heazlewoodite-millerite-godlevskite, whereas the most Ni-poor pentlandite was found intergrown with troilite. Pentlandites from the cumulate and high-level pyroxenites are richer in Co compared to pentlandites hosted in dunites. These differenences are considered to be a primary magmatic feature. Pd and Pt were routinely sought, but not detected, in sulphide and arsenide minerals from both the mafic and ultramafic portions of the ophiolite. However, Pd and Pt were both detected in Ni-Cu antimonide minerals from the cumulate dunite unit and in a dunite pod in harzburgite fro the Cliff locality. A paragenesis has been established for these Ni-Cu antimonides whereby breithauptite (NiSb) is replaced by Ni-Cu antimonide. Further replacement is represented by the Ni-rich antimonides. This sequence of replacement is closely linked to the alteration of the host sulphides, pentlandite and heazlewoodite. It is suggested that Pd and Pt are released during the alteration of pentlandite -> heazlewoodite -> Ni-Fe alloy (awaruite) and are subsequently partitioned into the Ni-Cu antimonide minerals.

Chapter 4

Sulphide phase equilibria, and a model for low temperature sulphide paragenesis

4.1 Introduction

A study of sulphide phase equilibria relevant to the sulphide mineralogy documented in Chapter 3 should contribute towards an understanding of the conditions of sulphide mineral genesis and post-depositional alteration of sulphides. Phase equilibrium relations at low temperatures, based on the observed parageneses from different lithologies in the complex are discussed, being limited by the available published experimental data. Recognition of equilibrium has been a problem in studies of both synthetic and natural sulphides (see Vaughan and Craig, 1978). However, knowledge of equilibrium relations among sulphides and metals is important in looking at both equilibrated and non-equilibrated systems, *i.e.* it is necessary to understand the equilibrium relations before disequilibrium among phases can be demonstrated.

The principle opaque phases included in the following discussion are those that have been characterized during the present study (Chapter 3), either by reflected light microscopy or microprobe techniques. A summary table of these different opaque minerals identified from the main lithologies of the Shetland ophiolite is given in table 4.1.

4.2. Low temperature equilibrium relations in the Fe-Ni-S system

Magmatic equilibrium phase relations in the Fe-Ni-S system were first studied by Kullerud and co-workers (*e.g.* Kullerud *et al.*, 1969). Lower temperature phase relations in the same system were investigated by Graterol and Naldrett (1971) and Misra and Fleet (1973), to clarify the re-equilibration (non-magmatic) histories of Fe-Ni sulphide deposits.

	pn	Co .pn	tr	hp	mp	py	cp	aw	hz	ml	gl	vi	mk	mr	cc	bn	dg	cv	bl. cv	Cu	or	nc	mc	gd	br	Ni, Cu Sb	ch	mt	fc	il
Gabbro-hosted sub-massive sulphides						√	√																					√		
Gabbros, basic dykes and plagiogranites	√	√		√	√	√	√							√					√									√		
High-level pyroxenite	√				√	√	√			-												√		√			√	√	√	√
Cumulate pyroxenite	√		?	?	?		√									√											√	√	√	
Cumulate pyroxenite, serpentinized	√			√	√	√	√		√	√	√			√		√	√	√		√	√		√				√	√	√	
Cumulate dunite, fresh	√		√					√	√											√	√					√	√	√	√	
Cumulate dunite serpentinized	√						√	√	√	√					√					√	√				√	√	√	√	√	
Dunite pod	√							√	√											√							√	√	√	
Dunite pod, Cliff	√								√	√	√				√					√	√				√	√	√	√	√	
Podiform chromite, Cliff																						√	√				√	√	√	
Talc-carbonate rock, Basal Thrust	√			√		√	√					√	√	√								√		√			√	√	√	

Table 4.1. Summary of the occurrence of the different opaque mineral phases determined in this study. Abbreviations of mineral phases are given below along with mineral formula. ? = type of pyrrhotite not defined.

pn	=	pentlandite; $(Fe, Ni)_9S_8$
Co.pn	=	cobaltpentlandite; $(Co, Fe, Ni)_9S_8$
tr	=	troilite; FeS
hp	=	hexagonal pyrrhotite; Fe_9S_{10}
mp	=	monoclinic pyrrhotite; Fe_7S_8
py	=	pyrite; FeS_2
cpy	=	chalcopyrite; $CuFeS_2$
aw	=	awaruite; Ni_3Fe
hz	=	heazlewoodite; Ni_3S_2
ml	=	millerite; NiS
gl	=	godlevskite; Ni_7S_6
vi	=	violarite; $FeNi_2S_4$
mk	=	mackinawite; $Fe_{1-x}S$
mr	=	marcasite; FeS_2
		chalcocite; Cu_2S
bn	=	bornite; Cu_5FeS_4
dg	=	digenite; Cu_9S_5
cv	=	covellite; CuS
bl.cv	=	blaubleibender covelline; (?)
Cu	=	native copper; Cu
or	=	orcellite; $Ni_{5-x}As_2$
nc	=	niccolite; NiAs
mc	=	maucherite; $Ni_{11}As_8$
gd	=	gersdorffite; (Ni, Co, Fe)AsS
br	=	breithauptite; NiSb
Ni, Cu Sb	=	Ni,Cu antimonide; $(Ni, Cu)_{5-x}Sb_2$
ch	=	chrome-spinel; $(Fe, Mg)(Cr,Al)_2O_4$
mt	=	magnetite; Fe_3O_4
fc	=	ferritchromit; $(Fe)(Cr)_2O_4$
il	=	ilmenite; $FeTiO_3$

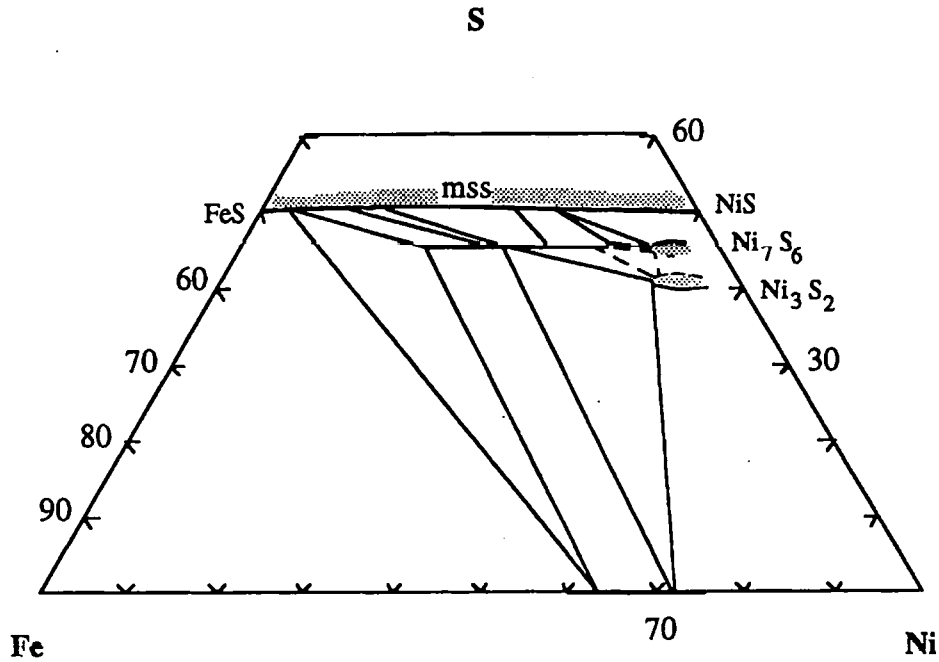

Fig. 4.1. Phase relations at 600°C in the Fe-Ni-S system, Misra and Fleet (1973).

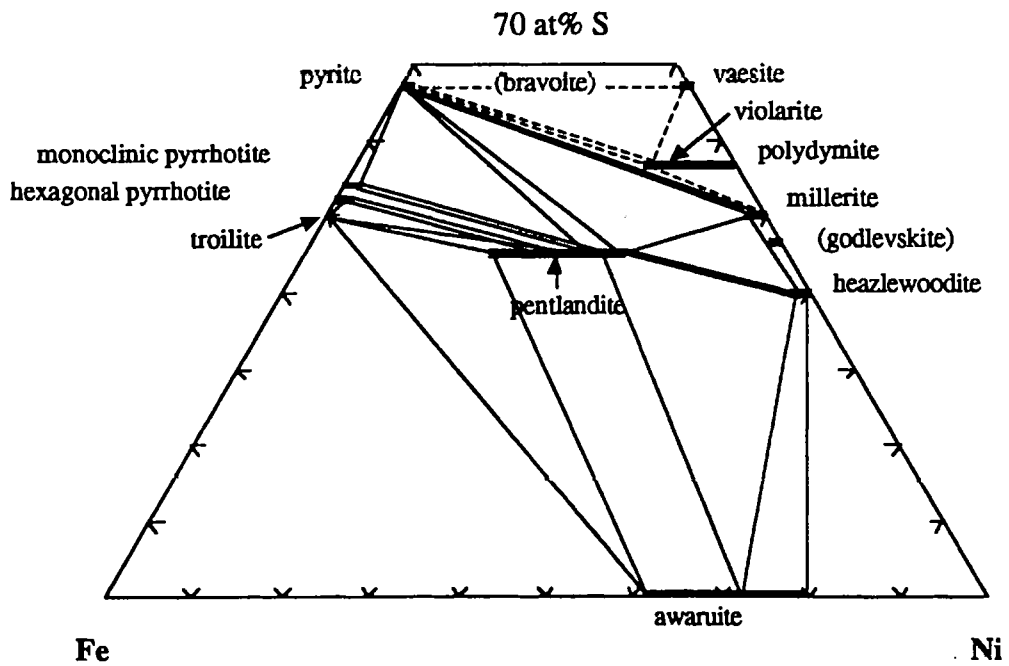

Fig. 4.2. Interpretative low-temperature phase diagram (140 °C) for the Fe-Ni-S system, Misra and Fleet (1973).

Phase relations at 600°C are shown in Fig. 4.1 (after Misra and Fleet, 1973). Higher temperature relationships are dominated by [$(FeNi)_{1-x}S$] monosulphide solid-solution (*mss*). This *mss* is quenchable through most of its compositional range. Below 610°C, pentlandite [$(FeNi)_9S_8$] is stable and exhibits a wide compositional range depending on the co-existing phases. Equilibrium relations within the Fe-Ni-S system below 200°C are not unequivocally established (Vaughan and Craig, 1978), and determination of them is frequently confused by disequilibrium. Shown in Fig. 4.2 is the interpretative low-temperature (140°C) phase equilibria diagram of the Ni-Fe-S system of Misra and Fleet (1973). This diagram, which differs from that proposed by Graterol and Naldrett (1971) whose tie-lines between violarite-polydimite solid solution and pentlandite prevents the stable co-existence of pyrite and millerite, is supported by apparent hypogene pyrite-millerite assemblages (*e.g.* Hudson and Groves, 1974) and by trends in higher temperature equilibria (Craig 1973). Godlevskite was not considered a stable phase in the interpretive diagram of Misra and Fleet (1973), mainly based on the observations of the replacement of godlevskite by millerite in ore specimens from Noril'sk, and the common occurrence of the natural assemblage pentlandite-millerite-heazlewoodite. Experimental difficulties encountered when establishing low temperature equilibrium relations make tie lines somewhat speculative. However, agreement between these low temperature experimental phase relations and phases commonly observed in low temperature natural assemblages (magmatic ores and meteorites) is encouraging.

4.2.1 Composition of pentlandite and heazlewoodite derived from experimental and natural studies

Pentlandite, varies in composition from atomic ratio Fe/Ni=1.98 to Fe/Ni=0.65 at 400°C (Shewman and Clark, 1970), and from Fe/Ni=1.91 to Fe/Ni=0.55 in natural materials, depending upon the mineral association (Misra and Fleet, 1973) (Fig.3. 34). The absence of natural iron or nickel end member compositions was explained by Vaughan and Craig (1978), and arises from metal-metal bonds within the cube-cluster of pentlandite. This restricts the total number of permissable d electrons in tetrahedral sites to seven (as in Co^{2+} or equal numbers of Fe^{2+} and Ni^{2+} ions). Misra and Fleet (1973) show that the variations in the solid solution limits

of pentlandite with temperature are asymmetrical and unsystematic. Iron solubility progressively increases with decrease in temperature, from 33 at.% Fe at 600°C to 40 at.% Fe at 285°C and then decreases with falling temperature to 30 at.% at 230°C. The Ni solubility limit of the pentlandite solid solution field reaches a maximum of 41 at.% Ni at 600°C and a minimum of 34 at.% Ni at 300°C. These results give a wider range of solubility limits than found from previous studies (*e.g.* Shewman and Clark, 1970), but are compatible with compositions measured from different natural nickel sulphide assemblages (Misra and Fleet, 1973). Kaneda *et al.* (1986) notes complete solid solution between [(Fe, Ni)$_{9-x}$ S$_8$] and [Co$_{9-x}$ S$_8$] at temperatures between 600-300°C and this solid solution field decomposes into two fields towards [(Fe, Ni)$_9$S$_8$] and [Co$_9$S$_8$] at 200°C.

The solubility of Fe in the [(Ni, Fe)$_3$S$_2$] (heazlewoodite) solid solution decreases with falling temperature from 11 at.% Fe at 600°C to 3 at.% Fe at 300°C (Misra and Fleet, 1973). The composition of this phase may approach [Ni$_3$S$_2$] at lower temperatures. They also state that the composition of heazlewoodite in the natural assemblage millerite-heazlewoodite-pentlandite(±godlevskite) is S deficient (38-39 at.% S) compared to [M$_3$S$_2$], and that total Fe+Co+Cu contents rarely exceed 1.0 at.%

4.3 Review of low temperature Cu-Fe-S phase equilibria

As with the Fe-Ni-S system, the equilibrium relations at low temperatures remain enigmatic (Vaughan and Craig, 1978). The general relations in this system has resulted from work by, *e.g.* Yund and Kullerud (1966) and Barton (1973). Essentially, phase equilibria at 400°C and above are dominated by three solid solutions: 1) chalcocite-digenite-bornite solid solution, 2) intermediate solid solution (*iss*) and 3) pyrrhotite solid solution (Fig. 4.3). The *iss* is referred to as isocubanite [CuFe$_2$S$_3$], a high temperature cubic phase by Oudin and Constantinou (1984). Pyrite and liquid sulphur are stable at high fS_2 whereas Fe and Cu are stable at low fS_2.

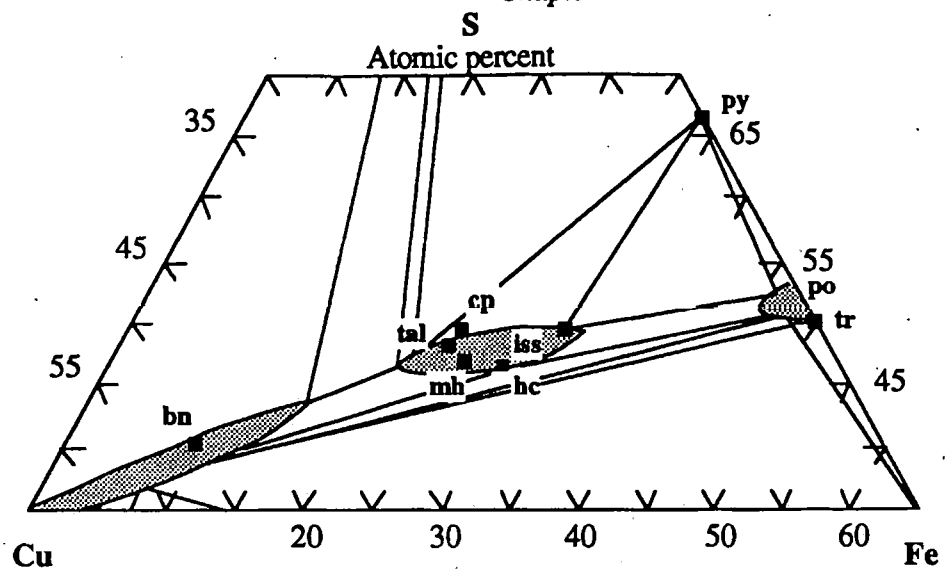

Fig. 4.3. Phase relations in the central portion of the Cu-Fe-S system at 600 ℃ (After Cabri 1973).

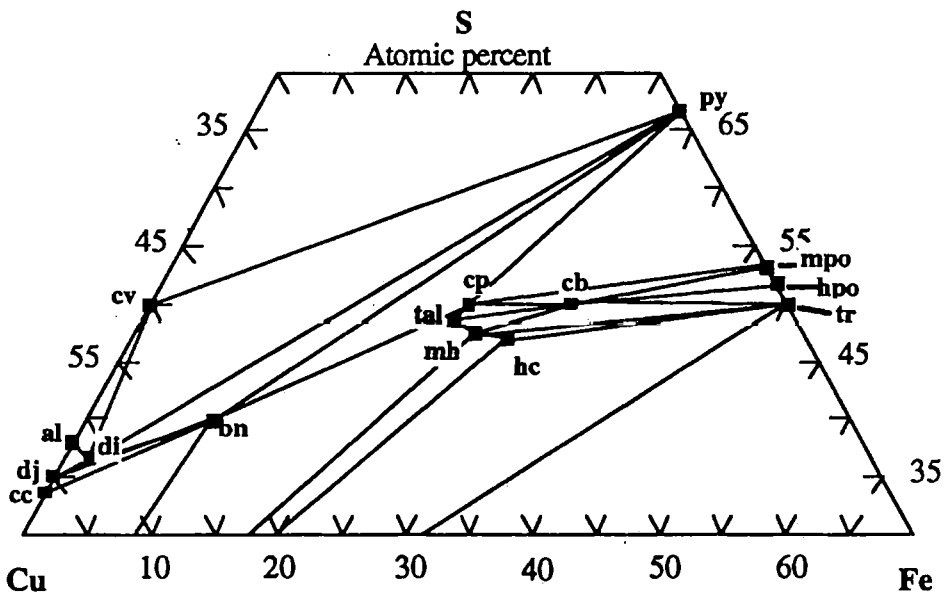

Fig. 4.4. Possible phase relations in the central portion of the Cu-Fe-S system at 25 ℃. After Vaughan and Craig, 1978.

Abbreviations in Figs. 4.3 and 4.4 = al, anilite; bn, bornite; cb, cubanite; cc, chalcocite; cp, chalcopyrite; cv covellite, di, digenite; dj, djurleite; hc, haycockite; hpo, hexagonal pyrrhotite; id, idaite; iss, intermediate solid solution; mh, mooihoekite; mpo, monoclinic pyrrhotite; py, pyrite; tal, talnakhite; tr, troilite

The *iss*, or isocubanite field is sulphur deficient relative to chalcopyrite. There is incomplete solid solution between the chalcocite-digenite-bornite phase and the *iss*. The *iss* is a distinct but

structurally similar phase to chalcopyrite (Barton, 1973). The pyrrhotite solid solution is a ternary extension of high temperature $Fe_{1-x}S$, the copper content of which is temperature dependent, exhibiting a maximum solubility of 4.5 wt.%, (Yund and Kullerud, 1966). The *iss* phase is unquenchable, except in the area close to the cubanite composition. Cabri (1973) divided the *iss* field into three quench zones: 1) Zone 1 quenches to chalcopyrite and/or a face centered cubic phase corresponding to the *iss* phase. 2) Zone 2 quenches to a primitive cubic phase that changes structure to a face centered cubic phase on heating to 200°C. 3) Zone 3, depending on the bulk composition, is characterized by either a primitive cubic phase and chalcopyrite, mooihoekite and a primitive cubic phase or a primitive cubic phase and one reflection at 6.2Å in the diffraction pattern. Two other phases, intermediate phases 1 and 2 are stable between the maximum thermal stability of the talnakhite (186°C) and the minimum thermal stability of the *iss* phase (520-525°C). Annealing to lower temperatures (>100°C), stabilizes talnakhite, mooihoekite, chalcopyrite and bornite. Two other phases stable at lower temperatures; cubanite and haycockite, were not synthesized by Cabri (1973). Therefore, an initial *iss* phase will decompose to an assemblage that consists of one or more mixtures of the Cu, Fe sulphides when allowed to equilibrate to lower temperatures. The bornite solid solution field (Fig. 4.3) contracts with decreasing temperature and eventually exsolves into two "roots", (digenite and bornite "roots") around 335°C (Yund and Kullerud, 1966). The phase relations at 25°C after Vaughan and Craig, (1978) are shown in Fig. 4.4.

4.4 Ni-Fe alloys and native copper

4.4.1 Binary phase relations in the Fe-Ni system

Phase relations in the Fe-Ni system are shown in Fig. 4.5 (Kubaschewski, 1982). The alloy awaruite identified in this work is formed under experimental conditions at 345°C and 52% Ni when γ-Fe-Ni undergoes eutectoid decomposition into α-Fe and awaruite. There are a limited number of environments that are so reducing that Fe-Ni alloys are stabilized.

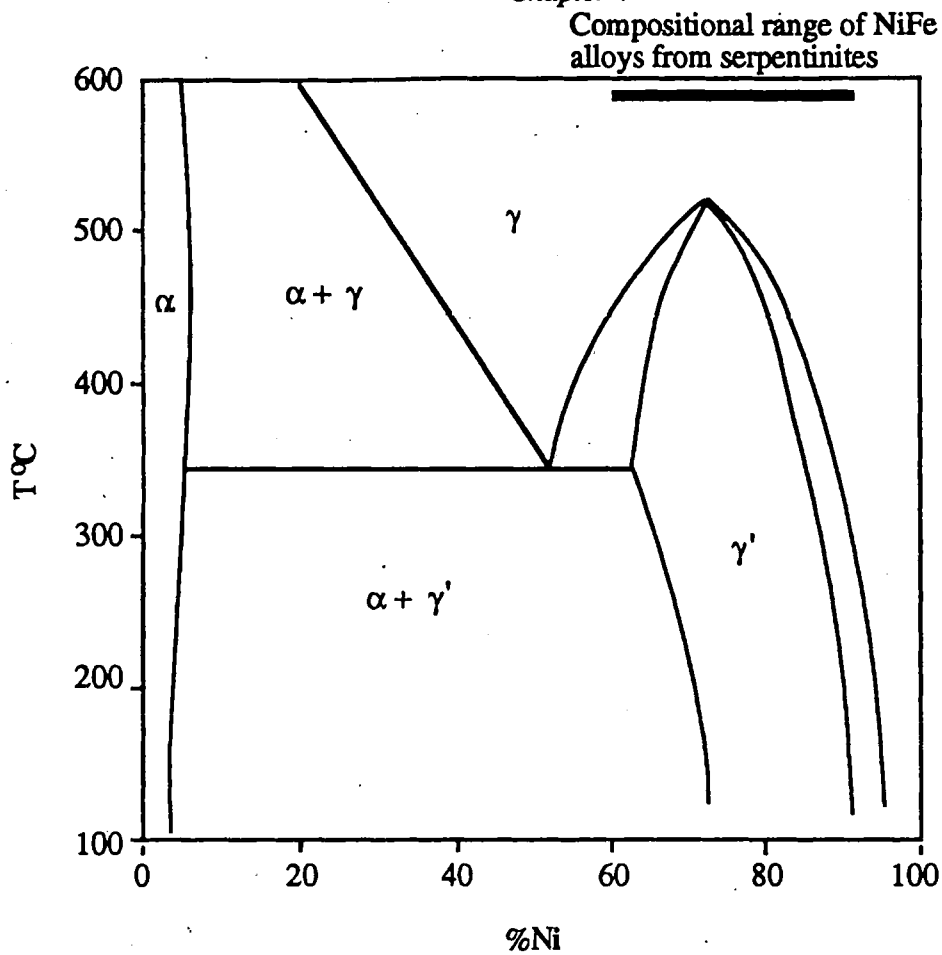

Fig. 4.5. One atmosphere phase diagram for the system Ni-Fe. αFeNi = kamacite, γFeNi = taenite, and γ NiFe = awaruite. Bar indicates the compositional range of Ni-Fe alloys from serpentinized peridotite. After Kubaschewski (1982).

Exsolution of kamacite from taenite is known in iron meteorites, whereas taenite-awaruite intergrowths have been reported in 'josephinite' (*e.g.* Botto and Morrison, 1976) and meteorites. Analyses of awaruite from natural assemblages in serpentinites indicate that awaruite coexisting with heazlewoodite only is richer in Ni (70-80 at.% Ni) than that coexisting with troilite-pentlandite (~62 at.% Ni) (Misra and Fleet, 1973).

Some temperature constraints may be derived from the composition of Fe-Ni alloys, (Botto and Morrison, 1976). Those serpentinites that contain taenite, *e.g.* Josephine Peridotite, were probably serpentinized in the stability field of antigorite. In contrast, lizardite/chrysotile serpentinites which are restricted to temperatures below 300°C (Evans *et al.*, 1976), contain awaruite or kamacite, but not taenite.

4.4.2 Native copper

Phase relations in the Cu-Fe, Cu-Co binaries indicate a solid miscibility gap from room temperature to 1000°C (Kubaschewski, 1982; Abrajano, 1984). A miscibility gap below 322°C in the Ni-Cu binary is supported by the absence of appreciable amounts of Ni in native Cu in serpentinites from the Zambales ophiolite (a maximum of 2.14 wt.% Ni) Abrajano (1984). Higher values of up to 4.34 wt.% Ni in native Cu reported by Abrajano (1984) are accompanied by higher sulphur in the electron microprobe analysis (3 wt.%) and possibly include a contribution from sulphide grains. Abrajano (1984) reports up to 4 wt.% Fe in native Cu and notes that on the basis of binary equilibrium relations at low temperatures (Kubaschewski, 1982), that true solution of Fe in native Cu is unlikely and ascribes these values to metastable solid solution or "true" occlusion of Fe in native copper.

4.5 Sulphide assemblages from the Shetland ophiolite

The following account considers the sulphides described in Chapter 3 from each lithology in terms of assemblages and compares them to the experimental phase relations discussed above.

4.5.1 Gabbros, dolerite dykes and plagiogranite

These lithologies carry a predominant assemblage of pyrrhotite-pyrite-marcasite-chalcopyrite±pentlandite-limonite-blaubleibender covelline-magnetite. Submassive sulphide mineralization from Mu Ness (Fig. 1.8) contains a different assemblage of euhedral pyrite-limonite-chalcopyrite-magnetite. Pyrrhotite ranges in composition from [$Fe_{9.17}S_{10}$] (hexagonal) to [Fe_7S_8] (monoclinic) varieties (Fig. 3.32). Monoclinic pyrrhotite is stable at temperatures <310°C (Craig and Scott, 1974), and the low Ni (0-0.38 wt.%) and low Cu (undetected) contents of pyrrhotites (Chapter 3) suggests that they are low temperature phases. Similarly all analysed Cu, Fe sulphides intergrown with pyrrhotite or pyrite are close to stoichiometric [$CuFeS_2$] and contain no detectable Ni, suggesting a low temperature paragenesis (Craig and Kullerud, 1969). A high temperature Fe-rich chalcopyrite has been produced experimentally, but stable stoichiometric chalcopyrite is thought to replace Fe-rich chalcopyrite during ageing of

fossil sulphide deposits (Oudin and Constantinou, 1984). The blebby texture of intergrown chalcopyrite and pyrrhotite (Fig. 3.1) is suggestive of a primary origin as an immisible sulphide liquid, but the compositions of these phases noted above, coupled with their intergrowth with greenschist facies silicate minerals (Chapter 2), suggests re-equilibration to low temperatures. Pyrite, intergrown with, and sometimes replacing, pyrrhotite and pyrite replacing secondary silicates, contain only traces of cobalt and have probably formed at low temperatures since primary pyrite, which exsolves from a *mss* at 400°C, is often Co-rich (Ewers and Hudson, 1972; Lachize *et al.*, 1991). Pyrite intergrown with chalcopyrite from submassive pyrite mineralization associated with primary euhedral magnetite from Mu Ness contains similarly low concentrations of Co (up to 0.17 at.% Co). Experimental phase relations indicate that the assemblage pyrite-chalcopyrite forms at temperatures <557°C (Craig and Kullerud, 1969). Euhedral, cobalt-rich pentlandite occurs as an intergrowth with pyrite which replaces hexagonal pyrrhotite in sheared gabbro suggesting a possible low temperature paragenesis. Blaubleibender covelline, which replaces chalcopyrite and limonite which replaces pyrite, magnetite and chalcopyrite are minerals typical of supergene weathering.

4.5.2 High-level pyroxenites

High-level pyroxenites carry an assemblage of pentlandite-monoclinic pyrrhotite-pyrite-chalcopyrite-violarite-niccolite-cobaltite-magnetite-'ferritchromit'-ilmenite. The natural occurrence of the assemblage pentlandite-monoclinic pyrrhotite-pyrite-chalcopyrite in ultramafic and mafic rocks is often considered to result from the subsolidus decomposition of a high-temperature monosulphide solid solution (Craig and Kullerud, 1969). However, some features of the textural relations of the sulphide phases from the high-level pyroxenites, coupled with their mineral chemistry, is indicative of formation at low temperatures. Firstly, the morphology and chemistry of pyrite is atypical of pyrite that has crystallized from a high temperature *mss* (Ewers and Hudson, 1972). The pyrite occurs as large spongy grains replacing altered silicate (Fig. 3.5) and contains <1 at.% Co, and so is considered to have formed at low temperatures. Furthermore, the composite monoclinic pyrrhotite-pentlandite intergrowths often occur as small (10-40μ) grains intergrown with secondary carbonates and serpentine and are often closely

associated with niccolite and cobaltite (Fig. 3.6), these two arsenides are typically formed during the serpentinization of peridotites (*e.g.* Panayiotou, 1986). Pentlandite from the high level pyroxenites contains 29.7-30 at.% Ni. Graterol and Naldrett (1971) and Misra and Fleet (1973) determined the compositional variations of natural pentlandites in a variety of sulphide assemblages. The average value of 29.8 at.% Ni in this study is more Ni-rich than reported for their assemblages containing pentlandite-monoclinic pyrrhotite and pentlandite-monoclinic pyrrhotite-pyrite, or for the assemblage monoclinic pyrrhotite-pentlandite reported by Shiga (1987) (maximum of 26.2 at.% Ni in pentlandite) and suggests disequilibrium in the high-level pyroxenite assemblage.

4.5.3 Cumulate pyroxenites

Two main sulphide assemblages have been recognized. The first consists of pentlandite-pyrrhotite-chalcopyrite-bornite-magnetite-chrome spinel-'ferritchromit' and is found in fresh pyroxenites where the sulphide aggregates occur interstitially to pyroxene crystals (Fig. 3.9). The second assemblage, which consists of pentlandite-monoclinic pyrrhotite-pyrite-marcasite-chalcopyrite-heazlewoodite-millerite-godlevskite-chalcocite-bornite-digenite-covellite-minor native Cu±orcelite±maucherite occurs in more altered pyroxenites, commonly where sulphide aggregates are intergrown with serpentine. As discussed briefly in Chapter 3, the pentlandite-bornite-chalcopyrite-magnetite bleb interstitial to clinopyroxene from a fresh pyroxenite (Fig. 3.9) is reminiscent of the interstitial texture commonly seen in Ni-Cu-Fe sulphides in magmatic ores, which are widely believed to have formed formed from a Cu-rich sulphide liquid and monosulphide solid solution (*mss*) phase at magmatic temperatures (*e.g.* Craig and Kullerud, 1969). However, the coexistence of chalcopyrite and bornite in this sample of pyroxenite is consistent with phase relations in the Cu-Fe-S system at temperatures <100°C (Cabri, 1973). Octahedrally oriented intergrowths of chalcopyrite in pentlandite occur in this bleb (Fig. 3.12) and lamellae of chalcopyrite also occur in pentlandite intergrown with serpentine. Similar intergrowths have also been noted in sulphides in intra-continental lherzolite massifs, (Garuti *et al.*, 1984; Lorand, 1989) and from the ultramafic zone of the Zambales ophiolite (Abrajano and Pasteris, 1989). Abrajano and Pasteris (1989) notes that this texture is atypical of magmatic ores

and that formation of such Cu-Fe sulphide lamellae by exsolution is not feasible because there is too much Cu in the bulk sulphide aggregate (pentlandite + Cu-Fe sulphide) than can be accommodated in the pentlandite structure.

The composition of pentlandite intergrown with chalcopyrite pyrrhotite and heazlewoodite ranges from 23.2 at.% Ni to 30.5 at.% Ni compared to 24.9-29.8 at.% Ni in the assemblage pentlandite-monoclinic pyrrhotite reported by Graterol and Naldrett (1971). Intergrain differences of up to 3.4 at.% Ni in pentlandite suggests local dis-equilibrium. Heazlewoodite which replaces pentlandite contains an average of 2.2 at.% Fe and is considered a low temperature phase since, from experimental work, the solubility of Fe in heazlewoodite decreases from about 11 at.% at 600°C to 3 at.% Fe at 300°C (Misra and Fleet, 1973). Heazlewoodite is sometimes replaced by godlevskite and millerite (Ixer and Prichard, 1989). As noted in section 4.2, Misra and Fleet (1973) omitted godlevskite from their low-temperature phase diagram (Fig. 4.2) on the basis of its replacement by millerite in samples from Noril'sk, and the common occurrence of the assemblage pentlandite-millerite-heazlewoodite which suggested to them that godlevskite was unstable at low temperatures. However, the relatively common occurrence of godlevskite in both pyroxenites and dunites from the Shetland ophiolite would suggest that in this case it is a low temperature equilibrium phase. The zonal sequence of Cu-minerals chalcopyrite-bornite-chalcocite-digenite-covellite-(native Cu) seen in individual grains hosted in altered silicate interstitial to pyroxene is similar to the oxidation sequence of chalcopyrite-bornite-digenite (chalcocite) and covellite observed in black smoker chimneys from modern sea-floor sulphide deposits (Oudin and Constantinou, 1984). The alteration sequence of these Cu-minerals in the Shetland samples is therefore thought to be due to oxidative supergene processes. Pyrite intergrown with pyrrhotite contains <0.3 at.% Ni with no detected Co and probably formed at low temperature (Ewers and Hudson, 1972). Fine grained pyrite intergrown with marcasite which replaces pyrrhotite is considered to result from supergene alteration as is the replacement of chalcopyrite by limonite.

4.5.4 Wehrlitic dunite, cumulate dunite, and dunite pods

These lithologies contain the following assemblages; pentlandite-troilite-native Cu; pentlandite-awaruite-native Cu; pentlandite-heazlewoodite-awaruite-native Cu-orcellite-Ni-Cu antimonide; pentlandite-heazlewoodite-millerite-awaruite-chalcopyrite-chalcocite-native Cu-orcellite-breithauptite-Ni-Cu antimonide. A dunite pod from the Cliff locality carries a different assemblage of pentlandite-heazlewoodite-millerite-godlevskite-chalcocite-native Cu-orcellite-breithauptite-Ni-Cu antimonide. These Ni and Ni, Fe sulphide assemblages are generally consistent with the low temperature ternary relations in the Fe-Ni-S system (Misra and Fleet, 1973) (Fig. 4.2).

Pentlandite-troilite has been found in only one sample out of 23 which include a wehrlitic dunite, cumulate dunites and dunite pods. The caries texture of the troilite (Fig.3.19), suggests that it is undergoing replacement (Chapter 3). The pentlandite intergrown with this troilite contains 19.6 at.% Ni and is the most Ni-poor pentlandite that has been analysed during this study. Misra and Fleet (1973) report the Ni-poor limit of pentlandite will be defined by the limiting composition of pentlandite in the assemblage troilite-pentlandite (they suggest 20 at.% Ni). The pentlandite composition reported in this study is therefore in agreement with Misra and Fleet's low temperature equilibrium composition of pentlandite coexisting with troilite. Abrajano and Pasteris (1989), report similarly low Ni-pentlandite (17 at.%) coexisting with troilite in the mafic zone of the Zambales ophiolite.

Pentlandite-awaruite occurs in partially serpentinized cumulate dunite (Chapter 3). As discussed in section 4.4.1, the formation of awaruite in all assemblages listed above is probably restricted to temperatures below 300°C. As noted in Chapter 3, there are apparently two generations of awaruite. The first occurrence is as intergrowths with pentlandite in cracks developed in pentlandite along octahedrally oriented cleavage planes. The second occurence is as 'anisotropic' awaruite which replaces heazlewoodite. Both the isotropic and 'anisotropic' alloys are compositionally similar (Fig. 3.35) and contain traces of S (0.88 and 1.07 at.% respectively). There are no compositional trends in awaruite chemistry between the different awaruite-bearing assemblages. Lundquvist (1947) report extremely low solubilities of S in Fe and Ni (0.06 at.%) and Misra and Fleet (1973) report only up to 0.5 at.% S in Fe, Ni alloy

synthesized in low-temperature experiments. The higher trace S contents observed in Shetland awaruite analyses may possibly be due to remnant trace S from precursor heazlewoodite or pentlandite which both alter to awaruite.

The low (average 0.2 at.%) Fe content of heazlewoodite grains in dunites is consistent with formation at temperatures <300°C (Misra and Fleet, 1973). Textural evidence (Chapter 3) suggests that godlevskite replaces heazlewoodite and so must have formed at similarly low temperatures to heazlewoodite. This is substantiated by the low Fe content of godlevskite (0.03 at.%) from the assemblage; pentlandite-heazlewoodite-millerite-godlevskite from a dunite pod in harzburgite, Cliff, which precludes its formation at high temperatures since the experimental study of Misra and Fleet (1973), show that the solubility of Fe in this phase is 8.5 at.% at 600°C and close to 6 at.% at 400°C. Kullerud and Yund (1962) showed that godlevskite was stable down to at least 200°C in the binary Ni-S system. The chemistry of pentlandite in this godlevskite-bearing assemblage from Cliff (pentlandite-heazlewoodite-millerite-godlevskite) shows intragrain disequilibrium with Ni contents ranging from 28.57-33.95 at.% Ni. This is in contrast to the narrow range of Ni contents in pentlandite of 34.5-34.9 at.% Ni in natural millerite-heazlewoodite-pentlandite (± godlevskite) reported by Misra and Fleet (1973). Nevertheless, the composition of the pentlandite in the assemblage pentlandite-heazlewoodite-millerite-godlevskite from the Cliff sample which contains the most Ni-rich pentlandite analysed from Unst in this study, is in agreement with the work of Graterol and Naldrett (1971), Harris and Nickel (1972) and Misra and Fleet (1973) who note that the most Ni-rich pentlandite occurs in the Ni-rich assemblage pentlandite-heazlewoodite-millerite (± godlevskite). The predominance of native Cu over and above Cu-Fe sulphides in the dunitic lithologies noted in Chapter 3 is common in serpentinites (*e.g.* Abrajano and Pasteris, 1989; Pederson, 1993) and has been ascribed to the desulphidization of precursor Cu-sulphide during serpentinization. The low Ni and Fe contents of native Cu from dunites from Unst is consistent with their formation at low temperatures (section 4.4.2).

4.5.5 Basal thrust

Talc-carbonate rocks from the basal thrust contain an assemblage of pentlandite-hexagonal/monoclinic pyrrhotite-pyrite-marcasite-chalcopyrite-violarite-mackinawite-vallerite-niccolite-cobaltite-magnetite-'ferritchromit'. Pyrrhotite compositions are close to hexagonal pyrrhotite but apparently extend to more sulphur-deficient compositions (Fig.3.32). The natural assemblage hexagonal pyrrhotite-pentlandite was not recognized in the compilation of natural pentlandite assemblages of Misra and Fleet (1973). Whether violarite in this assemblage is considered part of a low temperature equilibrium assemblage depends upon the different interpretations of the low temperature phase relations in the Fe-Ni-S system. For example, violarite is considered a stable phase in the low temperature Fe-Ni-S ternary by Graterol and Naldrett (1971), whose tie lines between violarite-polydymite solid solution and pentlandite, prevents the stable coexistence of pyrite and millerite proposed by Misra and Fleet (1973), (Fig. 4.2). Pyrite, marcasite, mackinawite and vallerite are all thought to be probable supergene phases (R. Ixer, *pers. comm.*).

4.6 Bulk base-metal content of sulphide aggregates

The bulk base-metal content of sulphide aggregates from the Shetland ophiolite have been calculated to ascertain whether any systematic variations with lithology can be recognized that are compatible with a magmatic fractionation. The calculated base-metal ratios are then compared with base-metal ratios of sulphide aggregates from other weakly mineralized ultramafic rocks.

Estimates of the bulk Ni, Fe, Cu and S content of the sulphide-magnetite aggregates from different lithologies of the Shetland ophiolite complex and their base-metal ratios are given in table 4.2. The calculations are based on estimates of the modal abundances, coupled with microprobe analyses of the sulphide, spinel (magnetite/'ferritchromit') plus the other minor base-metal-bearing opaque phases in the assemblages described in Chapter 3.

With reference to table 4.2, there is an overall decrease in the ratio Ni/(Ni+Fe) of sulphide aggregates on passing stratigraphically upward from dunites (0.49) to pyroxenite (0.30) and gabbro (0.01). Conversely Cu/(Cu+Ni) ratios show a concommitant increase,

dunite(0.14), pyroxenite (0.32) and gabbro (0.91). These trends are reflected by changes in the sulphide mineralogy with lithology, from pentlandite and heazlewoodite dominated assemblages in dunites, to pentlandite-pyrrhotite-chalcopyrite assemblages in pyroxenites and pyrrhotite-pyrite-chalcopyrite assemblages in gabbro (Chapter 3). Cu:Ni ratios calculated for dunite and pyroxenite-hosted sulphide aggregates are similar to those calculated by Lord (1991) from whole-rock XRF data from the stratigraphically lowest pyroxene-rich cumulates that are exposed in the ophiolite.

Lithology	*Assemblage*	*Bulk sulphur wt%*	*Ni/Fe*	*Ni/(Ni+Fe)*	*Cu/Ni*	*Cu/(Cu+Ni)*	*Cu/Ni Lord (1991)*
Talc-carbonate	Po-Pn-Viol-Cpy-Fc-Gf	34.27	0.31	0.24	0.05	0.05	
Cliff-dunite pod	Hz-Pn-Mt-Ml-Gd-Br-Cu-Cc	21.13	1.89	0.65	0.10	0.09	
Cumulate dunite fresh	Pn-Hz-Mt-Aw-Cu-Br*	22.13	0.64	0.39	0.18	0.15	0.12-0.35
Cumulate dunite serpentinized	Hz-Pn-Mt-Aw-Cu-Cpy-Cc-Br*	17.54	0.81	0.45	0.21	0.17	
Pyroxenite	Pn-Po-Cpy-Py-Hz-Ml-Mt-Bn-Cc-Cv-Cu	31.90	0.43	0.30	0.46	0.32	0.52
Gabbro	Po-Py-Cpy-Mt-Cv-Mar-Pn	37.90	0.013	0.01	9.50	0.91	

Table 4.2. Estimates of the bulk chemistry of sulphide/opaque oxide intergrowths from the Shetland ophiolite. Abbreviations for minerals as in table 4.1.

The changes in the bulk sulphide chemistry with lithology listed in table 4.2 is similar to the correlation between the class of host-rock and the Cu/(Cu+Ni) ratio of the ore noted by Naldrett (1973) in his classification of Ni-sulphide deposits. The Cu/(Cu+Ni) ratio tended to increase from ultramafic to less mafic host rocks (Naldrett, 1973). Hoatson and Keays (1989) noted that the Cu/(Cu+Ni) ratio was a useful fractionation index, increasing from ultramafic to mafic rocks and towards the main layer of sulphide mineralization in the ultramafic sequence in the Munni Munni layered intrusion, Western Australia. These fractionations occur because Cu accumulates in the melt during fractional crystallization whereas Ni is removed by crystallizing olivine. As a result, late sulphides formed during fractional crystallization of a basic magma will be Cu-rich. The changes in the bulk sulphide chemistry with stratigraphic height in the Shetland ophiolite is therefore probably a reflection of magmatic fractional crystallization processes.

The low average Cu/(Cu+Ni) ratio of sulphide aggregates in dunites from the Shetland ophiolite (0.12) is similar to ratios from other weakly mineralized serpentinites from continental

intrusions, ($3*10^{-4}$-0.13) and also to weakly mineralized serpentinized dunites in the Zambales ophiolite, Philippines (0.17) (table 4.3). Of those ophiolite-hosted deposits with Cu/(Cu+Ni) ratios >0.5 in table 4.3, the two ultramafic hosted occurences are demonstrably of hydrothermal origin whereas the other is magmatic, but mafic-hosted, and therefore will be expected to exhibit a higher Cu/(Cu+Ni) ratio due to its more evolved composition.

Mineralization	*Host lithology*	*Cu/(Cu+Ni)*	*Proposed genesis*	*Reference*
Banded magnetite and sulphide at periphery of podiform chromite bodies	Podiform chromite, Tsangli, Eritria, Greece	0.78	Hydrothermal	Economou and Naldett (1984)
Disseminated sulphide-rich stratiform layer	Gabbro, Haylayn block, Semail ophiolite, Oman	0.61	Magmatic	Lachize *et al.* (1991)
Lenses/veins of massive ore + disseminated ore	Shattered Serpentinite, Limassol Forest, Troodos ophiolite, Cyprus	>0.5	Hydrothermal	Panayiotou (1986)
Densely and sparsely disseminated ore	Serpentinized and chloritic rocks, ultramafic intrusion, Zimbabwe	0.13	Serpentinization and talc-carbonate alteration	Viljoen *et al.* (1976)
Disseminated Ni-Fe sulphides	Serpentinized ultramafic sills, Honeymoon Well, W.A.	$0.2\text{-}3*10^{-4}$	Serpentinization and talc-carbonate alteration	Donaldson and Bromley (1981)
Disseminated Ni-Fe sulphides	Serpentinized ultramafic intrusion, Black Swan, W.A.	0.03	Serpentinization and talc-carbonate alteration	Groves *et al.* (1974)
Disseminated Ni-Fe sulphides	Serpentinized dunites, Zambales ophiolite	0.17	Serpentinization	Calculated after Abrajano and Pasteris (1989)

Table 4.3. Cu/(Cu+Ni) ratios of sulphide aggregates from weakly mineralized ultramafic and mafic rocks.

4.7 Activity-activity diagrams and low temperature paragenesis of Ni-Fe sulphides and Ni-sulphides

4.7.1 Introduction

An important conclusion from the study of Fe-Ni sulphides in weakly mineralized ultramafic rocks is that the different sulphide mineral assemblages are a function of the different silicate alteration reactions in the host rock (Eckstrand, 1975). For example serpentinization of olivine in a dunite which may be represented by the equation;

(i) $6Fe_2SiO_4 + 7H_2O = 3Fe_3Si_2O_5(OH)_4 + Fe_3O_4 + H_2$

induces a reduction in the associated fluid phase (see Fig. 4.6). This is reflected by the fact that Ni-Fe alloys are found in partially serpentinized peridotites, commonly without any associated sulphide. Conversely, in carbonate bearing metaperidotites, the equilibria controlling oxygen fugacity can be represented by the equation;

(ii) $6FeCO_3 + O_2 = 2Fe_3O_4 + 6CO_2$.

Under such oxidizing conditions high sulphur minerals such as millerite were noted by Eckstrand (1975). High grade nickel sulphide deposits are self buffered with respect to oxygen and sulphur, therefore remaining largely unaffected by silicate alteration reactions. In a more elaborate treatment of sulphide and silicate alteration reactions in the ultramafic portion of part of the Zambales ophiolite, Abrajano and Pasteris (1989) explained spatial variations in fO_2 without recourse to carbonate-rich fluids, by variation in, i) silica activity (governed by the initial olivine:pyroxene ratio in the protolith. ii) Fe:Mg ratio in the protolith, (this has a compensating effect on i)) and iii) water:rock ratio.

In this section the nickeliferous opaque mineral assemblages from the dunites from Unst are qualitatively analysed using the thermochemical methods of Eckstrand (1975) and Abrajano and Pasteris (1989). The reaction boundaries for the isothermal (127°C) fO_2 *vs.* fS_2 diagram in Fig. 4.7 were taken from Eckstrand (1975) and Abrajano and Pasteris (1989). The assumption is made that the sulphide minerals within a thin section represent equilibrium assemblages and are compatible with published experimental Fe-Ni-S phase equilibria studies and studies of natural assemblages (section 4.2). The shaded area of the diagram in Fig. 4.7 delineates the

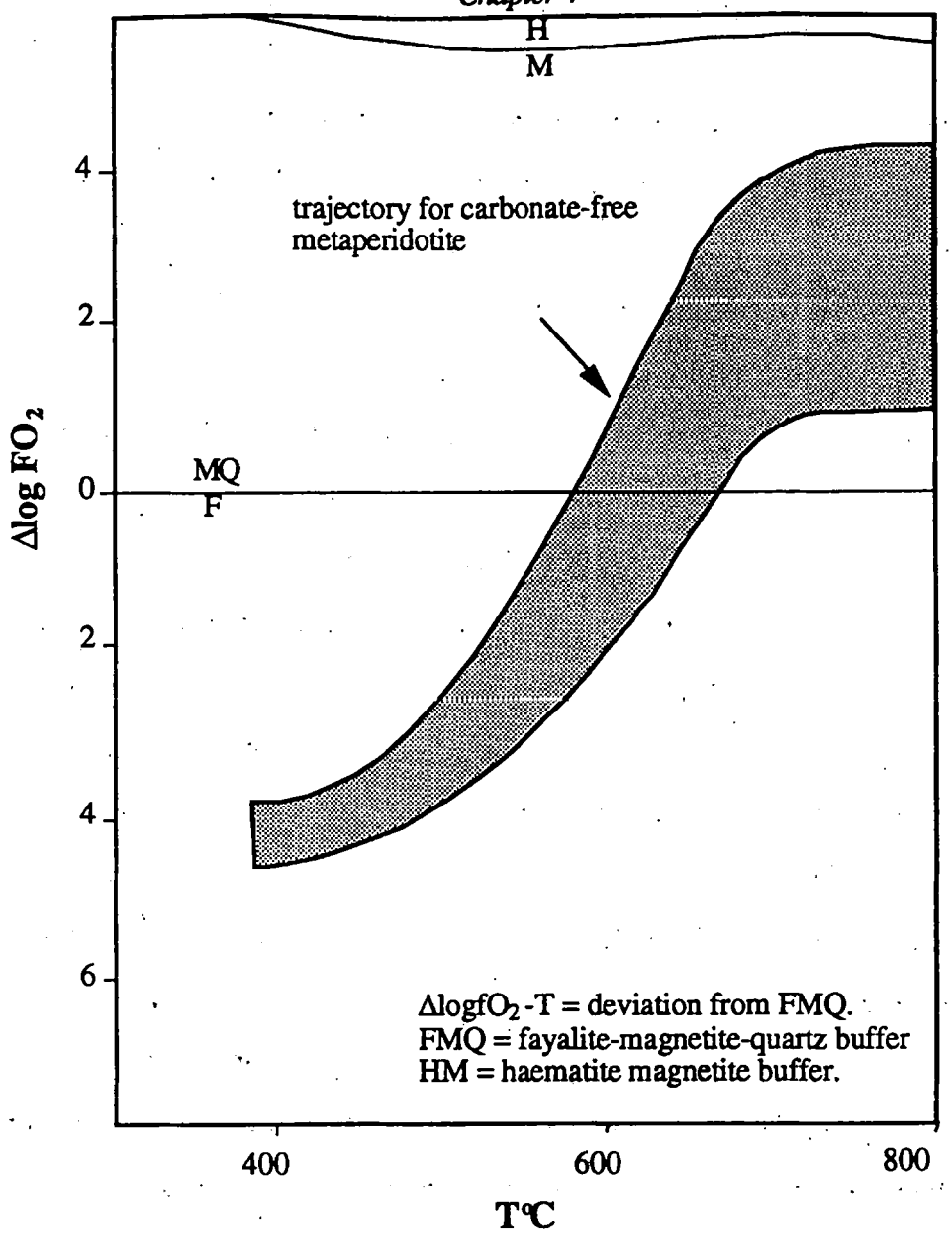

Fig. 4.6. Isobaric, $\Delta \log fO_2$-T projection showing the trajectory followed by fluids in metaperidotites during metamorphism, P=2kb (Frost, 1985).

stability field for magnetite since this phase occurs intergrown with sulphides in all the observed sulphide assemblages hosted in dunites from Unst. The approximate stability field of native Cu is also shown on Fig. 4.7. The stability field for godlevskite is omitted from Fig. 4.7 since there is some debate as to whether it is stable at low temperatures (Naldrett *et al.*, 1972; Misra and Fleet, 1973). However, Frost (1985) notes that, if shown, the stability field for this phase would occupy a narrow band between the stability fields of heazlewoodite and millerite.

4.7.2 Application to dunites from the Shetland ophiolite

In the Shetland dunites the proposed sulphide paragenesis is; 1) pentlandite-troilite-native Cu-magnetite; 2) pentlandite-awaruite-native Cu; 3) pentlandite-heazlewoodite-awaruite-native Cu and 4) pentlandite-heazlewoodite-awaruite(±millerite)-native Cu-magnetite. These assemblages seem to broadly correlate with differing degrees of serpentinization of the host dunites. Hence assemblage 1) occurs in dunite with substantial relict olivine, as does assemblage 2), whereas assemblages 3) + 4) are commonly developed in completely serpentinized dunite. A different assemblage consisting of pentlandite-heazlewoodite-millerite-godlevskite-magnetite-chalcocite-minor native Cu, occurs in a partially serpentinized dunites from the Cliff locality.

Fig. 4.7 shows that pentlandite-awaruite-native Cu-magnetite must represent the most reduced assemblage, whereas heazlewoodite-pentlandite-awaruite-native Cu (±millerite) from dunites with minor relict olivine, is stable at higher sulphur and oxygen fugacities. Frost (1985) noted that serpentinization will induce a strong zone of reduction (Fig. 4.6), and that once olivine is eliminated from the rock, the oxygen fugacity associated with that rock will increase markedly. This suggests that native metals and Ni-Fe alloys should occur in peridotites that have been only partially sepentinized (Frost, 1985), which is in agreement with the observations of Chamberlain *et al.* (1965) and Eckstrand (1975). Their absence in completely serpentinized rocks was explained by Ashley (1975) as due to alteration of awaruite to magnetite. However, in the

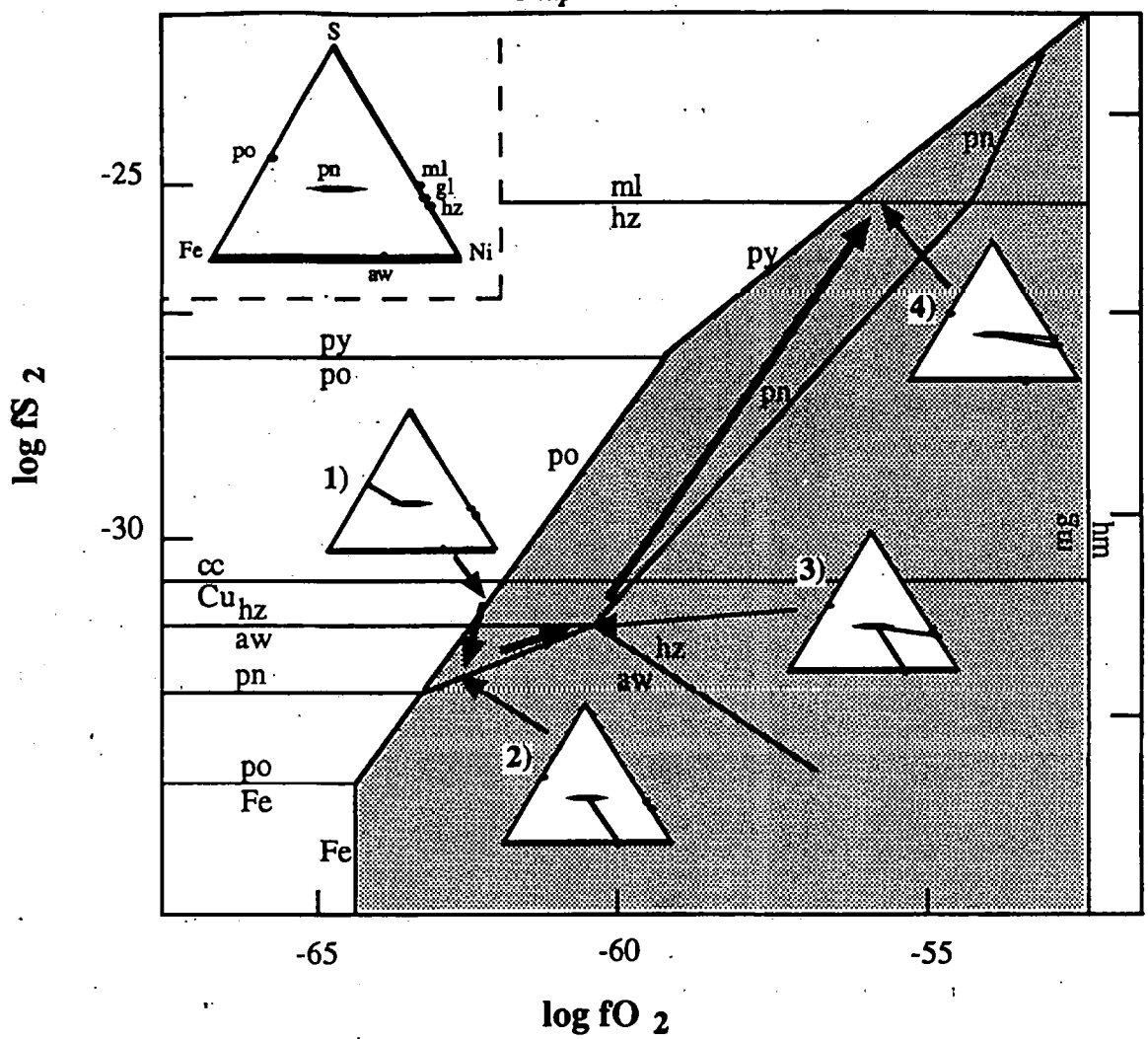

Fig. 4.7. Plot of $\log fO_2$ vs. $\log fS_2$ showing different sulphide assemblages hosted in dunites of the Shetland ophiolite and possible evolution of these assemblages (see text for explanation).

Shetland ophiolite, awaruite appears to be stable in both partially and completely serpentinized dunite, an observation apparently at odds with the above discussion. As noted in Chapter 3, there are two generations of awaruite in Unst serpentinites. The first occurs in partially serpentinized dunites intergrown with magnetite along octahedrally orientated fractures in pentlandite, whereas the second occurrence is as alteration margins to heazlewoodite in completely serpentinized dunites. The reason for the apparent stability of awaruite in both partially and totally serpentinized dunites in the Shetland ophiolite is unclear. The relatively large stability field of native Cu shown in Fig. 4.7 is generally consistent with its widespread occurrence in serpentinized dunites from Unst. However, the presence of native Cu in the

relatively 'oxidized' assemblage pentlandite-heazlewoodite-millerite-godlevskite-chalcocite from Cliff would apparently suggest disequilibrium.

The assemblage; pentlandite-heazlewoodite-millerite-godlevskite-magnetite-chalcocite-minor native Cu from the Cliff locality differs from the sulphide assemblages from other dunite pods and cumulate dunites from the complex. Firstly, no awaruite occurs after pentlandite or heazlewoodite at Cliff suggesting more oxidizing conditions than those that prevailed in the cumulate dunites. Secondly, the presence of minor native Cu in this relatively 'oxidized' assemblage would apparently suggest that it is a late phase in the paragenesis. One possible explanation for these differences is that the Cliff dunites were serpentinized under conditions of higher pCO_2 compared to other dunite pods and cumulate dunites. Such oxidizing conditions would inhibit the formation of awaruite. It is noted that the presence of antigorite serpentine in lithologies close to basal thrust is consistent with serpentinization under conditions of higher pCO_2.

4.8 Serpentinization and talc-carbonate alteration; models for the redistribution of sulphur and metals

The following section considers the flux of sulphur and base-metals between sulphide and silicate phases during the serpentinization and talc-carbonate alteration of the ultramafic portion of the ophiolite.

4.8.1 Serpentinized dunite pods and cumulate dunite

The replacement of pentlandite by heazlewoodite is almost ubiquitous in the ultramafic portion of the ophiolite. If is assumed that the replacement of pentlandite by heazlewoodite is isochemical with respect to sulphur;

i.e; $Fe_{4.5}Ni_{4.5}S_8 + 7.5Ni \rightarrow 4Ni_3S_2 + 4.5Fe$ (4.7)

Then 1 mole of pentlandite is replaced by 4 moles of heazlewoodite. Given the molar volumes of pentlandite (163.8 moles/cc) and heazlewoodite (40.95 moles/cc), then, if the observed heazlewoodite±pentlandite aggregates represent the original volume of the pentlandite grain before replacement, the molar volume of pentlandite/molar volume of heazlewoodite will

be 4. Since 163.8/40.95=4, then this substantiates the above reaction with respect to sulphur and suggests that there has been no volume increase or decrease within composite pentlandite-heazlewoodite aggregates. Reaction 4.7 requires that an extra 7.5 moles of nickel are required from a source other than pentlandite, whereas 4.5 moles of iron is liberated by the reaction. Nickeliferous phases that could contribute nickel to reaction 4.7 include olivine (0.15-0.45 wt.%) which when serpentinized may release Ni, and serpentine (0.09-0.17 wt.%). Magnetite (~1wt.%) is not considered a likely donor of Ni since much of the nickeliferous magnetite that is intergrown with pentlandite and heazlewoodite could itself have formed from the iron liberated from reaction 4.7, and may thus be co-genetic with heazlewoodite. Similarly, awaruite, which often forms as a replacement of heazlewoodite is not considered a likely donor of Ni to heazlewoodite.

4.8.2 Talc-carbonate sulphide assemblage from the basal thrust

The sulphide assemblage of serpentinized harzburgites from the Cliff locality consists of sparse, disseminated pentlandite-heazlewoodite-millerite-Cu sulphides-native Cu, (Ixer and Prichard, 1989). This differs from the pentlandite hexagonal/monoclinic pyrrhotite-pyrite-marcasite-chalcopyrite-violarite-mackinawite-vallerite-niccolite-cobaltite-magnetite-'ferritchromit' observed in talc-carbonate rock. As discussed in Chapter 2, the bulk rock chemistry of talc-carbonate altered rocks from the basal thrust is broadly consistent with their derivation from a harzburgitic protolith. It is possible that the sulphide-arsenide assemblage in the talc-carbonate lithologies developed in response to the alteration of harzburgite to talc carbonate rock. Textural evidence for this hypothesis includes the occurrence of pyrrhotite and niccolite as inclusions in secondary magnesite grains and the common replacement of 'ferritchromit' by hexagonal pyrrhotite (Fig. 3.29).

The formation of secondary Fe-sulphide in talc-carbonate rock has been documented by Donaldson (1981). During total talc-carbonate alteration, talc and magnesite is produced and nickel is redistributed to sulphide, with the formation of some Fe-sulphide, by the following reaction (Donaldson, 1981):

$(Mg_{2.815}Fe_{0.08}Ni_{0.005})Si_2O_5(OH)_4 + 0.826(Mg_{0.95}Fe_{0.05})CO_3$
Antigorite Magnesite

$+ 0.087(Fe_{0.970}Ni_{0.03})O.Fe_2O_3 + 0.004Ni_3S_2 + 1.434\ CO_2 + 0.12\ S$
Magnetite Heazlewoodite

$= 0.5(Mg_{2.900}Fe_{0.090}Ni_{0.010})Si_4O_{10}(OH)_2$
Talc

$+ 0.04(Fe_{0.97}Ni_{0.03})O.Fe_2O_3 + 2.26(Mg_{0.95}Fe_{0.05})CO_3$
Magnetite Magnesite

$+ 0.003(Ni_{4.5}Fe_{4.5})S_8 + 0.013Fe_7S_8 + 1.5\ H_2O + 0.127\ O_2$
Pentlandite Pyrrhotite

The quantity of iron sulphide produced in this reaction varies with the amount of magnetite consumed and the amount of sulphur introduced. In sulphide-free talc-carbonate rock, where magnetite is not present, talc contains all the available nickel and about 30% of the total iron (Donaldson, 1981). The remaining iron is partitioned into magnesite which contains about 10% FeO. Donaldson (1981) argued that up to 30% of sulphide nickel in ores averaging 0.7% nickel is of metamorphic origin and that in talc-carbonate ores this proportion may be higher. Iron sulphides of metamorphic origin formed up to 20% of the total sulphide fraction in talc carbonate altered disseminated nickel ores.

The partitioning of Cr, Ni, Fe and S between the secondary silicates and opaque minerals in a sample of talc-carbonate rock from the Shetland ophioite is considered below. The distribution of Fe, Ni and S in this sample of talc-carbonate rock is given in table 4.4. Table 4.4 shows that the majority of Fe is contained within magnesite, talc and dolomite with the remainder partitioned into magnetite, chromite and Fe-bearing sulphides. Talc contains about half the Ni budget of the rock and pentlandite and antigorite contain the majority of the remaining Ni.

Mineral	*V*	*(ρ)*	*Wt(g)*	*Wt.% miner -al*	*Wt. % Cr*	*Wt. % Ni*	*Wt% Fe*	*Wt. % S*	*ppm Cr*	*ppm Ni*	*ppm Fe*	*ppm S*
Magnesite	45	3	1.350	46.33	0	0	8.86	0	0	0	41048	0
Dolomite	3	2.85	0.086	2.95	0	0	2.25	0	0	0	664	0
Antigorite	12	2.6	0.310	10.64	0.22	0.14	6.87	0	234	149	7310	0
Quartz	4.5	2.65	0.180	6.18	0	0	0	0	0	0	0	0
Talc	35	2.75	0.963	33.05	0	0.21	2.60	0	0	694	8593	0
Pyrrhotite	0.065	4.6	0.003	0.10	0	0.12	59.8	39.24	0	1.2	598	392
Pentlandite	0.065	5	0.003	0.10	0	30.92	33.5	33.45	0	309	335	335
Violarite	0.02	4.79	0.001	0.03	0	35.3*	15.8	42.4*	0	106	47	127
Magnetite	0.1	5.2	0.005	0.17	0	0	98	0	0	0	1666	0
'ferritchromit'	0.25	5.09	0.013	0.45	38.1	0	44.7	0	1715	0	2012	0
Total									1949	1259	62273	854
									2811†	2343†	n.d.	1150‡

Table 4.4. Whole-rock Cr, Ni, Fe and S determinations for a sample of talc carbonate rock from the probe analysis of the constituent minerals compared to the whole-rock values determined by XRF (Cr, Ni and Fe)† and chemical extraction by Kiba reagent (S)‡.*Violarite compositional data from Shiga (1987). v = estimated volume of mineral in rock (cm^3), ρ = density of mineral (g/cm^{-3}). n.d.= not determined.

The total calculated Ni and S contents of the rock are greatly affected by the amount of Ni-sulphide present in the rock The volume percentages of the sulphide minerals are difficult to ascertain due to their sparse, fine-grained, disseminated occurrence and this uncertainty has a large effect on the calculated whole-rock Ni and S values. For example one volume percent pentlandite will contribute approximately 3000 ppm S to the whole-rock S content. The apparent shortfall in the whole-rock calculated Ni and S contents in table 4.4 compared to those values obtained by XRF (Ni) and wet chemical analysis (S) is therefore likely due to the underestimate of the % volume and proportions of the Ni-Fe and Fe sulphides.

If sulphur was introduced from the underlying metasediments and combined with Ni and Fe released from the silicate minerals during talc-carbonate alteration of a harzburgite protolith then it would be expected that the whole rock sulphur contents of talc carbonate rocks would be significantly higher than those of associated harzburgites. Consideration of whole rock sulphur values along the basal thrust (Chapter 6) reveals some locallized higher concentrations of sulphur in this zone (up to 1150ppm, average 266ppm S, n=14) over and above those values for harzburgite (98-150ppm S, n=3), the assumed protolith to the talc-carbonate rock. This sulphur could have combined with Ni and Fe released during the breakdown of silicate minerals during

talc-carbonate alteration to form the metamorphic sulphide assemblage seen in talc-carbonate rocks from the basal thrust.

Mobilization of sulphide in carbonate bearing portions of serpentinites has been reported by, *e.g.* Eckstrand (1975) and Groves and Keays (1979). This can be explained by considering the equilibrium reactions below (from Frost, 1985):

(i) $2FeS_2 + 5O_2 + 4HCl = 2FeCl_2 + 4SO_2 + 2H_2O$

(ii) $2FeS_2 + 2H_2O + 4HCl = 2FeCl_2 + 4H_2S + O_2$

Reaction (i) represents sulphate dominated fluids expected in an ultramafic talc-carbonate alteration zone. Reaction (ii) represents H_2S rich fluids from a partially serpentinized ultramafic rock. From reaction (i) it can be seen that an increase in fO_2 in the sulphate dominated fluid will enhance the solubility of sulphides, whereas in (ii) (H_2S dominated), an increase in fO_2 will decrease the sulphide solubility. Mobilization of sulphides from SO_2 rich environments is most likely to occur where there is a significant gradient in oxygen fugacity between different portions of a rock body (Frost, 1985). The chemical gradients necessary for the transport of sulphides from oxidizing environments are likely to occur near the upper stability limit of antigorite (upper greenschist to lower amphibolite facies) (Frost, 1985). Frost (1985) noted that these relations corroborated the earlier observations of Barrett *et al.* (1977), namely that sulphides in metaperidotite subjected to low grades of metamorphism were apparently not mobile, but sulphides in bodies metamorphosed to above the upper greenschist facies or lower amphibolite facies were mobile during metamorphism. Figs. 4.8 and 4.9 (from Frost, 1985), depict fO_2/fS_2 profiles across the talc-carbonate altered margin of a peridotite body. In Fig. 4.8 a primary peridotite is subjected to low-temperature alteration in response to infiltration by a fluid. This fluid contains enough CO_2 to produce significant amounts of carbonate on the outer part of the ultramafic body as well as a narrow margin of quartz and magnesite. The oxygen fugacity of the fluid will show a sharp rise in the carbonatized zone and will decrease towards the interior of the ultramafic body until it reaches a minimum at the serpentinization front. Low fO_2 at this point will cause XCO_2 to show

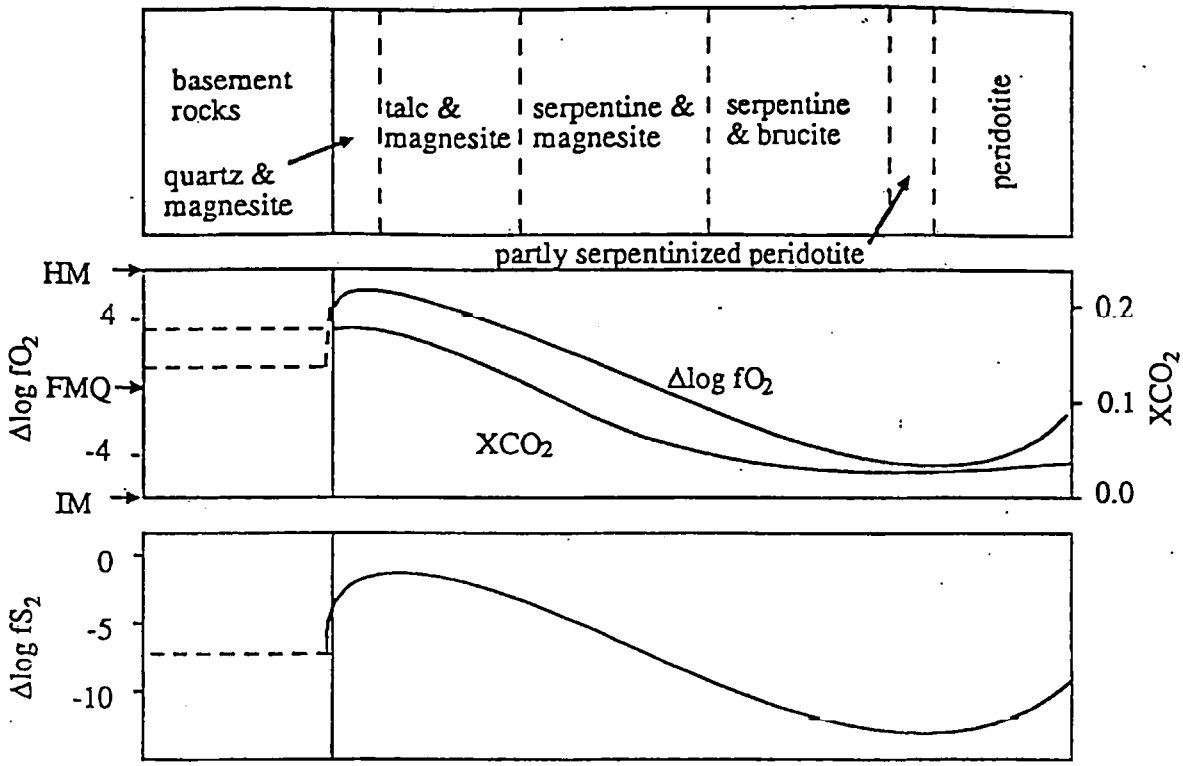

Fig. 4.8. Diagram showing variation in silicate mineral assemblages and fluid composition across a harzburgite body that is undergoing infiltration of a CO_2-bearing fluid ($T < 400\,^{\circ}C$). $\Delta\log fS_2$ refers to the difference between the sulphur fugacity of the fluid and the sulphur fugacity of a fluid where $fH_2S = fSO_2$, assuming that the total sulphur content of the rock is constant.

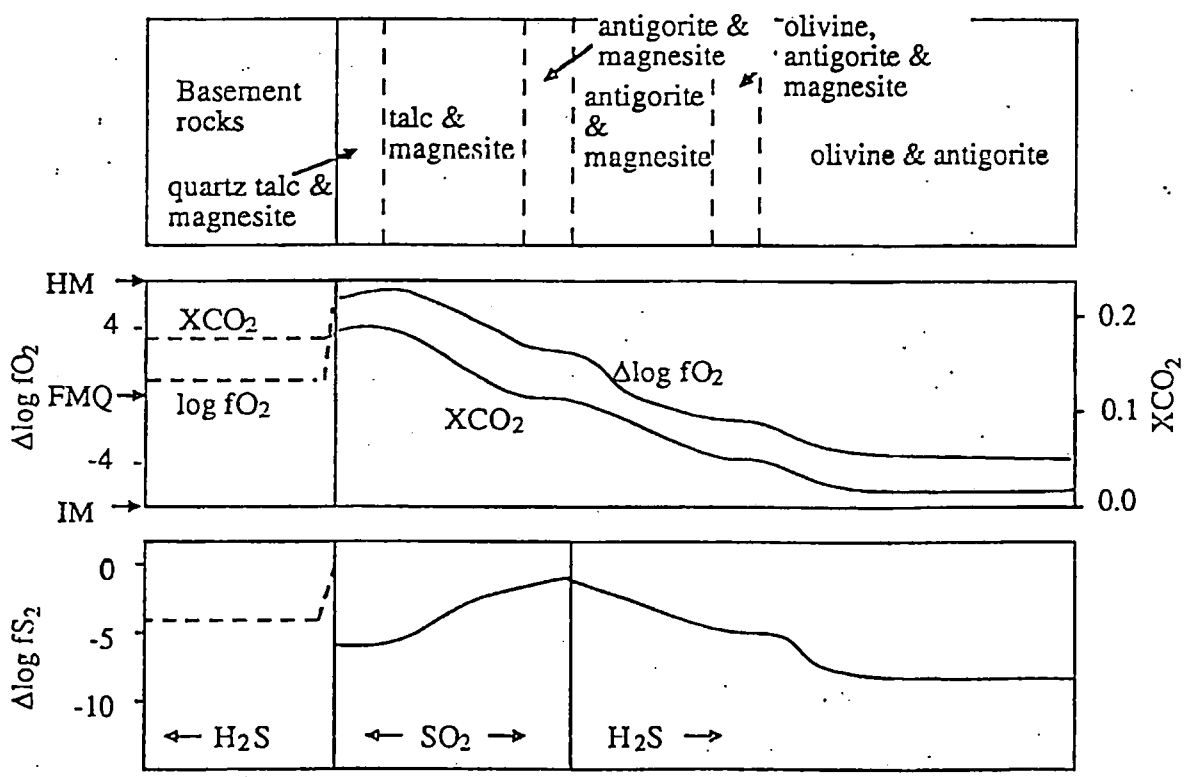

Fig. 4.9. Diagram showing variation in silicate mineral assemblages and fluid composition across a metaperidotite that has undergone upper greenschist or lower amphibolite facies metamorphism ($T = 500\,^{\circ}C$) subsequent to being serpentinized and carbonatized as in Fig. 4.8.

a corresponding decrease due to the conversion of CO_2 to CH_4. At the temperatures of <400°C considered for this process, the major sulphur species in the fluid throughout the metaperidotite will be H_2S. As a result, if the total sulphur in the rock were constant, the sulphur and oxygen fugacities would vary sympathetically. From equation (ii), the sulphides in the oxidized portions of the metaperidotite will be relatively insoluble in this situation and hence will not be mobile. In Fig. 4.9 the ultramafic body has undergone low-temperature hydration and carbonation with subsequent metamorphism to upper greenschist to lower amphibolite facies (T = 500°C). In this rock, brucite from the earlier assemblage has reacted with antigorite to form olivine, and bands of isobaric, univariant assemblages have formed between the isobaric divariant assemblages shown in Fig. 4.8. Although there is still a distinct CO_2 gradient across the body, the effects of buffering can be seen in the areas where isobarically univariant assemblages have formed. Oxygen fugacity shows a similar trend to that seen at lower temperatures but the range in values across the body is smaller. Because the sulphate/sulphide boundary lies within the range of oxygen fugacities encountered at the temperature under consideration, the gradient in sulphur fugacity across the body will show a distinct maximum, which, in Fig. 4.9, lies towards the interior of the talc-carbonate zone. These are the conditions under which sulphides in the carbonate zone may dissolve by reaction (i). Sulphides dissolved by such a process may be reprecipitated in areas of higher fS_2 that lie either inward from the carbonatized zone or at the contact between metaperidotite and the country rock, Fig. 4.9. Both these localities are areas of sulphide enrichment in nature (Groves *et al.*, 1974; Barrett *et al.*, 1977; Sanford, 1983). Such a mechanism could possibly explain the small enrichments in S noted in some talc-carbonate altered rocks at the basal thrust in the Shetland ophiolite.

4.9 Summary and conclusions

The sulphide mineralization in the Shetland ophiolite has re-equilibrated to low temperatures. In the gabbro unit, the sulphide mineral assemblages suggest re-equilibration to temperatures of <310°C with the common development of a supergene mineral paragenesis that formed during weathering. In high-level pyroxenites, the texture and mineral chemistry of pyrite

and the mineral chemistry of pentlandite indicates a low temperature genesis for the sulphides. It is noted that the development of cobaltite and niccolite, which are common in the high-level pyroxenites, are often ascribed to formation during the serpentinization of peridotite. In cumulate pyroxenites the coexistence of chalcopyrite and bornite suggests formation at <100°C for this association. Similarly low temperatures for the sulphide mineralization in this lithology are suggested by the octahedrally orientated intergrowths of chalcopyrite in pentlandite, the low Fe content of heazlewoodite and the low Ni and Co content of pyrite. Large intergrain differences in the Ni content of pentlandites, suggest local dis-equilibrium. Oxidative supergene weathering of sulphides in the cumulate pyroxenites is also common. The Ni and Ni-Fe sulphide assemblages in wehrlitic dunite, cumulate dunite and dunite pods are generally consistent with the low temperature (140°C) ternary relations in the Fe-Ni-S system. Pentlandite compositions from the different sulphide assemblages in these lithologies also indicate that the majority of these assemblages are low temperature equilibrium assemblages, although local disequilibrium is also apparent. Awaruite, which is commonly developed in dunites, was probably formed at temperatures below 300°C. The low average Fe content of heazlewoodite from all sulphide assemblages in wehrlitic dunite and dunites suggests a low temperature paragenesis for this phase. Godlevskite replaces heazlewoodite and so must have formed at similarly low temperatures to heazlewoodite which is substantiated by the low Fe content of godlevskite. Native Cu probably formed by the desulphidization of precursor Cu-sulphide during serpentinization and the low Ni and Fe contents of native Cu is consistent with formation at low temperatures. Talc-carbonate rocks from the basal thrust contain a secondary sulphide, arsenide and sulpharsenide assemblage, with pyrrhotite and niccolite as inclusions in secondary magnesite grains and the common replacement of 'ferritchromit' by hexagonal pyrrhotite. Whether violarite in this association is considered part of a low temperature equilibrium assemblage depends upon the different interpretations of the low temperature phase relations in the Fe-Ni-S system. A supergene sulphide assemblage of pyrite, marcasite, mackinawite and vallerite is also developed in talc-carbonate rocks.

The changes in the sulphide mineralogy with lithology, from pentlandite and heazlewoodite dominated assemblages in dunites, to pentlandite-pyrrhotite-chalcopyrite

assemblages in pyroxenites and pyrrhotite-pyrite-chalcopyrite assemblages in gabbro are mirrored by changes in the bulk sulphide chemistry with lithology which is due to magmatic fractional crystallization processes.

The low average Cu/(Cu+Ni) ratio of sulphide aggregates in dunites from the Shetland ophiolite is similar to ratios from other weakly mineralized serpentinites from continental intrusions, and also to weakly mineralized serpentinized dunites in the Zambales ophiolite, Philippines.

The paragenesis of sulphides in wehrlitic dunite, cumulate dunites and dunite pods (other than those at Cliff) is

(i) pentlandite-troilite-native Cu-magnetite

(ii) pentlandite-awaruite-native Cu

(iii) pentlandite-heazlewoodite-awaruite-native Cu

(iv) pentlandite-heazlewoodite-awaruite(±millerite)-native Cu-magnetite.

These assemblages seem to broadly correlate with differing degrees of serpentinization of the host dunites. For example assemblage (i), found in partially serpentinized dunites is the most the most reduced assemblage, whereas heazlewoodite-pentlandite-awaruite-native Cu (±millerite) from dunites with minor relict olivine, is stable at higher sulphur and oxygen fugacities.

A different assemblage of pentlandite-heazlewoodite-millerite-godlevskite-magnetite-chalcocite-minor native Cu, developed in dunite pods from the Cliff locality, may have been formed under more oxidizing conditions compared to other dunite pods and cumulate dunites.

The replacement of pentlandite by heazlewoodite is isochemical with respect to sulphur. The nickel required for the formation of heazlewoodite was probably derived from olivine or serpentine. Iron liberated during the formation of heazlewoodite may have contributed to the formation of secondary nickeliferous magnetite. The secondary sulphide assemblage in talc-carbonate rocks from the basal thrust formed under relatively more oxidized conditions compared to dunites and harzburgites, in response to chemical gradients developed at the contact between metaperidotite and the country rock.

Chapter 5

Techniques used to measure sulphur isotope ratios

5.1 A review of the techniques available for the measurement of sulphur isotope ratios

One of the aims of this thesis was to establish the sulphur isotope composition of sulphides in a suite of weakly mineralized ultramafic-mafic rocks from the Shetland ophiolite. It was hoped that by using sulphur isotopes it would be possible to distinguish 'hydrothermal', or secondary sulphides from 'primary,' or 'magmatic' sulphides. Since the variations in the sulphur isotope composition of magmatic sulphides from mineralized ultramafic rocks is often small, typically a few per mil, it was necessary to use a technique that gave $\delta^{34}S$ values to precisions of ±0.5‰ or better. A comparison of the conventional technique of sulphur isotope analysis on SO_2 gas by dynamic mass spectrometry, with other currently available techniques for measuring sulphur isotope ratios, along with the precision of each technique is given in table 5.1.

Of those techniques listed in table 5.1., coupled laser combustion and dynamic mass spectrometry offers both high precision and the ability to make spatially resolved analyses (Kelley and Fallick, 1990). This technique, along with the ion microprobe, would appear to be ideally suited to investigate any spatial sulphur isotope variations that may be present in the intimately intergrown sulphides in the Shetland ophiolite. However, disadvantages associated with the laser combustion technique (such as matrix effects) and the ion microprobe (relatively poor precision), made the use of a conventional combustion technique more appealing for the routine analysis of whole-rock samples and mineral separates of the type encountered herein. Work was concentrated on the development of an off-line system to give accurate sulphur isotope values and rapid sample throughput. Coupled with stepped combustion analysis, an indication of the relative sulphide mineral proportions in a given sample was hoped to be achieved.

Sulphur extraction technique	Instrumentation	Sample preparation	Minimum sample size	Spatial resolution	Precision	Pros.	Cons.	References
Combustion of sulphide with O_2 generated from a solid oxidant or bottled gas	Dynamic mass spectrometer and gas extraction line	Whole-rock powder or mineral separate. Sulphates commonly reduced to sulphide prior to analysis	Down to 1 µg S		$\delta^{34}S=\pm0.1‰$ (>1µgS) $\delta^{34}S=\pm0.8‰$ (<1µg S)	Routine, high precision sulphur isotope analysis.	Microscopic isotopic heterogeneities unresolved.	Burgess (1987)
Fluorination of sulphide to produce SF_6	Dynamic mass spectrometer and gas extraction line	Whole-rock powder or mineral separate	Typically 1mg S		$\delta^{33}S=\pm0.7‰$ $\delta^{34}S=\pm0.1‰$ $\delta^{36}S=\pm3‰$	Analysis of $^{33}S/^{32}S$, $^{34}S/^{32}S$ and $^{36}S/^{32}S$ ratios, extraterrestrial applications	Preparation of SF_6 involves toxic and reactive fluorine-bearing compounds	Burgess (1987)
Laser combustion of sulphide in O_2 atmosphere	Dynamic mass spectrometer and laser ablation	Polished block or mineral powder	1 µg S	250µ	0.25‰	High-precision spatially resolved, sulphur isotope analysis	Mineral specific isotope fractionations require correction factor to raw data	(Kelley and Fallick,1990)
Laser fluorination of sulphide to produce SF_6	Dynamic mass spectrometer and laser ablation	Polished block or mineral powder	?	?	$\delta^{33}S=\pm0.06‰$ $\delta^{34}S=\pm0.13‰$ $\delta^{36}S=\pm6.1‰$ (all measured on Canyon Diablo Troilite)	Spatially resolved sulphur isotope analysis	Preparation of SF_6 involves toxic and reactive fluorine-bearing compounds	Rumble *et al.* (1991)
Bombardment of sulphide with primary O^- beam and analysis of secondary ions	Ion microprobe with intergral sample chamber	Gold-coated polished block	0.1µg S	60µ	1-2‰	Spatially resolved, high resolution,sulphur isotope analysis	Moderate precision limited machine-access.	Deloule *et al.* (1986); Chaussidon and Demange, (1988)

Table 5.1 . Techniques curently available for the measurement of sulphur isotope ratios.

5.2 The modified 602E mass spectrometer

A detailed account of modifications to the standard 602E mass spectrometer are given in Burgess (1987). Operational protocol employed in this study for the instrument is essentially identical to that detailed by Burgess (1987). However, since a subsequent attempt to set up the instrument for carbon isotope analysis had been undertaken, and then the machine left in a state of disrepair, an initial period was spent setting up the 602E for sulphur isotope ratio analysis. The curent mass spectrometer ion source parameters for the analysis of sulphur dioxide gas differ from those of Burgess (1987) and are listed below;

Half-plate voltage 11V

Ion repeller voltage +3V

Electron energy 65V

Trap current 200μA

Magnet current 2.5A

Accelerating voltage 2.36kV (for m/z 66) and 3.14kV (for m/z 50)

Accelerating voltage m/z = 50 3.14kV

The mass spectrometer measures the isotopic composition of both SO_2^+ (m/z = 66/64) and SO^+ (m/z = 50/48). Since the mass spectra of SO^+ and SO_2^+ are complicated by the presence of ions containing ^{17}O and ^{18}O, corrections to the data are effected by computer software written by Drs R. Burgess and I.P. Wright (Burgess, 1987).

The mass spectrometer was not heated when undertaking sulphur isotope ratio measurements as no "memory" effects, manifested by a reduction in the true isotopic difference between reference and sample gas, were detected.

5.3 Reference gases and zero enrichment experiments

The isotopic reference gas SO_2-1 prepared by Burgess (1987) and assigned a $\delta^{34}S_{CDT}$ value of +10.16‰, was used for routine sulphur isotope analysis. For the zero enrichment experiments an aliquot of SO_2-1 gas from the reference bulb was expanded into the reference and sample inlets and the source pressures balanced at approximately 2x 10^{-8} mbar. After

allowing 1-2 minutes for the gas to equilibrate, the $\delta^{34}S$ value of the SO_2 gas in the sample inlet was determined relative to the SO_2 in the reference inlet, such that the reference gas in the sample inlet was treated as an unknown.

Number of analyses	*Date*	*66/64 reference ($\pm 1\sigma$)*	*66/64 sample ($\pm 1\sigma$)*	*$\delta^{34}S$ (sample vs. reference) $\pm 2\sigma$ errors*
5	6/6/89	0.05108 (0.00005)	0.05108 (0.00006)	+0.06 ±0.29
5	4/12/89	0.05102 (0.00005)	0.05103 (0.00004)	-0.01 ±0.11
9	20/3/90	0.05152 (0.00006)	0.05145 (0.0002)	+0.10 ±0.11

Table 5.2. Zero enrichment experiments performed on three separate aliquots of standard gas SO_2-1.

The results of a series of zero enrichments performed on three different aliquots of reference and sample gases on three separate days are given in table 5.2. The isotopic composition of SO_2-1 was regularly checked against SO_2 gas prepared from a solid Ag_2S standard (NZ1) which was prepared as an international standard for sulphur isotope studies by Robinson and Brenninkmeijer (1987) . NZ1 has a $\delta^{34}S$ value of -0.3‰ (Trahey, 1992). An aliquot of NZ1 was included as an unknown in each run of a batch of sulphide samples of unknown isotopic composition. The average of 27 analyses of NZ1 during this study by the sealed tube method (section 5.4.2.1) was +0.02±0.24‰. The 0.3‰ discrepancy between the $\delta^{34}S$ value of NZ1 measured during the present study (0‰) and the internationally agreed value of -0.3‰ suggests that the SO_2-1 reference gas used in the routine day to day running of the mass spectrometer has $\delta^{34}S$ value that is approximately 0.3‰ heavier than the value of +10.16‰ reported by Burgess (1987). That the $\delta^{34}S$ value of SO_2-1 did not fractionate further with time is demonstrated by the plot of the isotopic composition of NZ1 (measured against SO_2-1) determined over an eleven month period from June 1991 to May 1992 (Fig. 5.1). A correction for the 0.3‰ discrepancy between the $\delta^{34}S$ value determined for NZ1 in this study and the internationally agreed value has been applied to all the whole-rock sulphur isotope measurements reported in Chapter 6.

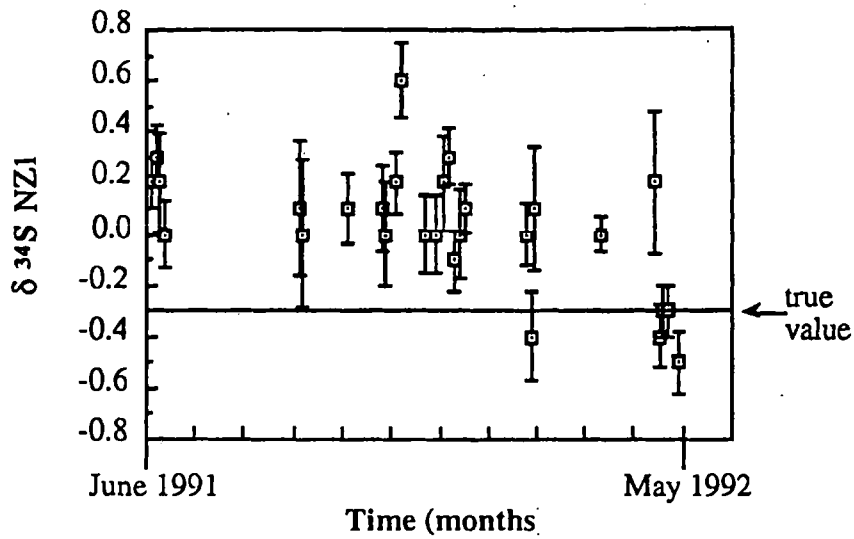

Fig 5.1. Plot of $\delta^{34}S$ measurements of standard NZ1 against the reference gas SO_2-1 performed over an eleven month period. This shows that the regular removal of aliquots of SO_2gas from the reference bulb had not caused significant fractionation of the residual SO_2 gas stored in the bulb.

A second sulphide, the interlaboratory standard chalcopyrite CP1, which has an assigned $\delta^{34}S$ value of -4.6‰ was also analysed during this study.

5.4 Techniques used to extract SO_2 gas from sulphides and native sulphur.

In the past, determinations of $\delta^{34}S$ values of sulphur-bearing materials either involved precursory conversion to $BaSO_4$ and reduction to H_2S by either graphite (Rafter, 1959), or by an HI-H_3PO_2-HCl solution (Thode *et al.*, 1961), followed by conversion of the H_2S to Ag_2S which was then oxidized to SO_2. Combustion of sulphides or native sulphur with a solid oxidant under high vacuum is now the most widespread technique by which SO_2 gas is produced for the mass spectrometric determination of $^{34}S/^{32}S$ ratios. In the past, different laboratories have employed a variety of oxidants to obtain quantitative yields of SO_2 from sulphides and native sulphur. For example, Fritz *et al.* (1974) used reagent grade Cu_2O or CuO which was intimately mixed with the sample and combusted at high temperature under vacuum, similarly Robinson and Kusakabe (1975) favoured the use of Cu_2O in the preparation of SO_2

from sulphide samples. Ueda and Krouse (1986) produced SO_2 gas by intimately mixing either sulphates or sulphides with V_2O_5 and SiO_2 after which the evolved SO_3 was converted to SO_2 by reaction with hot metallic copper. The production of SO_3 during the combustion of sulphides has been inferred to explain low yields of product SO_2 gas with an accompanying sulphur isotope fractionation, *e.g.* Sakai (1957). A 4:1 oxygen to sulphur atomic ratio was suggested by Fritz *et al.* (1974) to be optimum for the producton of quantitative yields of SO_2 on combustion of suphide with cuprous or cupric oxide. Robinson and Kusakabe (1975) were able to confirm the need for a stoichiometric excess of oxygen, in this case a ratio of 2:1 was found to be optimum, and used cuprous in favour of cupric oxide as the former was found to favour low pO_2 conditions negating the formation of SO_3 and sulphates.

5.4.1 Sulphur extraction line

At the outset of this project, the modified 602E mass spectrometer was coupled to a glass gas extraction line constructed by Burgess (1987) for the liberation of sulphur dioxide from sulphur-bearing materials. This glassline facilitates the conversion of reduced sulphur species to sulphur dioxide gas by combustion under high vacuum in pure oxygen. Oxidized sulphur species (sulphates), decompose on heating liberating sulphur dioxide gas. This glassline had fallen into disrepair and had also been contaminated with oil from the vacuum pumps. It was therefore decided to re-build the glassline to a configuration that was close to that described by Burgess (1987). A schematic diagram of this new glass extraction line is shown in Fig. 5.2.

In constructing this new glassline several features have been incorporated into its design that are absent from the glassline described by Burgess (1987). One of the most significant of

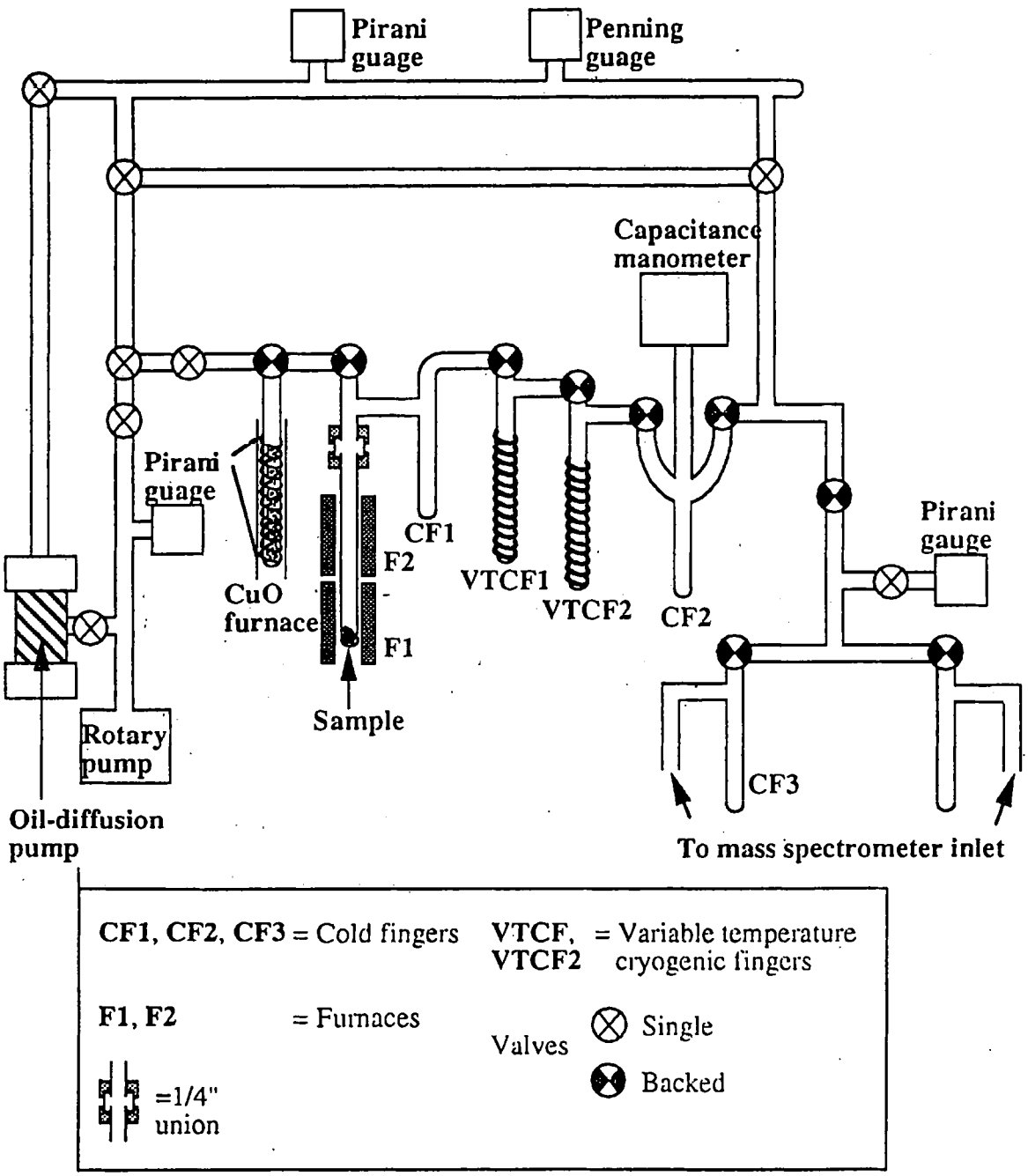

Fig. 5.2. Schematic diagram of the modified glassline used for the extraction of SO_2 gas for sulphur isotope ratio analysis.

these is the CuO 'finger'. This modification follows directly from the work of Burgess (1987), who suggested that careful control of the partial pressure of oxygen during combustion to suppress SO_3 production could be achieved by connecting a CuO finger directly to the combustion vessel. This would ensure a constant oxygen pressure during combustion, *i.e.* the extent of the equilibrium; $2CuO \Leftrightarrow 2Cu + O_2$ and hence oxygen pressure, is temperature dependent. The CuO finger was constructed by coiling resistance wire around evacuated quartz tubing containing wireform copper oxide sheathed in platinum foil (Boyd, 1988). The whole arrangement was then encased in quartz glass tubing. When heated to ~850°C via a variable transformer, O_2 was liberated. At 600°C any unreacted O_2 gas was resorbed. The quartz combustion section was joined to the pyrex glassline by a 1/4" union in place of the pyrex/quartz graded seal used by Burgess (1987). An additional benefit of this arrangement was that no on-line glassblowing was necessary to replace the combustion section after sample processing, as a new section of pre-baked quartz tubing was used for each experiment.

Yields of SO_2 gas obtained by combusting the sulphur-bearing material of interest are measured on a capacitance manometer (MKS Instruments, Inc., Massachusetts, U.S.A.) with a high accuracy sensor head that was maintained at a temperature of 110°C to prevent adsorption of SO_2 gas onto cold metal surfaces of the sensor head. The capacitance manometer was calibrated using CO_2 gas prepared by combusting a range of different sized microdiamonds weighing between 90 and 550 μg (Fig. 5.3).

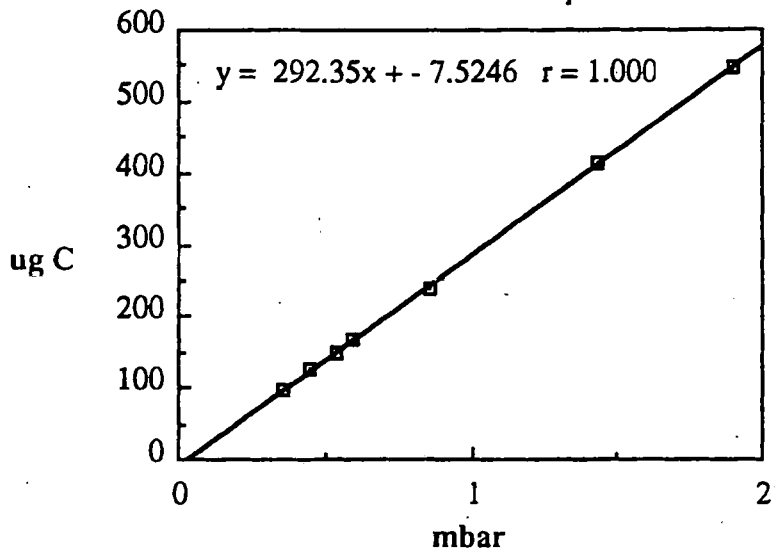

Fig.5.3. Diagram showing the variation in pressure (mbar) as indicated by the capacitance manometer for different sized aliquots of CO_2 produced from the combustion of different sized microdiamonds.

The use of microdiamonds to calibrate the baratron was justified because at the outset of this work quantitative yields of SO_2 gas were unobtainable using the combustion technique described below.

Sulphur isotope measurements of eight separate aliquots of between 185 and 308µg CP1 (65-108µg sulphur) obtained by combustion at 1200°C for 30 minutes with the combustion vessel open to the CuO finger at 850°C, gave a mean $\delta^{34}S$ value of -4.2 ± 1.0‰ compared to the accepted value of -4.6‰. Measured yields of SO_2 gas ranged from 48 to 87%. No correlation was observed between %yield of SO_2 and $\delta^{34}S$ of CP1 (Fig. 5.4).

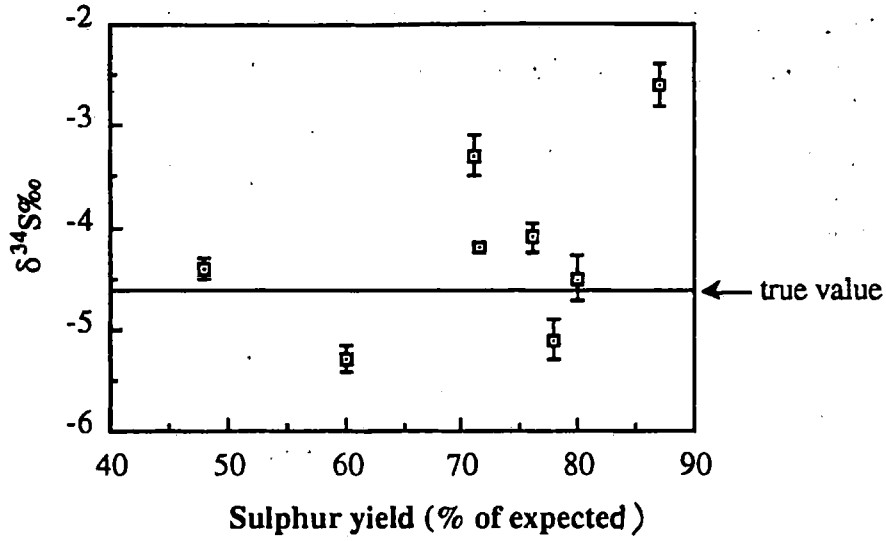

Fig. 5.4. Diagram showing the yields and isotopic composition of CP1 chalcopyrite measured using the modified glassline.

Low yields of SO_2 gas when combusting sulphides may be explained by the formation of SO_3 during the combustion process (Burgess, 1987). The formation of SO_3 recognized by Burgess (1987) was accompanied by a sulphur isotope fractionation resulting in SO_2 gas with significantly more negative $\delta^{34}S$ values. If SO_3 production was the root cause of the erroneous sulphur isotope and SO_2 yield measurements of standard CP1, then a correlation would be expected between the measured $\delta^{34}S$ value of CP1 and the yield of SO_2 gas produced from the combustion of CP1. Increasingly more negative $\delta^{34}S$ values should correlate with lower SO_2 yields as ^{34}S is partitioned into SO_3. From the limited data presented in Fig. 5.4., no such relationship between $\delta^{34}S$ of CP1 and the percentage yield of SO_2 is apparent suggesting that the problem may not arise from SO_3 production.

5.4.2 Combustion of sulphides using a sealed tube technique

Since the processing of the sulphide standard CP1 by the method outlined above was found to give consistently low yields of sulphur as SO_2, with an accompanying isotopic fractionation, an alternative method was sought whereby quantitative yields of SO_2 could be obtained for sulphur isotope analysis.

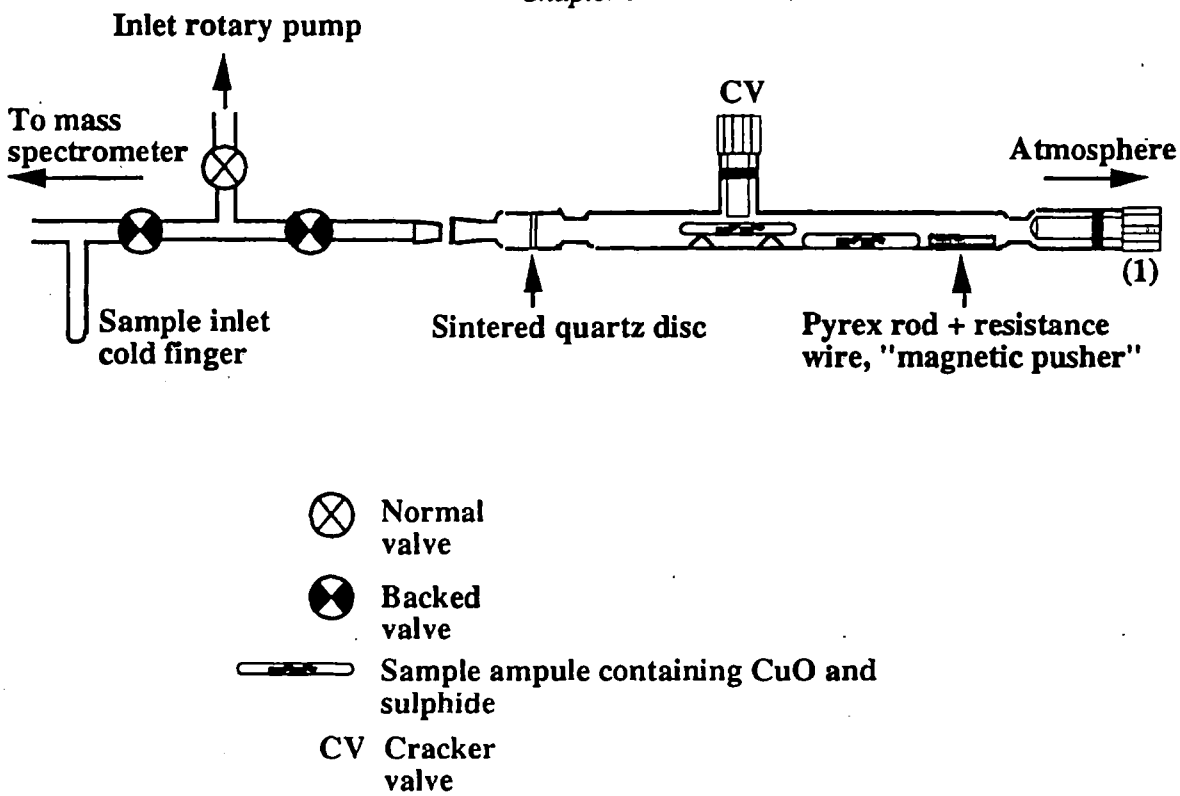

Fig. 5.5. Schematic diagram of apparatus for bulk sample gas extraction. The sample tube is loaded through valve (1) and then the apparatus is evacuated. Two sample tubes may be loaded at any one time and each one in turn is manipulated with a "magnetic pusher" under valve CV where they are cracked open. A sintered quartz disc prevents any glass fragments from entering the mass spectrometer vacuum line. SO_2 gas is frozen onto the sample inlet cold finger and subsequently admitted to the mass spectrometer where the sulphur yield and isotopic composition of the sample is determined.

The sealed-tube technique described herein has been investigated for a number of sulphides (pyrite, chalcopyrite, silver sulphide, cadmium sulphide) and also for native sulphur. Essentially, between 40 and 70 μg of sulphide sulphur is transferred to a quartz "bucket" pre-baked in air at 1100°C. Between 1.2 and 1.4 mg of wireform CuO (BDH chemicals, Poole England) is then placed in each sample bucket. Each bucket is then loaded into a separate pre-baked quartz tube of approximately 25cm length which are in turn attached to a glass "pump-down line" via 1/4" metal unions. A total of four samples could be loaded onto the pump-down line at any one time. The quartz tubes plus samples were then evacuated to a pressure of ~10^{-1} mbar by a rotary pump and then to <10^{-5} mbar by a turbo-molecular pump. Each sample tube was then heated ~4cm above the bottom of the tube (containing the sample and copper oxide) with an oxygen/hydrogen flame such that the quartz tubing collapsed forming a sealed evacuated ampoule containing the sample and copper oxide. The ampoules are then placed in a muffle furnace at 1100°C for 1/2 hour after which time they are removed and allowed to cool. Each ampoule is then scored approximately half way round its circumference. Two ampoules at a time are loaded into a specially constructed "cracker" (Fig. 5.5). These ampoules can then be manipulated by means of a magnetic pusher. The cracker is attached to the glass inlet manifold of the mass spectrometer via a B10 cone and socket and evacuated via a rotary pump to <10^{-1} mbar and then, via a diffusion pump, to <10^{-4} mbar. The sample inlet cold finger (CF3 in Fig. 5.2) is immersed in a small dewar of liquid nitrogen one minute prior to breaking open the sample ampoule by screwing down the cracker valve (Fig. 5.5). All condensibles are thus trapped down in the sample inlet cold finger and any non-condensibles are pumped away. The sample gas is then expanded into the mass spectrometer and a mass scan performed to check for contaminant gas. The amount of carbon impurity produced as CO_2 on combustion was always <3 μg and had no discernable effect on $\delta^{34}S$ values obtained from the sulphide standard NZ1. The yield of sulphur dioxide gas is measured by monitoring the major ion beam intensity (Fig. 5.6) which was calibrated using 3 to 100, ug aliquots of sulphur as SO_2 as measured on the glass-line capacitance manometer.

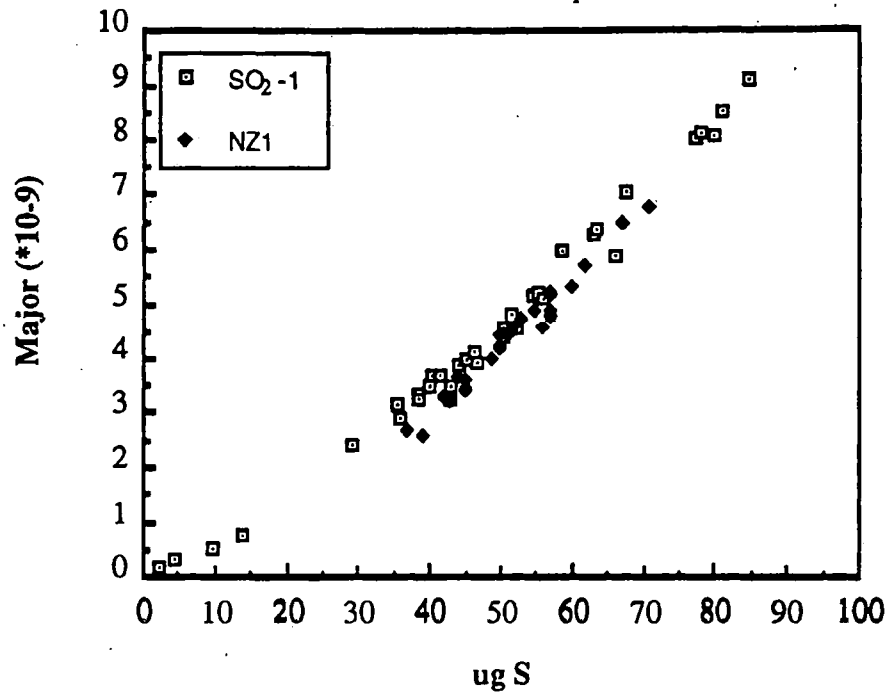

Fig. 5.6. Plot of major ion beam intensity of different sized aliquots of SO_2-1 reference gas as measured on the capacitance manometer. Superimposed upon this is the calculated yield of sulphur as SO_2 calculated from the major ion beam intensity from combustion of sulphide standard NZ1 using the sealed tube technique.

The calibration curve in Fig. 5.6 is clearly not linear which may be due to SO_2 gas being adsorbed onto the cold metal surfaces in the inlet of the mass spectrometer. However, this curve is still accurate to ± 5% and any isotope fractionation problems are avoided by running a standard with each sample batch.

5.4.2.1 Experiments using standard sulphides and native sulphur.

Experiments were undertaken in this study to determine whether a solid oxidant could be used in conjunction with a sealed tube technique for the production of quantitative amounts of SO_2 gas from pure sulphides. The chalcopyrite standard CP1 was chosen for these experiments as it had a well constrained $\delta^{34}S_{CDT}$ value and although its homogeneity at relatively small sample sizes was not known, Burgess (1987), had obtained reproducible results from µg-sized quantities of this mineral by bulk combustion. Wireform copper oxide was chosen as the oxidant since it had been used successfully by previous workers (*e.g.* Fritz *et.al.*, 1974). To find the optimum experimental conditions for the production of quantitative yields of SO_2 gas, a series of experiments were carried out in which chalcopyrite was combusted with varying proportions of

wireform copper oxide in [O]/[S] ratios of between 0.01 and 60, based on mass. The results of these experiments are shown in Fig. 5.7.

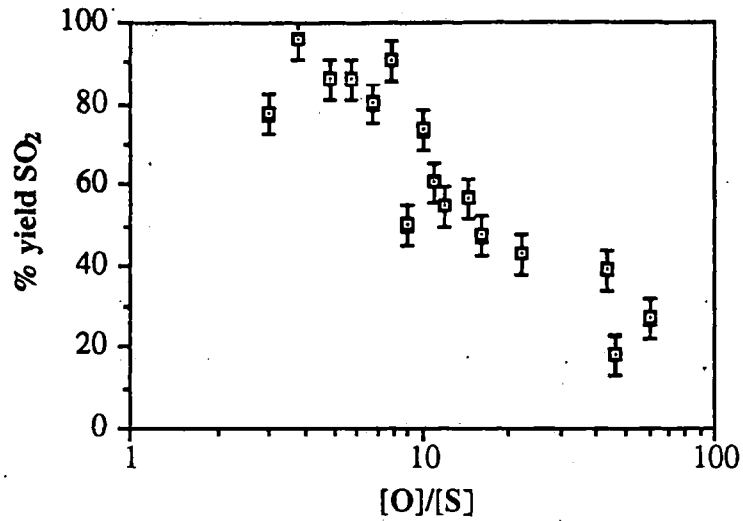

Fig. 5.7. Diagram showing how the yield of sulphur as SO_2 gas produced from combustion of chalcopyrite CP1 varies with different [O]/[S] ratios.

Fig. 5.7. shows that there is a correlation between the [O]/[S] ratio and the %yield of sulphur as SO_2 gas. Close to theoretical yields of SO_2 occur at [O]/[S] ratios of approximately 4:1 whereas progressively lower yields of SO_2 with increasing [O]/[S] are observed, with yields <40% SO_2 occurring at [O]/[S] ratios in excess of 40:1. Considering Fig.5.8, a reasonable correlation between [O]/[S] ratio and measured $\delta^{34}S$ is also observed with increasingly more negative $\delta^{34}S$ with increasing [O]/[S]. However, the $\delta^{34}S$ values measured at near optimum yields of SO_2 are some 2.5‰ heavier than the accepted value of -4.6‰ for CP1. The reason for the discrepancy between the measured and actual sulphur isotope values for this standard is unclear.

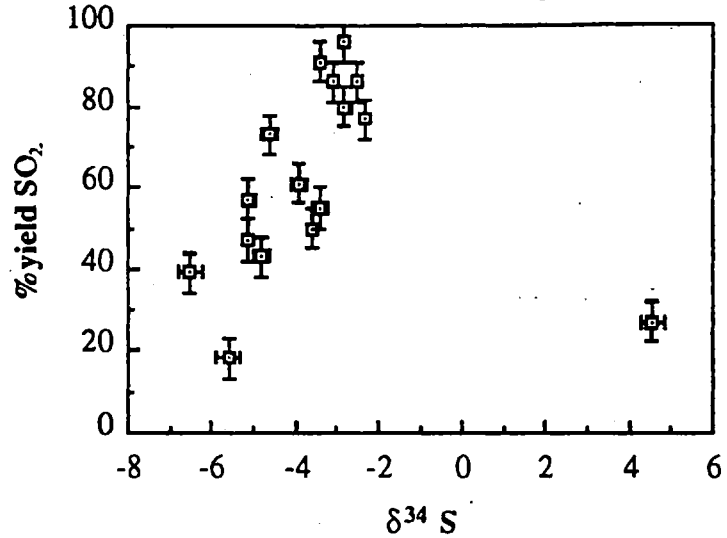

Fig. 5.8. Diagram showing the yields of sulphur as SO_2 gas and the measured $\delta^{34}S$ values of different aliquots of sulphide standard CP1 using the sealed tube technique.

Since near optimum yields of SO_2 occur at O:S ratios of approximately 4:1, experiments were carried out using aliquots of between 40 and 60µg silver sulphide standard NZ1 combusted at 1000°C with 1-1.3 mg of wireform CuO. Fig. 5.9 shows that good yields and reproducible sulphur isotope values were attainable on NZ1 using these parameters

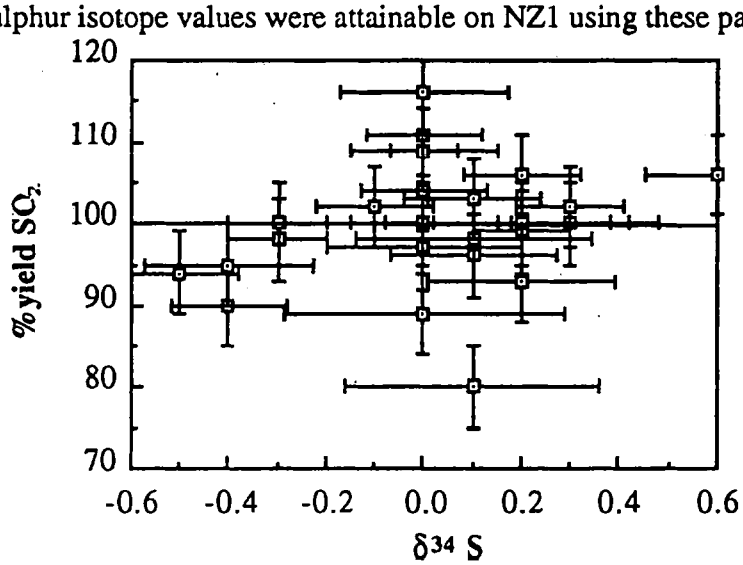

Fig. 5.9. Diagram showing the yields of sulphur as SO_2 gas and the measured $\delta^{34}S$ values of different aliquots of sulphide standard NZ1 using the sealed tube technique.

One advantage of the sealed-tube technique compared to on-line combustion is that native sulphur may be analysed without the problem of sublimation, as experienced by Burgess (1987).

Sample number	*Type of native sulphur*	*Sulphur yield**	*$\delta^{34}S$*
POA 79/1	pyroclastic sulphur	93	-9.4
POA 90/P	yellow "achnelith"	70	-9.8
POA 90/1/2	sulphur tephra	100, 103	-10.2, -10.2
POA 89/1/1	active sulphur pond	89, 103	-11.9, -11.8
POA 90/F	block in lake sediment	85	-12.3

Table 5.3. Yields and sulphur isotope values obtained on samples of native sulphur by the sealed tube technique, * sulphur yield (as SO_2) expressed as % expected (assuming pure sulphur).

Table 5.3 gives the yields of sulphur as SO_2 and sulphur isotope values of five samples of elemental sulphur from Poas Volcano, Costa Rica, supplied by Dr. C. Oppenheimer. Yields are close to theoretical for all analysed samples and $\delta^{34}S$ values are comparable with other $\delta^{34}S$ determinations of volcanic native sulphur (Oppenheimer, 1992).

5.4.3 On-line stepped-combustion of reference materials

The stepped combustion technique used in the present study involves the combustion of sulphur, sulphides, sulphates and sulphur-bearing rocks under high vacuum in pure oxygen in incremental heating steps usually from 0-1200°C. With reference to Fig. 5.2, all condensible gases (mainly SO_2, CO_2, H_2O) formed at each step are frozen onto a cold finger (CF1) maintained at -196°C by immersion in liquid nitrogen. Water is cryogenically separated from SO_2 and CO_2 by maintaining the first of two variable temperature cryogenic fingers (VTCF1) at -90°C. Failure to remove water from the product gases at this stage can result in poor quality $\delta^{34}S$ measurements (Burgess, 1987). This is very important since serpentinites from the Shetland ophiolite contain up to 11.4 wt% silicate-bound water (Chapter 2). The separation of

CO_2 from SO_2 is accomplished by cryogenic separation using VTCF2. The exact temperature necessary for a successful separation varies with the proportions of SO_2 and CO_2 in the frozen mixture (Burgess, 1987). For experiments carried out during the present study a temperature range of approximately -150°C to -120°C was identified as suitable to allow CO_2 to enter the gas phase while SO_2 remained frozen. Any evolved CO_2 is frozen onto a cold finger (CF2) at -196°C. CF2 is then allowed to heat up to room temperature which is attached to a capacitance manometer (CM) allowing measurement of the CO_2 pressure. CO_2 gas is then pumped away and the temperature of VTCF2 is raised to -110°C to liberate SO_2 whilst leaving behind any H_2O which may have been inadvertantly transferred from VTCF1 to VTCF2. Pure SO_2 is transferred to CF2 and the yield measured using the baratron (Fig. 5.3). The SO_2 gas is then transferred to the mass spectrometer for sulphur isotope ratio analysis.

Since some sulphides combust over discreet temperature intervals (Burgess, 1987), then it seemed possible that the intimately intergrown sulphides present in the Shetland ophiolite, which could not be separated for sulphur isotope analysis by conventional physical separation procedures, could be qualitatively resolved using the stepped combustion technique.

Sulphide	*Source/reference*	*Ideal formula*	*Bulk $\delta^{34}S$*
pyrite	Dept. Earth Sciences, Open University	FeS_2	+2.0
troilite	Bella Roca Troilite	FeS	-0.4
pentlandite	sulphide separate Unst, RLA 139	$(FeNi)_9S_8$	+3.1
heazlewoodite	sulphide separate, Unst, NB2-5	Ni_3S_2	+1.5
millerite	B.M. (Natural history) B.M. 1962, 36	NiS	not determined
chalcopyrite	CP1 interlaboratory standard	$CuFeS_2$	-4.6

Table 5.4. Source and chemistry of sulphides used for stepped combustion analysis.

Furthermore, any sulphate present in the rocks should be able to be resolved from the sulphides. Sulphide samples subjected to stepped combustion were selected to represent the sulphide mineralogy of the Shetland ophiolite as characterized by reflected light microscopy and

quantitative electron microprobe analysis. The chemistry and source of these reference sulphides is given in table 5.4.

Sample preparation of the sulphide samples pyrite, pentlandite, heazlewoodite and millerite involved crushing each to a grain size of <50μ. Troilite (from the Bella Roca meteorite) was already in the form of a mineral powder and required no further processing. 100-200μg aliquots of each of these sulphides were then taken for stepped combustion analysis. A pyroxenite from Unst (sample JM13) was chosen as a reference sample for stepped combustion analysis since, from microscope and electron microprobe studies, it had a well constrained mineralogy of chalcopyrite, pyrrhotite, pentlandite. JM13 was prepared by crushing approximately 0.5kg of this sample to 0.5cm fragments. Approximately 15 grams of these rock fragments were then ground for 8 minutes in an agate-lined tema barrel, until the powder was < 200 mesh size. Stepped combustion profiles of the individual sulphides are shown in Fig 5.10. Included in Fig 5.10 for comparison are the stepped combustion profiles for native sulphur and chalcopyrite CP1 determined by Burgess (1987).

Fig 5.10 shows that pentlandite and heazlewoodite are relatively more refractory (they both combust between 650-900°C) than either pyrite, troilite millerite and chalcopyrite (combustion range 200-600°C). Furthermore pyrite and troilite, which combust between 400-550°C, with a peak release at 550°C, combust at a higher temperature than chalcopyrite (peak release 200-400°C) (Burgess, 1987), and millerite, which shows a peak release of sulphur at 400-450°C. Within the suite of sulphides analysed there is apparently no relationship between the peak temperature of combustion and mineral chemistry of the different sulphides. For example, the nickel sulphide millerite (NiS) combusts between 400-450°C whereas heazlewoodite (Ni_3S_2) shows a peak release of sulphur at between 850-900°C. The reason for these different combustion temperatures was considered possibly to be caused by the relative differences in the bond strengths of these sulphides. Sulphides with higher bond strengths would be expected to combust at higher temperatures compared to sulphides with lower bond strengths. Fig 5.11 is a plot of the temperature of peak combustion for each of the sulphide minerals considered against the bond strength for each mineral. Bond strength is

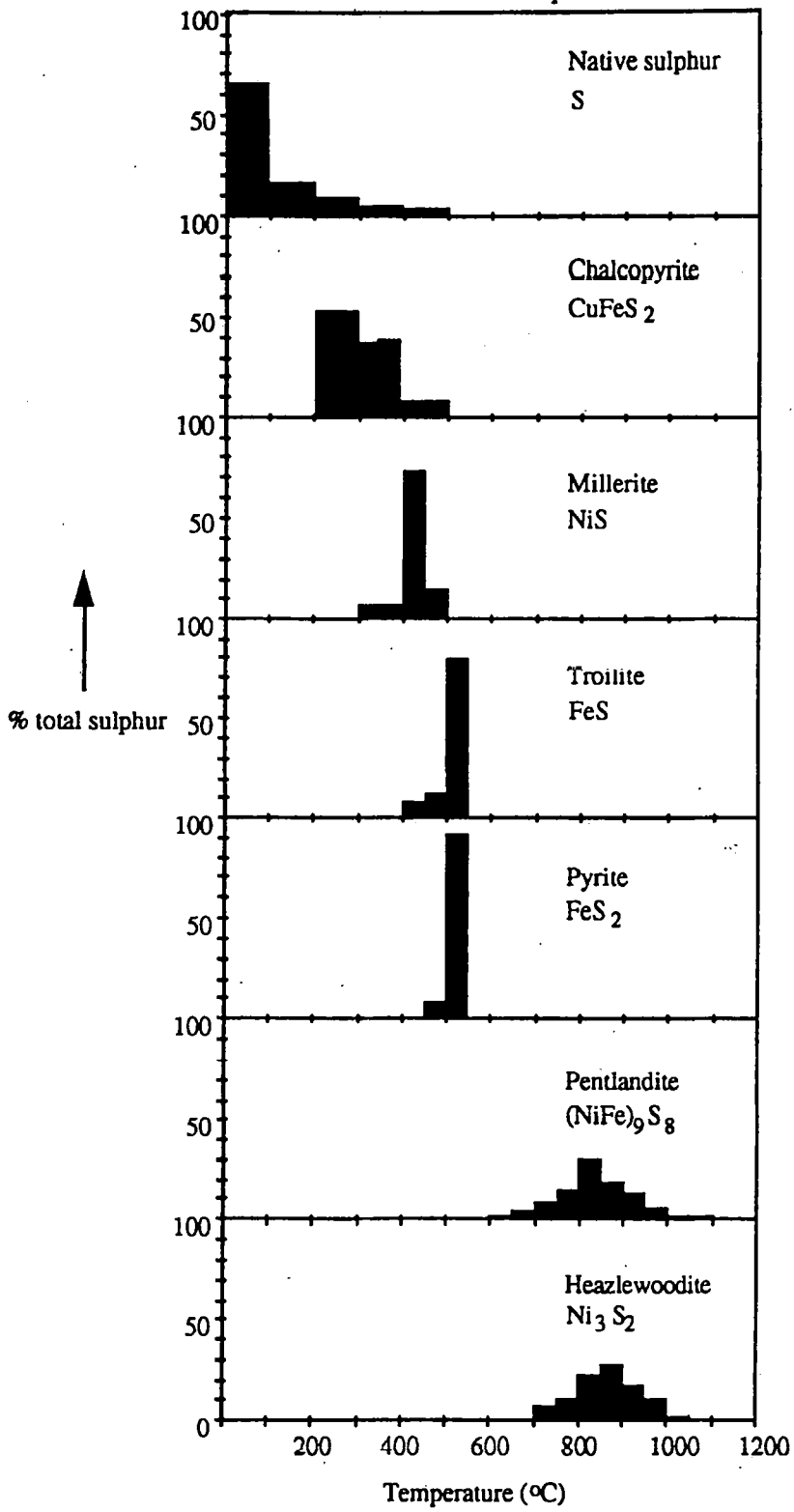

Fig. 5.10. Diagram showing the sulphur release profiles of some reference sulphide samples and native sulphur along with their mineral formulae analysed during the present study. Native sulphur and chalcopyrite data from Burgess (1987).

expressed as ΔG^{o}_{298K} (the Gibbs free energy of formation of the mineral at 25°C). From Fig 5.11 it is apparent that there is no simple relationship between the bond strength of the sulphides and the temperature of peak combustion. This suggests that neither the sulphide mineral chemistry nor the bond strength of the different sulphide minerals analysed by stepped combustion have major controls over the temperature at which the sulphides combust.

Only sulphur release profiles were obtained during the stepped combustion of the sulphides millerite, troilite and pyrite. No $\delta^{34}S$ measurements were made because the mass spectrometer was not operating correctly at the time the experiments were carried out. However, the cumulative $\delta^{34}S$ measurements obtained on SO_2 released during the stepped combustion of RLA 139 pentlandite and NB2-5 heazlewoodite gave $\delta^{34}S$ values of +0.8‰ and -0.5‰ respectively. Both these

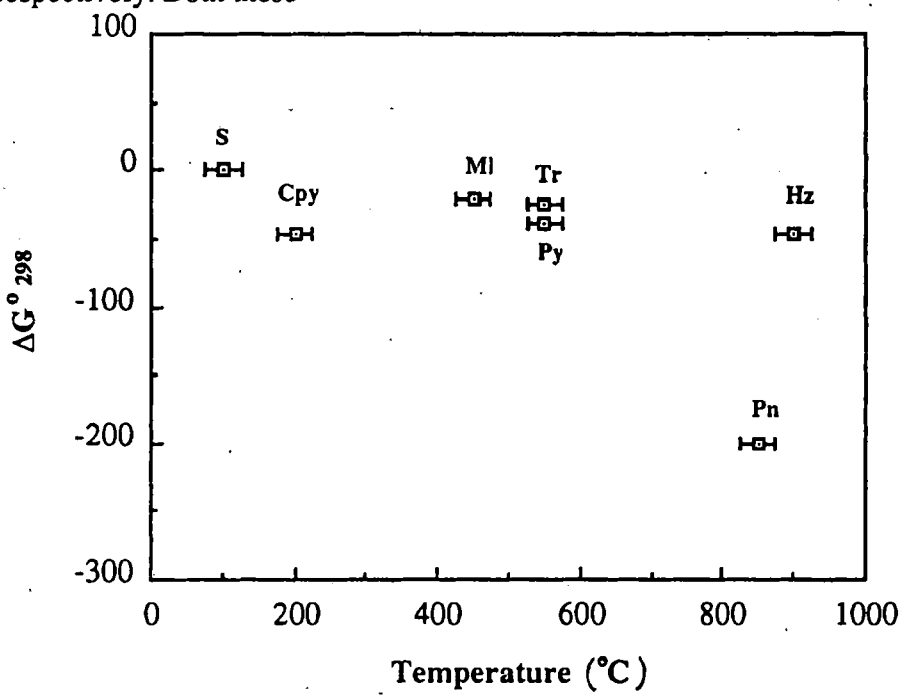

Fig 5.11. Plot of bond-strengths (ΔG^{o}_{298K}), except pentlandite (ΔG^{o}_{1100K}), of the different sulphide minerals used in the stepped combustion experiments against the peak temperature at which each of the sulphides combusts. Abbreviations; S, native sulphur; Cpy, chalcopyrite; Ml, millerite; Tr, troilite; Py, Pyrite; Hz, heazlewoodite, Pn, pentlandite. Thermodynamic data from Robie *et al.*, (1978) except chalcopyrite data (Robie *et al.*, 1985) and pentlandite data (Cemic and Kleppa, 1987).

measurements are approximately 2‰ lighter than the $\delta^{34}S$ values obtained from the bul combustion by the sealed tube technique of chemically extracted sulphur (section 5.5) from the samples. Burgess (1987) reported a similar difference between the cumulative $\delta^{34}S$ valu obtained from the stepped combustion of troilite (BRT) (-2.5‰) accompanied by a low yield c SO_2, and the value obtained by bulk combustion (-0.4‰) with a close to expected yield of SO This discrepancy in $\delta^{34}S$ values was ascribed to the formation of SO_3 during the steppe combustion of troilite. Therefore, $\delta^{34}S$ measurements obtained from stepped combustio experiments will be erroneous. For the purpose of the present study, where it is important t measure $\delta^{34}S$ values to a precision of ±0.5‰, isotope measurements from stepped combustio analysis are largely redundant.

The stepped combustion profile of an aliquot (53.6 mg) of sample JM13 is shown in Fi 5.12. This sample had an established sulphide mineralogy of approximately 50 p.t. chalcopyrite, 30 p.t.s pyrrhotite and 20 p.t.s pentlandite.

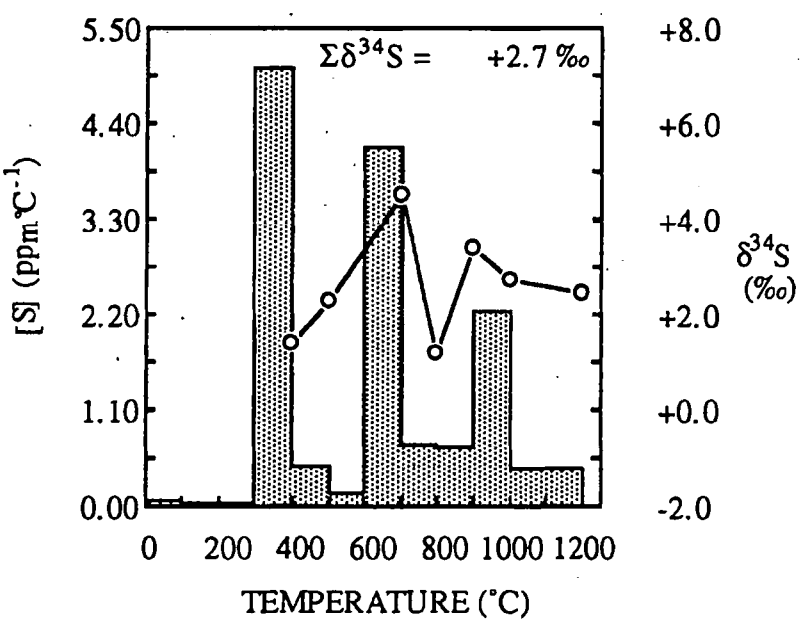

Fig. 5.12. Stepped combustion profile of a sample of pyroxenite containing intergrown chalcopyrite, pyrrhotite and pentlandite obtained using 100°C step sizes. The three discreet peaks in the sulphur release profile of this sample are ascribed to sulphur released from each of three different sulphide phases present in this sample.

It should be noted that this sample contains pyrrhotite ($Fe_{1-x}S$) in place of troilite (FeS). Since troilite is an end member of the pyrrhotite series, it was anticipated that the two minerals would combust over a similar temperature range. The experiment was carried out in 100°C step-sizes to see, in the first instance, whether chalcopyrite and pyrrhotite, which combust between approximately 400-550°C could be resolved from pentlandite, which combusts between 650-1000°C. The combustion profile obtained (Fig 5.12) shows three discreet release peaks, one between 300 and 400°C, another at 600-700°C and a third release between 900 and 1000°C. In comparison with the stepped combustion profiles of the individual reference sulphides in Fig 5.10, the lowest temperature sulphur release observed in sample JM13 (300-400°C) is consistent with the combustion of chalcopyrite. The 600-700°C release is intermediate between the stepped combustion profile of troilite, (which combusts between 500 and 550°C) and pentlandite and heazlewoodite (combustion range = 700-1000°C). This 600-700°C release is most likely due to the combustion of pyrrhotite. The 900-1000°C release in sample JM13 is within the range expected for the combustion of heazlewoodite or pentlandite. Therefore the stepped combustion of a rock sample containing the sulphides chalcopyrite, pyrrhotite and pentlandite (Fig 5.12) shows that these three minerals are resolvable from one another using 100°C step sizes. The cumulative $\delta^{34}S$ measurement obtained for sample JM13 (Fig 5.12) is +2.7‰ compared with the whole-rock value of +3.4‰ obtained by the modified Kiba method (section 5.5). The stepped combustion determination of the sulphur content of JM13 gives a value of 1420ppm S whereas the Kiba extraction method (section 5.5) gives a value of 3350 ppm S. As discussed earlier in this section, the discrepancy in $\delta^{34}S$ values between the cumulative stepped combustion $\delta^{34}S$ measurement of JM13 and the $\delta^{34}S$ value obtained from the chemical extraction of sulphur from a whole-rock sample, can be ascribed to the formation of SO_3 during stepped combustion analysis leading to low yields of sulphur and lighter than expected $\delta^{34}S$ measurements.

5.5 Chemical extraction of sulphur from rock samples

Since sulphides in the Shetland ophiolite complex often occur as intergrowths of two or more minerals that are often <500μ in size, isolation of pure sulphide phases for isotopic

analysis proved to be very difficult. However, in a few instances it was possible to characteriz individual sulphide phases by reflected-light microscopy, these could then be extracted from polished block of the rock specimen and combusted with CuO for isotope ratio analysis. A technique was therefore sought whereby sulphide and any sulphate that may be present in th rock specimen of interest could be extracted by chemical means and converted to a meta sulphide for isotope analysis. The method of Kiba *et al.* (1955), which has been proven i numerous earth science applications (*e.g.* Ueda and Sakai, 1984; Woodhead *et al.*, 1987 seemed a good candidate. Essentially, sulphates, equation (1), and sulphides, equation (2), ar reduced to hydrogen sulphide in a heated mixture of phosphoric acid containing Sn^{2+} as reducing agent (Kiba reagent) which was prepared from boiling of the $H_3PO_4/SnCl_2.2H_2O$ solution to remove chlorine as $HCl_{(g)}$ before treating samples:

$$SO_4^{2-} + 4Sn^{2+} + 10H^+ = H_2S + 4Sn^{4+} + 4H_2O \quad (1)$$

$$S^{2-} + 2H^+ = H_2S \quad (2)$$

With increasing concentrations of Sn^{2+} ions in the reagent, more sulphate will b reduced to H_2S, Ueda and Sakai (1983). The evolved H_2S is then passed through an absorbin solution under a stream of inert gas and precipitated as a metal sulphide (3):

$$S^{2-} + M^{2+} = MS_{(s)} \quad (3)$$

The metal sulphide precipitate may then be weighed to give a whole-rock sulphu estimate and subsequently analysed isotopically.

5.5.1 Experiments using silver nitrate

Silver nitrate was initially used as the absorbing solution, and processing of some pure sulphides was carried out using the apparatus shown in Fig 5.13. Between 9 to 65mg of sulphide and 10-25 ml of Kiba reagent (prepared from boiling of the $H_3PO_4/SnCl_2.2H_2O$ solution to remove chlorine as $HCl_{(g)}$ before treating samples) was transferred to a 250ml capacity, round-bottom flask. All pyrex glassware used was supplied by Cambridge Glassblowing (Cambridge, England). Nitrogen gas, of 99.999% purity taken from a $7.87m^3$

cylinder, pressurized to approximately 200bars (BDH Lab. Supplies, England), was then passed through the reaction vessel at a rate of approximately $0.8cm^3/s^{-1}$ for two minutes to remove any traces of gases (H_2S and other sulphur-bearing impurities), which might have been contained in the chemicals used to prepare the Kiba reagent.

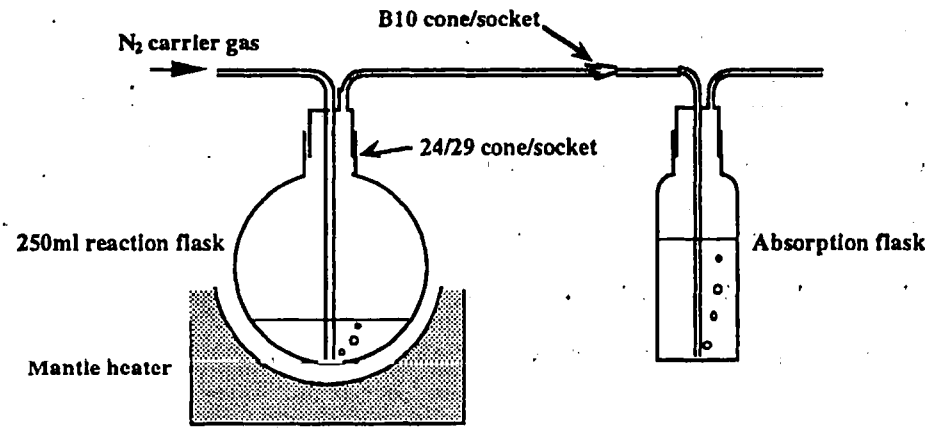

Fig 5.13. Schematic diagram of initial apparatus used for bulk rock sulphur extractions. The reaction flask contains Sn(II) chloride, orthophosphoric acid and the sulphur-bearing material. The absorption flask (B) contains silver nitrate solution for the precipitation of evolved sulphur as silver sulphide.

The reaction vessel was then connected to the remainder of the apparatus and heated at 280-300°C for about 15 minutes via a mantle heater (Electrothermal Engineering Ltd, ordered through Jencons (Scientific Ltd), Leighton Buzzard, England). Evolution of hydrogen sulphide was observed to occur over a period of about 5-10 minutes at temperatures in excess of about 150°C. An additional 20-30 minutes processing at >280°C was carried out to ensure satisfactory reduction of sulphides, after which time the mantle heater was turned off allowing the reaction flask to cool. The flow of nitrogen gas was terminated only after the temperature in the reaction vessel had dropped to below 100°C. The silver sulphide precipitate was filtered through filter paper (Whatman N°40) that had been dried at 80°C to remove any moisture. The silver sulphide precipitate was then washed several times with deionized water *via* a Buchner funnel mounted in a conical flask. The filtering process was speeded up by use of a water

suction pump which cut the time taken to filter a sample from approximately 20 minutes to 10 minutes.

Mineral	*Precipitate*	*% Recovery of sulphur*	*Number of analyses*	*True $\delta^{34}S$*	*$\delta^{34}S$ $\pm 2\sigma$ error*
pyrite B	silver sulphide	91	2	+11	+10.6 ± 0.2
chalcopyrite CP1	silver sulphide	68-88	2	-4.6	-4.4 ± 0.2
millerite	silver sulphide	106	-	-	-

Table 5.5. The results obtained from processing standard sulphide samples using Kiba reagent and silver nitrate solution.

The filtrate and filter paper were then dried at 100°C overnight and weighed to determine the quantity of silver sulphide present. From this it was possible to calculate the sulphur content of the material of interest. Table 5.5 shows the results of processing pure sulphide reference materials of known isotopic composition. For the pyrite and chalcopyrite sample, 'pyrite B', and CP1 respectively, no apparent isotopic fractionation is evident, and the error on the $\delta^{34}S$ measurements of ±0.2‰ are similar to the errors obtained from combusting NZ1 silver sulphide using the sealed tube technique. The sulphur yield from CP1 is much lower than the theoretical value. Kiba *et al.* (1955) reported that the yield of sulphur was significantly lower than theoretically expected when copper-bearing samples were analysed. This was ascribed to the formation of CuS during the reaction which is not decomposed by Kiba reagent. This problem was partially solved by adding metallic zinc to the solution which reduces copper(II) ions further to metallic copper. Ueda and Sakai (1983), however, report uniformly good yields (90%) for both pyrite and chalcopyrite treated with Kiba reagent when samples are intimately mixed with

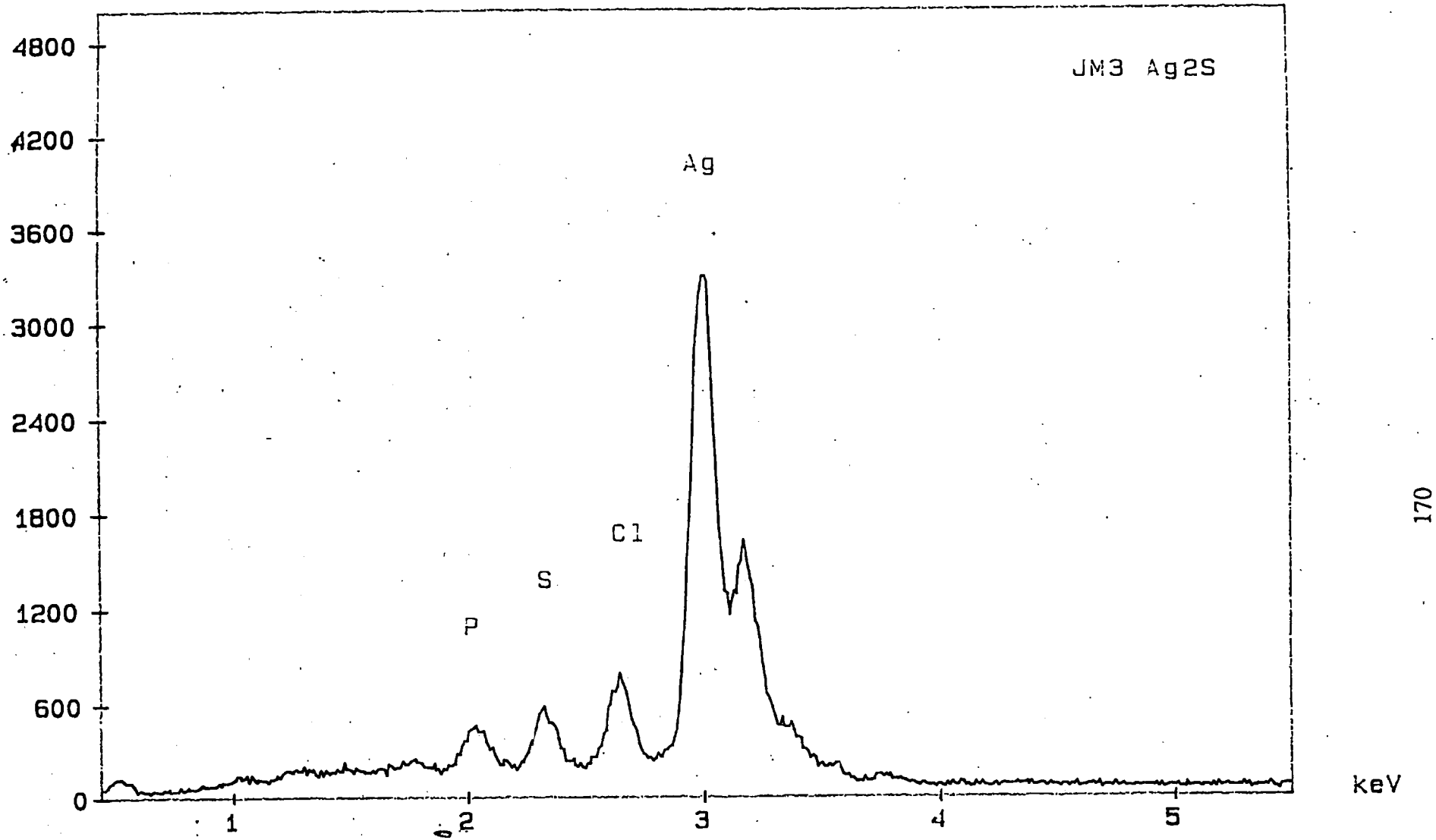

Fig. 5.14. X-ray spectra of silver sulphide precipitate. In addition to the peaks for silver and sulphur, note the presence of significant peaks in the spectra due to chlorine and phosphorous.

an inert powder thus suppressing the sample adhering to the walls of the reaction vessel on boiling.

Since acceptable $\delta^{34}S$ values were obtained on pure sulphide minerals, some whole rock powders from the Shetland ophiolite were processed according to the protocol described herein to ascertain whether sulphide and any sulphate sulphur that may be present in these rocks could be successfully extracted. Processing highly serpentinized whole rock powders from the Shetland ophiolite resulted in a pale-brown to milky precipitate forming in the absorbing vessel. The composition of one of these precipitates was qualitatively analysed using an X-ray detector attached to a JEOL JSM-820 SEM (appendix A.4). The X-ray spectra obtained (Fig 5.14) suggest that the chlorine and phosphorous are very significant components of the precipitate compared to sulphur. When this precipitate was subjected to sulphur isotope analysis by the sealed-tube method, a significant reduction in the measured 50/48 ratio of the SO_2 sample gas was noted. This could be due to isobaric interference at m/z = 48 by species such as $^{40}P^{18}O^+$ (m/z = 48). This interference resulted in erroneous $\delta^{34}S$ measurements. From the fact that this contamination was not experienced when processing pure sulphide samples, it could be inferred that the phosphorous and chlorine observed in the silver sulphides precipitated from processing rock powders from Shetland were derived from the rocks themselves. This possibility cannot be ruled out although major element analyses of rocks from the Shetland ophiolite (table 2.1 and table 2.2) indicate that phosphorous is only a trace constituent, forming between 0.02 and 0.12 wt.% of the rocks. A more plausible explanation is that the contamination observed in precipitates prepared from processing of powdered serpentinite is due to phosphorous and chlorine from the Kiba reagent being carried over to the absorbing solution with water evolved from the decomposition of hydrous silicates in the sample, perhaps as an oxy-chloride and $HCl_{(g)}$. The acidity of the absorbing solution will rise as $HCl_{(g)}$ passes through the solution rendering the silver sulphide precipitate soluble and forming an acid insoluble chloride. This could be responsible for the observed pale-brown to milky precipitates which are essentially Ag,S,Cl,P-bearing precipitates.

5.5.2 Experiments using cadmium acetate

In an attempt to alleviate the contamination of sulphide precipitates it was considered necessary to find a metal which formed an acid insoluble sulphide precipitate, *i.e* that satisfies the condition in equation (4):

$$K_{sp}(MS) << K_a(HS^-) \quad (4)$$

where K_{sp} (MS) is the solubility product of a metal sulphide and $K_a(HS^-)$ is the acid dissociation constant. Certain cations may be separated into groups on the basis of whether their sulphides precipitate in acidic solution.

Cation	*Solubility of sulphide in acid.*	*Ksp (metal sulphide, MS) at 18°C*	*Ksp (metalchloride, MCl_2) at temperature noted.*
Cd^{2+}	Soluble	$3.6*10^{-29}$	$5.93*10^{1}$ (20°C)
Cu^{2+}	Soluble	$8.5*10^{-45}$	$1.02*10^{-6}$ (18-20°C)
Fe^{2+}	Soluble in dilute acid	$3.7*10^{-19}$	$2.55*10^{1}$ (cold water) $6.98*10^{1}$ (hot water)
Pb^{2+}	Soluble	$3.4*10^{-28}$	$1.6*10^{-5}$ (25°C)
Mn^{2+}	Soluble in dilute acid	$1.4*10^{-15}$	Very soluble
Ag^{2+}	Soluble	$1.6*10^{-49}$	$1.56*10^{-10}$ (25°C)
Zn^{2+}	Very soluble	$1.2*10^{-23}$	$1.01*10^{3}$ (25°C)
Co^{2+}	Slightly soluble	$3.0*10^{-26}$	$1.25*10^{1}$ (cold water) $6.5*10^{1}$ (hot water)

Table 5.6. Solubility of transition metal sulphides and chlorides under acid conditions. For the purpose of the present study, cadmium (as cadmium acetate) was chosen as the absorbing solution as precipitating cadmium sulphide although slightly soluble in acid, forms an acid soluble chloride. Acetate ions from the cadmium acetate solution should buffer the pH of the absorbing solution by taking up H^+ ions and rendering cadmium sulphide insoluble.

For example, in a solution that has a pH of -0.5, the sulphides of Pb^{+}, Cu^{+}, Cd^{+}, and Sn^{2+} are insoluble, whereas the sulphides of Fe^{2+}, Co^{2+}, Ni^{2+}, and Zn^{2+} are soluble. When considering systems that involve sulphide precipitation, it must be noted that the $[H^+]$ concentration of a

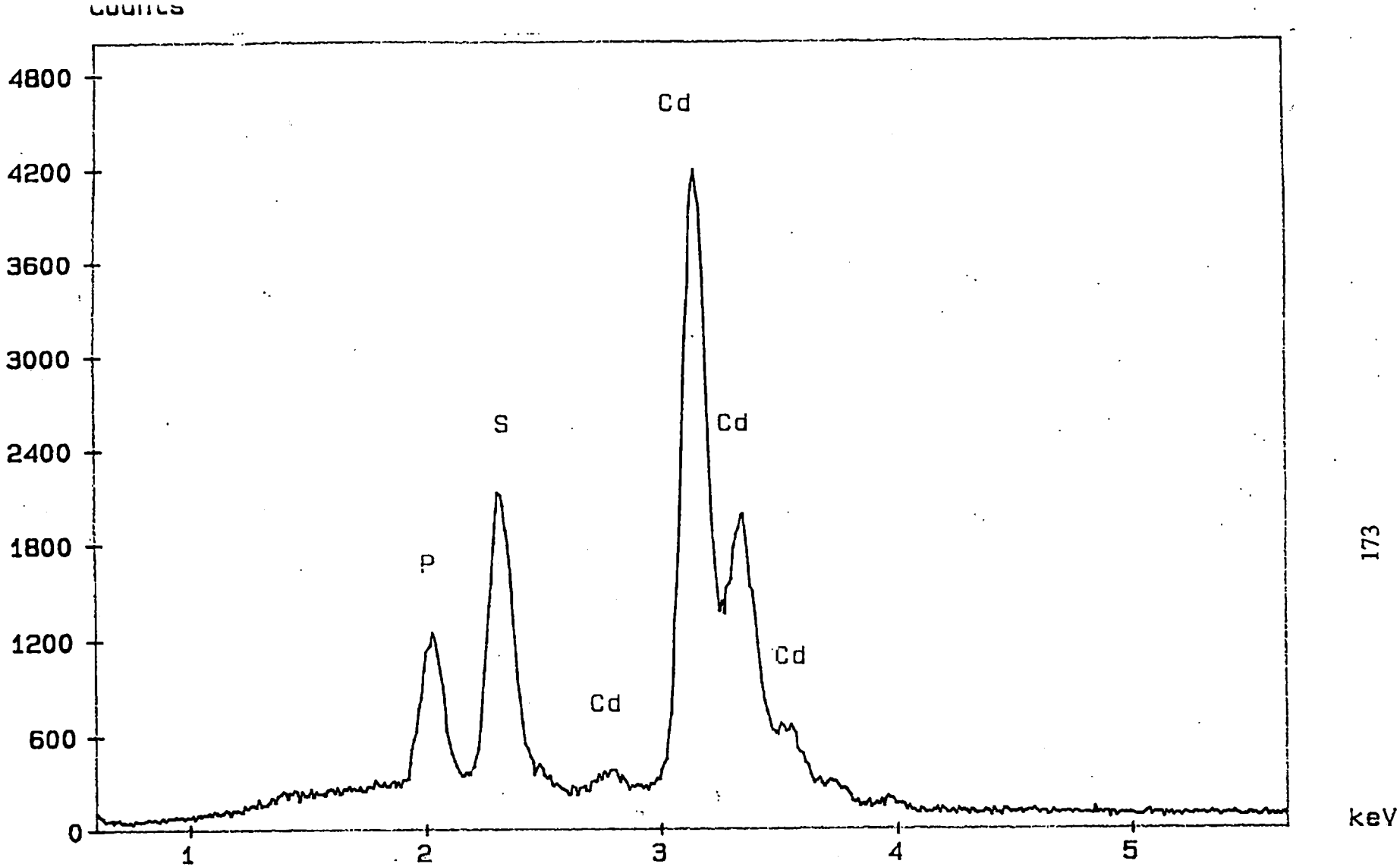

Fig. 5.15. X-ray spectra of cadmium sulphide precipitate. In addition to the peaks for cadmium and sulphur, note the presence of significant peaks in the spectra due to the presence of phosphorous.

solution increases when sulphides precipitate. In the case of the Kiba reagent under consideration, this is due to the production of HCl which dissociates in the absorbing solution increasing its pH.

Of a number of transition metal sulphides considered (see table 5.6), cadmium seemed to best satisfy the above requirements as it is only slightly soluble in acid and forms an acid soluble chloride. Cadmium acetate solution was chosen as a candidate absorbing solution since, considering the precipitation of cadmium sulphide, equation (5) in acid solution:

$$S^{2-} + Cd^{2+} = CdS_{(s)} \quad (5)$$

$$S^{2-} + H^{+} = HS^{-}_{(aq)} \quad (6)$$

$$Ac^{-} + H^{+} = HAc_{(aq)} \quad (7)$$

Acetate ions should buffer the pH of the solution by taking up H^+ ions hence negating the situation in equation (6) above. An experiment using cadmium acetate as the absorbing solution and Kiba reagent prepared from $SnCl_2.2H_2O/H_3PO_4$ and processing 38mg of CJP1 FeS_2, a pyrite from Silvermines, Eire, ($\delta^{34}S$ -46.7‰) supplied by Dr. A.E. Fallick, S.U.R.R.C., East Kilbride, by this method gave an apparent yield of sulphur of 107%. The orange colour of the CdS precipitate was typical of CdS precipitated under acid conditions. Subsequent isotope analysis of the CdS precipitate gave an anomalous $\delta^{34}S$ of -43.2‰ and low yield of sulphur. X-ray diffraction analysis of the precipitate identified it as hawleyite, (α-CdS, cubic), but qualitative SEM analysis revealed significant amounts of phosphorous (Fig 5.15). It is likely that this phosphorous was derived from the Kiba reagent, the phosphorous complexing with cadmium (Cotton and Wilkinson, 1972). Therefore, the use of cadmium acetate alleviated the problem of contamination of the sulphide precipitates with chlorine but significant amounts of phosphorous were still carried across from the Kiba reagent to the absorbing vessel. The presence of this phosphorous in the cadmium sulphide precipitates meant that, as sulphur yields were calculated by weighing the precipitates, all yield determinations were an overestimate of the

true sulphur content of the sample. In addition anomalously low $\delta^{34}S$ values were obtained by this method.

5.5.3 Experiments using silver nitrate, distilled water trap, and tin(II)oxide

As the root cause of the contamination problems were now thought to stem from (i) the Kiba reagent itself, (phosphorous and chlorine) and (ii) water derived from the decomposition of hydrous silicates in the powdered rock sample of interest, the experiment was modified as follows; (i) tin(II)oxide instead of tin(II)chloride was used to prepare the Kiba reagent, and (ii) a distilled water trap was inserted between the reaction vessel and the absorbing vessel (Fig. 5.16).

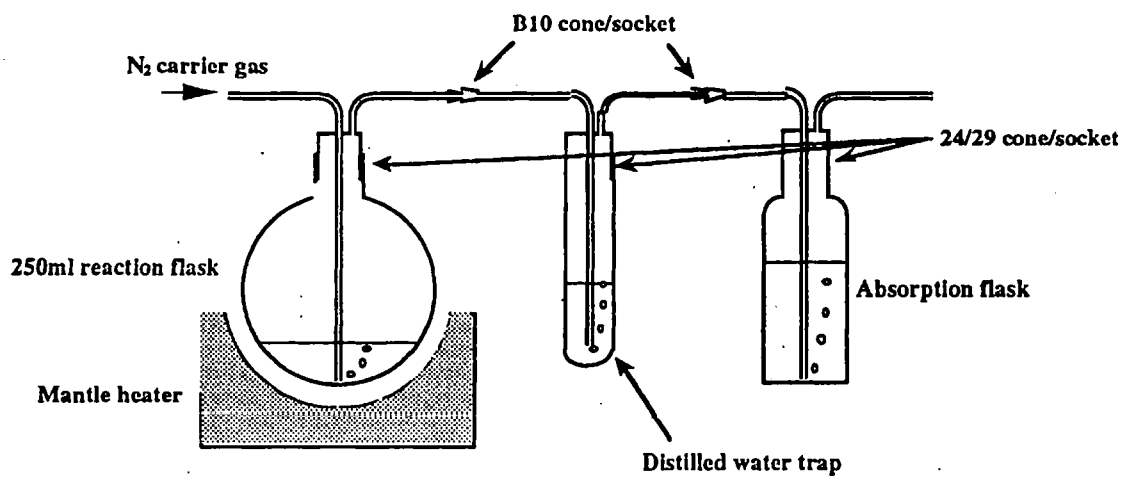

Fig 5.16. Schematic diagram of apparatus used for bulk rock sulphur extractions. The apparatus differs from that shown in Fig 5.13, in that a distilled water trap is inserted between the reaction flask and absorption flask.

However $H_2S_{(g)}$ is soluble in water (0.1M at 25°C) and so it was anticipated that a certain amount of the $H_2S_{(g)}$ evolved from the sample would be lost to the trap solution. Processing of different amounts of a Geological Survey of Japan (GSJ) rock reference sample, gabbro JGb-1, with an established sulphur concentration of 1950ppm, shows that for sample sizes of <10 grams, constant sulphur yields were obtained at about 90% of the expected value (table 5.7).

Another GSJ rock standard, JA-3, a Japanese andesite which contains 228ppm sulphur was analysed by the Kiba method. Yields were typically 100ppm less than the theoretical value (table 5.7). Although there are no established whole-rock $\delta^{34}S$ values for these two rock standards, reproducible $\delta^{34}S$ measurements by sealed tube combustion were obtained for standard JGb-1 ($\delta^{34}S$ = -0.6±0.7) and JA-3 ($\delta^{34}S$ = -11.7±0.4).

a)

Quantity of JGb-1 (g)	*Yield of sulphur (ppm)*	*% of expected yield*	*$\delta^{34}S$ of Ag_2S precipitate (‰)*
10.334	1732	88.8	0.2
6.331	1736	89.0	-1.3
4.490	1736	89.0	-0.2
0.990	1767	90.6	-1.2

b)

Quantity of JA-3 (g)	*ppm S measured*	*% of expected yield*	*$\delta^{34}S$ of Ag_2S precipitate (‰)*
15.520	191	83.8	-12.1
13.520	62	27.2	-11.6
11.980	118	51.8	-11.2
10.500	135	59.2	-11.9

Table 5.7. Measured whole-rock sulphur content and sulphur isotope values of two GSJ sulphur standards JGb-1 and JA-3. (a) JGb-1, a GSJ gabbro reference sample has an established sulphur concentration of 1950ppm and (b) JA-3, an andesite has an established sulphur concentration of 228ppm. The discrepancy between the sulphur concentrations measured during this study and the published sulphur concentrations are discussed in the text.

That H_2S was dissolved in the trap solution was indicated by the white precipitate which was formed after processing of sulphide and/or sulphate bearing material and may be due to the formation of sulphur by the following reaction:

$$H_2S_{(aq)} + 2H_2O_{(l)} = S_{(s)} + 2H_3O^+ + 2e^-$$

and was confirmed by idiometric titration in which the excess iodine left after the reaction with H_2S in the trap solution after processing JGb-1:

$$H_2S + I_2 = 2HI + S$$

was titrated against standard thiosulphate using starch as an indicator:

$2Na_2S_2O_3 + I_2 = Na_2S_4O_6 + 2NaI$

as a result of this experiment it was calculated that 9.4% sulphur was contained in the trap solution, in reasonable agreement with the 10±1% observed discrepancy noted above. This also indicated that the provision of only one silver nitrate trap was adequate suggesting that significant amounts of sulphur liberated from the sample of interest was not lost to atmosphere.

5.6 Conclusions

Bulk combustion and stepped heating of pure sulphides using the method outlined by Burgess (1987), was found to give consistently low yields of SO_2 with an accompanying isotopic fractionation. Therefore, an off-line, sealed-tube, bulk combustion technique has been developed which allows for the relatively rapid preparation of up to four sulphide samples at a time for isotope analysis. The average of 27 analyses of the international silver sulphide standard NZ1 by the sealed tube method was +0.02±0.24‰ compared to the internationally agreed value of 0.3‰ suggesting that the SO_2 1 reference gas used in the routine day to day running of the mass spectrometer has a $\delta^{34}S$ value that is approximately 0.3‰ heavier than the value of +10.16‰ reported by Burgess (1987). A correction for the 0.3‰ discrepancy between the $\delta^{34}S$ value determined for NZ1 in this study and the internationally agreed value has been applied to all the whole-rock sulphur isotope measurements reported in Chapter 6. A technique has been developed whereby sulphide-sulphur is liberated from whole-rock samples by reaction with Kiba reagent (Kiba *et al.*, 1955) and precipitated as silver sulphide. Processing of different amounts of a Geological Survey of Japan (GSJ) rock reference sample, gabbro JGb-1, with an established sulphur concentration of 1950ppm, shows that for sample sizes of <10 grams, constant sulphur yields were obtained at about 90% of the expected value. Reproducible $\delta^{34}S$ measurements were obtained from these silver sulphide precipitates by sealed-tube combustion but the precision of these $\delta^{34}S$ measurements is approximately ±0.5‰ compared to ±0.2‰ for NZ1 silver sulphide. One significant advantage of the sealed tube technique compared to on line combustion is that native sulphur may be analysed without the problem of sublimation experienced in using the former technique. Stepped combustion of a suite of different sulphide minerals that are representative of the sulphide mineralogy of the Shetland ophiolite has been

undertaken. Pentlandite and heazlewoodite both combust between 650-900°C whereas pyrite, troilite, millerite and chalcopyrite combust over a temperature range spanning 300-600°C. Pyrite and troilite, which combust between 400-550°C, with a peak sulphur release at 550°C, combust at a higher temperature than chalcopyrite (peak release 300-400°C, Burgess, 1987) and millerite, which shows a peak release of sulphur at 400-450°C. Stepped combustion of a pyroxenite rock sample containing chalcopyrite-pyrrhotite-pentlandite at 100°C temperature increments shows that these three sulphides are clearly resolvable at this step size. However, $\delta^{34}S$ measurements on SO_2 gas liberated during stepped combustion is typically 2‰ lighter than the true value.

Chapter 6

Sulphur, hydrogen, oxygen and helium isotope geochemistry

6.1 Introduction

The common occurrence of disseminated sulphides in many of the major lithologies of the Shetland ophiolite and their intimate association with PGM (Prichard *et al.*, 1994), means that the sulphur isotope geochemistry of these sulphides should place constraints on whether the sulphur in associated sulphides is of magmatic origin or whether it has been introduced from an external source. Any conclusions regarding the 'igneous' or 'hydrothermal' genesis of sulphides in the Shetland ophiolite based on sulphur isotope geochemistry alone must be complemented by textural studies of the sulphides and their host silicate mineralogy (Chapter 4) and on previous studies of ophiolitic rocks.

From the sulphide mineralogy and textural studies of sulphides it is thought that the disseminated sulphides which occur in the fresher rocks from dunite pods, cumulate ultramafics and the majority of the mafic sequence, initially crystallized from a magmatic immiscible sulphide liquid, but have re-equilibrated at low temperatures (Chapter 4). It would therefore be expected that if the source of sulphur is magmatic, then resultant sulphides would have $\delta^{34}S$ values that reflect a magmatic or mantle source, *i.e.* 0±3‰. However, as briefly discussed in Chapter 1, $\delta^{34}S$ values outside 0±3‰ in ophiolitic crust may be produced by processes operative within the mantle, in crustal magma chambers and also by hydrothermal alteration. Fig 6.1 is a compilation of sulphur isotope measurements of mineralized stratiform complexes, oceanic crust, ophiolites and seafloor sulphide mineralization and shows that the ranges of $\delta^{34}S$ measurements and the mean $\delta^{34}S$ value for each particular suite of rocks or deposit often falls well outside the magmatic range. Each of the main processes which are thought to produce $\delta^{34}S$ values outside the magmatic range are considered below.

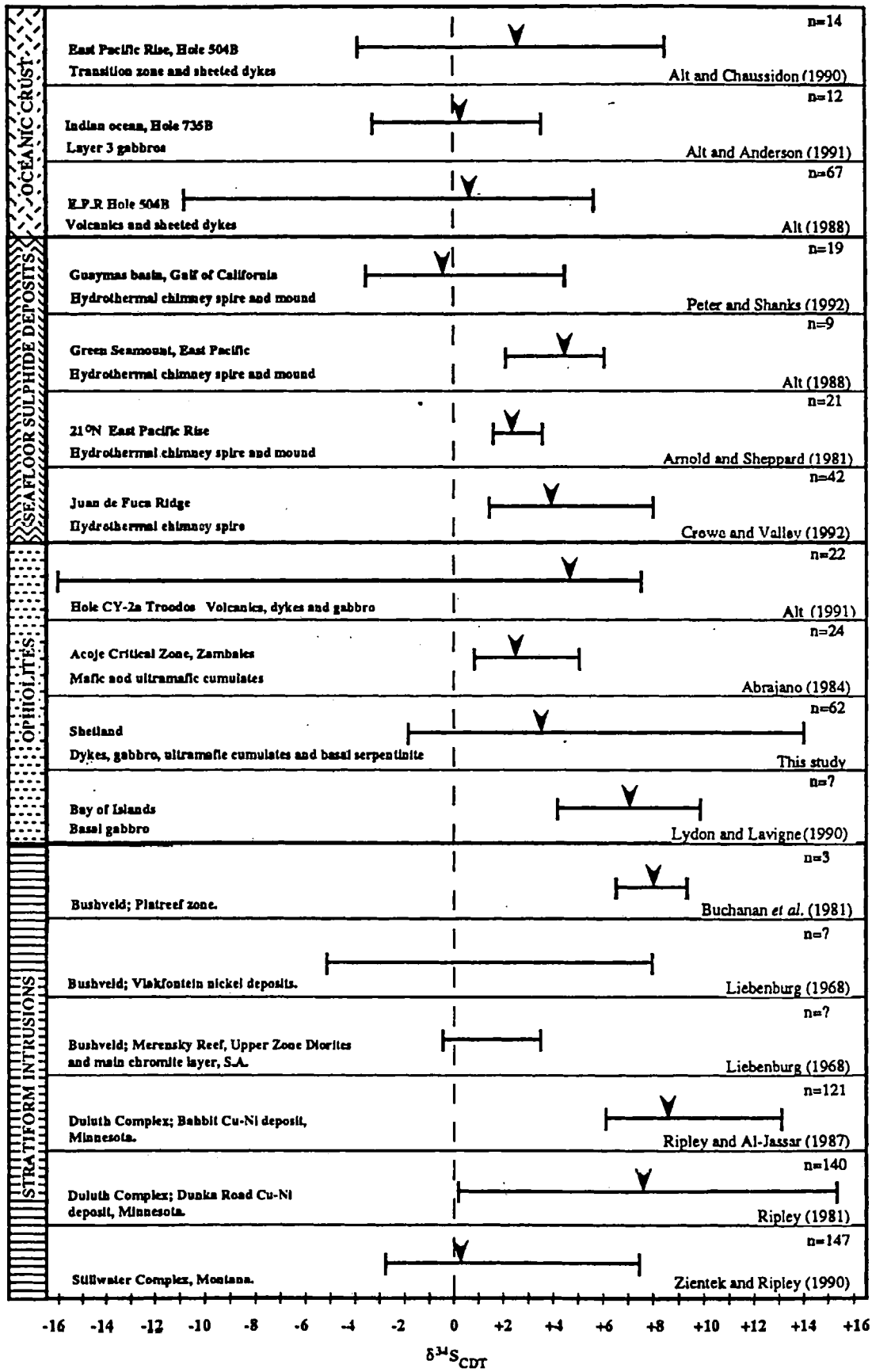

Fig 6.1. Range and mean values of $\delta^{34}S$ from oceanic crust, ophiolites and continental layered intrusions.

6.2 Mantle processes

Sulphur isotope studies of mantle derived rocks have led to the recognition of large scale sulphur isotope heterogeneity within the mantle (Chaussidon *et al.*, 1987, 1989; Chaussidon and Lorand, 1990; Ionov *et al.*, 1992). For example, sulphide inclusions in eclogitic diamond from Botswana with $\delta^{34}S$ values of+9±1‰ (Chaussidon *et al.*, 1987) were thought to result from the incorporation of ^{34}S-enriched altered oceanic crust into the subcontinental mantle. Subsequent to this, Chaussidon *et al.* (1989) investigated the sulphur isotope geochemistry of sulphide inclusions in a range of of minerals (olivine, pyroxene, ilmenite and garnet) from mantle-derived rocks (basalt glasses, peridotites, eclogites, kimberlites). A wide range in $\delta^{34}S$ was discovered (-6 to +9‰) with high-nickel sulphides, mostly from residual peridotite, having an average $\delta^{34}S$ value of +3±1‰. A high temperature sulphur isotope fractionation between liquid sulphide and sulphur dissolved in the silicate liquid was suggested to account for this enrichment in ^{34}S in residual peridotite after 10-20% partial melting of a mantle source containing an estimated 300ppm S.

Ionov *et al.* (1992) investigated the sulphur isotope geochemistry of mantle-derived garnet and spinel peridotite and pyroxenite xenoliths from southern Siberia and Mongolia. Fertile lherzolites had $\delta^{34}S$ values of +1±1‰ whereas in harzburgites values reached +4±1‰. These values were thought to reflect sulphur depletion during partial melting of peridotite mantle, coupled with sulphur isotope fractionation between residual peridotites and generated basaltic melts, a conclusion in agreement with Chaussidon *et al.* (1989). Contamination of the mantle source of volcanic rocks ($\delta^{34}S$ = 0‰) with a ^{34}S-enriched component has been invoked to explain the high average $\delta^{34}S$ values (+11.1±6.2‰) of volcanic rocks from the Mariana arc (Woodhead *et al.*, 1987) and Tertiary alkali basalts from Western Germany, which have $\delta^{34}S$ values ranging from +0.9 to +8.6‰ (Harmon *et al.*, 1987). In both cases subduction of altered, oceanic crust was the inferred source of the ^{34}S enrichments.

6.3 Crustal processes

6.3.1 Continental intrusions

Many large economic PGE occurrences are hosted within layered basaltic intrusions in continental settings (*e.g.* Noril'sk, Russia, (Czamanske *et al.* , 1992), Bushveld, South Africa, (Buchanan *et al.* , 1981)). The PGM often occur as solid-solutions in sulphides, arsenides and sulpharsenides, which are generally thought to have been precipitated initially from a sulphur-saturated host magma as immiscible sulphide droplets, into which base-metals (Ni, Cu, Fe) and PGE were strongly partitioned (*e.g.* Naldrett, 1981). Sulphide minerals in these intrusions occur either as disseminated, matrix or massive accumulations. Sulphur isotope studies of the sulphides from such intrusions have shown that, in addition to mantle-derived sulphur, assimilation of sulphur from an external source has played an important role, albeit sometimes locally, in saturating the magma with sulphur and hence inducing the exsolution of immiscible sulphide liquids. These can then become concentrated into an ore deposit of often characteristically lower tenor than sulphide mineralization in the rest of the deposit. Examples of this phenomenon are displayed by the Duluth Complex (Mainwaring and Naldrett, 1977; Ripley and Al-Jassar, 1987), Noril'sk (Godlevski and Grinenko, 1963), Stillwater Complex (Zientek and Ripley, 1990) and the Bushveld Complex (Buchanan *et al.* , 1981). Note that there is some evidence of small sulphur isotope variations of the order of several per mil, in some deposits which are thought to have been brought about by magmatic processes. For instance, Naldrett (1981) and Ripley (1983) both noted that $\delta^{34}S$ values of copper-rich sulphide were about 2‰ heavier than associated iron-rich sulphide. Ripley (1983), ascribed this phenomenon to the fractionation of sulphur isotopes between a silicate and sulphide liquid. Magmatic fractionation of sulphur isotopes in the Deer Lake Complex, Canada, is represented by a Rayleigh distillation process involving the build-up of isotopically heavy sulphur during magmatic fractionation resulting in a 2‰ enrichment of $\delta^{34}S$ of pyrite in the upper gabbros from the complex compared to the sulphides of lower mafic and ultramafic units from the same intrusion (Ripley, 1983).

6.3.2 Ophiolite complexes

In contrast to the large layered intrusions discussed above, chromitites and ultramafic-mafic cumulate rocks of ophiolite complexes are generally sulphide (and Pt and Pd)-poor. However, there are some notable exceptions including the ultramafic and mafic cumulates of the Acoje Critical Zone of the Zambales ophiolite (Orberger *et. al.*, 1988; Abrajano and Pasteris, 1989), and stratiform disseminations of sulphides and PGE in olivine-rich cumulates of the Leka ophiolite (Pedersen, 1993) and the Shetland ophiolite (Prichard and Lord, 1990). There is a paucity of $\delta^{34}S$ measurements of sulphides in ophiolitic cumulate rocks. Abrajano (1984) reports restricted mantle like sulphide and whole-rock $\delta^{34}S$ signatures of +2 to +3‰ from ultramafic cumulates from the Zambales ophiolite. Alt (1991) reports $\delta^{34}S$ values of +0.2 to +7.5‰ for sulphides from gabbros in the Cyprus Crustal Study Project drillhole Cy-4, Troodos ophiolite. The $\delta^{34}S$ values close to 0‰ were ascribed to primary MORB-like sulphur with higher values reflecting oceanic arc-like sulphur (+4 to +5‰) and local incorporation of seawater-derived sulphur during hydrothermal alteration.

6.4 Hydrothermal processes

Sub-oceanic metamorphism of oceanic crust by deep penetration of seawater can cause large-scale redistribution of sulphur and modify magmatic sulphur isotope signatures (Grinenko *et al.*, 1975; Edmond *et al.*, 1979). Experiments, theoretical modelling and measurements of sulphur in oceanic crust have led to a consistent model (*e.g.* Shanks *et al.*, 1981; Bowers, 1989) whereby most of the sulphate present in seawater, precipitates as anhydrite ($CaSO_4$) during heating in recharge areas. Only very small amounts of sulphate in solution can survive to high temperatures, where the sulphate is reduced to sulphide by reaction with ferrous iron in the crust, or through conversion of igneous pyrrhotite to pyrite (Alt *et al.*, 1989). Sulphur in deep hydrothermal fluids is dominantly 'basaltic' in composition ($\delta^{34}S$ = 0 to +1‰), and exists solely as sulphide. $\delta^{34}S$ values of seafloor vent fluids and sulphide deposits, which are up to +6‰, are attributed to local reduction of seawater sulphate in the near subsurface around the vents and within the deposits themselves

(Janecky and Shanks, 1988). The presence of anhydrite (40ppm), in the lower gabbros from Hole Cy–4, Troodos ophiolite and sulphide with $\delta^{34}S$ =+5.7‰ was cited by Alt (1991) as evidence for deep reduction of seawater-derived sulphur. In a model such as this, following Shanks and Seyfried (1987), seawater-derived sulphate is reduced at temperatures ≥ 250°C by the conversion of igneous pyrrhotite to secondary pyrite:

$$7FeS + 8H^{+} + SO_4^{2-} = 4FeS_2 + 4H_2O + 3Fe^{2+}.$$

However, this reaction, using seawater sulphate = +21‰ and basaltic pyrrhotite = 0‰ can only enrich the resultant sulphide up to +2.7‰, so to explain the higher $\delta^{34}S$ values additional seawater sulphate reduction must be involved, through oxidation of Fe^{2+} in olivine and pyroxene deep in the crust (*e.g.* Mottl *et al.*, 1979).

$$8Fe^{2+}\ 10H^{+} + SO_4^{2-} = 8Fe^{3+} + H_2S + 4H_2O.$$

Here H^{+} is supplied by the formation of chlorite, talc or amphibole. Quantitative reduction of sulphate by this reaction can result in sulphide with a $\delta^{34}S$ value of +21‰. This ^{34}S-rich sulphide can then be combined in hydrothermal solutions with variable proportions of igneous sulphur leached from basalts (+0.1‰, Sakai *et al.*, 1984) to produce the observed $\delta^{34}S$ values of sulphide in hydrothermal vent fluids and sulphide deposits (+0.9 to +7.4‰, *e.g.* Alt *et al.*, 1989). From the study of material recovered from the East Pacific (DSDP Hole 504B), which accesses a sheeted dyke complex (oceanic seismic layer 2) to a depth of 1233m below the seabed, Alt *et al.* (1989) proposed a model for the flux of sulphur between oceanic crust and seawater. Losses of basaltic sulphur from volcanics to seawater, fixation of seawater sulphate in the crust as sulphide deposits, and transfer of crustal sulphur from altered gabbros and dykes to sulphide deposits were thought to be the major processes affecting the distribution of sulphur in the crust. A schematic diagram showing these processes is given in Fig. 6.2. Hydrothermal alteration occurred in four different stages as the crust was generated at the spreading axis and moved away from the axis with time:

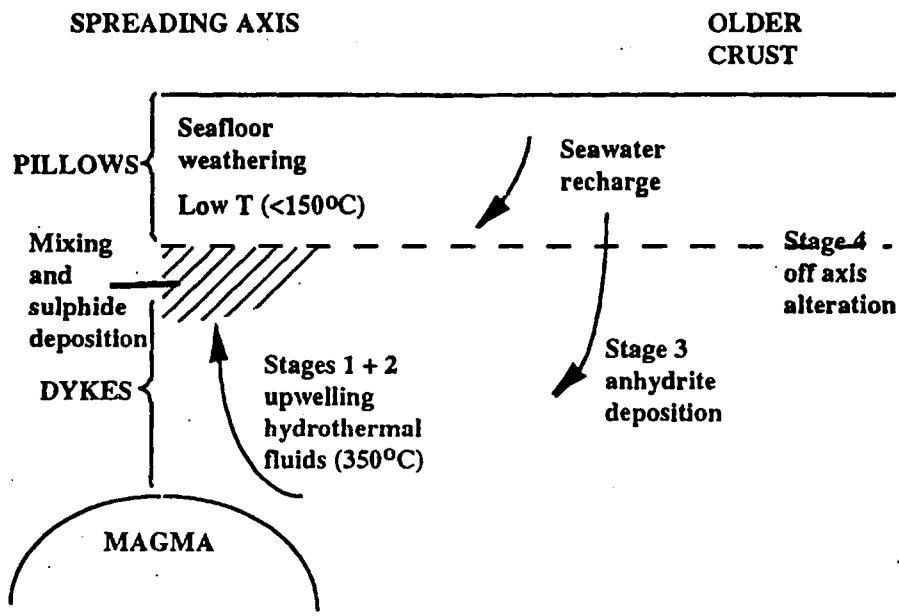

Fig 6.2. Diagram showing the major alteration stages and hydrothermal history of a modern spreading axis (DSDP site 504B). As freshly generated ocean crust moves away from the spreading axis, it passes through the various parts of a circulation cell and experiences different alteration processes. Similarly, a parcel of seawater evolves as it passes through different parts of the crust and reacts with the rock under various conditions. From Alt *et al.* (1989) (see text for further explanation).

(i) Stage 1 axial greenschist hydrothermal alteration of the crust by seawater at temperatures of 250-350°C and water/rock ratios of around 1.

(ii) Stage 2 axial upwelling of highly reacted 250-350°C hydrothermal fluids (metal enriched, Mg depleted) through the dykes, mixing of these fluids with cold seawater circulating in the overlying pillow section, and deposition of quartz + epidote + sulphide veins within the lithologic transition zone.

(iii) Stage 3 seawater recharge in the downwelling limb of a convection cell and formation of anhydrite in fractures.

(iv) Stage 4 off-axis alteration and formation of calcic zeolites at temperatures of 100-250°C.

Following on from this work on the oceanic crust, Alt (1991), reported the sulphide mineralogy, sulphur contents and sulphur isotopic composition of a section through the

Troodos ophiolite, Cyprus. It was concluded that processes affecting sulphur in the Troodos ophiolite were generally similar to those occuring within the oceanic crust, *i.e.* redistribution of sulphur within the crust and the incorporation of seawater-derived sulphur into the crust, and that this led to an overall positive shift in the $\delta^{34}S$ of the ophiolite. Anorthositic gabbros from the cumulate sequence of the Bay Of Islands ophiolite, yield $\delta^{34}S$ values of +7±3‰ (Lydon and Lavigne, 1990), suggesting that the sulphides derived a significant proportion of their sulphur from a fluid containing seawater sulphate. Post-obduction serpentinization and metamorphism of ophiolitic crust may lead to significant remobilization of sulphur from sulphides. In particular, talc-carbonate alteration along the basal thrust contact of ultramafic bodies with country rocks has been shown to be an environment conducive to the mobilization and redeposition of sulphides (Groves *et al.*, 1974) with the possible introduction of extraneous isotopically distinct sulphur.

6.5 Sulphur isotope geochemistry

6.5.1 Introduction

One of the primary aims of this study was to establish a sulphur isotope profile through the Shetland ophiolite. Once this had been achieved, specific problems related to aspects of sulphide mineral genesis in the complex could be addressed. The PGE-mineralization in the ophiolite, which is represented by discreet PGM (Prichard *et al.*, 1986) and Pd and Pt-bearing Ni-antimonides (Chapter 3) are often intimately intergrown with Ni-Fe sulphides and chromite. The association of anomalously high concentrations of PGE with sulphides and chromite has been cited as evidence for a primary magmatic origin for the PGE and sulphides (Lord, 1991). Sulphur isotope analysis of such 'magmatic' sulphides should give $\delta^{34}S$ values within the magmatic range of 0±3‰ defined by Ohomoto (1986). As outlined in Chapter 1, some uncertainty surrounds the exact source of the sulphur in sulphides intergrown with PGM from the Cliff locality. An attempt to ascertain whether the source of sulphur at Cliff is magmatic, remobilized or introduced by hydrothermal fluids can only be facilitated by comparing the $\delta^{34}S$ values of sulphides from Cliff with $\delta^{34}S$ values of

sulphides in equivalent lithologies from elsewhere in the ophiolite. This has been attempted by analysing sulphide-bearing dunite pods in harzburgite from Cliff, and comparing them with sulphide-bearing dunite pods in harzburgite from elsewhere in the ophiolite. Another problem addressed in this chapter is whether the process of serpentinization in the Shetland ophiolite is isochemical with respect to sulphur, *i.e.* whether sulphur produced by the desulphidation of nickel and copper-sulphides (now represented by Ni-Fe alloy (awaruite) and native Cu respectively) is conserved on the scale of a hand specimen or whether it moves for metres or 10's of metres within a lithology. Substantial loss of sulphur from a Ni-Fe, Cu-sulphide aggregate during serpentinization could theoretically significantly alter the $\delta^{34}S$ value of the residual sulphide. This problem is addressed in section 6.5.5.1. Primary pentlandite is often completely replaced by heazlewoodite (Chapter 3). The alteration of pentlandite to heazlewoodite in the ultramafic sequence of the Shetland ophiolite has been predicted to be isochemical with respect to sulphur (Chapter 4), such that the sulphur isotope composition of heazlewoodite should be similar to the precursor pentlandite. This problem is tackled using laser probe analysis of intergrown pentlandite and heazlewoodite in section 6.5.5.2. In section 6.5.6 the results of whole-rock sulphur isotope measurements and microprobe chrome-spinel analyses, obtained at intervals over approximately 1.5 metres of drill-core material containing enrichments of PGE and sulphides from the cumulate dunite unit, are presented. This data is compared to the igneous fractionation mechanism proposed by Prichard and Lord (1990) to explain the mineralogical fractionation of the PGM in this core material. Mobilization of sulphide in the carbonate-rich portions of the ophiolite in the vicinity of the basal thrust (Chapter 4) is addressed using sulphur isotopes in section 6.5.7. The source of sulphur in the hydrothermal mineralization from Mu Ness is discussed in section 6.5.8.

The whole-rock sulphur isotope geochemistry of samples from the Shetland ophiolite will reflect a mixture of potentially isotopically distinct sulphide and/or sulphate phases in the rock of interest. Unfortunately it proved impossible to separate these disseminated sulphide and sulpharsenide phases for sulphur isotope analysis and so it was not possible to make

$\delta^{34}S$ measurements on individual sulphide phases. Therefore, potentially significant sulphur isotope fractionations between co-existing or intergrown sulphide phases may be obscured during whole-rock sulphur isotope analysis. For example, isotopic disequilibrium between sulphide phases pyrite and chalcopyrite is a common feature of hydrothermally altered oceanic crust (Alt and Chaussidon, 1990) and it has been cited as evidence for kinetic fractionation during sulphide precipitation from hydrothermal solutions. The possibility of the presence of non-opaque sulphur-bearing phases in rocks from the Shetland ophiolite, which are difficult to recognize by conventional microscopy remains. For example, such mineral phases could include sulphates, such as anhydrite ($CaSO_4$), which has been found in hydrothermally altered oceanic crust (*e.g.* in recrystallized dykes at a depth of 1163m within basement, ODP Hole 504B) and which commonly have $\delta^{34}S$ values similar to that of seawater sulphate (+21‰; Rees *et al.*, 1978). Sulphate sulphur has also been found at a depth of ~1637m within the lower gabbros of the Troodos ophiolite, (Alt 1991). A first order approach to resolve distribution of sulphur within a hand specimen is that of stepped combustion analysis. Whole-rock sulphur isotope analyses are discussed in section 6.5.4.

6.5.2 Sampling

Samples were chosen to represent all the main lithologies and alteration styles of the ophiolite, *e.g.* from dunite with 60 modal% relict olivine to talc-carbonate altered rock. Sampling was biased towards those that contained visible sulphide minerals in field-exposure since, at the outset of the project, it was anticipated that individual sulphides would be able to be analysed for their sulphur isotope composition. However, if no sulphides were immediately visible in hand specimen then a representative sample of that particular lithology was taken. A map of the sample localities is given in Fig. 1.8.

6.5.3 Stepped combustion analysis

6.5.3.1 Introduction

From experiments outlined in Chapter 5 involving the stepped combustion of nickel, iron and copper sulphides it has been shown that the temperature interval over which the

peak sulphur release occurs may be used to infer the presence of a specific sulphide mineral phase. For example, pentlandite, (which combusts between = 800-900°C), should be resolvable from troilite, (peak combustion = 400-500°C) (Chapter 5). Burgess (1987) showed that the sulphate minerals gypsum and epsomite decomposed at temperatures in excess of 600°C, somewhat higher than for iron and copper-iron sulphides, whereas iron sulphate was found to decompose at 500-600°C.

6.5.3.2 Sulphur release profiles

The stepped combustion profiles of the different iron, nickel and copper sulphides, whose combustion temperatures have been determined in the present study (see Chapter 5) are shown again for reference in Fig. 6.3. These 'reference' profiles are now compared to those obtained from the stepped combustion of samples chosen to the different sulphide mineral assemblages in the Shetland ophiolite. Five samples, including whole-rock powders and sulphide mineral concentrates, were subjected to stepped combustion analysis in increments of either 50°C or 100°C, from room temperature to 1200°C. The results of these experiments are displayed in Fig. 6.4 and Fig. 6.5. Fig. 6.4 (a) shows two release profiles obtained from replicate analysis of a gabbro (JM1) with a sulphide mineralogy identified by reflected light microscopy of pyrrhotite plus lesser amounts of pyrite and minor chalcopyrite. The stepped combustion of JM1 (i) was conducted at 100°C step sizes whereas JM1 (ii) was combusted in 50°C step sizes. The maximum release of sulphur in samples JM1 (i) and JM1 (ii) occurs between 400 and 550°C demonstrating the reproducibility of this technique. Fig. 6.4 (b) shows replicate stepped combustion analysis of JM13 pyroxenite, which contains chalcopyrite, pyrrhotite and pentlandite, and was used as a reference sample in Chapter 5 (section 5.4.3). Three discreet sulphur release peaks are observed over identical temperature intervals in both samples JM13 (i) and JM13 (ii). The temperature interval over which the maximum release of sulphur occurs in JM1 (i) and JM1 (ii) (400 to 550°C), is somewhat lower than the sulphur release peak in sample JM13 ascribed to the combustion of pyrrhotite (600-700°C). However, the 400 and 550°C temperature interval over which the maximum release of sulphur occurs in sample JM1 is very similar to the temperature interval over

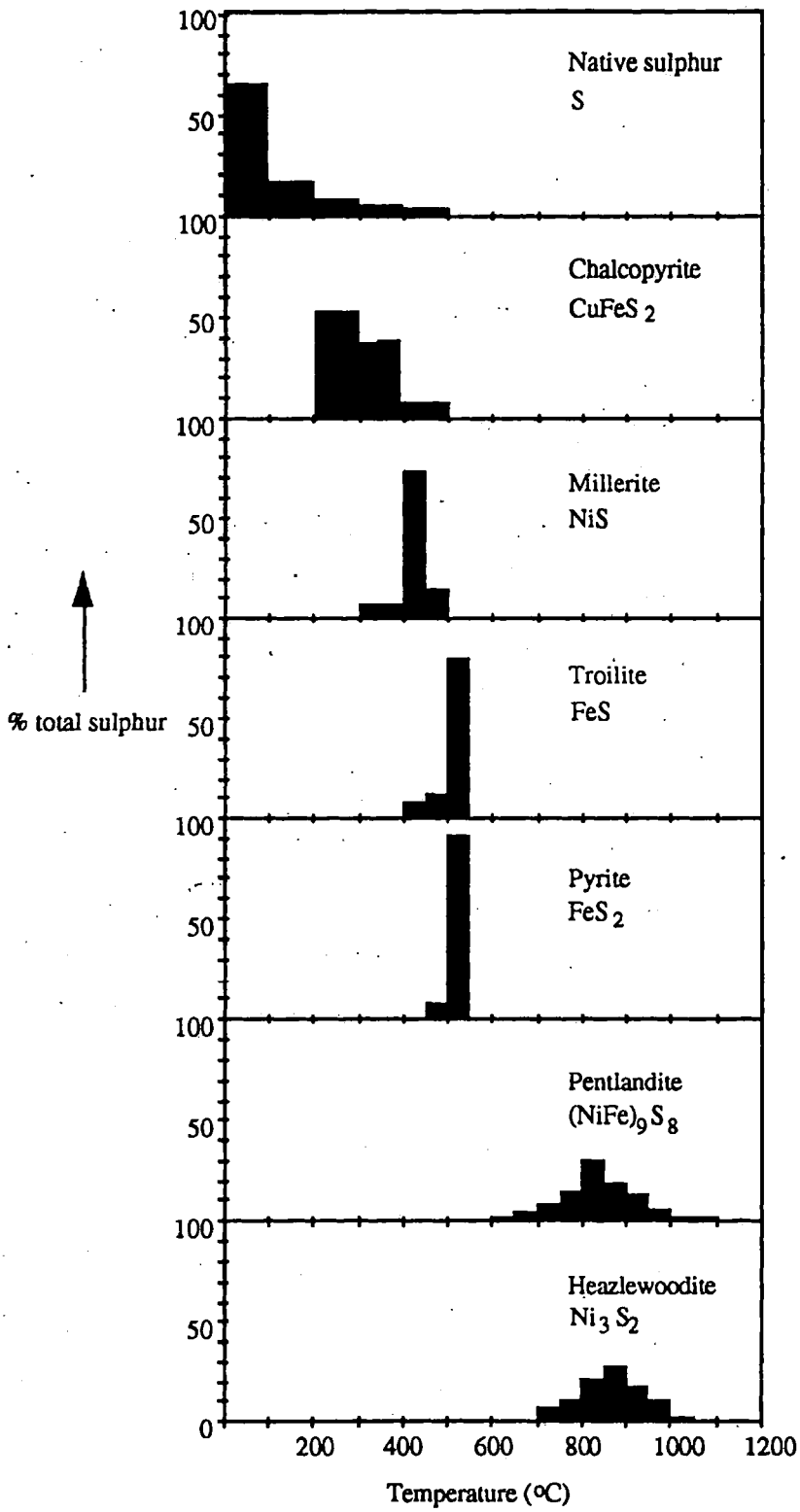

Fig 6.3. Diagram showing the sulphur release profiles of some reference sulphide samples and native sulphur along with their mineral formulae analysed during the present study. Native sulphur and chalcopyrite data from Burgess (1987).

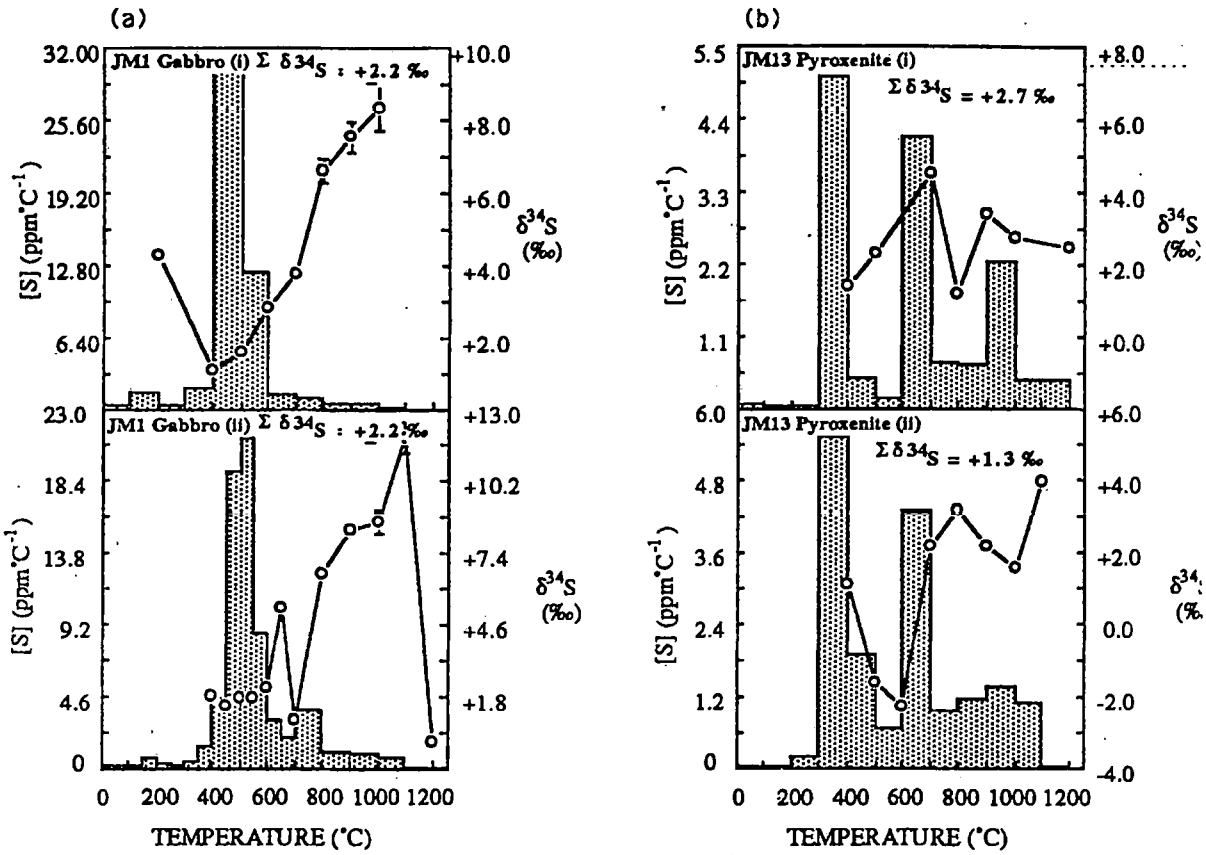

Fig. 6.4. Sulphur release profiles and sulphur isotope values for a gabbro and pyroxenite from the Shetland ophiolite. The two stepped combustion profiles for each of the gabbro (a) and pyroxenite samples (b) are replicate analyses. The stepped combustion profile of pyroxenite (i) is used as a reference for the stepped combustion of other sulphide-bearing samples from the Shetland ophiolite.

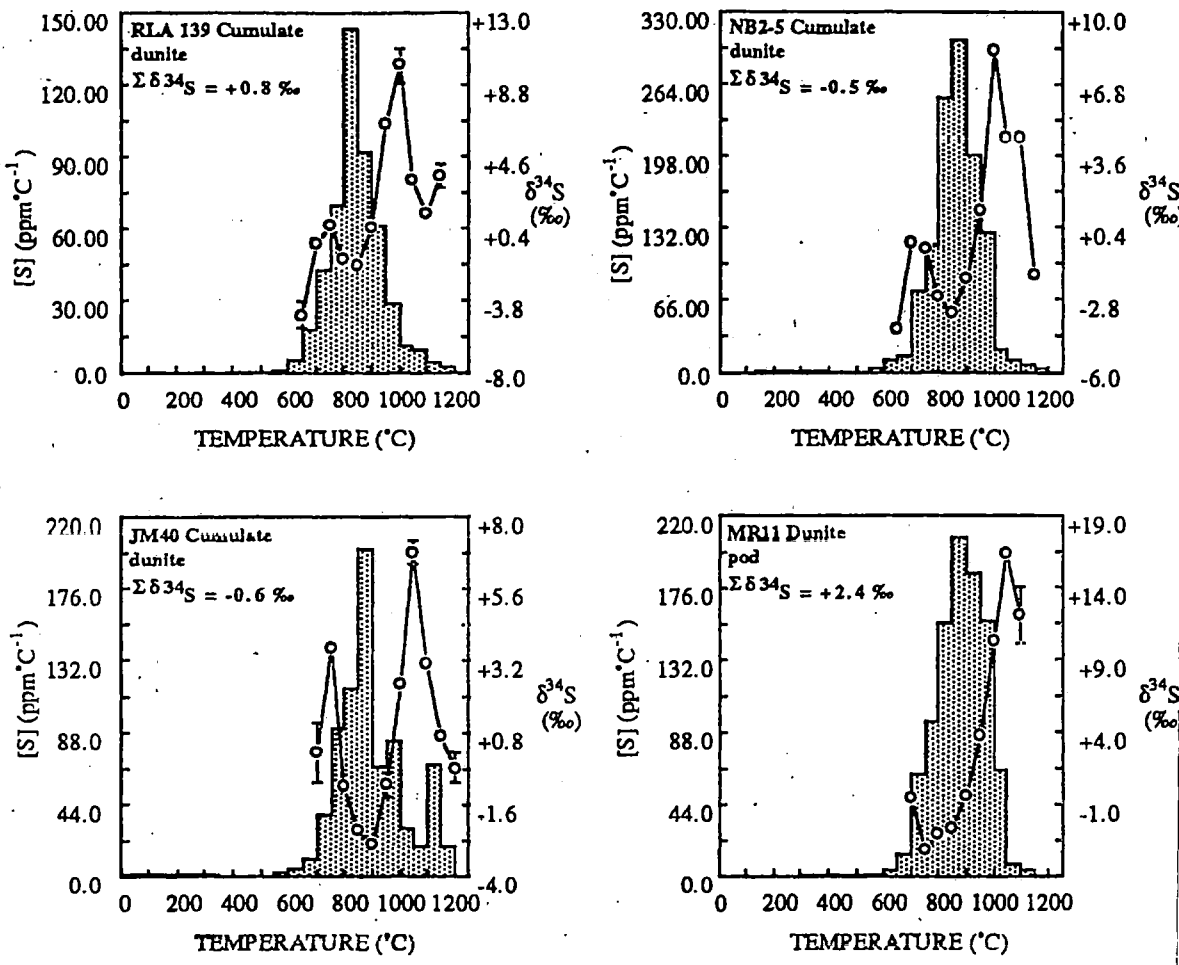

Fig. 6.5. Sulphur release profiles and sulphur isotope values for four different dunites from the Shetland ophiolite.

which the pure reference sulphides troilite and pyrite combust (Fig. 6.3). The discrepancy between the combustion temperature of the pyrrhotite in sample JM1 (Fig. 6.4 (a)) compared to the reference sample JM13 (Fig. 6.4 (h)) is unclear, but may arise from matrix effects within each sample. In sample JM1 the pyrrhotite is intergrown with pyrite which, with reference to Fig. 6.3, combusts at a similar temperature to pyrrhotite. In sample JM13, the pyrrhotite is intergrown with more refractory pentlandite which may supress the combustion of the pyrrhotite, resulting in the sulphur release peak from pyrrhotite being shifted to higher temperatures. Stepped combustion profiles of sulphide mineral concentrates from cumulate dunites and a dunite pod in harzburgite (Fig.6.5) are all very similar but differ markedly from the release profiles of the gabbro and the pyroxenite (Fig. 6.4). Sample RLA 139 (Fig. 6.5) which contains >80 p.t.s pentlandite was used as the reference material to establish the stepped combustion profile of pentlandite (Chapter 5). Similarly, sample NB2-5 (Fig. 6.5), which contains >75 p.t.s. heazlewoodite was used to calibrate the release profile of heazlewoodite. The majority of sulphur in all of the dunites in Fig. 6.5 is released between 600 and 1100°C, with peak releases occurring between 800 and 900°C and is therefore comparable to the release profile obtained from the stepped combustion of pentlandite and heazlewoodite (Fig. 6.3). These conclusions are in agreement with the sulphide mineralogy of these samples established by reflected light microscopy, *i.e.* pentlandite-heazlewoodite. Therefore, with recourse to the 'reference' stepped combustion profiles of Fig. 6.3 the release profiles obtained from the stepped combustion of rock powders and sulphide mineral concentrates from the Shetland ophiolite may be explained adequately by sulphur released from the combustion of pyrite, pyrrhotite chalcopyrite, pentlandite and heazlewoodite. The presence of significant amounts of sulphate minerals, contained within gabbro sample JM1 (Fig. 6.4(b)) is effectively negated by the stepped combustion profile of this sample. However, the presence of minor sulphate in the sample of pyroxenite and the sulphide-bearing dunites would be masked by the heazlewoodite and pentlandite release profiles in these samples. The possibility of the presence of minor sulphate minerals in these samples cannot, therefore, be ruled out. Gunn *et al.* (1985) note the presence of an unidentified Ni-

Fe sulphate as a weathering product of pentlandite from the Cliff locality, and such sulphates may be widespread alteration products of Ni-Fe sulphides in the complex.

6.5.3.3 Sulphur isotopes

A comparison of the $\Sigma\delta^{34}S$ values of the Shetland samples obtained by stepped combustion along with those $\delta^{34}S$ values obtained by bulk combustion of Ag_2S which represents chemically extracted whole-rock sulphur, are shown in table 6.1. It can be seen that the $\delta^{34}S$ values obtained from the stepwise experiments are between 0.7 and 3.6‰ (average -2.1 ± 1.0‰) lighter than the equivalent whole-rock values. This is similar to the observed kinetic isotope fractionations reported by Burgess (1987) between the $\delta^{34}S$ values of troilite obtained by stepped combustion (-2.5‰) and that obtained by bulk combustion (-0.4‰).

Sample	*ppm S stepwise*	*ppm S bulk*	*$\Sigma\delta^{34}S$ stepwise*	*$\delta^{34}S$ bulk*	*$\delta^{34}S$ stepwise-bulk*
JM1	4901	14587	+2.2	+4.8	-2.6
JM13	1419	3350	+2.7	+3.4	-0.7
JM40	n.d.	733	-0.6	+3.0	-3.6
RAL139	n.d.	1250	+0.8	+3.1	-2.3
NB2-5	n.d.	1450	-0.5	+1.5	-2.0
MR11	n.d.	825	+2.4	+4.0	-1.6

Table 6.1. Comparison of the cumulative $\delta^{34}S$ ($\Sigma\delta^{34}S$) obtained by stepped combustion analysis with the bulk $\delta^{34}S$ of samples from whole-rock chemical extraction the Shetland ophiolite. n.d. = no sulphur content determined since sample was a mineral concentrate.

The reason for this discrepency has been discussed in Chapter 5 and is considered to arise from the production of SO_3 during the stepped combustion experiments (Burgess, 1987) The large changes in $\delta^{34}S$ values, *e.g.* -2.9‰ to +6.8‰ during the combustion of essentially monominerallic samples (*e.g.* JM40, Fig. 6.5) (which contains >70% pentlandite p.t.s.) are considered to be due to kinetic isotope effects during combustion. Therefore from

the stepped combustion analysis of whole-rock powders and sulphide mineral concentrates from the Shetland ophiolite the following conclusions may be reached. i) The minerals chalcopyrite, pyrrhotite and heazlewoodite/pentlandite can be resolved from one another by stepped combustion. ii) Sulphide is the dominant sulphur-bearing phase in these rocks and sulphate is probably insignificant. However it is possible that significant sulphate may have formed during weathering by the supergene oxidation of sulphide to sulphate (Gunn *et al.*, 1985). Such sulphates produced by non-equilibrium oxidation of sulphides should show $\delta^{34}S$ values essentially identical to those of the initial sulphides. Such a relationship has been observed between 'supergene' sulphate and 'hypogene' sulphides, where $\delta^{34}S$ sulphate ≈ $\delta^{34}S$ sulphide. iii) Previous studies established that $\delta^{34}S$ measurements during stepped combustion analysis are depleted by approximately 2‰ compared with $\delta^{34}S$ measurements obtained from whole-rock samples. When this fractionation is taken into account, the $\sum\delta^{34}S$ stepped combustion values obtained during this study are similar to the whole-rock $\delta^{34}S$ values of chemically extracted sulphur. Whole-rock sulphur isotope analysis can therefore be expected to reflect the total sulphide $\delta^{34}S$ of a rock.

6.5.4 Whole-rock sulphur concentration and isotope measurements

Whole-rock sulphur determinations were carried out on 67 different samples from the Shetland ophiolite and underlying metasediments (appendix B.3). All sulphur determinations are considered accurate to ± 50ppm and are a measure of total sulphur in the sample, *i.e.* both acid-soluble sulphide and any sulphate sulphur (Chapter 5). Wide ranges in the sulphur contents of the different lithologies are apparent which in part reflect the different styles of mineralization in the ophiolite. For example, the gabbro unit is host to both finely disseminated sulphide mineralization (<800ppm S) and also hydrothermal pyrite mineralization (>3.6 wt.%S). Sulphur contents and $\delta^{34}S$ values were also determined on six samples of metasedimentary rocks adjacent to the basal thrust near Loch of Cliff and also at Nor Wick (Fig. 1.8), because it was thought that disseminated sulphides in talc-carbonate rocks at the basal thrust could have derived a portion of their sulphur from the metasedimentary sequence (see section 6.5.7).

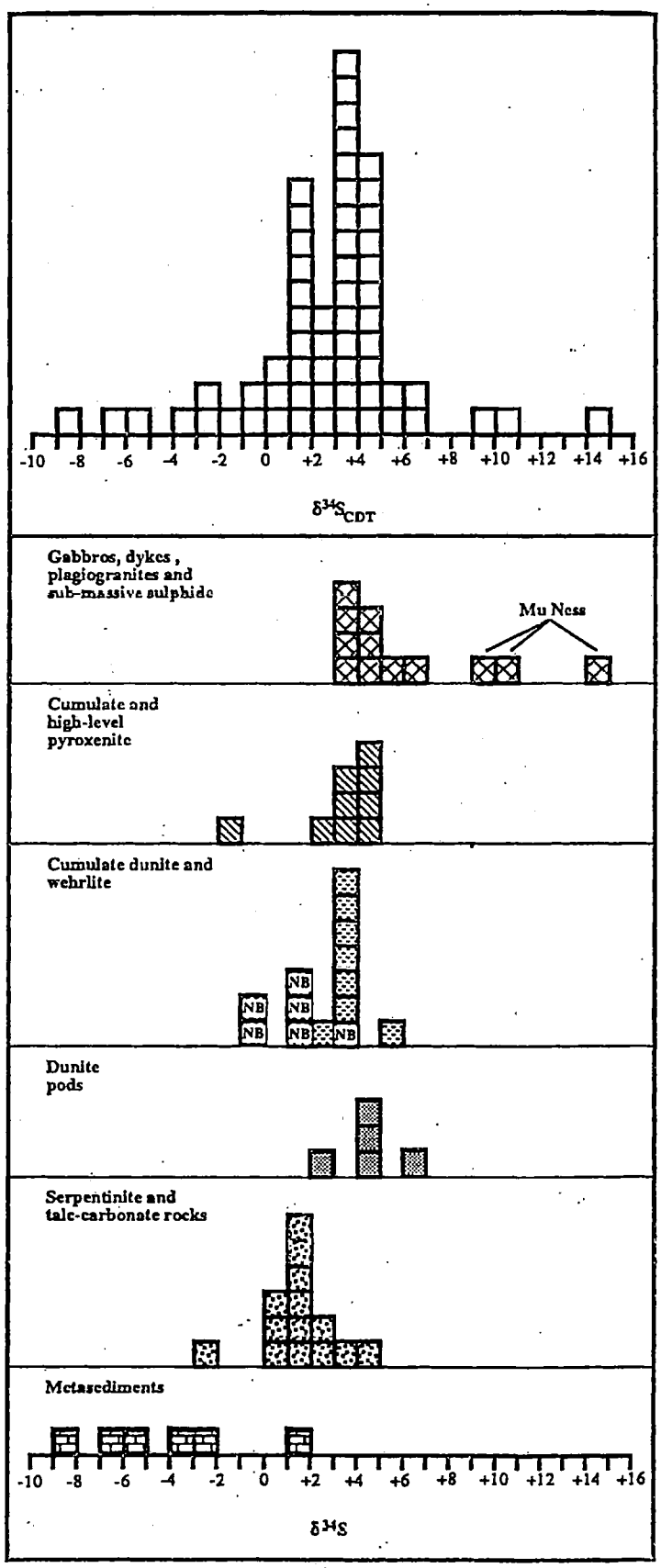

Fig. 6.6. Histograms showing; a) the distribution of $\delta^{34}S$ values for all lithologies of the Shetland ophiolite including samples of metasediments and b) each main lithology of the Shetland ophiolite. NB = analyses from NB-2 borehole (see section 6.5.6).

54 of the 67 samples analysed for their whole-rock sulphur contents were also subjected to sulphur isotope analysis. The results are displayed as a histogram in Fig. 6.6. The $\delta^{34}S$ values for the entire sample suite from the ophiolite, excluding the data for the underlying metasediments, range from -2.4 to +14‰, and have an average value of +3.3±2.7‰.

Metasedimentary rocks

These rocks, tentatively assigned an Upper Dalradian age by Flinn, (1985) include 5 samples of pelitic schists, a mass of impure limestone from Loch of Cliff, and one sample of schist from The Taing, Nor Wick. They contain 66-3010ppm S, average 1604ppm. $\delta^{34}S$ values range from +1.6 to -8.1‰ with a mean $\delta^{34}S$ value of -4.2±3.4‰. Lowry *et al.* (1992) report a range of $\delta^{34}S$ values for Grampian Dalradian-hosted sulphide mineralization from -6 to +42‰.

Serpentinite and talc-carbonate rocks

Samples were collected from close to the basal thrust at Loch of Cliff and from the vicinity of the basal thrust at Shure Taings, Clibberswick Block, where the basal thrust contact is exposed on the beach. These samples include rocks altered to talc-magnesite/calcite-serpentine as well as serpentinized harzburgites. Sulphur contents are generally low, 52-1150ppm average 267ppm, (n=16). and exhibit a range of $\delta^{34}S$ values from -2.4 to +4.6‰ with a mean value of +1.3±1.6‰.

Harzburgite, dunite pods and ultramafic cumulates

Three harzburgite samples contain 98-150ppm S. Whole-rock sulphur isotope analysis of harzburgite was often limited by low sulphur contents. However, two analyses were possible; these are from the Cliff locality which has $\delta^{34}S$ values of +1.2‰ and +5.7‰. Six samples taken from dunite pods hosted in harzburgite contain 82-980ppm, average 328ppm sulphur and have a mean $\delta^{34}S$ value of +4.3±1.4. As outlined in Chapter 1, some uncertainty surrounds the exact source of the sulphur in sulphides intergrown with PGM hosted in a dunite pod from the Cliff locality. In this study, whole-rock sulphur

isotope analysis of the PGE-enriched envelope (50 ppm ΣPt + Pd) to partially serpentinized sulphide-bearing dunite (4 ppm ΣPt + Pd, Lord, 1991) was inhibited by the extremely low sulphur content of samples of the former lithology (<50 ppm). Two sulphur isotope analyses of samples from the sulphide-bearing dunite (301 to 980ppm S), which contain approximately 4 ppm ΣPt + Pd, gave $\delta^{34}S$ values of +4.0 and +4.4‰. Another dunite pod from Cliff, with an unconstrained PGE content, contained 218ppm S and had a $\delta^{34}S$ value of +4.4‰. A whole-rock $\delta^{34}S$ measurement from a dunite pod from north of Hagdale (Fig. 1.5) gave a $\delta^{34}S$ value of +2.5‰. Fourteen samples of cumulate dunite and a wehrlitic dunite contain 322-1679 ppm (average 942ppm) sulphur and have a mean $\delta^{34}S$ value of +2.5±1.5‰. Seven samples of cumulate pyroxenite have 204-3350ppm (average 787ppm) sulphur and a mean $\delta^{34}S$ value of +2.9±2.0‰. Two samples of high-level pyroxenite contain 496-602ppm sulphur and have $\delta^{34}S$ values of +3.5‰ and +4.6‰. The average sulphur isotope values of all these lithologies are all close to the 'magmatic' values of Ohomoto (1986).

Gabbro and dyke complex

Seven samples were analysed from the gabbro and dyke complex near Nuda, another from the gabbro of Uyea Island, and one from Mu Ness (Fig. 1.8). These rocks display a wide range in sulphur content from 148-14587ppm (average 3356ppm) sulphur. The mean $\delta^{34}S$ value for the sample suite is +4.3±1.2‰.

Submassive pyrite mineralization and plagiogranite, Mu Ness

An amphibole pegmatite, gabbro and plagiogranite are host to hydrothermal pyrite mineralization and contain 1040ppm (plagiogranite) to 3.6wt% sulphur (gabbro). $\delta^{34}S$ values for these samples range from +9.6 to +14.0‰ (Fig. 6.6).

6.5.4.1 Sulphur contents: Discussion

The sulphur contents of samples from the Shetland ophiolite are generally proportional to the amount of visible sulphide in hand specimen. Serpentinized harzburgites contain an average of 145ppm S. Disseminated sulphide mineralization from a limited

number of samples from dunite pods, cumulate dunites and cumulate pyroxenites have average sulphur contents of 328, 941 and 787ppm respectively. In the gabbro complex, the wide range in sulphur contents reflects different styles of sulphide mineralization. Four samples of gabbro with sulphur contents <800ppm contain sparse disseminated blebby sulphides. Samples with >1000ppm S include gabbro with veinlets of euhedral pyrite mineralization that is of hydrothermal origin. Serpentinized harzburgites contain an average of 145ppm S whereas talc-carbonate altered rocks from the basal thrust contain an average of 267ppm S.

The higher average sulphur contents for the crustal ultramafic rocks compared to the harzburgites is in general agreement with observations from other ophiolite complexes. For example, Leblanc *et al.* (1991) noted that the sulphur concentration was 3 to 4 times higher in the dunites from the Masqad area of the Oman ophiolite compared to the underlying harzburgites, an enrichment thought to be of magmatic origin (Lorand, 1988) possibly due to the scavenging of sulphur from the solid residue during high degrees of partial melting (Ionov *et al.*, 1992). The average sulphur content for the Shetland ophiolite, excluding the pyrite mineralization at Mu Ness, is 981ppm (which compares favourably to estimates of the sulphur content of MORB crust, 960±60ppm (Czamanske and Moore, 1977)), and 1782ppm if these three samples are included. However, since the sampling of the different ophiolite lithologies was biased towards those that contained visible sulphide minerals in hand specimen, then the figure of 981ppm may well be an overestimate of the average sulphur content of the ophiolite.

6.5.5 Sulphur isotopes and low temperature equilibration and alteration of sulphides in the ultramafic cumulates and dunite pods

In Shetland, the sulphides display a complex subsolidus history which attests to mobilization of sulphur and metals, and the formation of new, lower temperature, sulphide/oxide assemblages. These events are discussed in some detail in Chapters 3 and 4.

6.5.5.1. Reduction of sulphides during serpentinization

If it is assumed that reactions such as:

$$2(Fe\ Ni)_9\ S_8 + 9.5Ni + 16H_2 \rightarrow 4\tfrac{1}{2}\ Fe\ Ni_3 + 16H_2S$$

Pentlandite Awaruite

occur during serpentinization of Shetland dunites, and temperatures of serpentinization were <500°C (upper limit of serpentine stability), then some simple sulphur isotope fractionation mechanisms may be postulated. Equilibrium isotope fractionation between sulphur-bearing phases relative to H_2S as a function of temperature have been established from experimental studies (Kajiwara and Krouse, 1971). For example, they found fractionation factors for $\Delta\delta^{34}S_{Fe_8S_9-H_2S}$ of 0.5‰ at 200°C. The effect of serpentinization on sulphur isotopes can thus be evaluated semi-quantitatively. In the Shetland dunites, the assemblage pentlandite-awaruite occurs only in partially serpentinized lithologies in which extremely reducing conditions can be developed (Frost, 1985). The former presence of pyrrhotite and chalcopyrite in dunites may be tentatively inferred from the fact that native copper associated with pentlandite could have been produced from the reduction of a precursor Cu-Fe-sulphide phase. It may be arbitrarily inferred that Shetland dunites contained ~20% pyrrhotite and ~5% chalcopyrite (from observed native copper abundance) of the total sulphide assemblage. If it is further assumed that sulphur loss was not considerably reduced by formation of secondary pentlandite then it can be calculated that sample JM41, a cumulate dunite, had an initial sulphur content of 430ppm compared with 350ppm which is the measured value. The loss of 80ppm sulphur occurred subsequent to the crystallization of a monosulphide solid solution (MSS) and cupriferous intermediate solid solution (ISS). Assuming an isotopic fractionation factor between FeS and H_2S of 0.5‰ at 200°C ($\Delta\delta^{34}S_{CuFeS_2-H_2S}$ is negligible at 200°C), Kajiwara and Krouse (1971), and a Rayleigh distillation model:

$R_l/R_{lo} = f^{(1/\alpha - 1)}$

where; f = fraction of residual sulphur = 350/450 = 0.814

α = fractionation factor (1.0005 for FeS – H_2S) = 0.9995

R_l = average isotope ratio of the evolved H_2S = ?

R_{lo} = isotope ratio of initial bulk sulphide; (0‰) 0.05‰

then it can be calculated that an 80ppm sulphur loss would result in residual sulphide with a $\delta^{34}S$ value of +0.1‰. This small positive shift in $\delta^{34}S$ is less than the combined errors on chemical separation and isotopic measurement of the technique used (Chapter 5). Therefore, in partially serpentinized peridotites, a sulphur loss of ~20% as H_2S from precursor pyrrhotite and chalcopyrite would cause a small sulphur isotopic shift in the observed sulphide assemblage. The small (<5%) in situ reduction of pentlandite and heazlewoodite to awaruite seen in the partially serpentinized dunites and wehrlites could induce a 0.1‰ enrichment in residual pentlandite, assuming pentlandite and heazlewoodite have similar fractionation factors to NiS_2 relative to H_2S, and $\alpha NiS_2 - H_2S$ at 200°C = 2‰. Again this is a small isotope effect such that the observed reduction of the sulphide assemblages observed in the Shetland ophiolite will have a negligible effect on the whole-rock $\delta^{34}S$ value of serpentinized dunites.

6.5.5.2. Alteration of pentlandite to heazlewoodite: In situ laser $\delta^{34}S$ determinations

From calculations in Chapter 4 involving the molar volumes of pentlandite and heazlewoodite it was considered that the alteration of pentlandite to heazlewoodite was isochemical with respect to sulphur. If this were the case then it was expected that the sulphur isotope composition of heazlewoodite and pentlandite would be identical. Since these two sulphides are usually intimately intergrown as ~1-2mm aggregates, hand picking and physical separation of the two phases was impossible. In order to circumvent this problem the sulphur isotope compositions of pentlandite and heazlewoodite were investigated using a laser microprobe technique in collaboration with Drs A.E. Fallick and P

McConville, (Isotope Geology Unit, Scottish Universities Research and Reactor Centre, East Kilbride, Glasgow, Scotland). A polished block was prepared of a sample of cumulate dunite (sample NB2-1) which contained grains (up to 2mm in diameter) of intergrown heazlewoodite and pentlandite. $\delta^{34}S$ laser probe analyses were performed on these intergrowths. The results of these experiments are listed in table 6.2. A sample of heazlewoodite (sample # BM1925, 1036) from the Department of Mineralogy, British Museum (Natural History), London, was used for determining fractionation of sulphur isotopes on laser combuston is about 90% pure assuming Ni_3S_2 stoichiometry. Kelley and Fallick (1990) showed that sulphur isotopes ($^{34}S/^{32}S$) were fractionated by between 0 and 8‰ during laser combustion compared to $\delta^{34}S$ values obtained by conventional combustion techniques. However, they showed that this fractionation was mineral specific and reproducible. The heazlewoodite fractionation correction ($\delta^{34}S^{std}_{conv} - \delta^{34}S^{std}_{laser}$) used is +1.9‰ at the oxygen pressures and laser powers detailed in table 6.2. The same correction factor (+1.9‰) is applied to pentlandite, since, as a first approximation, this is not unreasonable as small (0.5-2.0‰) and reproducible enrichments in ^{32}S are observed using the oxygen pressures and laser powers detailed in table 6.2.for a wide range of sulphide compositions (Kelley and Fallick, 1990). The mean $\delta^{34}S$ value for pentlandite is +3.16‰ compared to a mean of +3.79‰ for heazlewoodite. The mean inter and intra-grain sulphur isotope compositions of pentlandite and heazlewoodite from NB2-1 therefore differ by 0.63‰. However, due to the small number of samples analysed, the uncertainties in the corrections applied to the $\delta^{34}S$ laser data, and possibly some evidence for $\delta^{34}S$ variation in pentlandite within sample NB2-1 of a few ‰, (table 6.3), this difference may not be real. Therefore, since the laser probe data for pentlandite and heazlewoodite are essentially identical this fact supports the idea that replacement of pentlandite by heazlewoodite is isochemical with respect to sulphur (Chapter 4). The whole-rock $\delta^{34}S$ analysis of sulphur extracted by the modified Kiba method (Chapter 5) from sample NB2-1 is +3.6‰. This is very similar to the laser probe data for pentlandite and heazlewoodite presented in table 6.2. This close agreement between the laser and whole-rock $\delta^{34}S$ determinations indicates that

Sample No.	Mineral	Run No.	Laser (Watts)	pO_2 (mbar)	CO_2 (µmol)	SO_2 (µmol)	$\delta^{34}S_{meas}$ (‰)
BM, 1925, 1036 Heazlewoodite.							
Conventional			Weight (mg)				
i	Heaz.	SA1399	8.9			66.74	+3.39
ii	Heaz.	SA1400	7.1			52.09	+3.41
						Mean	**+3.40**
						(n=2)	**± 0.01**
Laser							
a	Heaz.	LS0916	0.75	456	0.15	2.65	+1.43
b	Heaz.	LS0917	0.75	381	0.06	0.78	+1.48
c	Heaz.	LS0918	0.75	317	0.08	1.10	+1.75
d	Heaz.	LS0919	0.75	265	0.05	0.47	(+1.96)
						Mean	**+1.55**
						(n=3)	**± 0.14**
Fractionation correction = 3.4‰ - 1.5‰ = +1.9‰							
NB2 disseminated heazlewodite/pentlandite aggregates							
1	Heaz.	LS0912	0.75	736	n.d.	n.d.	n.d.
2	Heaz.	LS0913	0.75	738	0.01	0.01	n.d.
3	Pent.	LS0914	0.75	635	0.04	0.07	(+6.32)
4	Pent.	LS0915	0.75	546	0.03	0.05	+3.31
5	Pent.	LS1057	1.50	704	0.06	0.25	+3.31
6	Pent.	LS1058	0.75	610	0.02	0.09	+2.87
						Mean	**+3.16**
						(n=3)	**± 0.21**
7	Heaz.	LS1059	3.0	526	0.04	0.78	+3.72
8	Heaz.	LS1060	3.0	453	0.06	0.55	+3.70
9	Heaz.	LS1061	3.0	392	0.02	0.18	+3.95
						Mean	**+3.79**
						(n=3)	**± 0.12**

Table 6.2 Details of $\delta^{34}S$ determinations carried out on pentlandite and heazlewoodite by laser combustion.

the vast majority of sulphur within sample NB2-1 is contained in pentlandite and heazlewoodite. From the calculation involving the reduction of pentlandite to awaruite and the alteration of pentlandite to heazlewoodite, the whole-rock sulphur isotope analysis of cumulate ultramafic rocks is expected to closely approximate the sulphur isotope composition of the sulphides when they crystallized from an immiscible sulphide liquid. The mean $\delta^{34}S$ values for whole-rock samples of dunite pods (+4.3‰), cumulate dunite and wehrlite (+2.5‰), cumulate pyroxenite (+2.9‰) and high-level pyroxenite (+4.1) are close to, but often slightly outside, the magmatic range of 0±3‰ Ohomoto (1986). These consistently positive $\delta^{34}S$ values would suggest that the primary sulphides derived their sulphur from a ^{34}S-enriched source. The supra-subduction zone origin proposed for the Shetland ophiolite (Prichard and Lord, 1988) suggests that the primary sulphur in the mantle source region of the Shetland ophiolite may have had $\delta^{34}S$ values comparable to modern oceanic arcs (about +4‰) compared to MORB +0.1±0.5‰. Such a ^{34}S-enriched source could account for the 'heavy' sulphur isotope values observed in the crustal ultramafic rocks and dunite pods.

6.5.6. Magmatic fractionation of sulphur isotopes in a stratiform mineralized horizon from the cumulate dunite unit

The sulphur isotope geochemistry of the PGE and sulphide enriched core material from hole NB2 was investigated to see if the mineralogical fractionations noted by Prichard and Lord (1990) correspond to any systematic trends in the sulphur isotope geochemistry. A schematic diagram of this mineralized section of core is shown in Fig 6.7. A 2-3cm thick disseminated chrome-spinel layer marks the stratigraphic base of the mineralized horizon and is followed by a concentration of disseminated Ni-Fe sulphides over a distance of ~1 metre with associated disseminated, sometimes euhedral, chrome spinel crystals which are sometimes intergrown with sulphides and magnetite. The embayed margins of the sulphides suggest a textural position interstitial to relict olivine, now completely pseudomorphed by serpentine. Native copper is closely associated with the sulphides and also occurs in cm long cross-cutting veins which are more abundant at the top of the mineralized horizon

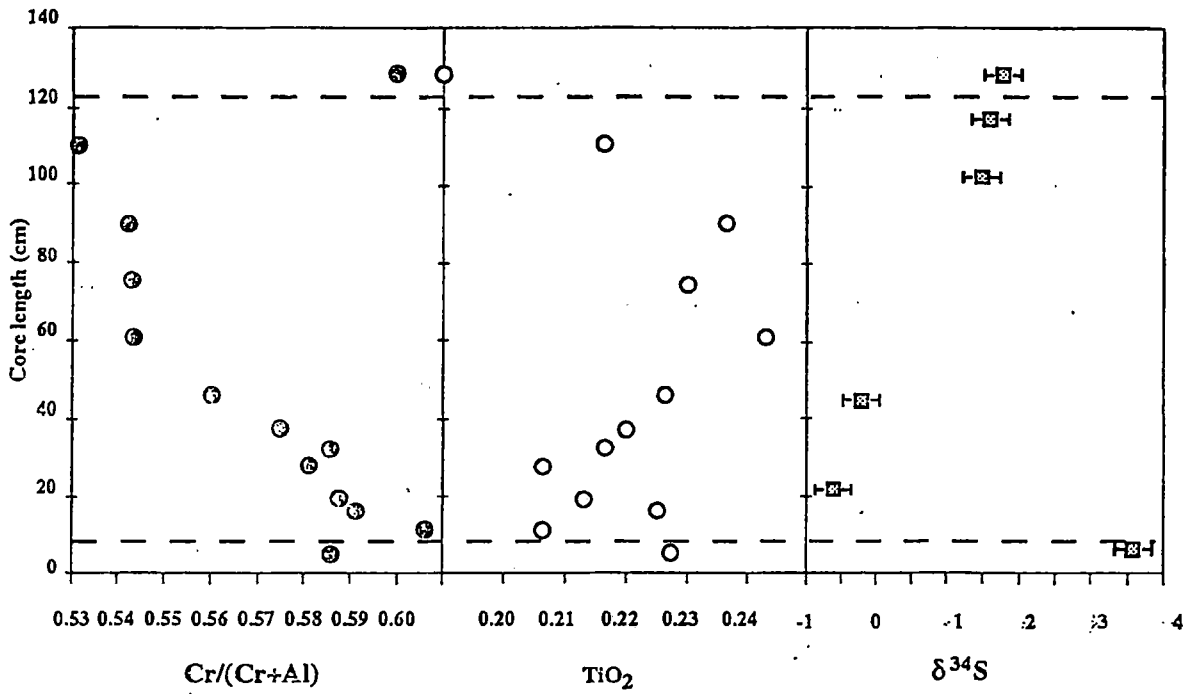

Fig. 6.7. Variation in chemistry of disseminated chrome spinel and whole-rock $\delta^{34}S$ with stratigraphic height in core NB-2, cumulate dunite unit.

(Prichard and Lord, 1990). The core is almost completely serpentinized, with typically <1 modal percent olivine which eliminates the use of the Mg # of olivine as a fractionation index. In only one of the polished thin sections prepared from the core was there sufficient fresh olivine to obtain a quantitative electron microprobe analysis. The analysis was obtained from olivine interstitial to the basal layer of disseminated chrome-spinel. It has a composition which is magnesian, Mg # 91.08, compared to other probe analyses from the cumulate dunite unit, Mg # 87.50-89.78 (n=5). Chrome-spinel is the only major relict primary mineral in the core material whose mineral chemistry has the potential to be used as an indicator of fractional crystallization. The Cr/(Cr+Al) ratio of chrome-spinel has been used to model cumulus fractionation processes in ultramafic and mafic rocks. For example, Jaques (1981), observed decreasing Cr/(Cr+Al) and Mg/(Mg+Fe) in spinels from the olivine cumulates of the Marum ophiolite which is the anticipated spinel trend for low pressure fractional crystallization (Dick and Bullen, 1984; Roberts, 1986). Therefore, the average of 2-4 probe analyses of disseminated chrome spinel grains from each of the 13 polished thin sections available which covered the 140cm of core material were obtained (appendix B2). Well developed euhedral crystals of chrome spinel with negligible alteration to ferritchromit were chosen for analysis in an attempt to negate the effects of secondary alteration processes on the primary spinel chemistry. The mineral chemistry of the chrome spinels from NB2 are within the range of the compositions of disseminated chrome spinel from the dunite unit reported by Gass *et al* (1982). The molar Cr/(Cr+Al) and titanium content of these analyses are plotted against core height in Fig. 6.7. The Cr/(Cr+Al) ratio shows significant variation with stratigraphic height in the core, decreasing from ~0.605 near the base of the section and approaching 0.53 towards the top of the section. The titanium content of chrome-spinel also shows significant variations from low titanium (0.20 wt.% TiO_2) near the base of the section to ~0.24 wt.% TiO_2 near the top of the section. At the top of the section there is a large shift in Cr/(Cr+Al) to ~0.6 accompanied by a drop in TiO_2 to ~0.19 wt.%. A smaller and opposite shift in Cr/(Cr+Al) and TiO_2 occurs in chrome-spinel from the stratigraphically lowest portion of the core, a few cm below the basal layer of disseminated chrome-spinel. In addition to the chrome-spinel probe data six whole-rock sulphur isotope analyses were

obtained over 140cm of drillcore from hole NB2. The sulphur isotope data for NB2 are highlighted in Fig. 6.6. The $\delta^{34}S$ values show that a difference of ~4‰ exists between core material immediately below the thin, basal horizon of chromite concentration (+3.6‰) and that the chromite + sulphide layer immediately above this has a $\delta^{34}S$ value of -0.6‰. Samples taken from progressively higher stratigraphic levels in the core become increasingly more ^{34}S enriched, attaining a value of +1.8‰ from the stratigraphically highest available sample.

The general trend of decreasing Cr/(Cr+Al) of chrome-spinel coupled with a corresponding increase in TiO_2 is the trend expected in chrome-spinel chemistry during fractional crystallization. The abrupt reset in the Cr/(Cr+Al) at the top of the core to higher values (similar to those near the base of the core) and the corresponding drop in TiO_2 could be due to a new input of relatively less evolved magma into a magma chamber now represented by the olivine cumulates. The basal chromite layer in the core has been postulated to represent the base of an input of primitive magma into the cumulate dunite pile (Prichard and Lord, 1990). Therefore, from the chrome-spinel probe data, the top of this magma input could be delineated by the shift to more primitive chrome-spinel compositions observed approximately 120cm above the basal chromite layer. The sulphur isotope data also tend to support this model. A closed system Rayleigh fractionation model, where sulphides precipitate from a finite reservoir of sulphur (HS^- species dissolved in silicate melt), would result in progressively more ^{34}S-enriched sulphides being precipitated as the magma evolves through closed-system fractionation. However, the abrupt change in chrome-spinel chemistry to less evolved compositions at the top of the core is not reflected by a corresponding reset in whole-rock $\delta^{34}S$. One reason for this discrepancy could be due to the relatively poor resolution of the whole-rock $\delta^{34}S$ measurement (average of ~11cm of core material) compared to the chrome spinel data which was obtained from a polished thin section which sampled ~3cm of core material. Alternatively, the sulphides and chrome-spinels, once precipitated from the proposed magma input, could have settled at different

velocities which would result in the observed offsets between chrome-spinel chemistry and $\delta^{34}S$.

6.5.7 The source of sulphur in talc-carbonate rocks

The spatial distribution of $\delta^{34}S$ in the vicinity of the basal thrust is shown in Fig 6.8 (a) (Cliff) and Fig. 6.8 (b) (Nor Wick). The average $\delta^{34}S$ value of 14 samples of serpentinites and talc-carbonate rock taken from both of these localities from close to the basal thrust is +0.9±1.5‰. Harzburgite and associated dunite pods have average. $\delta^{34}S$ values of +3.5 (n=2) and +4.3‰ (n=5) respectively. Metasediments from beneath the basal thrust have $\delta^{34}S$ values ranging from +1.6 to -8.1‰, average -4.2‰ (n=6). Consideration of whole rock sulphur values along the basal thrust, reveals some localized higher concentrations in this zone (up to 1150ppm, average 266ppm S, n=14) over and above those values for harzburgite (98-150ppm S, n=3), the assumed protolith to the talc-carbonate rock. Fig. 6.9. is a plot of the whole-rock $\delta^{34}S$ of metasediments and talc-carbonate rocks against their corresponding sulphur contents. The slightly more ^{34}S depleted values of rocks from close to the basal thrust compared to harzburgite and dunite pods could be explained by introduction of a proportion of isotopically light sulphur from the metasediments beneath the basal thrust. This sulphur could have combined with Ni and Fe released during the breakdown of silicate minerals during talc-carbonate alteration (Chapter 4) to form a metamorphic sulphide asemblage. Furthermore Fig. 6.8 (b) shows that, at Nor Wick, there is a trend to lighter $\delta^{34}S$ values on approaching the basal thrust. This would tend to substantiate the contention made above, namely that there is some mixing between isotopically light sulphur introduced from the metasediments and more ^{34}S-enriched sulphur in the basal ophiolite lithologies.

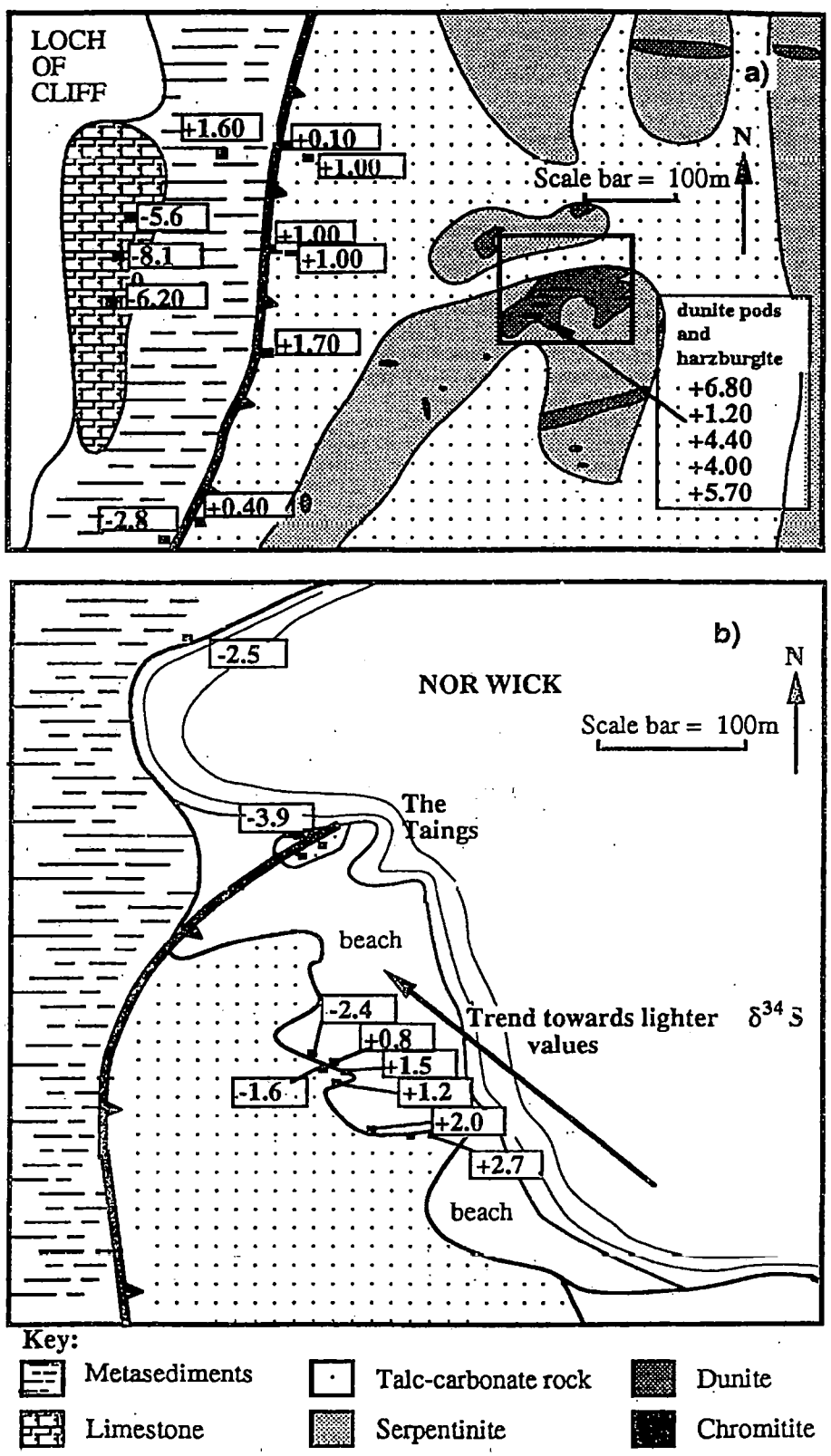

Fig. 6.8. Spatial distribution of whole-rock $\delta^{34}S$ values at a) Loch of Cliff and b) Nor Wick.

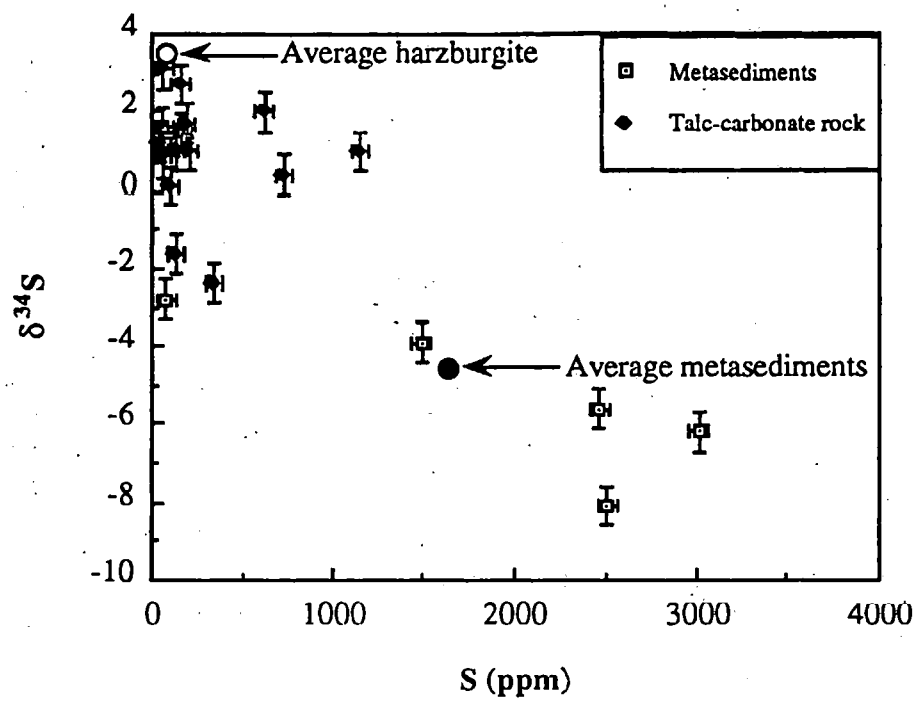

Fig. 6.9. Plot of whole-rock S content against $\delta^{34}S$ of talc-carbonate and metasedimentary rocks from the Shetland ophiolite. The average values for harzburgite (the assumed protolith of talc-carbonate rocks) and the metasediments are also plotted. The field for the talc-carbonate rocks lies intermediate between these two averages suggesting that the talc-carbonate rocks may contain sulphur derived from both harzburgite and metasediments.

6.5.8 The genesis of sulphides in submassive pyrite mineralization, Mu Ness; sulphur and helium isotope constraints

The gabbro and dyke complex yield a mean $\delta^{34}S$ value of +4.5‰ that are close to the magmatic values postulated for the ultramafic sequence. However, the sub-massive pyrite mineralization (mean $\delta^{34}S$ = +11.5‰) is significantly heavier and is considered to result from the precipitation of sulphide from a ^{34}S-enriched hydrothermal fluid. By analogy with other studies of ophiolitic crust, this fluid could be of seawater origin (Janecky and Shanks, 1988).

Location/sample	*Weight (mg)*	*Extraction technique*	*^4He (10^{-7})*	*R/R_a*
Unst MNG (pyrite)	121.3	600°C	8.4±0.08	0.29±0.06

Table 6.3. Helium isotope measurements of a sample of sub-massive pyrite from Mu Ness. Absolute abundance measurements of ^4He are subject to a ±3% uncertainty. R/R_a is a measured $^3He/^4He$ ratio normalized to the air value. R/R_a measurements have a reproducibility of ± 5%. R_a = atmospheric $^3He/^4He$ ratio.

Helium isotope analysis has been carried out to investigate whether the hydrothermal pyrite mineralization from Mu Ness has any affinity with modern mid-ocean ridge sulphide deposits.

Investigation into the isotopic composition of helium and sulphur in hydrothermal fluids trapped in sulphides and sulphates from 21°N on the East Pacific Rise in collaboration with Finlay Stuart at the University of Manchester during this study led to the recognition of a correlation trend between the helium isotopic composition of the trapped fluid inclusion and the $\delta^{34}S$ value of the host sulphide or sulphate (Stuart *et al.*, 1992). Fluids trapped by the sulphides from hydrothermal chimneys at 21°N, East Pacific Rise, have $^3He/^4He$ ratios indistinguishable from 350°C vent fluid (Fig. 6.10). These helium isotope ratios are slightly lower than those measured for Mid Ocean Ridge basalts and are thought to reflect the radiogenic ingrowth of ^4He in the ocean crust. Sulphate $^3He/^4He$ ratios are significantly lower than the vent fluid and represent a dilution by ambient seawater. The $^3He/^4He$-$\delta^{34}S$ correlation (Fig 6.10) confirms a simple mixing relationship (Stuart *et al.*, 1992).

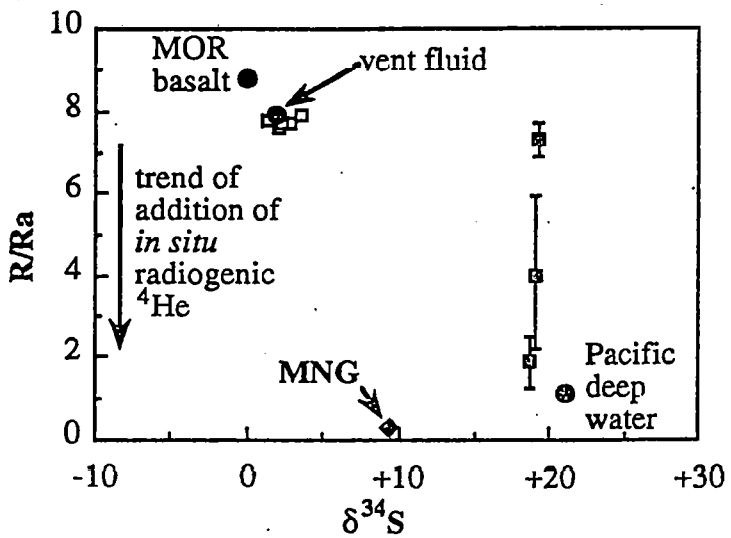

Fig. 6.10. Covariation of He and S in hydrothermal fluids at 21°N, East Pacific Rise. Mineral $\delta^{34}S$ values are plotted against the $^3He/^4He$ ratio of fluids released by crushing. The sulphides from the high temperature chimneys are characterized by mantle-derived helium and corresponding low $\delta^{34}S$ values close to the value of vent fluid $\delta^{34}S_{H_2S}$. While local basalts have acted as the main source of helium and sulphur in the hydrothermal fluids, sulphide $\delta^{34}S$ values are slightly higher than measured MOR basalt =+0.1‰. This reflects the addition of isotopically heavy S through the reduction of seawater sulphate. The lower $^3He/^4He$ ratios of the sulphate samples record the increasing dilution by Pacific deep water and is paralleled by an increase in the value of the mineral $\delta^{34}S$ towards the value of seawater. The data for pyrite sample MNG from the Shetland ophiolite may have initially plotted on a mixing line between vent fluid and seawater (Pacific deep water) but now has a helium isotope composition that may have been significantly modified by the addition of *in situ* radiogenic ^4He from U and Th although its $^3He/^4He$ ratio is higher than that of typical radiogenic He and must require the contribution of a component of mantle-derived volatiles. After Stuart *et. al.* (1992). Open squares = sulphides, closed squares = sulphates.

Two samples of pyrite separated from sub-massive pyrite mineralization from the gabbro complex at Mu Ness were subjected to helium isotope analysis at the University of Manchester. One of these pyrite samples (MNA) did not contain enough He on which to perform an analysis but the other sample (MNG) contained sufficient He for He isotope analysis and the results are displayed in table 6.3. Drawing conclusions from absolute He abundances is dangerous as this is likely to be cruicially dependant on the amount of fluid trapped by the mineral. This amount may be controlled by grain size, the degree to which He has been lost (*e.g.* by diffusion or recrystallization), and the contribution of in situ radiogenic He rather than the initial concentration in solution. MNG has a $^{3}He/^{4}He$ ratio higher than that of typical radiogenic He (0.01-0.07 x R_a) and must require a contribution of mantle-derived volatiles. The high $^{3}He/^{36}Ar$ ratios of MNG (F. Stuart, *pers. comm.*) rules out air as a source of the He in the sample. Furthermore, the $^{6}Li(n,\alpha)^{3}He$ reaction can be ruled out as a source of ^{3}He as Li contents are extremely low (F. Stuart, *pers. comm.*). The trapped fluids in sample MNG are broadly similar to the fluids trapped in sulphide and sulphate minerals from 21°N, East Pacific Rise (Fig. 6.10). Mid Ocean Ridge $^{3}He/^{4}He$ ratios are typically 8-10 R_a, and in the past were probably higher, while those for back-arc basins and subduction environments are generally lower, reflecting the input of crustal material to the basalt source region. However, without the knowledge of U and Th concentrations and the diffusivity of He in sulphides, it is not possible to determine whether the $^{3}He/^{4}He$ value for sample MNG reflects the true fluid value trapped at the time of sulphide precipitation, or has been compromized by the addition of *in situ* radiogenic ^{4}He. This latter scenario may be the most plausible, since MNG is from a fragment of ~470Ma oceanic crust and would be expected to develop a significantly modified $^{3}He/^{4}He$ ratio over the past ~470Ma from U and Th decay.

6.6 Hydrogen and oxygen isotope data

In order to place constraints on the serpentinization and hydrothermal alteration of the Shetland ophiolite, hydrogen isotope analyses have been carried out on a suite of nineteen whole-rock samples representative of the main lithologies present within the complex. Some

additional oxygen isotope analyses have also been obtained. Details of the techniques used to measure hydrogen and oxygen isotope ratios are given in appendix A.6 and A.5 respectively. Since it has been postulated that ophiolites are preserved fragments of oceanic crust (*e.g.* Coleman, 1977) numerous stable isotope studies have been carried out on these rocks. These have shown that systematic downward decrease of $\delta^{18}O$ whole-rock values (from ~+14‰) is linked with increasing metamorphic grade which ranges from low temperature alteration to high-amphibolite facies (*e.g.* Spooner *et al.*, 1974; Stakes *et al.*, 1984).

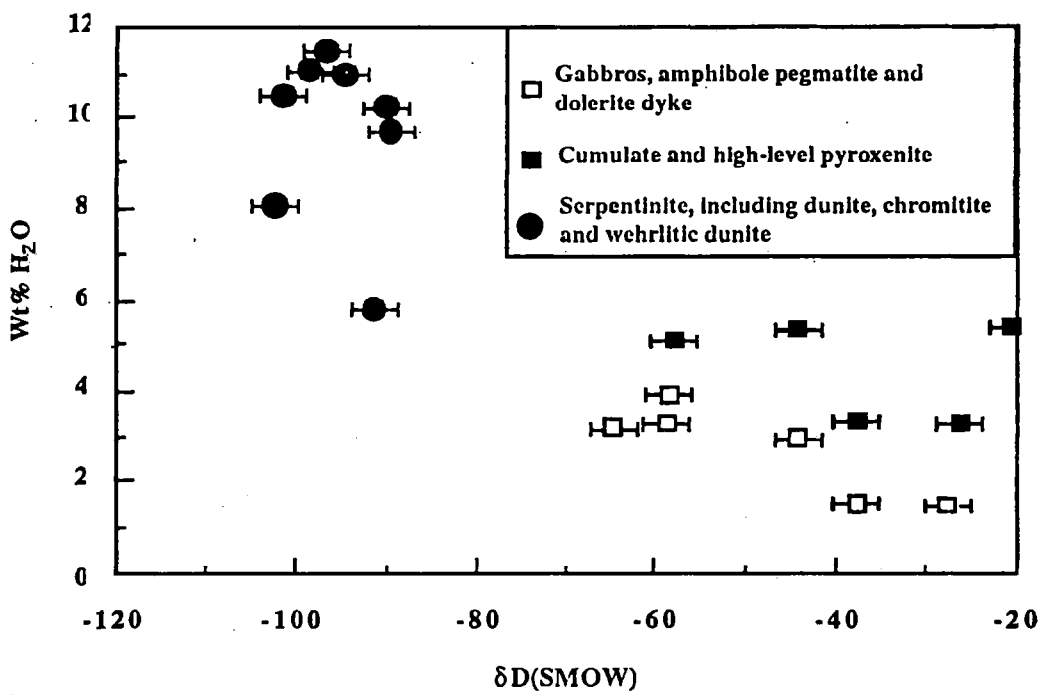

Fig. 6.11. Plot of δD vs. water content of different lithologies from the Shetland ophiolite.

This "$\delta^{18}O$ signature" is interpreted to result from hydrothermal interaction between seawater and the oceanic crust with temperature increasing, and water/rock ratios decreasing, downwards. Additional evidence of hydrothermal interaction is shown by the occurrence of oxygen isotope disequilibrium among coexisting plagioclase-pyroxene pairs (*e.g.* Gregory

and Taylor, 1981). Hydrogen isotope studies of ophiolite terrains have been used to constrain the source of serpentinizing fluids to either "oceanic" or "meteoric". δD whole rock values between –70 and –20‰ can be expected for rocks interacting with seawater, similar to most of the δD values of modern cored oceanic samples (Stakes and Taylor, 1982). However at low temperatures, seawater alteration gives rise to lower $\delta D_{WHOLE\ ROCK}$ values of ≤–95‰ (Savin and Epstein, 1970) Meteoric fluids can produce even lower δD's. The range of δD values for the Shetland ophiolite is –20 to –104‰. In the mafic and ultramafic sections of the Shetland ophiolite, samples have [H_2O^+] concentrations higher than 1%, unlike those of fresh ocean ridge magmas (0.15–0.35 wt.%, Kyser and O'Neil, 1984). Considering samples from the Shetland ophiolite, of the ultramafic samples, the freshest pyroxenite, sample JM11, with >70% clinopyroxene contains 5.39 wt.% [H_2O^+]. Highly serpentinized dunites contain up to 11.44 wt.% [H_2O^+], whereas gabbros contain on average ~3 wt.% [H_2O^+]. These high [H_2O^+] concentrations are attributed to hydration events recorded by the hydrous minerals which occur in all studied samples (Chapter 2)

Fig. 6.11 shows a plot of $\delta D_{(SMOW)}$ *vs.* wt.% [H_2O^+] for samples from the Shetland ophiolite. The data in Fig 6.11 fall into two distinct groups. Firstly, those rocks with δD of -88 to -104‰ with [H_2O^+] > 5.5 wt.% including harzburgite, podiform chromite, dunite and wehrlite, and secondly, clinopyroxenites and rocks from the gabbro complex, with δD of –20 to –65‰ and [H_2O^+] < 5.5 wt.%. The δD values of the mafics and clinopyroxenites (average –43‰ n = 11) is compatible with δD values expected from a seawater hydration event although other fluids ("magmatic", "metamorphic" or "meteoric") cannot be completely ruled out. On the basis of equilibrium hydrogen isotope fractionation between serpentine and water (Wenner and Taylor, 1973) the low $\delta D_{WHOLE\ ROCK}$ of the olivine-rich (or once olivine-rich) ultramafic section cannot be attributed to oceanic hydration (which leads to serpentines whose δD values are between –70 and –30‰ (Wenner and Taylor, 1973; Sheppard, 1980). Water, taken from the land-locked Loch of Cliff, and presumed to represent local meteoric water, has a δD value of –43‰. Wenner and Taylor (1973) suggest an equilibrium fractionation of -48‰ between serpentine and water at

100°C. The 45‰ difference between the heaviest ultramafic serpentinite sample from the Shetland ophiolite ($\delta D = -88‰$), and present day meteoric water ($\delta D = -43‰$) is, therefore, compatible with low temperature exchange of serpentine with local meteoric fluids as has been proposed to explain the δD values of many continental serpentines in ultramafic ophiolitic rocks (Barnes and O'Neil, 1969; Ikin and Harmon, 1983). The close juxtaposition between a wehrlite with δD of –94‰ and pyroxenite with a heavier δD of –59‰ is taken as evidence that aerial exchange of hydrogen isotopes between the wehrlite and meteoric water has been more extensive than in the pyroxenite sample, effectively overprinting any earlier 'oceanic hydration' signature in the wehrlite.

Six whole-rock $\delta^{18}O$ measurements have been performed on different lithologies from the Shetland ophiolite. All $\delta^{18}O$ measurements are reported in ‰ relative to SMOW. Two samples of gabbro ($\delta^{18}O$ values of +5.8 and +5.0‰) and a sample of cumulate pyroxenite ($\delta^{18}O = +5.3$) are close to magmatic values for fresh mid-ocean ridge basalts (+5.8 ± 0.3‰; Taylor, 1968). Gabbros in classic ophiolites such as Troodos and Semail typically have values of +4 to +6‰, as do seafloor gabbros (Ito and Clayton, 1983). However, Gregory and Taylor (1981) note that such primary magmatic values can equally be produced by seafloor hydrothermal alteration processes. A sample of amphibole pegmatite and dolerite dyke are ^{18}O-enriched ($\delta^{18}O$ = +6.5‰ and +10.0‰ respectively) compared to the gabbros and the sample of pyroxenite. By comparison with the conclusions of Gregory and Taylor (1981) these ^{18}O-enrichments could be produced by interaction of these lithologies with a strongly ^{18}O-shifted fluid in addition to retrograde exchange at lower temperatures. A single whole-rock oxygen isotope measurement of a serpentinized dunite sample from the transition zone between harzburgite and cumulate dunite yields a $\delta^{18}O$ value of +7.9‰. The δD value of this sample is -98.6‰ and it plots within the field of ophiolitic serpentines of Wenner and Taylor (1973). The favoured model at present is oceanic hydration of the cumulate section with a later meteoric water overprint in the olivine-bearing ultramafic cumulates and harzburgite. The idea of seawater-sulphate reduction to explain the

high $\delta^{34}S$ values in high-level gabbro mineralisation is not, therefore, negated by the hydrogen and oxygen isotope data.

6.7 Conclusions

The distribution of sulphur in a representative suite of samples from the Shetland ophiolite has been investigated by stepped combustion. Sulphur released from the combustion of pyrite, pyrrhotite, chalcopyrite, pentlandite and heazlewoodite can adequately explain the observed release profiles in these samples and suggests that sulphate sulphur is not a significant component of these rocks. Whole-rock sulphur isotope analyses have been made on a suite of 67 samples from the Shetland ophiolite, chosen to represent all the main lithologies and alteration styles present, and including samples from the underlying metasedimentary sequence. The mean $\delta^{34}S$ values for whole-rock samples of harzburgite (+3.5‰), dunite pods (+4.3‰), cumulate dunite and wehrlite (+2.5‰), cumulate pyroxenite (+2.9‰) high-level pyroxenite (+4.1‰) and gabbro (+4.3‰) are close to but slightly outside the magmatic range of 0±3‰ Ohomoto (1986). The consistently positive $\delta^{34}S$ values would suggest that the primary sulphides derived their sulphur from a ^{34}S-enriched source compatible with the supra-subduction zone origin proposed for the Shetland ophiolite (Prichard and Lord, 1988). Talc-carbonate rocks from close to the basal thrust have an anomalously low mean $\delta^{34}S$ value of +0.9‰ which could be explained by introduction of a proportion of isotopically light sulphur from the metasedimentary sequence (mean $\delta^{34}S$ = -4.2‰) beneath the basal thrust. Calculations show that loss of 20% sulphur as H_2S during the serpentinization of a magmatic sulphide assemblage in cumulate dunite will only result in a small positive (0.1‰) shift in the $\delta^{34}S$ value of the residual sulphide. $\delta^{34}S$ laser probe data for intergrown pentlandite and heazlewoodite are essentially identical which supports the idea that the replacement of pentlandite by heazlewoodite is isochemical with respect to sulphur (Chapter 4). The variation in $\delta^{34}S$ and chrome-spinel chemistry over 1.5 metres of mineralized core material from the cumulate dunite unit is explained with recourse to the fractional crystallization of a fresh input of magma into the cumulate dunite pile. Thus

$\delta^{34}S$ variations in the order of 4‰ within the cumulate dunites can be readily explained by magmatic fractional crystallization processes. $\delta^{34}S$ values for pyrite mineralization in a gabbro, amphibole pegmatite and plagiogranite from Mu Ness, range from +9.6 to +14.0‰ are thought to result from the precipitation from a ^{34}S-enriched fluid, which, by analogy with other studies of ophiolitic crust, could have been derived from Caledonian seawater sulphate. A pyrite sample from Mu Ness ($\delta^{34}S$ = +9.6‰), hosted in gabbro has a $^{3}He/^{4}He$ ratio higher than that of typical radiogenic He and must require a contribution of mantle-derived volatiles The trapped fluids in this sample has a $^{3}He/^{4}He$ ratio broadly similar to fluids emanating from recent mid-ocean ridges but this ratio has probably been significantly modified by the in situ decay of U and Th to ^{4}He over the past ~470Ma. The alteration of the ophiolite has been constrained using whole-rock hydrogen and oxygen isotope analysis. The data is consistent with oceanic hydration of the gabbros, dykes and pyroxenites and a meteoric water overprint in the olivine-bearing ultramafic cumulates and harzburgite.

Conclusions

7.1 Summary

The sulphide assemblages from the cumulate ultramafics, dunite pods and mafic lithologies of the Shetland ophiolite formed by the low temperature re-equilibration of a precursor magmatic sulphide assemblage. This research has described these assemblages in detail and identified the mineral awaruite and a new assemblage of Pd ± Pt-bearing, Ni-Cu antimonides intergrown with Ni-Fe sulphides and Ni-Fe alloys from the cumulate dunite unit and a dunite pod in harzburgite from the Cliff locality. The paragenesis of these antimonides is closely linked to the alteration of the intergrown Ni-Fe sulphides. Comprehensive stable isotope analyses have been performed for the first time on these rocks. Sulphur isotope analysis suggests that the majority of the sulphides from the mafic and ultramafic portions of the ophiolite retain a magmatic sulphur isotope signature, including a sulphide and PGE-rich dunite pod from the Cliff locality. Trends in disseminated in chrome-spinel mineral chemistry and whole-rock sulphur isotope data over approximately 1.5 metres of sulphide-rich core material from the NB-2 borehole in the cumulate dunite unit is consistent with magmatic fractionation processes. In talc-carbonate altered rocks from close to the basal thrust, the sulphides may have derived a portion of their sulphur from the underlying metasedimentary sequence. At the top of the ophiolite sequence sulphur, hydrogen and oxygen isotope data are consistent with a hydrothermal overprint by seawater derived fluids. Sub-massive pyrite mineralization may have derived a portion of its sulphur from Caledonian seawater sulphate and helium isotope analysis of trapped fluid inclusions within the pyrite indicates broad parallels with fluids currently emanating from the East Pacific Rise at 21°N. Whole-rock hydrogen and oxygen isotope analysis is consistent with hydrothermal alteration of the mafics and cumulate pyroxenites by a seawater-derived fluid, with a later meteoric water overprint in the olivine-bearing ultramafic cumulates and harzburgite.

The main conclusions from studies of the silicate and sulphide mineralogy and mineral chemistry are summarized in section 7.2 and is followed by a summary of the development of techniques used to measure sulphur isotope ratios and the stable isotope geochemistry of the Shetland ophiolite (section 7.3).

7.2 Secondary silicate and sulphide paragenesis for the Shetland ophiolite

Although the Shetland ophiolite displays a primary lithological sequence of harzburgite containing dunite pods overlain by a layered sequence of dunite, wehrlite, pyroxenite and gabbro the rocks are extensively altered. Limited X-ray diffraction and wavelength dispersive electron microprobe analysis of ultramafic rocks from the complex has identified the serpentine polymorphs lizardite, antigorite and chrysotile. Lizardite occurs in undeformed cumulate dunites and may be related to earlier static serpentinization of the ophiolite. As noted by earlier workers, antigorite is spatially associated with zones of dislocation within the ultramafic complex. Pervasive infiltration of the ophiolite with a CO_2-bearing fluid may have facilitated the conversion of lizardite to antigorite.

The ultramafic unit is characterized by a disseminated Ni-Fe sulphide assemblage whereas the gabbro unit contains disseminated to sub-massive Fe and Cu-Fe sulphides. This is manifested in calculated Cu/(Cu+Ni) ratios of the sulphide assemblages which increase stratigraphically upwards from dunites to pyroxenites and finally gabbros. The low average Cu/(Cu+Ni) ratios of sulphide aggregates from the cumulate dunite unit are similar to ratios from weakly mineralized serpentinites from continental intrusions and serpentinized dunites from the Zambales ophiolite.

The sulphide assemblage recognized in the gabbro complex is pyrrhotite-pyrite-marcasite-chalcopyrite-pentlandite-'limonite'-blaubleibender covelline. A sub-massive pyrite-chalcopyrite mineralization is developed in the upper gabbros.

High-level pyroxenites are extensively altered and carry an assemblage of pentlandite-monoclinic pyrrhotite-pyrite-chalcopyrite-violarite-niccolite-cobaltite. In the pyroxene cumulates, pentlandite-pyrrhotite-chalcopyrite-bornite occurs, interstitial to fresh clinopyroxene in reltively unaltered lithologies whereas pentlandite-heazlewoodite-millerite-godlevskite-monoclinic pyrrhotite-pyrite-marcasite-chalcopyrite-chalcocite-bornite-digenite-covellite-native Cu-orcelite-maucherite occur in more altered lithologies.

The sulphide assemblages recognized in the dunite cumulates and dunite pods, other than Cliff are; i) pentlandite-troilite-native Cu; ii) pentlandite-awaruite-native Cu; iii) pentlandite-heazlewoodite-awaruite-native Cu-orcelite-Ni-Cu antimonide; iv) pentlandite-heazlewoodite-millerite-awaruite-chalcopyrite-chalcocite-native Cu-orcelite-breithauptite-Ni-

Cu antimonide. These assemblages broadly correlate with increasing degrees of serpentinization of the host rocks with resultant increasing sulphur and oxygen fugacities, *i.e.* assemblage i) is developed in the freshest dunites whereas assemblage iv) occurs in completely serpentinized dunites. A dunite pod from Cliff carries a different assemblage of pentlandite-heazlewoodite-millerite-godlevskite-chalcocite-native Cu-orcelite-breithauptite-Ni-Cu antimonide and may have formed under more oxidizing conditions compared to the other dunite pods and cumulate dunites. A paragenesis for the different Ni-antimonide minerals in cumulate dunites and in a dunite pod at Cliff is proposed whereby breithauptite, enclosed in heazlewoodite and pentlandite, is replaced by Ni-Cu(Fe-Pd±Pt) antimonide commonly forming lamellar intergrowths with breithauptite enclosed in heazlewoodite, awaruite and altered silicate.

At the basal thrust, the assemblage; pentlandite-hexagonal/monoclinic pyrrhotite-pyrite-marcasite-chalcopyrite-violarite-mackinawite-vallerite-niccolite-gersdorffite in talc-carbonate rocks developed in more oxidizing conditions as a result of chemical gradients at the contact between peridotite and country rock.

The sulphides from the Shetland ophiolite have re-equilibrated at low temperatures as manifested, for example, by the low trace element contents of pyrite and pyrrhotite. The Ni-Fe and Cu-Fe sulphide mineral assemblages from the ultramafic part of the ophiolite are consistent with published low temperature equilibrium phase relations in the Ni-Fe-S and Cu-Fe-S systems respectively. However large inter-grain variations in pentlandite chemistry in some specimens from the ultramafic part of the ophiolite suggests disequilibrium on a small scale.

7.3 Techniques used to measure sulphur isotope ratios and the stable isotope geochemistry of the Shetland ophiolite

A sealed tube technique has been developed for the rapid routine analysis of sulphur isotope ratios of pure sulphide phases to a precision of ±0.5‰. One significant advantage of this technique is that sulphur isotope measurements may be performed on elemental sulphur, which using conventional combustion techniques, tends to sublime on heating. The chemical extraction of sulphur at concentrations as low as 100ppm from whole-rock powders shows that sulphur isotope analysis of the resultant sulphide precipitate as silver sulphide gives

reproducible $\delta^{34}S$ values. This technique has been used to attain whole-rock $\delta^{34}S$ values of sulphide-bearing samples from the Shetland ophiolite.

Stepped combustion analysis of whole-rock powders and sulphide mineral separates from the Shetland ophiolite has been carried out to elucidate the distribution of sulphur within samples from different lithologies of the ophiolite. The Ni-sulphide heazlewoodite and the Ni-Fe sulphide pentlandite combust at significantly higher temperatures (~800-900°C) compared to the Fe-sulphides pyrrhotite and pyrite and the Cu-Fe sulphide chalcopyrite (~200-550°C). An experiment conducted on a rock sample containing a mixture of pentlandite-pyrrhotite-chalcopyrite indicates that, at step sizes of 100°C, these three minerals can be resolved from one another. Stepped combustion analyses of rocks from the Shetland ophiolite indicate that sulphur in these rocks is probably almost exclusively contained within sulphides. Unfortunately, $\delta^{34}S$ measurements on sulphur released during stepped combustion experiments was fractionated by approximately 2‰.

The average whole-rock $\delta^{34}S$ value of 39 representative samples from the ophiolite, excluding those from talc-carbonate rocks from the basal thrust and sub-massive pyrite mineralization at Mu Ness give a magmatic sulphur isotope value of +3.4%. This value is closer to $\delta^{34}S$ values of modern oceanic arcs ($\delta^{34}S$ = +4‰) compared to MORB ($\delta^{34}S$ = +0.1±0.5‰) and is consistent with the proposed supra subduction zone setting of the Shetland ophiolite. A stratiform mineralized layer from the cumulate dunite unit shows a possible magmatic fractionation of sulphur isotopes with a shift in $\delta^{34}S$ from -0.6 to +3.6‰ correlated to changes in associated disseminated chrome-spinel mineral chemistry. This 4‰ variation in $\delta^{34}S$ can account for much of the variation in $\delta^{34}S$ values observed in the ultramafic cumulates. Loss of sulphur as H_2S from a magmatic sulphide assemblage in the cumulate dunite unit during serpentinization will only result in a small positive (0.1‰) shift in the $\delta^{34}S$ of the residual sulphide. In situ laser analysis of intergrown pentlandite and heazlewoodite indicates negligible sulphur isotope fractionation between the two phases which is supported by calculations which indicate that the replacement of pentlandite by heazlewoodite is isochemical with respect to sulphur. Talc-carbonate rocks from close to the basal thrust have an average $\delta^{34}S$ value of +0.9‰ which can be explained by the introduction of a proportion of isotopically light sulphur from the metasedimentary sequence (mean $\delta^{34}S$ = -4.2‰). Sub-massive sulphide mineralization from the gabbro unit has

anomalously heavy $\delta^{34}S$ values of +9.6 to +14‰ which may be due to reduction of Caledonian seawater sulphate. He-isotope analysis suggests that trapped fluid inclusions in pyrite from this sub-massive sulphide mineralization from Mu Ness has broad similarities to fluids currently emanating from the East Pacific Rise. Whole-rock hydrogen and oxygen isotope analysis of the ultramafic and mafic complex are consistent with oceanic hydration of the cumulate section of the ophiolite with a later continental meteoric water overprint in the olivine-bearing ultramafic cumulates.

Appendices

Appendix A. Analytical techniques

A.1 Wavelength dispersive microprobe analysis

A Cambridge Instruments Microscan 9 (M9) was used to collect the majority of the microprobe data in this study. The M9 incorporates a fully automated computerized system which controls spectrometer angles, count times, crystal selection and specimen position. In addition, on-line ZAF corrections are performed automatically. An accelerating potential of 20kV and a specimen current of 3.05×10^{-8} amps were used for all analyses. For the analysis of the majority of sulphide grains, a defocussed 15μ diameter electron beam was used. For smaller grains the beam was focussed to around 6-7μ. The instrument was calibrated daily using the mineral standards and operating conditions listed in table A1.

Element	*Standard*	*% element*	*Spectrometer*	*Peak angle*
Fe	pyrite APY	46.55	A	28.674
Ni	metal	100.00	A	24.272
Co	metal	100.00	A	26.370
S	pyrite APY	53.45	A	37.788
Cu	metal	100.00	B	22.450
As	metal	100.00	B	16.954
Sb	metal	100.00	A	23.056
Ag	metal	100.00	A	28.237
Pd	metal	100.00	A	29.950
Pt	metal	100.00	A	19.034

For sulphide minerals the pyrite (FeS_2) standard APY was routinely analysed to monitor instrument precision.

A.2 Energy dispersive microprobe analyses

Sulphide analyses at the beginning of this work were obtained using a Geoscan energy dispersive electron microprobe and a Link 860 analyser system using a ZAF4 - FLS deconvolution program. The analytical conditions used for this technique are listed below;

Accelerating potential	30kV
Beam current	2.5nA
Beam diameter range	2-10μ
Count time	200 seconds
Spectrum range	0-20KeV

Cobalt metal was used as a spectrum gain drift monitor (counted between every four unknowns). The calibration standards used are the same as listed in table A1 above.

A.3 XRF analyses

An energy dispersive Link Systems Mecca 20 was used for both major and trace element analyses. Major element analyses were obtained from glass discs and trace elements from pressed powder pellets. The analytical proceedure for this technique is given in Potts (1984). The international rock standard PCC-1 was included in each run of a batch of unknown samples.

A.4 Scanning electron microscope (SEM)

A JEOL JSM-820 SEM was used both for standardless qualitative analyses and X-ray mapping. This SEM has facilities for the observation of both backscattered and secondary electron emissions. An air-lock is fitted which allows rapid sample changeover. The microscope is fitted with a Kevex Quantum™ Si(Li) detector. This detector is linked to a Kevex Delta 4™ computer system which enables processing of acquired spectra and X-ray maps.

An accelerating voltage of 25keV and a working distance (the distance between the sample surface and detector) of 39mm was used for both obtaining qualitative analyses and X-ray maps. The spectra obtained from a sample are processed to allow for escape peaks and counts from background emissions are removed. The constituent peaks of the spectra

are then deconvoluted to remove the effects of overlapping peaks. A gaussian fit is then synthesized for each peak and used in the region of interest. For X-ray mapping a 1-5μs processing time is used resulting in a high density of counts which gives compositional information but poor image resolution.

A.5 Oxygen isotope analysis

Oxygen was liberated from samples by a fluorination reaction induced by heating the sample with radiation from a Nd/YAG laser (wavelength=1064nm). The fluorination reagent used was chlorine trifluoride. Isotopic analyses were performed on a VG Isotopes Ltd. SIRA 24 mass spectrometer. Powdered NBS28 quartz was used as a standard and gave a mean $\delta^{18}O$ value of +9.3±0.3‰ compared to the certified value of +9.6‰.

A.6 Hydrogen isotope analysis

Water was obtained from whole-rock powders by pyrolysis at 1100°C after pre-baking the sample to 200°C for two hours to remove any atmospheric moisture that may have been present in the sample. Water generated by this pyrolysis is transferred to a reduction furnace and reduced to hydrogen by zinc at 450°C. The hydrogen is then admitted to the mass spectrometer for D/H ratio measurement. All D/H measurements performed on a modified VG SIRA 24 mass spectrometer and are expressed in conventional δ-notation relative to SMOW (Standard Mean Ocean Water). Standards used were two NBS (National Bureau of Standards) water standards; V-SMOW, defined as 0‰, and SLAP δD=-428‰. A solid standard, NBS#30 biotite (δD=-64‰) was routinely included in a batch of unknown samples. Precision is ±2‰ for >20μmol hydrogen.

A.7 Helium isotope analysis

Sulphide samples were washed ultrasonically in methanol prior to a 36 hour vacuum baking at ~200°C to reduce the contribution of adsorbed atmospheric noble gases. Gas extraction was performed by crushing samples in vacuo in a triple assembly of screw crushers constructed from (modified) commercially available vacuum valves. $^3He/^4He$ ratio measurements were determined in an all-metal MAP 215 mass spectrometer dedicated to

analysis of terrestrial samples and capable of resolving $^3He^+$ from interfering HD^+. From routine measurements of 10^{-6}cc air the reproducibility of $^3He/^4He$ ratio measurements was 3% (1σ) and for ^4He abundance measurements ±5% (1σ).

Appendix B. Analytical data

B.1 Whole-rock X-ray diffraction patterns

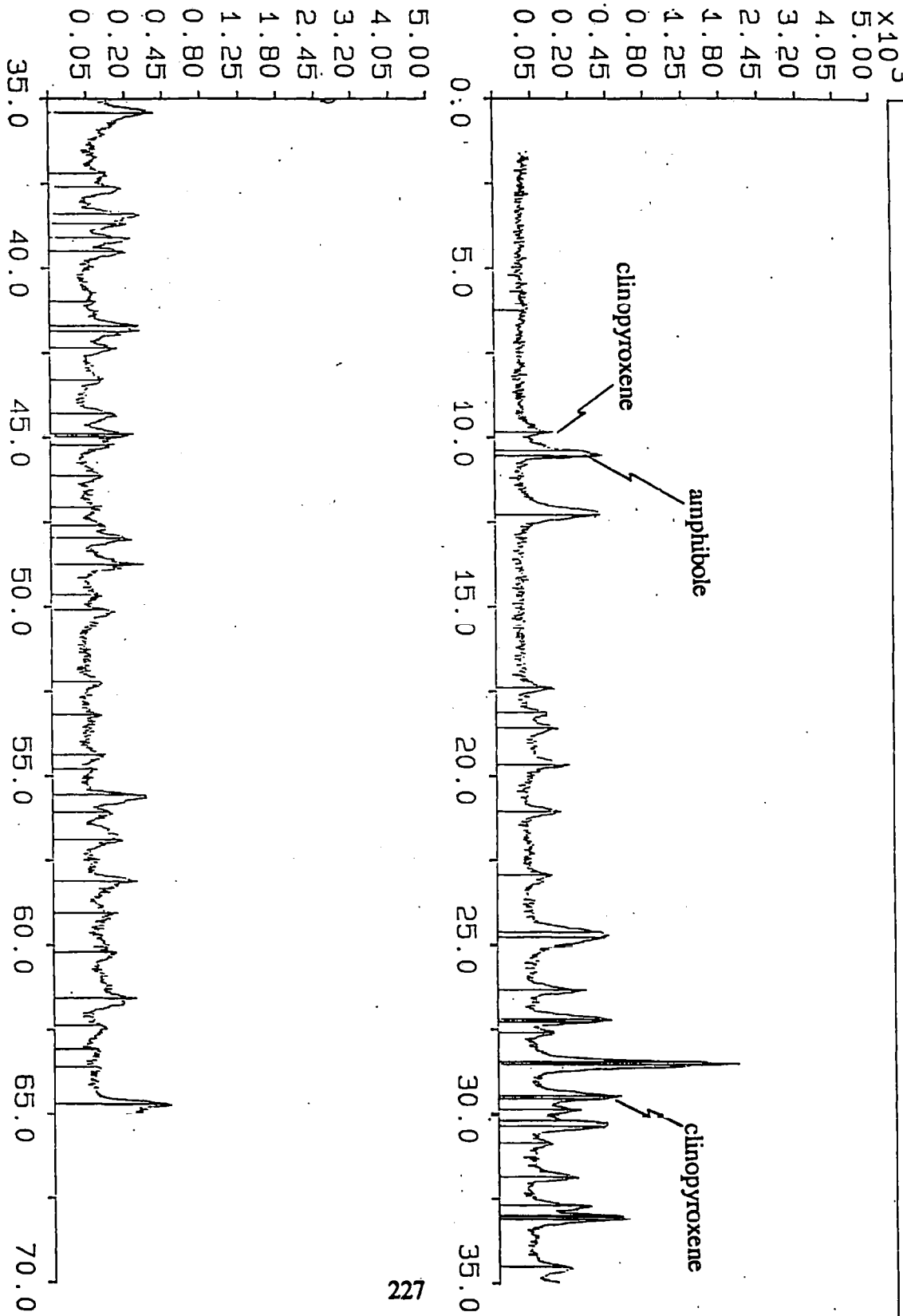

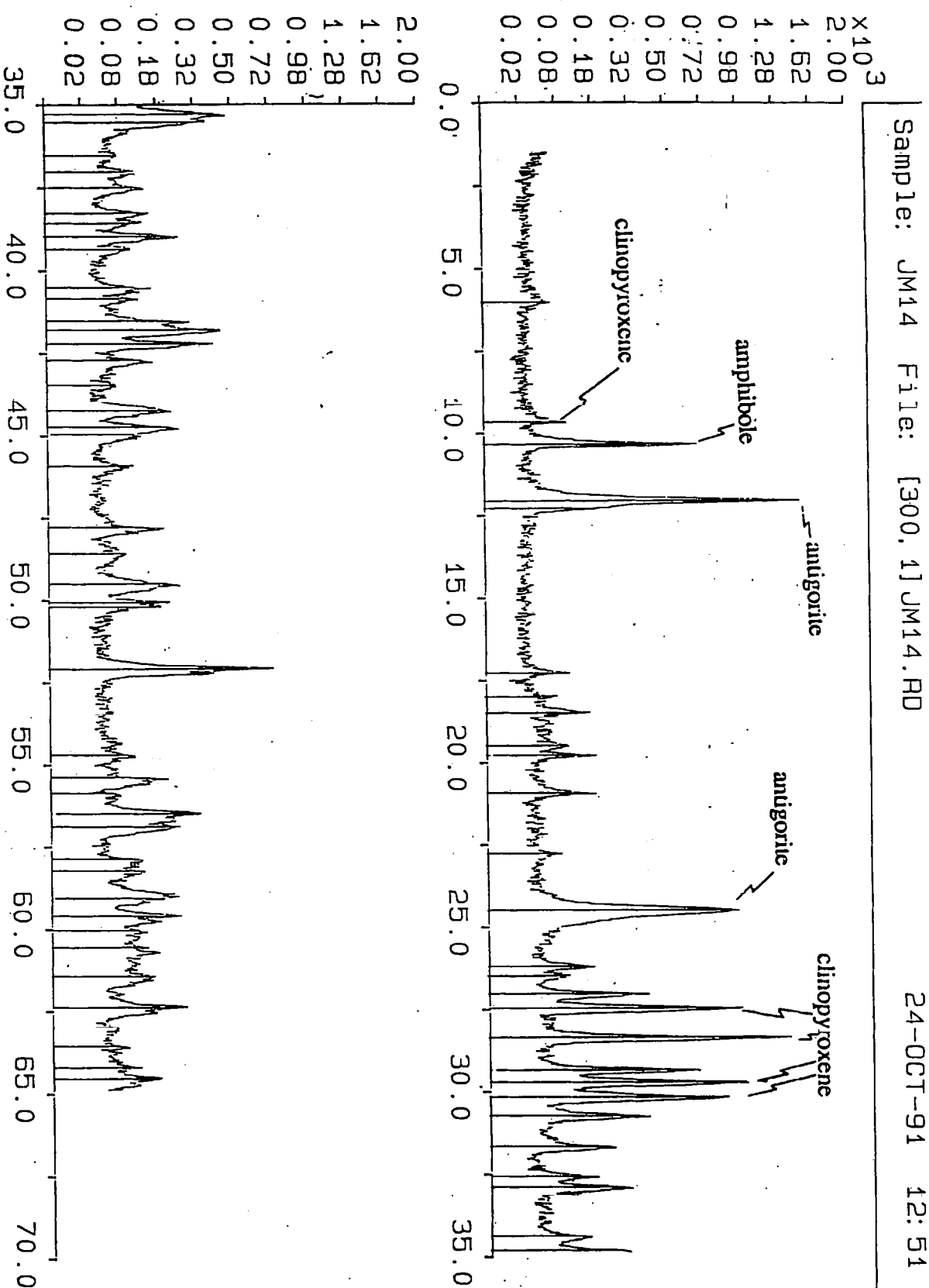
Sample: JM14 File: [300, 1] JM14.RD
24-OCT-91 12:51
x10^3
clinopyroxene
amphibole
antigorite
antigorite
clinopyroxene

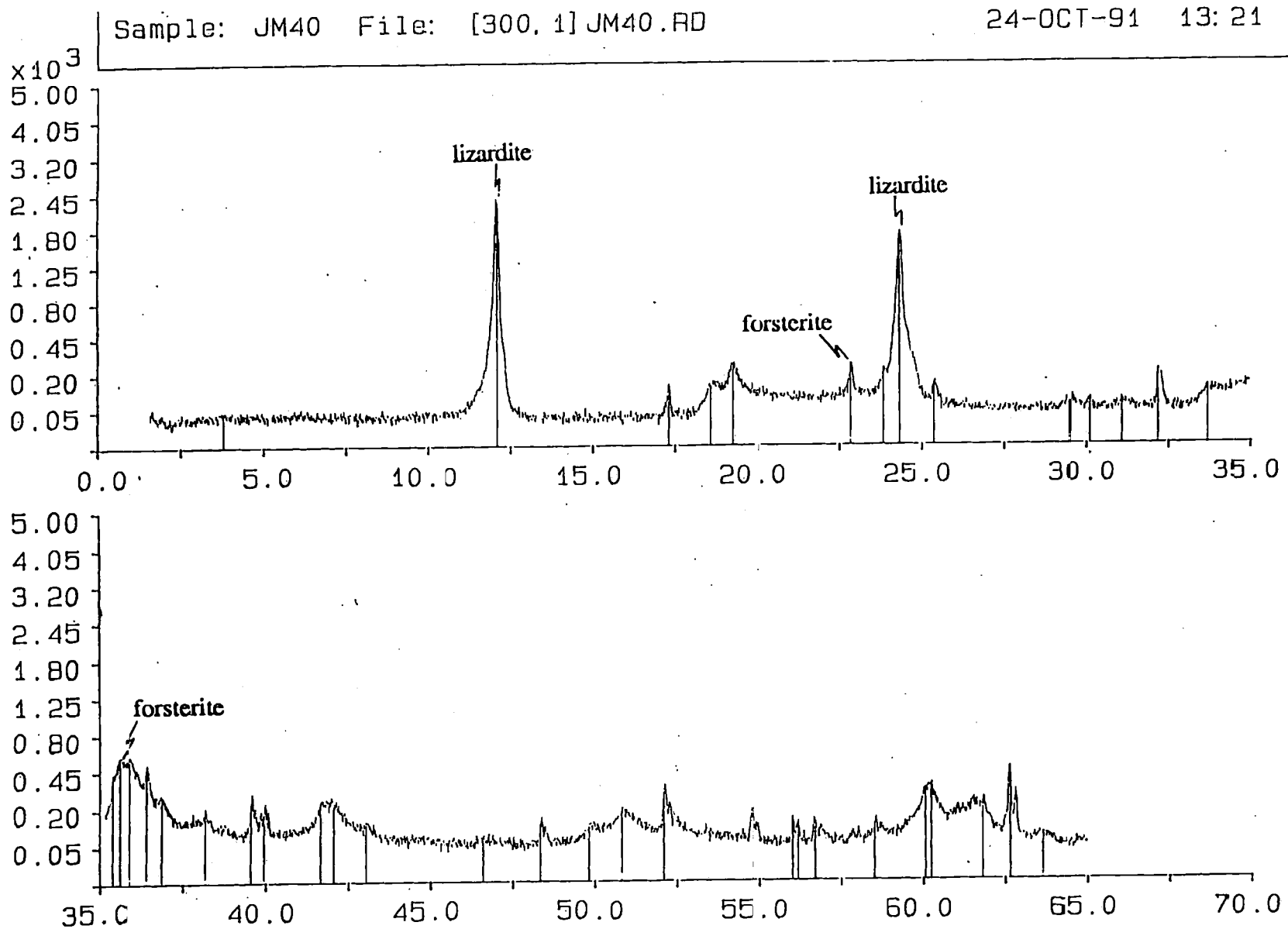
Sample: JM40 File: [300, 1] JM40.RD
24-OCT-91 13: 21
x10 3
5.00
4.05
3.20
2.45
1.80
1.25
0.80
0.45
0.20
0.05
lizardite
lizardite
forsterite
0.0
5.0
10.0
15.0
20.0
25.0
30.0
35.0
forsterite
35.0
40.0
45.0
50.0
55.0
60.0
65.0
70.0

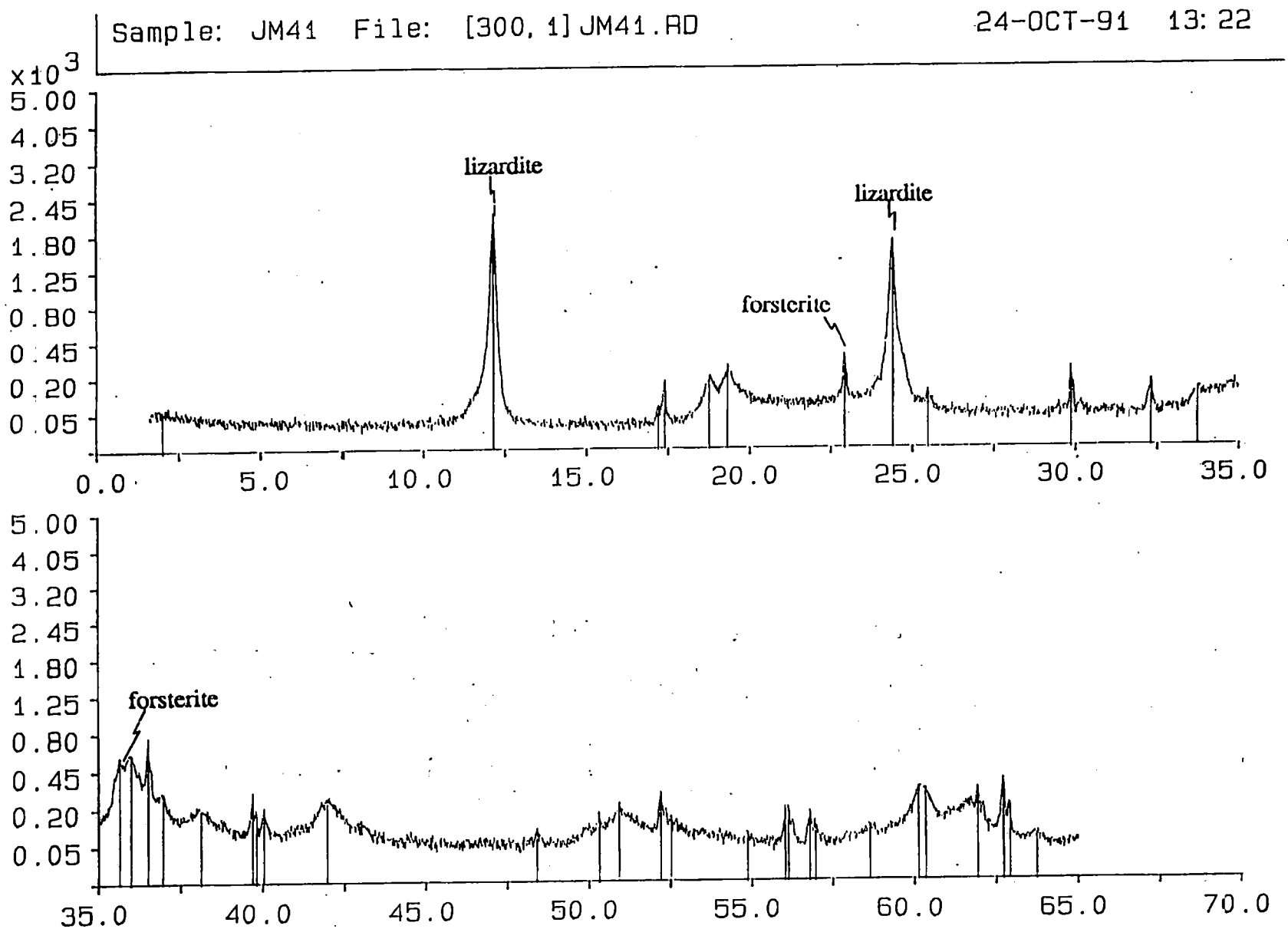
Sample: JM41 File: [300,1]JM41.RD
24-OCT-91 13:22
x10 3
5.00
4.05
3.20
2.45
1.80
1.25
0.80
0.45
0.20
0.05
lizardite
lizardite
forsterite
0.0
5.0
10.0
15.0
20.0
25.0
30.0
35.0
forsterite
35.0
40.0
45.0
50.0
55.0
60.0
65.0
70.0

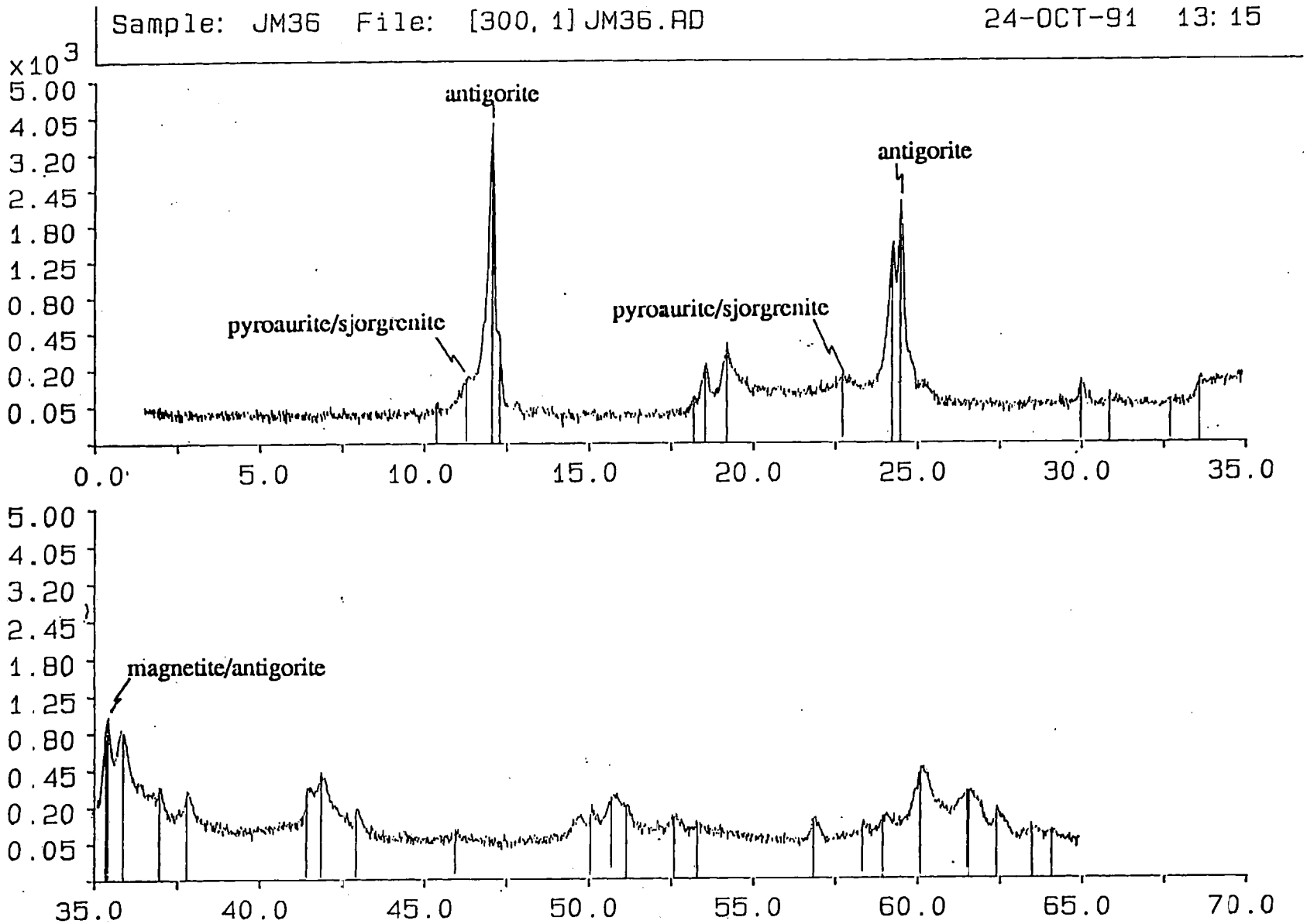
Sample: JM36 File: [300,1]JM36.RD 24-OCT-91 13:15
x10^3
5.00
4.05
3.20
2.45
1.80
1.25
0.80
0.45
0.20
0.05
antigorite
antigorite
pyroaurite/sjorgrenite
pyroaurite/sjorgrenite
0.0
5.0
10.0
15.0
20.0
25.0
30.0
35.0
magnetite/antigorite
35.0
40.0
45.0
50.0
55.0
60.0
65.0
70.0

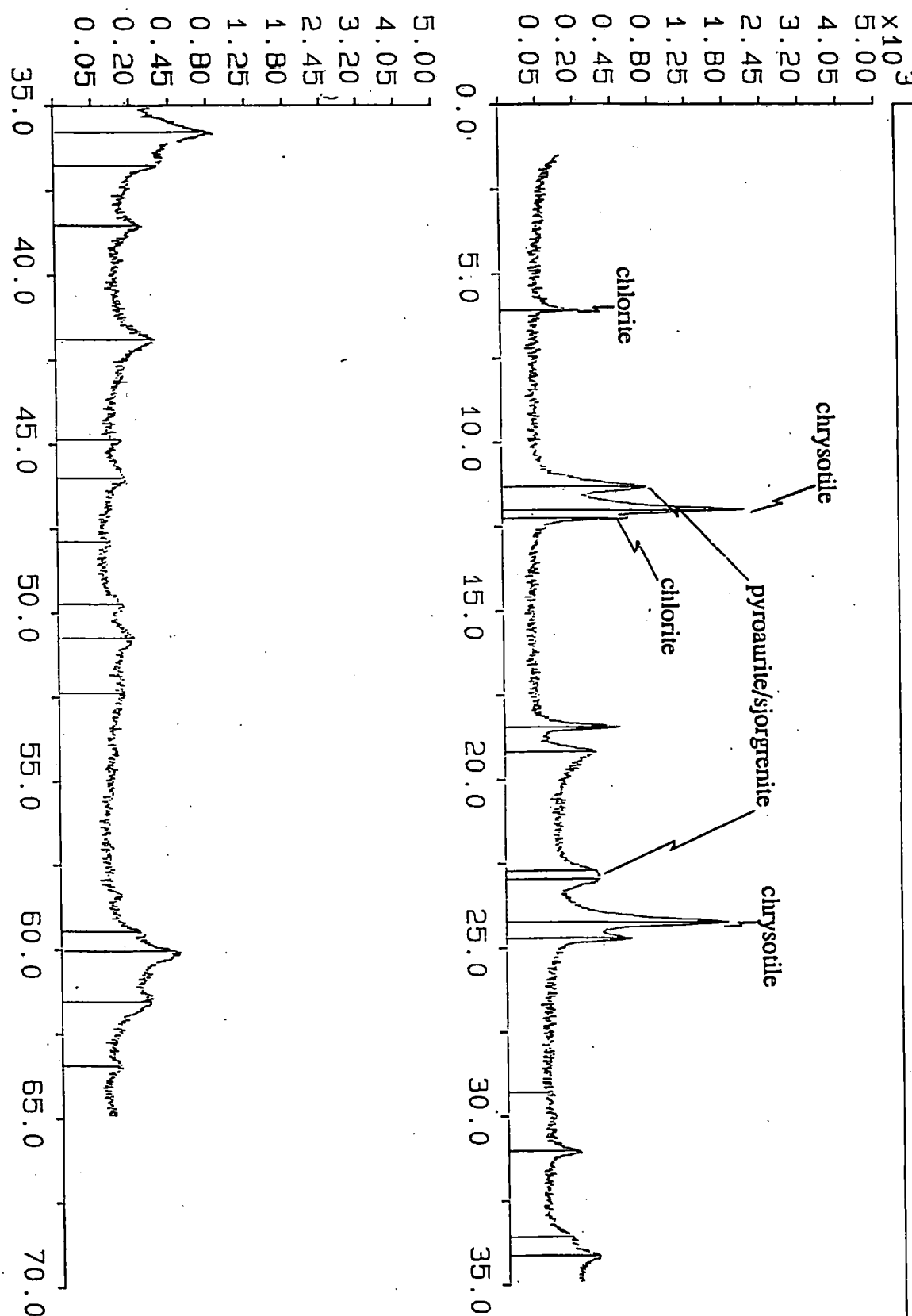
Sample: GRA File: [300,1]GRA.RD
24-OCT-91 13:08
x10 3
chrysotile
chlorite
pyroaurite/sjorgrenite
chlorite
chrysotile

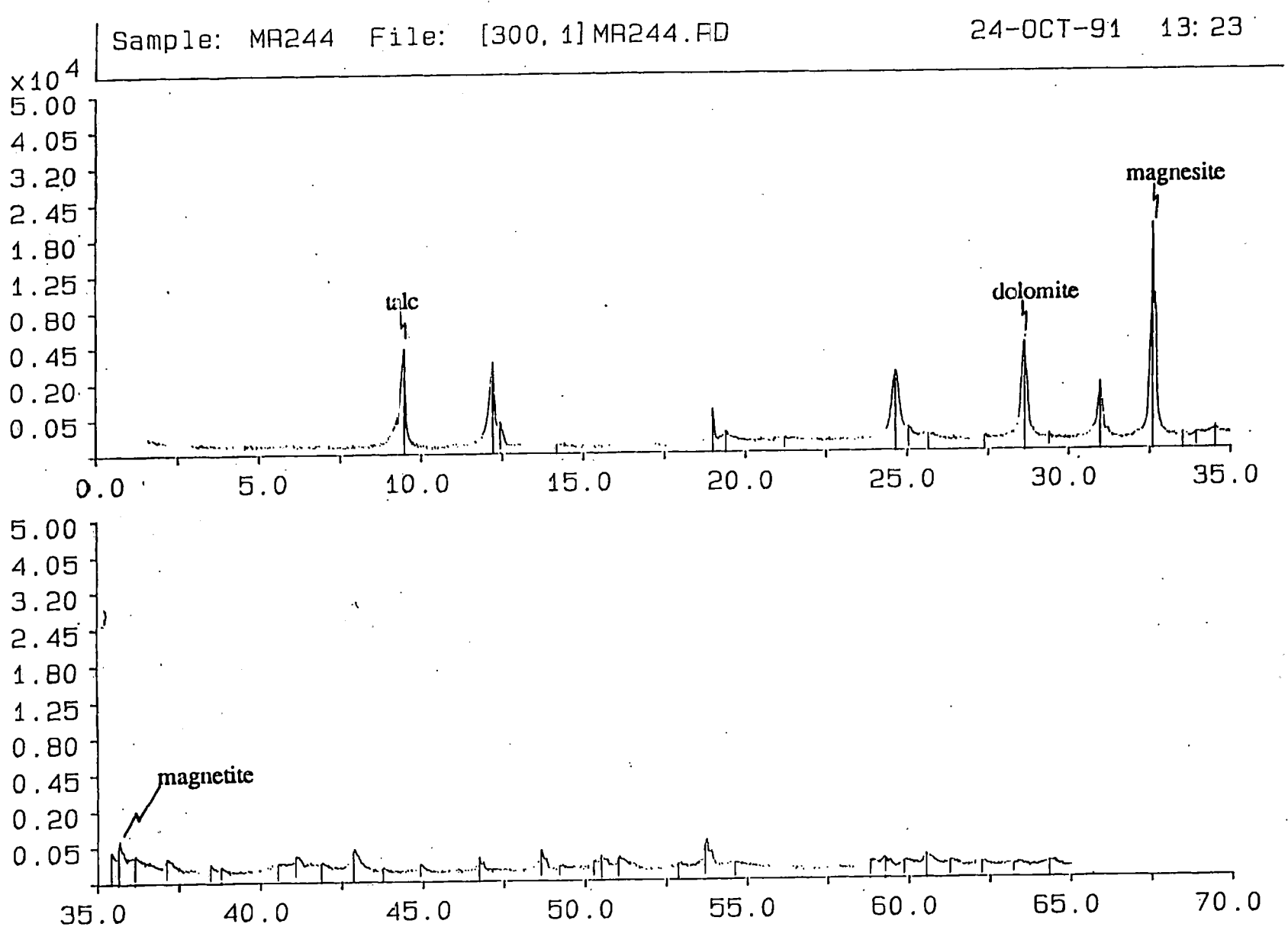
Sample: MR244 File: [300,1]MR244.RD 24-OCT-91 13:23
x10^4
5.00
4.05
3.20
2.45
1.80
1.25
0.80
0.45
0.20
0.05
talc
dolomite
magnesite
0.0
5.0
10.0
15.0
20.0
25.0
30.0
35.0
magnetite
35.0
40.0
45.0
50.0
55.0
60.0
65.0
70.0

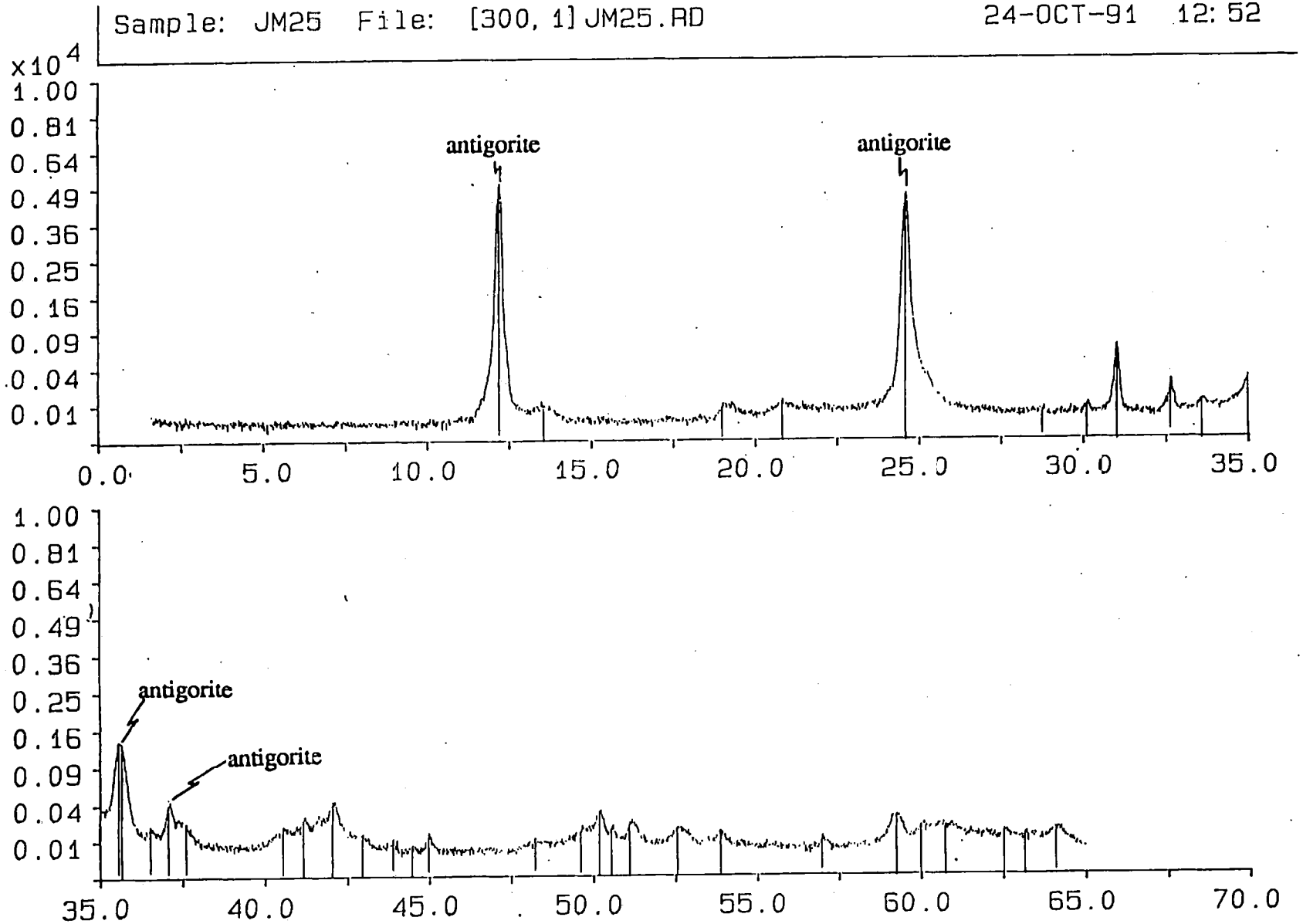
Sample: JM25 File: [300, 1] JM25.RD
24-OCT-91 12:52
x10^4
1.00
0.81
0.64
0.49
0.36
0.25
0.16
0.09
0.04
0.01
antigorite
antigorite
0.0
5.0
10.0
15.0
20.0
25.0
30.0
35.0
antigorite
antigorite
35.0
40.0
45.0
50.0
55.0
60.0
65.0
70.0

B.2 Probe data tables

All probe analyses were determined on a Cambridge Instruments Microscan 9 wavelength dispersive electron microprobe except those analyses prefixed by JMslp which were obtained with a Cambridge Instruments Geoscan energy dispersive electron microprobe; nd = element not sought.

Amphiboles

Sample	*MNA xca*	*MNA xcb*	*MNA xcc*	*MNA xcd*	*MNA xce*	*MNG kxc*	*MNG kxg*	*MNG kxh*	*JM1 jmp*	*JM1 jmq*	*JM1 jmr*	*JM3 lxb*	*JM3 lxc*
Wt% oxide													
NaO	0.59	0.57	0.75	0.07	0.78	0.45	0.17	0.32	0.99	0.08	0.70	0.76	0.02
MgO	13.84	14.05	13.33	16.55	13.18	14.67	15.51	15.65	15.99	16.03	14.70	19.31	19.57
Al2O3	3.27	2.74	3.74	0.90	3.70	3.01	1.46	2.31	4.73	0.94	4.00	4.33	0.11
SiO2	51.52	52.31	51.16	55.16	50.97	53.25	55.21	54.28	54.86	55.28	52.85	53.28	56.88
K2O	0.05	0.05	0.05	0.01	0.06	0.03	0.01	0.01	0.01	0.01	0.02	0.00	0.00
CaO	12.37	12.42	12.16	13.24	11.84	12.45	12.84	12.63	12.27	13.18	12.17	13.18	13.25
TiO2	0.16	0.20	0.33	0.02	0.33	0.26	0.06	0.11	0.53	0.02	0.48	0.19	0.02
Cr2O3	0.00	0.00	0.00	0.00	0.00	0.00	0.00	0.00	0.00	0.00	0.00	0.38	0.05
MnO	0.36	0.34	0.34	0.36	0.36	0.45	1.17	0.62	0.48	0.23	0.36	0.11	0.11
Fe2O3	14.61	14.29	15.45	10.96	15.15	15.37	13.52	13.87	12.77	10.88	11.83	7.07	7.50
NiO	0.00	0.00	0.01	0.00	0.00	0.00	0.00	0.01	nd	nd	nd	0.01	0.00
Total	96.77	96.97	97.32	97.27	96.37	99.95	99.95	99.81	102.3	96.65	97.11	98.62	97.51
Form. units (23 O)													
NaO	0.17	0.16	0.21	0.02	0.23	0.12	0.05	0.09	0.26	0.02	0.19	0.21	0.01
MgO	3.04	3.07	2.92	3.54	2.91	3.12	3.27	3.31	3.21	3.37	3.10	4.02	4.10
Al2O3	0.57	0.47	0.65	0.15	0.65	0.51	0.24	0.39	0.69	0.16	0.67	0.71	0.02
SiO2	7.59	7.67	7.53	7.91	7.56	7.60	7.82	7.70	7.38	7.81	7.47	7.44	7.99
K2O	0.01	0.01	0.01	0.00	0.01	0.01	0.00	0.00	0.00	0.00	0.00	0.00	0.00
CaO	1.95	1.95	1.92	2.03	1.88	1.90	1.95	1.92	1.77	1.99	1.84	1.97	1.99
TiO2	0.02	0.02	0.04	0.00	0.04	0.03	0.01	0.01	0.05	0.00	0.05	0.02	0.00
Cr2O3	0.00	0.00	0.00	0.00	0.00	0.00	0.00	0.00	ns	ns	ns	0.04	0.01
MnO	0.04	0.04	0.04	0.04	0.04	0.05	0.14	0.07	0.05	0.03	0.04	0.01	0.01
Fe2O3	1.80	1.75	1.90	1.31	1.88	1.84	1.60	1.65	1.29	1.16	1.26	0.83	0.88
NiO	0.00	0.00	0.00	0.00	0.00	0.00	0.00	0.00	ns	ns	ns	0.00	0.00
Total	15.19	15.16	15.22	15.02	15.20	15.18	15.08	15.14	14.71	14.54	14.62	15.26	15.00

Amphiboles

Sample	*JM3 lxd*	*JM3 lxe*	*JM3 lxf*	*JM3 lxg*	*JM6 psh*	*JM6 psi*	*JM6 psj*	*JM6 psk*	*JM6 psl*	*JM6 psm*	*JM6 psn*	*JM21 amc*	*JM21 amd*
W% oxide													
NaO	0.40	0.02	0.10	0.06	1.11	0.93	0.46	1.05	0.79	0.73	0.70	0.00	0.01
MgO	20.85	19.74	19.99	19.74	13.38	14.23	16.81	15.75	15.17	16 71	15.81	22.76	22.62
Al2O3	1.95	0.13	1.12	0.25	6.62	6.38	2.97	5.53	5.05	4.04	3.97	0.04	0.02
SiO2	55.80	56.57	56.42	57.10	49.21	50.58	53.47	50.62	51.35	52.19	52.11	58.68	58.72
K2O	0.00	0.00	0.00	0.01	0.03	0.05	0.01	0.02	0.02	0.01	0.02	0.00	0.00
CaO	12.88	13.23	13.05	13.35	10.75	11.83	11.71	11.25	11.44	11.14	11.18	13.45	13.54
TiO2	0.13	0.02	0.04	0.02	0.60	0.31	0.20	0.39	0.33	0.20	0.29	0.04	0.02
Cr2O3	0.17	0.05	0.17	0.10	0.00	0.02	0.02	0.00	0.00	0.00	0.00	0.00	0.00
MnO	0.14	0.13	0.11	0.11	0.40	0.36	0.31	0.28	0.40	0.34	0.31	0.11	0.11
Fe2O3	5.01	7.45	7.76	7.47	15.45	12.78	10.95	11.92	12.29	11.49	12.06	1.86	1.82
NiO	0.04	0.00	0.01	0.01	0.00	0.00	0.01	0.00	0.00	0.00	0.00	0.02	0.03
Total	97.37	97.34	98.83	98.24	97.55	97.47	96.92	96.81	96.84	96.85	96.45	96.97	96.89
Form. units (23 O)													
NaO	0.11	0.01	0.03	0.02	0.32	0.26	0.13	0:30	0.22	0.20	0.20	0.00	0.00
MgO	4.33	4.14	4.14	4.10	2.92	3.07	3.60	3.41	3.28	3.60	3.43	4.66	4.63
Al2O3	0.32	0.02	0.18	0.04	1.14	1.09	0.50	0.95	0.86	0.69	0.68	0.01	0.00
SiO2	7.78	7.96	7.84	7.96	7.22	7.33	7.68	7.35	7.46	7.54	7.58	8.06	8.07
K2O	0.00	0.00	0.00	0.00	0.01	0.01	0.00	0.00	0.00	0.00	0.00	0.00	0.00
CaO	1.92	2.00	1.94	2.00	1.69	1.84	1.80	1.75	1.78	1.72	1.74	1.98	1.99
TiO2	0.01	0.00	0.00	0.00	0.07	0.03	0.02	0.04	0.04	0.02	0.03	0.00	0.00
Cr2O3	0.02	0.01	0.02	0.01	0.00	0.00	0.00	0.00	0.00	0.00	0.00	0.00	0.00
MnO	0.02	0.02	0.01	0.01	0.05	0.04	0.04	0.03	0.05	0.04	0.04	0.01	0.01
Fe2O3	0.58	0.88	0.90	0.87	1.89	1.55	1.32	1.45	1.49	1.39	1.47	0.21	0.21
NiO	0.00	0.00	0.00	0.00	0.00	0.00	0.00	0.00	0.00	0.00	0.00	0.00	0.00
Total	15.10	15.03	15.06	15.02	15.31	15.23	15.11	15.28	15.19	15.20	15.16	14.94	14.93

Pyrrhotite

Lith.	*Sample no.*	*Probe no.*	*Fe*	*Ni*	*Co*	*S*	*Cu*	*As*	*Sb*	*Ag*	*Pd*	*Pt*	*Tot.*
gabbro	JM1	JMslp26	60.12	0.00	0.00	39.29	0.00	0.00	ns	ns	ns	ns	99.41
gabbro	JM1	JMslp27	60.48	0.00	0.00	39.09	0.00	0.00	ns	ns	ns	ns	99.56
gabbro	JM1	SUA	60.49	0.00	0.21	38.27	0.06	0.07	ns	ns	ns	ns	99.1
gabbro	JM1	SUC	60.81	0.01	0.21	39.61	0.02	0.04	ns	ns	ns	ns	100.7
gabbro	JM1	SUH	60.35	0.00	0.20	38.56	0.00	0.05	ns	ns	ns	ns	99.16
gabbro	JM2	JMA	60.74	0.00	0.00	39.02	0.00	0.00	ns	ns	ns	ns	99.76
gabbro	JM2	JMC	60.79	0.00	0.00	39.02	0.00	0.00	ns	ns	ns	ns	99.81
gabbro	JM2	JMD	60.67	0.00	0.00	39.00	0.00	0.00	ns	ns	ns	ns	99.67
gabbro	JM5	JMslp76	59.76	0.38	0.00	39.62	0.00	0.00	ns	ns	ns	ns	99.77
gabbro	RLO61	POB	59.27	0.01	0.07	37.52	0.10	0.30	0.00	0.00	0.03	0.13	97.43
gabbro	RLO61	POC	59.80	0.00	0.07	38.41	0.02	0.10	0.00	0.04	0.01	0.10	98.55
gabbro	RLO61	POD	59.91	0.00	0.08	38.56	0.06	0.00	0.00	0.01	0.03	0.10	98.75
gabbro	RLO61	PON	60.29	0.00	0.08	38.6	0.06	0.02	0.00	0.04	0.08	0.18	99.35
gabbro	RLO61B	PCB	60.13	0.00	0.08	37.64	0.02	0.00	0.00	0.00	0.06	0.00	97.93
gabbro	RLO61B	PCD	60.13	0.00	0.07	38.47	0.02	0.05	0.00	0.03	0.03	0.00	98.80
h.l.px.	JM44	JMslp98	58.61	1.51	0.00	39.69	0.00	0.00	0.00	0.00	0.00	0.00	99.81
c.px.	JM13	JMslp17a	60.76	0.00	0.00	39.23	0.00	0.00	0.00	0.00	0.00	0.00	99.98
c.px.	JM13	JMslp17b	60.08	0.00	0.00	39.04	0.00	0.00	0.00	0.00	0.00	0.00	99.12
c.px.	JM13	JMslp19	60.61	0.00	0.00	39.23	0.00	0.00	0.00	0.00	0.00	0.00	99.84
c.px.	JM13	JMslp20	59.89	0.00	0.00	39.37	0.00	0.00	0.00	0.00	0.00	0.00	99.26
c.px.	JM13	JMslp20	59.89	0.00	0.00	39.37	0.00	0.00	0.00	0.00	0.00	0.00	99.26
c.px.	JM13	JMslp21	59.29	0.00	0.00	39.18	0.00	0.00	0.00	0.00	0.00	0.00	98.47
c.px.	NA17	SUT	59.50	0.13	0.12	38.87	0.15	0.11	0.00	0.01	0.04	ns	98.93
c.px.	NA18	JMslp159	58.12	1.00	0.00	38.61	0.36	0.00	0.00	0.00	0.00	0.00	98.09
c.px.	NA18	JMslp160	58.12	1.00	0.00	38.61	0.36	0.00	0.00	0.00	0.00	0.00	98.09
c. dn.	JM39	POA	62.45	0.00	0.11	36.34	0.03	0.00	0.00	0.01	0.03	0.10	99.07
tc-carb.	JM32	JBI	59.89	0.08	0.12	37.91	0.01	0.00	0.00	0.00	0.03	0.07	98.11
tc-carb.	JM32	JBI*2	59.80	0.06	0.12	38.65	0.00	0.11	0.01	0.00	0.03	0.00	98.78
tc-carb.	JM32	JBJ	59.98	0.06	0.13	38.13	0.00	0.01	0.00	0.00	0.03	0.01	98.35
tc-carb.	JM32	JBK	59.46	0.06	0.12	38.14	0.01	0.10	0.01	0.01	0.03	0.01	97.95
tc-carb.	MR244	JMR	61.04	0.23	0.08	36.95	0.25	0.00	0.00	0.01	0.01	0.00	98.57
tc-carb.	MR244	JMR*2	60.64	0.18	0.12	37.70	0.19	0.01	0.00	0.03	0.03	0.09	98.99
tc-carb.	MR244	JMT	59.74	1.72	0.13	37.52	0.19	0.07	0.00	0.03	0.06	0.04	99.50
tc-carb.	MR244	JMV	60.66	0.10	0.10	38.38	0.12	0.05	0.00	0.01	0.04	0.04	99.50
tc-carb.	MR244	JMW	59.93	0.11	0.11	38.77	0.21	0.05	0.00	0.01	0.01	0.18	99.38

Chalcopyrite

Lith.	*Sample no.*	*Probe no.*	*Fe*	*Ni*	*Co*	*S*	*Cu*	*As*	*Sb*	*Ag*	*Pd*	*Pt*	*Tot.*
dol. dk.	JM5	JMslp73	30.32	0.00	0.00	34.6	33.23	0.00	0.00	0.00	0.00	0.00	98.15
gabbro	JM1	JMslp22	30.58	0.00	0.00	34.64	34.78	0.00	0.00	0.00	0.00	0.00	99.99
gabbro	JM1	JMslp25	30.21	0.00	0.00	34.38	35.05	0.00	0.00	0.00	0.00	0.00	99.64
gabbro	RLO61	CPA	30.72	0.00	0.12	34.6	33.33	0.00	0.00	0.01	0.03	0.00	98.81
gabbro	RLO61	CPB	30.59	0.00	0.06	34.46	33.63	0.09	0.00	0.01	0.04	0.00	98.88
gabbro	RLO61B	CPY	30.11	0.00	0.03	34.57	33.99	0.00	0.00	0.00	0.03	0.00	98.73
h.l. px.	JM20	JMslp169	28.80	0.00	0.00	33.73	37.00	0.00	0.00	0.00	0.00	0.00	99.52
h.l.wh.	RLO58	RAL	29.78	0.06	0.05	34.67	33.41	0.00	0.00	0.01	0.04	ns	98.02
c.px.	JM13	JMslp21	32.66	0.00	0.00	34.9	31.66	0.00	0.00	0.00	0.00	0.00	99.21
c.px.	JM13	JMslp21b	30.32	0.00	0.00	34.78	34.13	0.00	0.00	0.00	0.00	0.00	99.23
c.px.	JM14	SUB	29.63	0.00	0.03	33.44	34.84	0.04	0.00	0.01	0.06	ns	98.05
c.px.	JM14	SUC	29.85	0.01	0.08	33.73	33.99	0.30	0.00	0.01	0.03	ns	98.00
c.px.	JM14	SUD	30.14	0.00	0.06	33.75	34.00	0.00	0.00	0.01	0.06	ns	98.02
c.px.	JM14	SUE	29.91	0.00	0.05	33.65	34.20	0.00	0.00	0.01	0.04	ns	97.87
c.px.	JM14	SUF	29.8	0.00	0.01	33.78	34.08	0.05	0.00	0.03	0.03	ns	97.78
c.px.	NA13	JMslp147	30.28	0.00	0.00	33.75	34.38	0.00	0.00	0.00	0.00	0.00	98.41
c.px.	NA17	SUR	30.49	0.00	0.05	34.38	34.45	0.01	0.00	0.01	0.06	ns	99.45
tc-carb.	MR244	JMX	29.77	0.00	0.06	34.63	33.9	0.05	0.00	0.00	0.04	0.00	98.45

Bornite

Lith.	*Sample no.*	*Probe no.*	*Fe*	*Ni*	*Co*	*S*	*Cu*	*As*	*Sb*	*Ag*	*Pd*	*Pt*	*Tot.*
c. px.	NA14	JMslp39	12.80	1.17	0.00	26.20	57.98	0.00	0.00	0.00	0.00	0.00	98.14

Chalcocite

Lith.	*Sample no.*	*Probe no.*	*Fe*	*Ni*	*Co*	*S*	*Cu*	*As*	*Sb*	*Ag*	*Pd*	*Pt*	*Tot.*
dn.pod	MR11	RCU	0.46	0.03	0.01	19.94	79.77	0.00	0.00	0.04	0.01	0.00	100.3

Pyrite

Lith.	*Sample no.*	*Probe no.*	*Fe*	*Ni*	*Co*	*S*	*Cu*	*As*	*Sb*	*Ag*	*Pd*	*Pt*	*Tot.*
a.peg.	MNA	JMslp111	46.2	0.00	0.00	52.91	0.00	0.00	0.00	ns	ns	ns	99.12
a. peg.	MNA	JMslp112	46.21	0.00	0.00	53.11	0.00	0.00	0.00	ns	ns	ns	99.32
a. peg.	MNA	JMslp113	46.31	0.00	0.24	53.13	0.00	0.00	0.00	ns	ns	ns	99.68
a. peg.	MNA	JMslp114	46.47	0.00	0.00	53.23	0.00	0.00	0.00	ns	ns	ns	99.69
gabbro	MNG	JMslp108	46.67	0.00	0.00	53.01	0.00	0.00	0.00	ns	ns	ns	99.68
gabbro	MNG	JMslp109	46.56	0.00	0.00	53.13	0.00	0.00	0.00	ns	ns	ns	99.69
gabbro	MNG	JMslp110	46.06	0.00	0.25	53.14	0.00	0.00	0.00	ns	ns	ns	99.45
gabbro	JM1	JMslp23	46.97	0.00	0.00	53.61	0.53	0.00	0.00	ns	ns	ns	101.1
gabbro	JM1	JMslp23b	46.66	0.00	0.00	53.62	0.00	0.00	0.00	ns	ns	ns	100.3
gabbro	JM1	JMslp24	46.56	0.00	0.00	52.94	0.00	0.00	0.00	ns	ns	ns	99.5
gabbro	JM1	JMslp28	47.25	0.00	0.00	53.59	0.00	0.00	0.00	ns	ns	ns	100.8
gabbro	JM1	SUD	46.80	0.00	0.16	52.81	0.00	0.23	0.00	0.00	0.00	0.00	100
gabbro	JM2	JMB	47.50	0.00	0.00	52.68	0.00	0.00	0.00	0.00	0.00	0.00	100.2
gabbro	JM3	PYB	46.49	0.00	0.09	52.99	0.01	0.00	0.00	0.00	0.00	0.00	99.58
h.l. px.	JM20	JMslp166	46.49	0.49	0.00	53.91	0.00	0.00	0.00	0.00	0.00	0.00	100.9
h.l. px.	JM20	JMslp167	47.04	0.00	0.00	53.47	0.00	0.00	0.00	0.00	0.00	0.00	100.5
h.l. px.	JM20	JMslp170	45.91	0.00	1.06	53.55	0.00	0.00	0.00	0.00	0.00	0.00	100.5
h.l. px.	JM21	APD	44.80	0.11	0.67	52.3	0.01	0.20	0.00	0.01	0.01	0.06	98.17
h.l. px.	JM21	APE	44.66	0.15	0.85	52.3	0.02	0.41	0.00	0.01	0.04	0.00	98.44
h.l. px.	JM23	APG	44.67	0.12	0.81	52.84	0.01	0.29	0.00	0.00	0.00	0.06	98.8
h.l. px.	JM23	APH	44.02	0.17	1.06	52.9	0.00	0.48	0.00	0.00	0.03	0.02	98.68
h.l. px.	JM23	APJ	43.88	0.09	1.06	52.69	0.00	0.37	0.00	0.00	0.03	0.08	98.20
h.l. px.	JM23	APK	44.90	0.09	0.46	53.57	0.02	0.00	0.00	0.01	0.04	0.00	99.09
h.l. px.	JM23	APL	44.05	0.14	1.01	52.74	0.00	0.66	0.00	0.01	0.01	0.05	98.67
h.l. px.	JM44	JMslp29	46.72	0.00	0.00	53.17	0.00	0.00	0.00	0.00	0.00	0.00	99.89
h.l. px.	JM44	JMslp31	46.02	0.00	0.00	52.61	0.00	0.00	0.00	0.00	0.00	0.00	98.63
h.l. px.	JM44	JMslp97	46.49	0.00	0.00	53.72	0.00	0.00	0.00	0.00	0.00	0.00	100.2
c.px.	NA18	JMslp154	45.50	0.35	0.00	51.65	0.00	0.00	0.00	0.00	0.00	0.00	97.49
c.px.	NA18	JMslp155	45.16	0.37	0.00	52.00	0.00	0.00	0.00	0.00	0.00	0.00	97.52

Pentlandite

Lith.	*Sample no.*	*Probe no.*	*Fe*	*Ni*	*Co*	*S*	*Cu*	*As*	*Sb*	*Ag*	*Pd*	*Pt*	*Tot.*
h.l. px.	JM44	JMslp30b	26.40	37.91	1.76	32.86	0.00	0.00	ns	ns	ns	ns	98.93
h.l. px.	JM44	JMslp30c	26.80	38.04	1.59	32.54	0.00	0.00	ns	ns	ns	ns	98.97
h.l. px.	JM44	JMslp30d	26.69	38.26	1.45	32.68	0.00	0.00	ns	ns	ns	ns	99.08
h.l. px.	JM44	JMslp32e	27.06	38.37	1.51	32.8	0.00	0.00	ns	ns	ns	ns	99.74
h.l. px.	JM45	JMslp102	26.27	37.68	1.55	32.79	0.00	0.00	ns	ns	ns	ns	98.29
h.l.wh.	RLO58	RAF	27.85	36.23	1.64	32.75	0.07	0.00	0.01	0.01	ns	ns	98.56
c.px.	JM13	JMslp18	32.14	33.15	1.71	32.67	0.00	0.00	0.00	0.00	ns	ns	99.66
c.px.	JM13	JMslp19x	31.86	32.48	2.20	32.18	0.00	0.00	0.00	0.00	ns	ns	98.71
c.px.	JM14	SUG	29.08	27.89	1.72	32.94	7.35	0.00	0.00	0.01	0.00	ns	98.99
c.px.	JM14	SUH	30.08	33.89	2.14	32.75	0.85	0.00	0.00	0.01	0.03	ns	99.75
c.px.	JM14	SUH*2	28.29	32.42	1.98	32.86	3.16	0.00	0.00	0.01	0.04	ns	98.76
c.px.	NA3	JMslp43	27.04	37.29	2.49	32.43	0.00	0.00	0.00	0.00	ns	ns	99.25
c.px.	NA3	JMslp43b	27.39	37.04	2.17	32.47	0.00	0.00	0.00	0.00	ns	ns	99.07
c.px.	NA3	JMslp44	27.06	36.40	2.36	32.25	0.00	0.00	0.00	0.00	ns	ns	98.07
c.px.	NA3	JMslp44b	26.88	36.19	2.50	32.09	0.00	0.00	0.00	0.00	ns	ns	97.66
c.px.	NA3	JMslp45	27.77	37.34	1.95	32.54	0.00	0.00	0.00	0.00	ns	ns	99.60
c.px	NA3	JMslp46	24.07	36.23	5.85	32.68	0.00	0.00	0.00	0.00	ns	ns	98.83
c.px	NA3	JMslp47	26.97	35.33	4.72	32.76	0.00	0.00	0.00	0.00	ns	ns	99.78
c.px.	NA15	SUK	24.72	39.06	3.02	32.18	0.05	0.18	0.00	0.01	0.01	ns	99.23
c.px.	NA15	SUL	26.14	37.09	3.31	32.62	0.05	0.18	0.00	0.00	0.03	ns	99.42
c.px.	NA15	SUN	25.95	37.33	3.62	32.17	0.02	0.00	0.00	0.00	0.04	ns	99.13
c.px.	NA15	SUO	25.49	37.41	3.57	32.42	0.03	0.20	0.00	0.01	0.03	ns	99.16
c.px.	NA21	JMslp115	25.70	37.63	2.41	32.42	0.00	0.00	0.00	0.00	ns	ns	98.16
c.px.	NA21	JMslp116	27.14	36.06	2.99	32.61	0.00	0.00	0.00	0.00	ns	ns	98.81
c.px.	NA21	JMslp117	27.52	36.69	1.68	32.20	0.00	0.00	0.00	0.00	ns	ns	98.09
c.px.	NA21	JMslp118	28.94	36.01	1.60	32.30	0.00	0.00	0.00	0.00	ns	ns	98.84
c.px.	NA25c	JMslp62	25.84	38.14	2.92	32.72	0.00	0.00	0.00	0.00	ns	ns	99.62
c.px.	NA25c	JMslp65	25.37	39.25	3.05	32.61	0.00	0.00	0.00	0.00	ns	ns	100.3
c.px.	NA25c	JMslp68	28.75	35.24	2.91	32.64	0.00	0.00	0.00	0.00	ns	ns	99.56
c.px.	NA27	NAA	28.83	35.39	2.43	32.32	0.00	0.16	0.00	0.01	0.01	ns	99.21
c.px.	NA27	NAD	29.08	35.26	1.55	32.85	0.01	0.01	0.00	0.01	0.01	ns	98.84
c.px.	NA27	NAE	29.85	33.88	2.89	32.32	0.05	0.01	0.00	0.01	0.04	ns	99.05
c.px.	NA27	NAH	29.76	33.72	2.87	32.53	0.07	0.04	0.00	0.00	0.04	ns	99.04
wh.dn.	JM37	JMslp130	27.97	37.64	1.77	31.72	0.00	0.00	0.00	0.00	0.00	ns	99.10
c. dn.	JM39	PNA	38.40	25.36	1.99	33.67	0.06	0.00	0.00	0.01	0.03	0.03	99.55
c. dn.	JM40	JMslp33	36.92	28.48	0.88	32.48	0.00	0.00	0.00	0.00	0.00	0.00	98.76
c. dn.	JM40	JMslp34	35.13	30.55	1.01	32.35	0.00	0.00	0.00	0.00	0.00	0.00	99.04
c. dn.	JM40	JMslp34b	35.58	29.36	1.25	32.35	0.00	0.00	0.00	0.00	0.00	0.00	98.53
c. dn.	JM40	JMslp34c	36.01	29.08	0.93	32.73	0.00	0.00	0.00	0.00	0.00	0.00	98.76
c. dn.	JM40	JMslp35	34.97	31.18	0.98	32.95	0.00	0.00	0.00	0.00	0.00	0.00	100.1
c. dn.	JM40	JMslp39	35.62	31.29	0.91	32.81	0.00	0.00	0.00	0.00	0.00	0.00	100.6
c. dn.	JM40	JMslp123	34.33	31.58	1.13	32.27	0.00	0.00	0.00	0.00	0.00	0.00	99.30
c. dn.	JM40	JMslp133	34.78	31.29	0.88	32.30	0.00	0.00	0.00	0.00	0.00	0.00	99.25
c. dn.	JM40	JMslp134	31.79	33.82	0.67	32.18	0.00	0.00	0.00	0.00	0.00	0.00	98.46
c. dn.	JM40	JMslp136	35.88	30.03	0.88	32.57	0.00	0.00	0.00	0.00	0.00	0.00	99.36
c. dn.	JM40	JMslp138	35.99	29.48	0.98	32.41	0.00	0.00	0.00	0.00	0.00	0.00	98.86
c. dn.	JM40	JMslp140	35.77	29.38	1.11	32.57	0.00	0.00	0.00	0.00	0.00	0.00	98.83
c. dn.	JM40	JMslp161	34.51	30.35	0.70	31.94	0.00	0.00	0.00	0.00	0.00	0.00	97.50

Pentlandite

Lith.	*Sample no.*	*Probe no.*	*Fe*	*Ni*	*Co*	*S*	*Cu*	*As*	*Sb*	*Ag*	*Pd*	*Pt*	*Tot.*
c. dn.	JM40	JMslp162	34.51	31.25	0.80	32.82	0.00	0.00	0.00	0.00	0.00	0.00	99.38
c. dn.	JM40	JMslp163	35.82	31.01	0.94	33.01	0.00	0.00	0.00	0.00	0.00	0.00	100.8
c. dn.	JM40	JMslp164	34.61	30.81	0.71	32.31	0.00	0.00	0.00	0.00	0.00	0.00	98.44
c. dn.	JM40	JMslp165	33.96	32.14	0.80	32.58	0.00	0.00	0.00	0.00	0.00	0.00	99.49
c. dn.	NB1N	PNA	30.93	34.19	1.35	33.09	0.02	0.14	0.00	0.00	0.03	0.00	99.75
c. dn.	NB1N	PNB	30.32	34.59	1.33	33.06	0.06	0.00	0.00	0.01	0.03	0.00	99.40
c. dn.	NB1N	PNF	30.02	34.17	1.20	33.16	0.03	0.06	0.01	0.01	0.04	0.03	98.73
c. dn.	NB1N	PNJ	33.10	32.30	1.14	33.43	0.15	0.07	0.00	0.01	0.04	0.00	100.2
c. dn.	NB1N	PNK	32.53	33.08	1.09	33.77	0.09	0.00	0.00	0.01	0.03	0.00	100.6
c. dn.	NB1N	UNB	29.56	35.46	1.43	32.72	0.02	0.05	0.00	0.01	0.04	0.03	99.32
c. dn.	NB1N	PNO	31.77	32.58	1.22	32.51	0.01	0.00	0.00	0.03	0.04	0.10	98.26
c. dn.	NB1N	PNP	32.88	32.35	1.26	33.55	0.02	0.16	0.00	0.00	0.04	0.16	100.4
c. dn.	NB1N	PNR	29.43	34.23	1.96	33.16	0.42	0.00	0.01	0.00	0.01	0.00	99.22
c. dn.	NB1N	PNU	28.16	36.54	1.99	32.89	0.08	0.07	0.01	0.01	0.04	0.00	99.79
c. dn.	NB1N	PNV	29.52	34.88	2.08	33.26	0.05	0.02	0.01	0.03	0.03	0.07	99.95
c. dn.	NB2a	PEA	31.67	32.56	1.11	33.37	0.07	0.00	0.00	0.00	0.00	0.00	98.78
c. dn.	NB2a	PEG	33.93	30.48	1.02	35.85	0.00	0.00	0.00	0.00	0.00	0.00	101.3
c. dn.	NB2a	PEH	32.85	33.00	0.77	34.04	0.02	0.00	0.00	0.00	0.00	0.00	100.7
c. dn.	NB2a	PEL	31.96	32.22	1.32	35.29	0.01	0.00	0.00	0.00	0.00	0.00	100.8
c. dn.	NB2-2	BRK	32.33	33.36	0.47	31.68	0.58	0.12	0.00	ns	0.03	0.03	98.60
c. dn.	NB2Ba	BBT	35.80	28.70	0.74	32.71	0.01	0.04	0.00	0.00	0.03	0.00	98.05
c. dn.	NB2Ba	BBU	33.98	30.51	0.84	32.49	0.00	0.13	0.00	0.01	0.03	0.00	97.99
c. dn.	NB2Ba	BBV	35.10	29.80	0.38	33.26	0.00	0.01	0.00	0.01	0.01	0.01	98.58
c. dn.	NB2Bb	NBB	34.34	31.07	0.47	33.21	0.02	0.06	0.00	0.04	0.01	0.15	99.37
c. dn.	NB2Bb	NBC	33.91	30.68	0.55	32.95	0.05	0.04	0.00	0.01	0.06	0.04	98.29
c. dn.	NB2Bb	NBF	35.47	29.52	0.55	33.41	0.00	0.04	0.00	0.01	0.03	0.16	99.19
c. dn.	NB2Bb	NBG	35.64	29.53	0.50	33.59	0.06	0.10	0.00	0.03	0.01	0.07	99.53
c. dn.	NB2Bb	NBH	35.16	30.06	0.75	33.32	0.05	0.04	0.01	0.03	0.07	0.09	99.58
c. dn.	NB2Bb	NBI	33.11	30.35	0.74	32.98	0.19	0.00	0.00	0.03	0.00	0.07	97.47
c. dn.	NB2Bb	NBJ	33.61	30.89	0.73	33.73	0.01	0.10	0.01	0.01	0.03	0.00	99.12
c. dn.	NB2Bb	NBK	35.04	29.44	0.80	33.38	0.01	0.12	0.00	0.01	0.03	0.15	98.98
c. dn.	NB2Bb	NBM	33.91	29.86	0.80	33.17	0.01	0.10	0.01	0.00	0.01	0.06	97.93
c. dn.	NB2Bb	NBQ	35.35	29.29	0.47	33.56	0.01	0.10	0.00	0.01	0.06	0.10	98.95
c. dn.	NB2Bb	NBR	35.68	28.83	0.44	33.55	0.02	0.07	0.00	0.01	0.03	0.09	98.72
c. dn.	NB2C	PFH	33.75	31.05	0.76	32.69	0.05	0.00	0.00	0.00	0.00	0.00	98.30
c. dn.	NB2G	PFB	31.95	34.37	1.13	32.4	0.07	0.00	0.00	0.00	0.00	0.00	99.92
c. dn.	NB2H	BRD	33.13	31.61	1.02	32.99	0.09	0.00	0.00	0.01	0.04	0.00	98.89
c. dn.	NB2K	PNL	29.92	33.12	1.52	32.57	0.24	0.07	0.00	0.01	0.04	0.10	97.59
c. dn.	NB3V	PNA	34.04	31.67	0.95	33.25	0.06	0.00	0.00	0.00	0.04	0.00	100.0
c. dn.	NB3V	PNB	34.02	31.41	1.06	33.26	0.05	0.07	0.00	0.01	0.04	0.00	99.92
c. dn.	NB3V	PND	33.79	31.01	1.02	33.04	0.05	0.16	0.00	0.03	0.04	0.01	99.15
c. dn.	NB3V	PNE	34.77	30.46	1.06	33.15	0.05	0.07	0.01	0.01	0.04	0.00	99.62
c. dn.	NB3V	PNF	34.99	29.84	0.99	32.36	0.45	0.07	0.00	0.00	0.04	0.12	98.86
c. dn.	NB3V	PNH	34.96	30.47	0.75	33.21	0.03	0.16	0.01	0.01	0.03	0.12	99.75
c. dn.	NB3V	PNI	33.82	31.40	1.00	33.18	0.01	0.07	0.00	0.01	0.03	0.01	99.53
c. dn.	NB3V	PNJ	35.09	29.41	1.24	33.38	0.08	0.11	0.01	0.00	0.03	0.09	99.44
c. dn.	RLO80B	PLA	32.75	33.25	0.96	32.00	0.03	0.04	0.00	0.01	0.03	0.00	99.07

Pentlandite

Lith.	*Sample no.*	*Probe no.*	*Fe*	*Ni*	*Co*	*S*	*Cu*	*As*	*Sb*	*Ag*	*Pd*	*Pt*	*Tot.*
c. dn.	RLO80B	PLC	32.76	32.76	1.02	32.48	0.01	0.05	0.00	0.00	0.04	0.00	99.12
c. dn.	RLO80B	PLD	33.36	32.06	1.05	32.07	0.07	0.00	0.00	0.01	0.01	0.00	98.63
c. dn.	RLO80B	PLF	33.80	31.57	1.04	32.06	0.03	0.00	0.00	0.01	0.04	0.00	98.55
c. dn.	RLO80B	PLI	32.09	33.83	0.91	32.24	0.02	0.00	0.00	0.01	0.03	0.00	99.13
c. dn.	RLO80B	PLK	31.98	33.45	0.94	32.66	0.05	0.04	0.00	0.01	0.06	0.00	99.19
c. dn.	RLO80B	PLM	32.02	33.51	0.85	32.61	0.01	0.30	0.01	0.01	0.01	0.00	99.33
c. dn.	RLO80B	PLU	33.42	31.79	0.83	32.25	0.05	0.00	0.00	0.01	0.03	0.00	98.38
c. dn.	RLO80A	PMA	33.46	31.93	0.99	32.37	0.10	0.06	0.01	0.03	0.01	0.00	98.96
c. dn.	RLO80A	PMC	33.03	31.99	0.95	32.61	0.07	0.00	0.01	0.01	0.01	0.00	98.68
c. dn.	RLO80A	PME	33.06	31.42	1.06	32.3	0.48	0.00	0.00	0.03	0.04	0.00	98.39
c. dn.	RLO80A	PMF	33.50	31.70	1.01	32.59	0.12	0.06	0.00	0.00	0.03	0.00	99.01
c. dn.	RLO80A	PMQ	32.69	32.23	0.97	31.88	0.09	0.10	0.00	0.01	0.01	0.00	97.98
c. dn.	RLO80A	PMR	32.69	32.40	0.95	31.58	0.14	0.13	0.01	0.01	0.04	0.00	97.95
t. dn.	JM42	JMslp81	35.73	30.10	0.69	32.76	0.00	0.00	0.00	0.00	0.00	0.00	99.28
t. dn.	JM42	JMslp85	35.33	31.00	0.39	32.82	0.00	0.00	0.00	0.00	0.00	0.00	99.54
t. dn.	JM42	JMslp86	35.80	30.37	0.73	32.96	0.00	0.00	0.00	0.00	0.00	0.00	99.85
t. dn.	JM42	PNA	35.26	30.32	0.69	32.70	0.03	0.07	0.00	0.01	0.04	0.00	99.12
t. dn.	JM42	PNB	35.13	30.37	0.68	32.97	0.08	0.02	0.01	0.01	0.06	0.00	99.33
t. dn.	JM42	PNI	34.63	31.31	0.57	32.46	0.16	0.11	0.00	0.00	0.01	0.00	99.25
t. dn.	JM42	PNP	33.68	31.75	0.70	32.20	0.17	0.00	0.31	0.00	0.03	0.00	98.84
t. dn.	JM42	PNR	34.55	31.03	0.56	31.97	0.06	0.00	0.00	0.01	0.04	0.00	98.22
t. dn.	JM42	PNT	35.24	31.04	0.61	32.29	0.11	0.05	0.00	0.01	0.04	0.00	99.39
t. dn.	JM42	PNX	31.77	38.66	0.53	28.05	0.20	0.05	0.01	0.03	0.03	ns	99.49
dn.pod.	MR11	RBM	23.80	42.70	0.46	31.46	0.20	0.20	0.00	0.01	0.04	0.00	98.87
dn.pod.	MR11	RBN	26.94	38.81	0.54	32.12	0.16	0.05	0.01	0.00	0.03	0.00	98.66
dn.pod.	MR11	RBQ	28.26	37.12	0.48	32.26	0.44	0.16	0.00	0.01	0.03	0.00	98.76
dn.pod.	MR11	RBT	29.31	36.21	0.46	32.38	0.14	0.34	0.01	0.01	0.04	0.00	98.90
tc-carb.	JM32	JMF	33.73	31.47	1.19	32.49	0.02	0.01	0.00	0.01	0.03	0.07	99.02
tc-carb.	JM32	JBA	33.80	31.45	1.08	33.22	0.01	0.00	0.00	0.01	0.04	0.00	99.61
tc-carb.	JM32	JBB	32.27	31.84	1.12	33.63	0.00	0.12	0.00	0.01	0.04	0.00	99.03
tc-carb.	JM32	JBL	33.86	30.35	0.82	33.74	0.06	0.00	0.00	0.01	0.01	0.07	98.92
tc-carb.	JM32	JBM	33.14	30.58	0.79	33.21	0.01	0.08	0.00	0.00	0.03	0.03	97.87
tc-carb.	JM32	JBO	34.26	30.72	0.78	33.20	0.02	0.01	0.00	0.01	0.01	0.04	99.05
tc-carb.	JM32	JBQ	33.01	30.05	0.78	34.63	0.01	0.00	0.00	0.03	0.06	0.00	98.57

Cobalt pentlandite

Lith.	*Sample no.*	*Probe no.*	*Fe*	*Ni*	*Co*	*S*	*Cu*	*As*	*Sb*	*Ag*	*Pd*	*Pt*	*Tot.*
gabbro	RLO61	COA	5.76	1.64	59.92	30.56	0.00	0.00	0.00	0.01	0.01	ns	97.90
gabbro	RLO61	COA(ii)	6.61	1.56	58.22	32.00	0.00	0.00	0.00	0.01	0.03	ns	98.43

Heazlewoodite

Lith.	Sample no.	Probe no.	Fe	Ni	Co	S	Cu	As	Sb	Ag	Pd	Pt	Tot.
c. px.	NA21	JMslp119	0.68	72.01	0.00	25.74	0.00	0.00	0.00	0.00	0.00	0.00	98.43
c. px.	NA21	JMslp121	0.65	72.45	0.00	26.01	0.00	0.00	0.00	0.00	0.00	0.00	99.11
c. px.	NA3	JMslp45b	1.09	73.54	0.00	26.16	0.00	0.00	0.00	0.00	0.00	0.00	100.8
c. px.	NA15	SUM	5.14	68.08	0.43	27.00	0.12	0.13	0.00	0.01	0.03	ns	101.0
c. px.	NA15	SUN	5.08	67.33	0.42	26.82	0.12	0.29	0.00	0.01	0.04	ns	100.1
c. px.	NB1N	PNN	0.46	72.93	0.04	27.24	0.10	0.01	0.00	0.03	0.03	0.01	100.9
c. dn.	NB2-2	HZA	0.05	74.18	0.00	25.72	0.59	0.06	0.00	ns	0.03	0.07	100.7
c. dn.	NB2C	PFL	0.34	70.87	0.00	27.41	0.08	0.00	0.00	0.00	0.00	0.00	98.70
c. dn.	NB2G	PEN	0.03	71.32	0.00	27.60	0.02	0.14	0.00	0.00	0.00	0.00	99.11
c. dn.	NB2G	PEO	0.04	71.55	0.00	28.87	0.08	0.09	0.00	0.00	0.00	0.00	100.6
c. dn.	NB2G	PEP	0.02	71.27	0.00	28.65	0.02	0.18	0.00	0.00	0.00	0.00	100.1
c. dn.	NB2G	PER	0.07	71.45	0.00	27.35	0.00	0.02	0.00	0.00	0.00	0.00	98.89
c. dn.	NB2G	PET	0.21	71.43	0.00	26.27	0.01	0.07	0.00	0.00	0.00	0.00	97.99
c. dn.	NB2G	PEW	0.04	71.11	0.00	26.05	0.01	0.12	0.00	0.00	0.00	0.00	97.33
c. dn.	NB2G	PEX	0.03	71.00	0.00	27.19	0.07	0.20	0.00	0.00	0.00	0.00	98.49
c. dn.	NB2G	PEY	0.04	71.43	0.00	25.99	0.04	0.14	0.00	0.00	0.00	0.00	97.64
c. dn.	NB2G	PFA	0.04	71.93	0.00	26.95	0.04	0.05	0.00	0.00	0.00	0.00	99.01
c. dn.	NB2G	PFC	0.06	71.90	0.00	26.69	0.05	0.07	0.00	0.00	0.00	0.00	98.77
c. dn.	NB2G	PFE	0.04	71.32	0.00	27.35	0.05	0.05	0.00	0.00	0.00	0.00	98.81
c. dn.	NB2G	PFG	0.05	71.29	0.00	27.22	0.02	0.09	0.00	0.00	0.00	0.00	98.67
c. dn.	NB2H	BRB	0.02	72.02	0.04	27.37	0.04	0.01	0.00	0.01	0.04	0.00	99.55
c. dn.	NB2H	BRJ	0.13	71.27	0.00	25.92	0.03	0.00	0.21	0.00	0.06	0.00	97.62
c. dn.	NB2J	HZA	0.43	73.11	0.02	27.38	0.11	0.00	0.00	0.01	0.03	0.00	101.1
c. dn.	NB2J	HZB	0.04	72.67	0.00	27.08	0.07	0.29	0.00	0.01	0.03	0.18	100.4
c. dn.	NB2K	PNK	0.12	72.96	0.03	26.31	0.11	0.00	0.00	0.01	0.04	0.10	99.68
c. dn.	NB2K	PNM	0.22	73.33	0.04	26.83	0.11	0.01	0.00	0.01	0.04	0.00	100.6
c. dn.	NB2K	PNN	0.04	73.38	0.02	26.11	0.10	0.08	0.00	0.01	0.04	0.06	99.84
c. dn.	NB2K	PNP	0.03	73.13	0.03	26.72	0.10	0.02	0.00	0.01	0.06	0.00	100.1
t. dn.	JM42	PNC	1.68	72.48	0.03	26.42	0.10	0.00	0.00	0.01	0.01	0.00	100.7
dn.pod	MR11	RBD	0.02	74.00	0.05	25.66	0.01	0.13	0.00	0.01	0.06	0.00	99.94
dn.pod	MR11	RBE	0.05	71.30	0.01	27.27	0.09	0.27	0.00	0.01	0.06	0.00	99.06
dn.pod	MR11	RBF	0.11	72.83	0.02	25.79	0.08	0.23	0.22	0.00	0.04	0.00	99.32
dn.pod	MR11	RBL	0.10	72.21	0.05	27.73	0.10	0.47	0.00	0.01	0.08	0.00	100.8
dn.pod	MR11	RBR	0.05	73.56	0.01	26.35	0.11	0.00	0.00	0.01	0.03	0.00	100.1
dn.pod	MR11	RBZ	0.01	73.89	0.02	26.51	0.14	0.24	0.00	0.01	0.06	0.00	100.9
dn.pod	MR11	RCC	0.04	73.47	0.02	26.56	0.12	0.14	0.00	0.01	0.06	0.00	100.4
dn.pod	MR11	RCE	2.10	72.66	0.03	26.47	0.04	0.00	0.00	0.01	0.06	0.00	101.4
dn.pod	MR11	RCJ	0.02	73.26	0.02	26.21	0.10	0.12	0.00	0.01	0.04	0.00	99.78
dn.pod	MR11	RCN	1.20	72.69	0.01	25.84	0.11	0.20	0.00	0.01	0.04	0.00	100.1
dn.pod	MR11	RCQ	0.37	73.16	0.03	25.14	0.08	0.19	0.00	0.01	0.07	0.00	99.05
dn.pod	MR11	RCS	0.03	73.12	0.01	25.7	0.11	0.35	0.00	0.01	0.03	0.00	99.36

Godlevskite

Lith.	Sample no.	Probe no.	Fe	Ni	Co	S	Cu	As	Sb	Ag	Pd	Pt	Tot.
dn. pod	MR11	RBV	0.10	68.04	0.00	31.13	0.04	0.13	0.00	0.01	0.03	ns	99.48

Awaruite

Lith.	*Sample no.*	*Probe no.*	*Fe*	*Ni*	*Co*	*S*	*Cu*	*As*	*Sb*	*Ag*	*Pd*	*Pt*	*Tot.*
c. dn.	JM40	JMslp141	23.43	59.13	0.00	0.51	0.00	0.00	0.00	0.00	0.00	0.00	83.07
c. dn.	JM40	JMslp142	25.44	72.25	0.64	0.31	0.00	0.00	0.00	0.00	0.00	0.00	98.63
c. dn.	RLO80A	PMO	21.31	64.07	0.09	0.27	3.60	0.00	0.00	0.01	0.04	0.00	89.39
c. dn.	RLO80A	PMS	26.63	56.62	0.15	5.46	1.09	0.00	0.00	0.04	0.05	0.00	90.04
c. dn.	RLO80B	PLB	22.88	61.74	0.10	0.49	0.22	0.00	0.00	0.01	0.01	0.00	85.45
c. dn.	NB2Bb	NBE	25.70	50.36	0.15	0.01	2.61	0.13	0.00	0.01	0.04	0.00	79.01
c. dn.	NB2C	PFK	22.76	62.19	0.00	1.10	0.26	0.00	0.00	0.00	0.00	0.00	86.31
c. dn.	NB2G	PEZ	24.78	68.02	0.04	0.36	0.20	0.10	0.00	0.00	0.00	0.00	93.5
c. dn.	NB2H	BRC	28.42	66.37	0.05	0.83	0.33	0.03	0.00	0.01	0.01	0.00	96.05
c. dn.	NB2H	BRK	27.78	59.95	0.08	0.67	0.41	0.12	0.00	0.02	0.03	0.00	89.06
c. dn.	NB2H	BRX	24.73	52.43	0.06	0.31	0.29	0.00	0.00	0.01	0.01	0.00	77.84
c. dn.	NB2H	BRZ	27.04	58.84	0.09	0.38	0.48	0.00	0.00	0.04	0.03	0.00	86.9
c. dn.	NB2H	AWS	23.03	63.54	0.07	0.50	0.32	0.00	0.00	0.00	0.02	0.07	87.55
c. dn.	NB2J	BED	26.81	64.18	0.07	0.32	0.44	0.00	0.00	0.00	0.06	0.00	91.88
c. dn.	NB2J	AWA	27.47	67.12	0.07	0.44	0.41	0.21	0.00	0.00	0.05	0.01	95.78
c. dn.	NB2K	AWD	21.78	58.37	0.19	3.14	0.35	0.06	0.00	0.02	0.01	0.09	84.01
c. dn.	NB2K	AWE	22.77	63.83	0.08	0.63	0.43	0.03	0.00	0.01	0.04	0.13	87.95
c. dn.	NB2K	AWP	23.26	66.58	0.10	0.46	0.53	0.11	0.00	0.01	0.01	0.00	91.06
c. dn.	NB2K	AWQ	20.81	59.62	0.05	0.47	0.20	0.07	0.00	0.01	0.05	0.00	81.28
c. dn.	NB3V	AWB	22.88	62.54	0.07	0.57	0.43	0.00	0.00	0.01	0.04	0.01	86.55
t. dn.	JM42	JMslp79	27.45	68.55	0.00	0.41	0.65	0.00	0.00	0.00	0.00	0.00	97.06
t. dn.	JM42	JMslp88	26.10	67.71	0.00	0.57	0.67	0.00	0.00	0.00	0.00	0.00	95.04
t. dn.	JM42	PNF	25.76	66.77	0.09	0.27	0.43	0.00	0.00	0.01	0.02	0.00	93.35
t. dn.	JM42	PNO	26.81	58.79	0.17	8.54	0.58	0.00	0.00	0.04	0.04	0.00	94.97
t. dn.	JM42	AWC	26.22	70.84	0.12	0.88	0.83	0.00	0.00	0.01	0.04	0.01	98.95

Native Cu

Lith.	*Sample no.*	*Probe no.*	*Fe*	*Ni*	*Co*	*S*	*Cu*	*As*	*Sb*	*Ag*	*Pd*	*Pt*	*Tot.*
wh.dn.	JM37	JMslp144	0.71	0.00	0.00	0.00	99.41	0.00	0.00	0.00	0.00	0.00	100.1
c. dn.	JM40	JMslp135	0.25	0.00	0.00	0.00	102.5	0.00	0.00	0.00	0.00	0.00	102.7
c. dn.	JM40	JMslp313	0.25	0.00	0.00	0.00	101.3	0.00	0.00	0.00	0.00	0.00	101.5
c. dn.	NB2J	BEF	1.08	0.53	0.04	0.03	99.93	0.07	0.00	0.01	0.04	0.00	101.7
c. dn.	NB3V	CUA	0.77	0.26	0.01	0.11	99.24	0.07	0.00	0.01	0.02	0.00	100.5
c. dn.	NB3V	CUB	1.20	1.36	0.02	0.11	98.94	0.13	0.00	0.02	0.01	0.00	101.8
dn.pod	MR11	RCX	1.35	0.04	0.00	0.08	99.90	0.01	0.01	0.02	0.05	0.00	101.5

Orcelite

Lith.	*Sample no.*	*Probe no.*	*Fe*	*Ni*	*Co*	*S*	*Cu*	*As*	*Sb*	*Ag*	*Pd*	*Pt*	*Tot.*
c. px.	NA25B	JMslp51	0.23	56.32	0.00	0.00	0.00	41.5	0.00	0.00	0.00	0.00	98.04
c. px.	NA25B	JMslp53	0.22	60.10	0.00	0.44	0.82	37.79	0.45	0.00	0.00	0.00	99.83
c. px.	NA25B	JMslp54	0.18	60.56	0.00	0.61	0.63	36.83	0.31	0.00	0.00	0.00	99.12
c. px.	NA25C	JMslp61	0.64	60.32	0.00	0.64	0.00	38.97	0.83	0.00	0.00	0.00	101.4
c. px.	NA25C	JMslp67	0.24	57.84	0.00	0.32	0.64	40.07	1.11	0.00	0.00	0.00	100.2
c. px.	NA25C	JMslp67B	0.46	58.96	0.00	0.36	0.54	39.68	0.70	0.00	0.00	0.00	100.7
c. dn.	NB2-2	BRG	1.95	65.59	0.01	0.13	0.64	32.4	1.04	0.00	0.04	0.01	101.2
c. dn.	NB2-2	BRH(ii)	2.19	66.18	0.02	0.08	0.11	31.05	1.00	0.00	0.01	0.05	100.7
c. dn.	NB2-2	BRQ(ii)	1.68	65.85	0.01	0.13	0.15	31.84	1.04	0.00	0.05	0.05	100.8
c. dn.	NB2-2	BRR(iii)	2.17	65.30	0.02	1.14	0.16	30.52	0.84	0.00	0.05	0.00	100.2
c. dn.	NB2-2	PNE(ii)	0.27	66.54	0.02	0.08	0.09	32.48	1.22	0.00	0.04	0.14	100.9
c. dn.	NB2G	SBA	0.20	64.12	0.00	0.01	0.13	32.01	1.48	0.01	0.05	0.05	98.01
dn. pod	MR11	RBA	0.06	62.35	0.01	0.59	0.69	33.01	2.18	0.01	0.06	0.00	98.96
dn. pod	MR11	RBB	0.14	62.13	0.00	0.54	0.70	33.63	2.11	0.01	0.08	0.00	99.34
dn. pod	MR11	RBC	0.06	63.26	0.03	0.09	0.05	35.34	0.90	0.01	0.03	0.00	99.77
dn. pod	MR11	RBO	1.31	62.90	0.01	0.54	0.11	34.54	0.80	0.01	0.03	0.00	100.3
dn. pod	MR11	RCA	0.11	66.19	0.01	0.08	0.23	33.86	0.84	0.01	0.03	0.00	101.4
dn. pod	MR11	RCG	0.50	63.00	0.03	0.08	0.10	35.92	0.74	0.01	0.04	0.00	100.4
dn. pod	MR11	RCH	0.48	61.58	0.06	0.70	0.50	34.76	1.37	0.01	0.05	0.00	99.51
dn. pod	MR11	RCI	0.13	64.22	0.04	0.35	0.63	32.89	1.48	0.00	0.08	0.00	99.82
dn. pod	MR11	RCK	0.21	65.58	0.00	0.07	0.20	33.58	0.70	0.02	0.06	0.00	100.4
dn. pod	MR11	RCP	0.09	60.08	0.02	1.49	0.44	35.67	2.17	0.01	0.12	0.00	100.1

Maucherite

Lith.	*Sample no.*	*Probe no.*	*Fe*	*Ni*	*Co*	*S*	*Cu*	*As*	*Sb*	*Ag*	*Pd*	*Pt*	*Tot.*
c. px.	NA25C	JMslp63	0.57	50.49	0.45	0.44	0.8	46.88	0.59	0.00	0.00	0.00	100.2
c. px.	NA25C	JMslp66	0.87	49.31	0.38	0.41	0.00	45.87	0.66	0.00	0.00	0.00	97.48
c. dn.	RLO51	RLE	0.27	50.47	1.86	0.18	0.08	48.00	0.21	0.04	0.05	0.05	101.2
ch.pod	JM33	JMslp175	1.28	49.43	0.00	0.62	1.99	47.53	0.00	0.00	0.00	0.00	100.8
ch.pod	JM33	JMslp178	1.18	48.29	0.00	0.71	2.40	46.15	0.00	0.00	0.00	0.00	98.72
ch.pod	JM33	JMslp179	1.08	50.13	0.00	0.72	1.30	47.43	0.00	0.00	0.00	0.00	100.7
ch.pod	JM33	JMslp180	0.31	50.85	0.00	0.28	0.00	47.15	0.00	0.00	0.00	0.00	98.58

Niccolite

Lith.	*Sample no.*	*Probe no.*	*Fe*	*Ni*	*Co*	*S*	*Cu*	*As*	*Sb*	*Ag*	*Pd*	*Pt*	*Tot.*
h.l. px.	JM45	JMslp99	2.32	42.64	0.38	1.86	0.00	53.98	0.00	0.00	0.00	0.00	101.2
ch.pod	JM33	JMslp172	0.16	44.41	0.00	0.67	0.51	55.46	0.00	0.00	0.00	0.00	101.2
ch.pod	JM33	JMslp173	0.24	44.00	0.00	0.74	0.78	54.74	0.00	0.00	0.00	0.00	100.5
ch.pod	JM33	JMslp176	0.00	44.65	0.00	0.71	0.74	54.77	0.00	0.00	0.00	0.00	100.9
ch.pod	JM33	JMslp177	0.36	44.4	0.00	0.54	0.00	54.26	0.00	0.00	0.00	0.00	99.55
ch.pod	JM33	JMslp181	0.00	44.49	0.00	0.92	0.48	55.74	0.00	0.00	0.00	0.00	101.6

Cobaltite

Lith.	*Sample no.*	*Probe no.*	*Fe*	*Ni*	*Co*	*S*	*Cu*	*As*	*Sb*	*Ag*	*Pd*	*Pt*	*Tot.*
h.l. px.	JM44	JMslp48	2.27	4.87	28.14	18.75	0.00	45.83	0.00	0.00	0.00	0.00	99.86
h.l. px.	JM44	JMslp49	2.23	5.06	28.93	19.10	0.00	46.78	0.00	0.00	0.00	0.00	102.1
h.l. px.	JM44	JMslp50	2.40	5.14	27.72	18.82	0.00	47.08	0.00	0.00	0.00	0.00	101.2
h.l. px.	JM45	JMslp103	2.41	4.97	27.96	19.35	0.00	46.62	0.00	0.00	0.00	0.00	101.3
h.l. px.	JM45	JMslp104	2.23	4.15	29.74	19.64	0.00	46.19	0.00	0.00	0.00	0.00	102.0
h.l. px.	JM45	JMslp106	3.51	6.47	25.73	19.64	0.00	46.57	0.00	0.00	0.00	0.00	101.9
tc-carb.	MR244	JM1*1	3.82	10.64	21.83	19.76	0.00	46.37	0.00	0.00	0.14	0.17	102.7
tc-carb.	MR244	JM1*2	3.88	10.69	21.55	19.48	0.00	46.26	0.00	0.01	0.10	0.00	102.0
tc-carb.	MR244	JM1*3	3.88	10.60	21.86	19.52	0.00	45.91	0.00	0.01	0.03	0.01	101.8
tc-carb.	MR244	ASA	3.90	10.89	21.32	19.42	0.00	45.07	0.00	0.01	0.03	0.06	100.7
tc-carb.	MR244	ASB	6.81	11.16	19.31	20.41	0.00	43.61	0.01	0.03	0.07	0.03	100.8
tc-carb.	MR244	ASD	3.98	11.06	21.08	19.45	0.00	45.58	0.01	0.01	0.08	0.01	101.3
tc-carb.	MR244	ASE	3.74	10.67	20.75	19.21	0.00	44.88	0.00	0.00	0.29	0.04	99.58

Magnetites

Sample	JM21 MTE	JM21 MTF	JM21 MTG	JM21 MTH	NB 2-2 MTA	NB 2-2 MTB	NB 2-2 MTC	NB 2-2 MTD	NB 2-2 MVA	NB 2-2 MVB	NB 2-2 MVC	RL O80B MTH	RL O80B MTJ
Wt% oxide													
MgO	1.27	1.09	2.94	3.88	0.92	1.20	1.63	0.97	1.28	1.40	1.46	1.60	0.13
Al2O3	0.03	0.00	0.03	0.03	0.00	0.00	0.03	0.00	0.00	0.00	0.00	ns	ns
TiO2	ns	ns	ns	ns	0.03	0.04	0.06	0.04	0.06	0.04	0.04	ns	ns
SiO2	1.19	2.12	2.31	3.00	0.13	0.13	0.40	0.16	0.19	0.24	0.16	0.57	0.19
FeO	93.22	93.79	93.57	92.43	98.53	98.34	96.93	98.42	97.14	96.30	96.97	95.36	98.12
Cr2O3	2.66	1.77	0.09	0.21	0.00	0.05	0.25	0.00	0.33	0.63	0.77	0.00	0.00
MnO	0.07	0.07	0.04	0.04	0.06	0.10	0.07	0.07	0.10	0.08	0.10	ns	ns
CoO	0.08	0.07	0.06	0.07	ns	ns	ns	ns	ns	ns	ns	0.19	0.15
NiO	0.07	0.07	0.01	0.06	0.30	0.48	0.44	0.51	0.46	0.47	0.47	1.01	0.44
Total	98.59	98.98	99.05	99.72	99.97	100.3	99.81	100.2	99.56	99.16	99.97	99.74	99.03
Form. units (32 O)													
Mg	0.58	0.49	1.32	1.71	0.42	0.55	0.74	0.74	0.59	0.64	0.66	0.82	0.06
Al	0.01	0.00	0.01	0.01	0.00	0.00	0.01	0.01	0.00	0.00	0.00	ns	ns
Ti	ns	ns	ns	ns	0.01	0.01	0.01	0.01	0.01	0.01	0.01	ns	ns
Si	0.36	0.64	0.69	0.89	0.04	0.04	0.12	0.12	0.06	0.07	0.05	0.15	0.06
Fe	22.23	22.13	21.91	21.28	23.54	23.39	23.05	23.05	23.26	23.11	23.09	22.93	23.66
Cr	0.64	0.42	0.02	0.05	0.00	0.01	0.06	0.06	0.08	0.15	0.19	0.00	0.00
Mn	0.02	0.02	0.01	0.01	0.01	0.03	0.02	0.02	0.03	0.02	0.03	ns	ns
Co	0.02	0.02	0.01	0.02	ns	ns	ns	ns	ns	ns	ns	0.05	0.04
Ni	0.02	0.02	0.00	0.01	0.07	0.12	0.11	0.11	0.11	0.12	0.12	0.25	0.11
Total	23.88	23.74	23.97	23.98	24.09	24.15	24.12	24.12	24.14	24.12	24.15	24.2	23.93

Magnetites

Sample	RL O80B MTK	MR 11 MTA	MR 11 MTB	MR 11 MTC	MR 11 MTD	MR 11 MTE	MR 11 MTF	MR 11 MTG	MR 11 MTH	MR 11 MTI	MR 11 MTJ	MR 11 MTK	MR 244 MTC
Wt% oxide													
MgO	0.08	0.97	1.20	1.18	0.83	0.95	0.97	1.01	1.18	0.87	1.15	0.85	8.97
Al2O3	ns	ns	ns	ns	ns	ns	ns	ns	ns	ns	ns	ns	0.70
TiO2	ns	ns	ns	ns	ns	ns	ns	ns	ns	ns	ns	ns	ns
SiO2	0.19	0.11	0.08	0.08	0.08	0.11	0.08	0.21	0.11	0.08	0.13	0.11	6.85
FeO	97.51	94.67	94.30	94.22	93.71	93.66	96.90	93.37	94.34	95.03	95.77	94.64	44.65
Cr2O3	0.00	0.34	0.29	0.00	0.00	0.00	0.02	0.00	0.00	0.40	0.00	0.00	38.17
MnO	ns	0.08	0.07	0.07	0.06	0.08	0.08	0.06	0.07	0.04	0.08	0.07	0.40
CoO	0.17	0.15	0.17	0.15	0.17	0.17	0.15	0.14	0.12	0.11	0.14	0.17	ns
NiO	0.46	2.46	1.78	3.48	4.89	3.76	1.29	4.50	2.76	2.60	1.81	3.29	0.06
Total	98.41	98.78	97.89	99.18	99.74	98.73	99.49	99.29	98.58	99.13	99.08	99.13	99.8
Form. units (32 O)													
Mg	0.04	0.45	0.56	0.55	0.38	0.44	0.45	0.47	0.55	0.41	0.53	0.39	3.53
Al	ns	ns	ns	ns	ns	ns	ns	ns	ns	ns	ns	ns	0.22
Ti	ns	ns	ns	ns	ns	ns	ns	ns	ns	ns	ns	ns	ns
Si	0.06	0.03	0.02	0.02	0.02	0.03	0.02	0.07	0.03	0.02	0.04	0.03	1.81
Fe	23.73	22.92	22.90	22.82	22.68	22.82	23.31	22.62	22.92	22.99	23.10	22.92	9.18
Cr	0.00	0.08	0.07	0.00	0.00	0.00	0.01	0.00	0.00	0.10	0.00	0.00	7.97
Mn	ns	0.02	0.02	0.02	0.01	0.02	0.02	0.01	0.02	0.01	0.02	0.02	0.09
Co	0.04	0.04	0.04	0.04	0.04	0.04	0.04	0.03	0.03	0.03	0.03	0.04	ns
Ni	0.11	0.61	0.45	0.87	1.22	0.95	0.32	1.13	0.69	0.65	0.45	0.82	0.01
Total	23.98	24.15	24.06	24.32	24.35	24.3	24.17	24.33	24.24	24.21	24.17	24.22	22.81

NB-2 chrome-spinels

Sample	NB2-BBa	NB2-BBb	NB2-BBc	NB2-BBf	NB2-BBg	NB2-BCa	NB2-BCb	NB2-BCc	NB2-BDa	NB2-BDb	NB2-BDc	NB2-BEa	NB2-BEb
Wt% oxide													
Cr2O3	45.66	45.83	45.62	44.41	44.77	43.64	43.46	43.99	44.37	43.67	43.55	44.80	44.58
Al2O3	19.85	20.02	19.88	20.64	20.69	20.47	20.5	20.67	21.15	21.46	20.99	20.81	21.28
TiO2	0.20	0.21	0.21	0.22	0.23	0.22	0.20	0.22	0.20	0.22	0.20	0.20	0.22
SiO2	0.05	0.05	0.08	0.08	0.08	0.08	0.08	0.05	0.08	0.08	0.08	0.08	0.08
Fe2O3	5.13	5.13	5.22	5.62	5.01	5.60	6.17	5.57	5.51	5.61	5.68	5.36	5.09
FeO	17.10	16.98	16.80	16.91	16.71	16.93	17.18	16.31	16.38	17.10	16.90	16.73	16.57
MgO	11.80	12.03	12.07	12.09	12.14	11.76	11.71	12.25	12.52	12.12	11.99	12.27	12.47
MnO	0.24	0.20	0.20	0.20	0.23	0.22	0.24	0.18	0.18	0.21	0.21	0.20	0.13
NiO	0.09	0.06	0.06	0.09	0.12	0.09	0.07	0.12	0.12	0.09	0.09	0.12	0.12
CaO	0.01	0.01	0.03	0.03	0.01	0.08	0.09	0.05	0.03	0.01	0.04	0.01	0.01
Total	100.1	100.5	100.2	100.3	99.99	99.09	99.69	99.41	100.5	100.6	99.72	100.6	100.6
Form. units (32 O)													
Cr	9.05	9.04	9.02	8.75	8.83	8.71	8.63	8.72	8.68	8.55	8.61	8.79	8.72
Al	5.87	5.89	5.86	6.06	6.09	6.09	6.07	6.11	6.17	6.27	6.19	6.09	6.20
Ti	0.04	0.04	0.04	0.04	0.04	0.04	0.04	0.04	0.04	0.04	0.04	0.04	0.04
Si	0.01	0.01	0.02	0.02	0.02	0.02	0.02	0.01	0.02	0.02	0.02	0.02	0.02
Fe3	0.97	0.96	0.98	1.05	0.94	1.06	1.17	1.05	1.03	1.05	1.07	1.00	0.95
Fe2	3.59	3.54	3.51	3.52	3.49	3.57	3.61	3.42	3.39	3.54	3.54	3.47	3.43
Mg	4.41	4.47	4.50	4.49	4.52	4.42	4.38	4.58	4.62	4.47	4.47	4.54	4.60
Mn	0.05	0.04	0.04	0.04	0.05	0.05	0.05	0.04	0.04	0.04	0.04	0.04	0.03
Ni	0.02	0.01	0.01	0.02	0.02	0.02	0.01	0.02	0.02	0.02	0.02	0.02	0.02
Ca	0.00	0.00	0.01	0.01	0.00	0.02	0.02	0.01	0.01	0.00	0.01	0.00	0.00
Total	24.01	24.01	24.01	24.01	24.01	24.01	24.01	24.01	24.01	24.01	24.01	24.01	24.01

NB-2 chrome-spinels

Sample	NB2-BEc	NB2-BFa	NB2-BFb	NB2-BFc	NB2-BGa	NB2-BGb	NB2-BGc	NB2-BIa	NB2-BIb	NB2-BIc	NB2-BJa	NB2-BJb	NB2-BJc
Wt% oxide													
Cr2O3	44.15	43.79	43.40	43.37	42.51	42.85	42.11	41.69	40.95	41.80	40.86	41.78	41.42
Al2O3	21.20	21.58	21.51	21.61	22.45	22.19	22.44	22.97	23.61	23.50	23.43	23.43	23.16
TiO2	0.23	0.23	0.23	0.20	0.22	0.23	0.23	0.25	0.23	0.25	0.23	0.23	0.23
SiO2	0.05	0.08	0.08	0.05	0.05	0.08	0.05	0.08	0.05	0.05	0.08	0.05	0.08
Fe2O3	5.31	5.45	5.33	5.61	5.32	5.61	5.67	5.70	5.66	5.30	5.74	5.29	5.25
FeO	17.01	16.97	16.96	16.94	16.20	16.89	16.69	17.49	17.08	16.25	16.81	16.17	16.76
MgO	12.10	12.19	12.08	12.12	12.59	12.30	12.30	12.01	12.25	12.82	12.36	12.80	12.30
MnO	0.17	0.21	0.18	0.19	0.18	0.21	0.19	0.21	0.20	0.18	0.20	0.17	0.19
NiO	0.10	0.13	0.09	0.10	0.09	0.12	0.09	0.12	0.06	0.10	0.10	0.13	0.07
CaO	0.00	0.04	0.03	0.03	0.03	0.01	0.04	0.01	0.03	0.01	0.01	0.01	0.03
Total	100.3	100.7	99.89	100.2	99.63	100.5	99.81	100.5	100.1	100.3	99.82	100.1	99.49
Form. units (32 O)													
Cr	8.67	8.56	8.55	8.51	8.33	8.36	8.26	8.12	7.97	8.10	7.97	8.11	8.12
Al	6.21	6.29	6.32	6.33	6.56	6.46	6.56	6.67	6.86	6.79	6.82	6.79	6.77
Ti	0.04	0.04	0.04	0.04	0.04	0.04	0.04	0.05	0.04	0.05	0.04	0.04	0.04
Si	0.01	0.02	0.02	0.01	0.01	0.02	0.01	0.02	0.01	0.01	0.02	0.01	0.02
Fe3	0.99	1.01	1.00	1.05	0.99	1.04	1.06	1.06	1.05	0.98	1.07	0.98	0.98
Fe2	3.54	3.51	3.53	3.52	3.36	3.49	3.46	3.60	3.52	3.33	3.47	3.32	3.47
Mg	4.48	4.49	4.48	4.48	4.65	4.52	4.55	4.41	4.50	4.68	4.55	4.69	4.54
Mn	0.04	0.04	0.04	0.04	0.04	0.04	0.04	0.04	0.04	0.04	0.04	0.04	0.04
Ni	0.02	0.03	0.02	0.02	0.02	0.02	0.02	0.02	0.01	0.02	0.02	0.03	0.01
Ca	0.00	0.01	0.01	0.01	0.01	0.00	0.01	0.00	0.01	0.00	0.00	0.00	0.01
Total	24.01	24.01	24.01	24.01	24.01	24.01	24.01	24.01	24.01	24.01	24.01	24.01	24.01

NB-2 chrome-spinels

Sample	NB2-BKa	NB2-BKb	NB2-BKc	NB2-BLa	NB2-BLb	NB2-BLc	NB2-BMa	NB2-BMb
Wt% oxide								
Cr2O3	41.39	40.83	40.77	41.07	40.48	40.75	45.52	45.24
Al2O3	22.57	23.54	23.52	24.27	24.35	23.69	20.43	20.33
TiO2	0.23	0.23	0.25	0.20	0.22	0.23	0.18	0.20
SiO2	0.05	0.08	0.08	0.05	0.05	0.05	0.05	0.05
Fe2O3	6.03	5.74	5.43	5.08	4.95	5.50	4.31	5.06
FeO	15.70	16.71	16.97	16.14	16.62	16.97	17.06	17.35
MgO	12.84	12.45	12.19	12.90	12.42	12.21	11.79	11.73
MnO	0.18	0.22	0.22	0.15	0.20	0.20	0.20	0.21
NiO	0.09	0.06	0.06	0.07	0.12	0.10	0.09	0.10
CaO	0.01	0.03	0.06	0.03	0.05	0.05	0.01	0.01
Total	99.09	99.89	99.55	99.95	99.46	99.75	99.64	100.3
Form. units (32 O)								
Cr	8.13	7.96	7.98	7.95	7.89	7.96	9.04	8.94
Al	6.61	6.84	6.86	7.01	7.08	6.90	6.05	5.99
Ti	0.04	0.04	0.05	0.04	0.04	0.04	0.03	0.04
Si	0.01	0.02	0.02	0.01	0.01	0.01	0.01	0.01
Fe3	1.13	1.07	1.01	0.94	0.92	1.02	0.81	0.95
Fe2	3.26	3.44	3.51	3.31	3.43	3.51	3.58	3.63
Mg	4.76	4.57	4.50	4.71	4.56	4.49	4.41	4.37
Mn	0.04	0.05	0.05	0.03	0.04	0.04	0.04	0.04
Ni	0.02	0.01	0.01	0.01	0.02	0.02	0.02	0.02
Ca	0.00	0.01	0.02	0.01	0.01	0.01	0.00	0.00
Total	24.01	24.01	24.01	24.01	24.01	24.01	24.00	24.01

B.3 Isotope data

Stepped combustion data for sulphur

nm = no measurement.

JM1 gabbro (a)

Temp	Type	[S] (ng)	[S] (ppm)	$\delta^{34}S$ (‰)	σ (±‰)
100	C	1590	30.2	nm	nm
200	C	7800	148	+4.2	0.3
300	C	1000	19.0	nm	nm
400	C	9600	182	+1.1	0.2
500	C	157400	2987	+1.6	0.1
600	C	64400	1222	+2.8	0.1
700	C	6740	128	+3.8	0.2
800	C	4800	91.1	+6.6	0.3
900	C	2600	49.3	+7.5	0.4
1000	C	2300	43.6	+8.3	0.6
1100	C	100	1.90	nm	nm
1200	C	nm	nm	nm	nm

JM1 gabbro (b)

Temp	Type	[S] (ng)	[S] (ppm)	$\delta^{34}S$ (‰)	σ (±‰)
150	C	700	12.9	nm	nm
200	C	1500	27.7	nm	nm
250	C	600	11.1	nm	nm
300	C	200	3.70	nm	nm
350	C	1000	18.5	nm	nm
400	C	3500	64.7	+1.8	0.3
450	C	12000	222	+1.4	0.1
500	C	51000	943	+1.7	0.1
550	C	57000	1054	+1.7	0.1
600	C	23000	425	+2.1	0.2
650	C	8000	148	+5.2	0.4
700	C	5000	92.4	+0.8	0.2
800	C	20000	370	+6.5	0.1
900	C	5300	98.0	+8.2	0.4
1000	C	4800	88.7	+8.5	0.5
1100	C	2800	51.8	+11.8	0.6
1200	C	nm	nm	+0.0	0.0

JM13 pyroxenite (a)

Temp	Type	[S] (ng)	[S] (ppm)	$\delta^{34}S$ (‰)	σ (±‰)
100	C	300	5.60	nm	nm
200	C	100	1.87	nm	nm
300	C	100	1.87	nm	nm
400	C	27000	504	+1.4	0.2
500	C	2300	42.9	+2.3	0.3
600	C	700	13.1	nm	nm
700	C	22000	410	+4.5	0.2
800	C	3700	69.0	+1.2	0.3
900	C	3600	67.2	+3.4	0.3
1000	C	11800	220	+2.7	0.1
1200	C	4500	84.0	+2.4	0.2

JM13 pyroxenite (b)

Temp	Type	[S] (ng)	[S] (ppm)	$\delta^{34}S$ (‰)	σ (±‰)
100	C	100	1.03	nm	nm
200	C	200	2.06	nm	nm
300	C	1900	19.6	nm	nm
400	C	53500	552	+1.1	0.1
500	C	18200	188	-1.7	0.1
600	C	6200	64.0	-2.3	0.3
700	C	41500	428	+2.1	0.2
800	C	9300	96.0	+3.1	0.2
900	C	11000	114	+2.1	0.2
1000	C	13000	134	+1.5	0.1
1100	C	10600	109	+3.9	0.2
1200	C	300	3.10	nm	nm

RLA 139 cumulate dunite

Temp	Type	[S] (ng)	[S] (ppm)	$\delta^{34}S$ (‰)	σ (±‰)
400	C	nm	nm	nm	nm
450	C	nm	nm	nm	nm
500	C	nm	nm	nm	nm
550	C	nm	nm	nm	nm
600	C	760	31.0	nm	nm
650	C	5680	232	-4.7	0.8
700	C	20930	854	-0.6	0.3
750	C	51940	2120	+0.5	0.4
800	C	83830	3422	-1.6	0.2
850	C	174760	7133	-1.9	0.2
900	C	111480	4550	+0.3	0.3
950	C	73950	3018	+6.4	0.2
1000	C	34570	1411	+9.9	1.0
1050	C	13130	536	+3.1	0.4
1100	C	10670	436	+1.2	0.4
1150	C	4700	192	+3.4	0.7
1200	C	2120	86.5	nm	nm

NB2-5 cumulate dunite

Temp	Type	[S] (ng)	[S] (ppm)	$\delta^{34}S$ (‰)	σ (±‰)
200	C	5.00	0.308	nm	nm
250	C	nm	nm	nm	nm
300	C	nm	nm	nm	nm
350	C	nm	nm	nm	nm
400	C	5.00	0.308	nm	nm
450	C	nm	nm	nm	nm
500	C	nm	nm	nm	nm
550	C	nm	nm	nm	nm
600	C	1730	107	nm	nm
650	C	7980	492	-4.2	0.4
700	C	11840	730	-0.4	0.3
750	C	59000	3638	-0.7	0.3
800	C	92200	5686	-2.7	0.2
850	C	202600	12494	-3.5	0.1
900	C	245940	15166	-2.0	0.2
950	C	159160	9815	+1.0	0.2
1000	C	102150	6299	+8.3	0.4
1050	C	16000	987	+4.4	0.2
1100	C	8450	521	+4.4	0.3
1150	C	5560	343	-1.7	0.5
1200	C	2750	170	nm	nm

JM40 cumulate dunite

Temp	Type	[S] (ng)	[S] (ppm)	$\delta^{34}S$ (‰)	σ (±‰)
300	C	930	52.7	nm	nm
350	C	60.0	3.40	nm	nm
400	C	nm	nm	nm	nm
450	C	nm	nm	nm	nm
500	C	nm	nm	nm	nm
550	C	nm	nm	nm	nm
600	C	1100	62.3	nm	nm
650	C	4188	237	+0.0	3.5
700	C	9440	535	+0.1	1.0
750	C	33170	1878	+3.6	0.3
800	C	79530	4503	-1.0	0.2
850	C	100530	5693	-2.5	0.3
900	C	176920	10018	-2.9	0.3
950	C	59120	3348	-1.0	0.4
1000	C	72720	4118	+2.3	0.2
1050	C	24920	1411	+6.8	0.4
1100	C	15780	894	+3.1	0.4
1150	C	60410	3421	+0.7	0.2
1200	C	15280	865	-0.4	0.5

MR11 dunite pod

Temp	Type	[S] (ng)	[S] (ppm)	$\delta^{34}S$ (‰)	σ (±‰)
300	C	60.0	6.48	nm	nm
350	C	270	29.2	nm	nm
400	C	2.00	0.216	nm	nm
450	C	3.00	0.324	nm	nm
500	C	6.00	0.648	nm	nm
550	C	3.00	0.324	nm	nm
600	C	3.00	0.324	nm	nm
650	C	1200	130	nm	nm
700	C	5890	636	-0.7	0.5
750	C	28390	3066	-4.2	0.2
800	C	43220	4667	-3.2	0.5
850	C	70990	7666	-2.7	0.1
900	C	95180	10279	-0.5	0.1
950	C	85230	9204	+3.6	0.3
1000	C	71730	7746	+10.2	0.3
1050	C	29640	3201	+16.3	0.3
1100	C	3160	341	+12.0	2.0
1150	C	1640	177	nm	nm
1200	C	nm	nm	nm	nm

Whole rock sulphur contents and sulphur isotopes.

Lithology	*Sample no.*	*S (ppm)*	$\delta^{34}S_{CDT}$(‰)
dolerite dyke	JM5	2765	+4.5
dolerite dyke	JM9	2925	+3.4
amph. pegmatite	MNA	15465	+10.9
sub-massive sulphide	MNG	36205	+9.6
plagiogranite	mn130	1040	+14.0
gabbro	JM1	14587	+4.8
gabbro	JM2	3080	+4.4
gabbro	JM3	700	+3.0
gabbro	JM6	602	+3.2
gabbro	JM8	5189	+3.6
gabbro	mn68	205	+6.3
gabbro	mn236	148	+5.9
high level pyroxenite	JM44	602	+4.6
high level pyroxenite	JM45	496	+3.5
cumulate pyroxenite	JM10	641	+4.2
cumulate pyroxenite	JM13	3350	+3.4
cumulate pyroxenite	JM14	345	+4.0
cumulate pyroxenite	NA3	204	+4.4
cumulate pyroxenite	NA16	210	-1.3
cumulate pyroxenite	NA21	510	+2.2
cumulate pyroxenite	NA14	250	+3.2
wehrlitic dunite	JM37	486	+5.0
cumulate dunite	JM38	325	+3.8
cumulate dunite	JM39	322	+3.9
cumulate dunite	JM40	917	+3.0
cumulate dunite	JM41	508	+3.1
cumulate dunite	JM42	700	+2.5
cumulate dunite	RLA139	1440	+3.1
cumulate dunite	RLMO63	1679	+3.4
cumulate dunite	NB2-1	552	+3.6
cumulate dunite	NB2-2a	780	-0.6
cumulate dunite	NB2-3a	1604	-0.2
cumulate dunite	NB2-5	1630	+1.5
cumulate dunite	NB2-6	1540	+1.6
cumulate dunite	NB2-7	1200	+1.8
dunite pod	JM34	218	+4.4
dunite pod	JM43	300	+2.5
dunite pod	MR11	980	+4.0
dunite pod	MR12	301	+4.4
dunite pod	MR2	125	+6.3
dunite pod	MR6	142	n.m.
dunite pod	MR8	82	n.m.
harzburgite	MR1	150	+1.2
harzburgite	MR5	98	n.m.
harzburgite	MR7	140	+5.7
talc/carbonate serpentinite	JM31	202	+1.0
talc/carbonate serpentinite	JM32	1150	+1.0
talc/carbonate serpentinite	MR242	192	+1.0
talc/carbonate serpentinite	MR244	730	+0.4
talc/carbonate serpentinite	CMR150	91	n.m.
serpentinite	MR58	131	+1.0

Whole-rock sulphur contents and sulphur isotopes

Lithology	*Sample no.*	*S (ppm)*	$\delta^{34}S_{CDT}$(‰)
serpentinite	MR59	104	+0.1
serpentinite	MR130	62	+3.1
serpentinite	CMR148	72	n.m.
harzburgite	CMR149	160	+2.7
serpentinite	CMR151	620	+2.0
serpentinite	CMR152	52	+1.2
serpentinite	CMR153	170	+1.5
serpentinite	CMR154	345	-2.4
serpentinite	CMR155	59	+0.8
serpentinite	CMR156	130	-1.6
limestone	JM27	3110	-6.2
limestone	MR62	2513	-8.1
limestone	MR236	2468	-5.6
schist	JM30	77	n.m.
schist	MR121	91	-2.8
schist	MR60	59	+1.6
schist	CMR157	1490	-3.9

Whole rock δD and $\delta^{18}O$ measurements

Lithology	*Sample*	$\delta D_{(SMOW)}$(‰)	*Wt% H_2O*	$\delta^{18}O_{(SMOW)}$(‰)
dolerite dyke	JM5	-64.90	3.20	+10.0
amphibole pegmatite	MNA	-37.80	1.60	+6.5
gabbro	MNG	-27.80	1.50	+5.8
gabbro	JM1	-58.50	3.96	5.03
gabbro	JM2	-44.30	3.00	n.m.
gabbro	JM3	-59.00	3.29	n.m.
high level pyroxenite	JM4	-44.00	5.30	n.m.
high level pyroxenite	JM44	-37.80	3.38	n.m.
cumulate pyroxenite	JM11	-20.40	5.39	n.m.
cumulate pyroxenite	JM13	-58.10	5.10	n.m.
cumulate pyroxenite	JM14	-26.30	3.28	+5.3
wherlitic dunite	JM37	-94.30	11.00	n.m.
cumulate dunite	JM39	-89.40	9.73	n.m.
cumulate dunite	JM40	-89.80	10.30	n.m.
cumulate dunite	JM41	-102.00	8.10	n.m.
cumulate dunite	JM42	-98.60	11.08	+7.9
dunite pod	JM34	-101.20	10.50	n.m.
dunite pod	JM36	-96.60	11.44	n.m.
podiform chromite	JM35	-91.40	5.80	n.m.
fresh water	Loch of Cliff (1)	-39.20	n.m.	n.m.
fresh water	Loch of Cliff (2)	-46.00	n.m.	n.m.
seawater	Burrafirth	-14.40	n.m.	n.m.

Appendix C. Sample locality map

Appendix D. Rock sample management catalogue

| | | |

										Originator			
Rock sample management/catalogue file guide - Page 2 - Analytical Information										J. Maynard			
18	19	20	21	22	23	24	25	26	27	28	29	30	31
Analytical sample prep. 2			Whole-rock Analysis			Separated Mineral Analysis			In Situ mineral Analysis		High Res. Imaging &	Fluid Inclusion Analysis	
ple prepared for:-													
XRF Maj.	XRF Tr.	INAA	Elemental Technique	Rad'gen. Isot. System	Stable Isot. System	Elemental Technique	Rad'gen. Isot. System	Stable Isot. System	Elemental	Isotopic	Cryst'graph. Properties	Gas species	Isotope System
(date/code)	(date/code)	(date/code)	(code)	(code)	(code)	(method:mins)	(system:mins)	(system:mins)	(method:mins)	(method:mins)	(method:mins)	(method:mineral)	(system:mineral)
G	P		XM,XT		S,O,D/I				MP:py,po,cp,ap				
G	P		XM,XT		S,D/I				MP:py,po,cp				
G	P		XM,XT		S,D/I				MP:py,po,cp,ap				
G	P		XM,XT		D/I								
G	P		XM,XT		S,O,D/I				MP:py,po,cp				
G	P		XM,XT		S				MP:py,po,cp,ap				
	P		XT										
G	P		XM,XT		S				MP:py,po				
G	P		XM,XT		S				MP:py,po,cp				
G	P		XM,XT		S								
G	P		XM,XT		D/I								
G	P		XM,XT		S								
G	P		XM,XT		S,D/I				MP,SEM:po,cp,pn,py				
G	P		XM,XT		S,O,D/I				MP:pn,cp				
G	P		XM,XT										
G	P		XM,XT										
G	P		XM,XT										
G	P		XM,XT						MP:py,cp				
									MP:py,ap,mt				
G	P		XM,XT										
									MP:py				
	P		XT										
G	P		XM,XT										
	P		XT		S								
	P		XT										
	P		XT		S								
G	P		XM,XT		S								
	P		XT		S				MP:po,pn				
	P		XT						MP:mc,nc				
	P		XT		S,D/I								
	P		XT		D/I								
G	P		XM,XT		D/I								
G	P		XM,XT		S,D/I				MP:pn,hz,Cu				
G	P		XM,XT		S				MP:pn				
G	P		XM,XT		S,D/I				MP:po,pn,Cu				
G	P		XM,XT		S,D/I				MP:pn,hz,aw,Cu				
G	P		XM,XT		S,D/I				MP:pn,Cu				
G	P		XM,XT		S,O,D/I				MP,SEM:py,po,cpy				
G	P		XM,XT		S				MP:pn,				
G	P		XM,XT		S,D/I				MP:py,po,pn,gd				
G	P		XM,XT		S				MP:pn,gd,nc				
G	P		XM,XT		S,O,D/I				MP:py,cp,ap				
G	P		XM,XT		S,O,D/I				MP:py,cp,ap				

Abrajano, T.A. (1984) The petrology and low-temperature geochemistry of the sulfide-bearing mafic-ultramafic units of the Acoje Massif, Zambales ophiolite, Philippines. Ph.D. Thesis, Washington University, 475pp.

Abrajano, T.A. Jr. & Pasteris, J.D. (1989) Zambales Ophiolite, Philippines II: Sulfide petrology of the critical zone of the Acoje Massif. *Cont. Min. Pet.* **103**, p64–77.

Alt, J.C. (1988) Chemistry and sulfur isotope composition of massive sulphide and associated deposits on Green Seamount, E. Pacific. *Economic Geology*, **83**, p1026–1033.

Alt, J.C. (1991) A sulphur isotope profile through the Troodos ophiolite, Cyprus; preliminary results & implications. *In* Ophiolite Genesis and Evolution of the Oceanic Lithosphere, Tj Peters *et al.* (eds.). Ministry of Petroleum and Minerals, Sultanate of Oman. p427-443.

Alt, J.C., Anderson, T.F. & Bonnell, L.B (1989) The geochemistry of sulfur in a 1.3km section of hydrothermally altered oceanic crust, DSDP Hole 504B. *G.C.A.* **53**, p1011-1023.

Alt, J.C. & Chaussidon, M. (1990) Ion microprobe analyses of the sulphur isotopic composition of sulfides in hydrothermally altered rocks, DSDP/ODP Hole 504B.Part B *In Proc. Ocean Drilling Program, Leg 111* (K. Becker *et al.* eds) **Vol. III**, p41-45.

Alt, J.C. & Anderson, T.F. (1991) Mineralogy and isotopic composition of sulfur in Layer 3 gabbros from the Indian Ocean, Hole 735B. *Proc. Ocean Drilling Program, Scientific Results.* **118**; p113-125.

Amin, M.S. (1954). Notes on the Ultrabasic body of Unst, Shetland Islands. *Geol. Mag.* **91**, p399–406.

Anonymous (1972) Penrose field conference on ophiolites. *Geotimes* **17**, p24-25.

Arnold, M. & Sheppard, S.M.F. (1981) East Pacific Rise at latitude 21° N: isotopic composition and origin of hydrothermal sulphur. *E.P.S.L.*, **56**, p 148–156.

Ashley, P.M. (1975). Opaque mineral assemblages formed during serpentinization in the Coolac ultramafic belt, New South Wales. *Jorn.Geol. Soc. Aust.*, **22**, p91–102.

Auclair, M.A., Gauthier, M., Trottier, J., Jébrak, M. & Chartrand, F. (1993) Mineralogy, and Paragenesis of the Eastern Metals Serpentinite-Associated Ni-Cu-Zn Deposit, Quebec Appalachians. *Economic Geology*, **68**, p123–138.

Ault, W.U. & Kulp, J.L. (1959) Isotopic geochemistry of sulfur. *G.C.A.* **16**, p201–235.

Barnes, I. & O'Neil, J.R. (1969) The relationship between fluids in some fresh Alpine-type ultramafics and possible modern serpentinization, western United States. *Geol. Soc. Am. Bull.*, **80**, p1947–1960.

Barton, P.B. (1973) Solid solutions in the systems Cu-Fe-S. I. The Cu-S and CuFe-S joins. *Economic Geology*, **68**, p455–463.

Barrett, F.M., Binns, R.A., Groves, D.I., Marston, R.J. & McQueen, K.G. (1977) Structural history and metamorphic modification of Archean volcanic-type nickel deposits, Yilgarn Block, W.A. *Economic Geology*, **72**, p195–223.

Botto, R.I. & Morrison, G.H. (1976) Josephinite: a unique nickel-iron. *Am. Jour. Sci.* **276**, p241-274.

Bowers, T.S. (1989) Stable Isotope Signatures of Water-Rock Interaction in Mid-Ocean Ridge Hydrothermal Systems: Sulfur, Oxygen and Hydrogen. *J. Geophys. Research* **49**, No.B5, p5775-5786.

Boyd, S.R. (1988) A study of carbon and nitrogen isotopes from the Earth's mantle. Unpublished Ph.D. Thesis. Open University.

Brzozowski, T.J. (1977) VLF electromagnetic surveys and associated studies in north Dartmoor and Unst. Unpublished Ph.D. Thesis, Chelsea College.

Buchanan, D.L., Nolan, J., Suddaby, P., Rouse, J.E., Viljoen, M.J., Davenport, J.W.J. (1981) The Genesis of Sulphide Mineralization in a Portion of the Potgietersous Limb of the Bushveld Complex. *Economic Geology*, **76**, p568–579.

Burgess, R. (1987) An investigation of sulphur in carbonaceous and enstatite chondrites by stepped combustion. Unpublished Ph.D. Thesis. Open University.

Cabri, L.J. (1973) New Data on Phase Relations in the Cu-Fe-S System. *Economic Geology*, **68**, p443–454.

Cemic, L. Kleppa, O.J. (1987). High temperature calorimetry of sulphide systems II. standard enthalpies of formation of pentlandite and violarite. *Phys. Chem. Minerals*, **14**, 52–57.

Chamberlain, J.A., McLeod, C.R., Traill, R.J. & Lachance, G.R. (1965) Native metals in the Muskox intrusion. *Can. Jorn. Earth Sci.*, **2**, p188–215.

Chausssidon, M., Albarede, F. & Sheppard, S.M.F. (1987) Sulfur isotope heterogeneity in the mantle from ion microprobe measurements of sulphide inclusions in diamonds. *Nature*. **330**, p242–244.

Chausssidon, M. & Demange, J.C. (1988) Instrumental mass fractionation in ion microprobe studies of sulphur isotopic ratios. *In :Secondary Ion Mass Spectrometry*, **VI**, Benninghoven, A., Huber, A.M., & Werner, H.W. (eds.). Wiley & Sons, New York. p937-940.

Chausssidon, M., Albarede, F. & Sheppard, S.M.F. (1989) Sulfur isotope variations in the mantle from ion microprobe analyses of micro-sulphide inclusions. *E.P.S.L.*, **92**, p144–156.

Chausssidon, M. & Lorand, M. (1990) Sulfur isotope composition of orogenic spinel lherzolite massifs from Ariege (North-Eastern Pyrenees, France): An ion microprobe study. *G.C.A.*, **54**, p2835–2846.

Coleman, R.G. (1977) *Ophiolites: Ancient Oceanic Lithosphere* Springer, Berlin, 229pp.

Coleman, R.G. Husto, C.C., Elboushi, I.M., Al-Hinai, K.M. & Bailey, E.H. (1979) The Semail ophiolite and associated massive sulfide deposits, Sultanate of Oman. *In* Evolution and mineralization of the Arabian-Nubian shield, vol.2, Al-Shanti, A.M.S. ed. *I.A.G.A. Bulletin, No.3*, p179-192.

Constantinou, G. & Govett G.J.S. (1973) Geology, geochemistry and genesis of Cyprus sulphide deposits. *Economic Geology*, **68**, p843–858.

Cotton, F.A. & Wilkinson, G. (1972) Advanced inorganic chemistry. Third edition, Wiley & Sons, New York.

Craig, J.R., & Kullerud, G. (1969) Phase relations in the Cu-Fe-Ni-S system and their application to magmatic ore deposits. *In* Magmatic Ore Deposits (H.D.B. Wilson, ed.). *Economic Geology Monograph*, **4**, p344-358.

Craig, J.R. (1973) Pyrite-pentlandite assemblages and other low temperature relations in the Fe-Ni-S system. *Amer.J.Sci.* **273A**, p496–510.

Craig, J.R. & Scott, S.D. (1974) Sulfide phase equilibria. *In* Mineral. Soc. Am. Short Course Notes, 1. Ribbe, P.H. (ed). pCs-1-Cs-110.MSA, Washington, DC.

Crowe, D.E. & Valley, J.W. (1992) Laser microprobe study of sulfur isotope variation in a sea-floor hydrothermal spire, Axial Seamount, Juan de Fuca Ridge, eastern Pacific. *Chem. Geol.*, **101**, p63–70.

Czamanske, G.K & Moore, J.G. (1977) Composition and phase chemistry of sulphide globules in basalt from the M.A.R. rift valley near 37° N Lat. *Geol. Soc. Am. Bull.*, **88**, p587–559.

Czamanske, G.K., Kunilov, V.E., Zientek, M.L., Cabri, L.J., Likhachev, A.P., Calk, L.C., & Oscarson, R.L. (1992) A proton-microprobe study of magmatic sulfide ores from the Noril'sk-Talnakh District, Siberia. *Can. Min.*, **30**, p249–287.

Deloule, E. & Allegre, C. (1986) Pb and S-isotope microstratigraphy in galena crystals from Mississippi valley-type deposits. *Economic Geology*, **81**, p1307–1321.

Dewey, J.F. & Shackleton, R.M. (1984) A model for the evolution of the Grampian tract in the early Caledonides and Appalachians. *Nature*, **312**, p115-121.

Dick, H.J.B. & Bullen, T. (1984) Chromian spinels as a petrogenetic indicator in abyssal and alpine-type peridotites and spatially associated lavas. *Cont. Min. Pet.*, **86**, p54–76.

Donaldson, M.J. (1981) Redistribution of Ore Elements During Serpentinisation and Talc-Carbonate Alteration of Some Archean Dunites, W.A. *Economic Geology*, **76**, p1698–1713.

Donaldson, M.J. & Bromley, C.J. (1981) The Honeymoon Well Nickel Sulfide Deposits. W.A. *Economic Geology*, **76**, p1550–1564.

Eckstrand, O.R. (1975) The Dumont Serpentinite: A model for control of nickeliferous opaque mineral assemblages by alteration reactions in ultramafic rocks. *Economic Geology*, **70**, p183–201.

Economou, M. & Naldrett, A.J. (1984) Sulphides associated with Podiform Bodies of Chromite at Tsangli, Eretria, Greece. *Mineral. Deposita*, **19**, p287-297.

Edmond, J.M., Measures, C., McDuff, R.E., Chan, L.H., Collier, R., Grant, B., Gordon, L.I., & Corliss, J.B. (1979) Ridge crest hydrothermal activity and the balances of the major and minor elements in the ocean: The Galapagos Data. *E. P. S. L.*, **46**, p1-18.

Evans, B.W., Johannes, W., Oterdoom, H. & Trommsdorff, V. (1976) Stability of chrysotile and antigorite in the serpentine multisystem. *Schweiz. miner. petrogr. Mitt.*, **56**, p79-93.

Ewers, W.E. & Hudson, D.R. (1972) An interpretive study of a Ni-Fe sulfide ore intersection, Lunnan Shoot, Kambalda, W. A. *Economic Geology*, **67**, p1075–1092.

Flinn, D. (1970) Some aspects of the geochemistry of the metamorphic rocks of Unst & Fetlar, Shetland. *Proc. Geol. Assoc.*, **81**, p509–527.

Flinn, D. (1985) The Caledonides of Shetland. *In* The Caledonide Orogen - Scandinavia and related areas. Gee, D.G. and Sturt, B.A. (eds). Wiley, New York. p1159–1172.

Foose, M.P, Economou, M. & Panayiotou, A. (1985) Compositional and mineralogic constraints on the genesis of ophiolite hosted nickel mineralization in the Pevkos Area, Limassol Forest, Cyprus. *Mineral. Deposita* , **20**, p234-240.

Fritz, P., Drimmie, R.J. & Nowicki, V.K. (1974) Preparation of sulfur dioxide for mass spectrometer analyses by combustion of sulfides with copper oxide. *Anal. Chem.*, **46**, p164–166.

Frost, B.R. (1985) On the stability of sulfides, oxides and native metals in serpentinite. *J. Petrol.*, **26**, part 1, p31–63.

Garson, M.S. & Plant, J. (1973) Alpine Type Ultramafic rocks and Episodic Mountain Building in the Scottish Highlands. *Nature* (Phys. Sci.), **242**, p34–38.

Garuti, G., Gorgoni, C. & Sighinolfi, G.P. (1984) Sulfide mineralogy and chalcophile element abundances in the Ivrea-Verbano mantle peridotites (western Italian Alps). *E.P.S.L.* **70**, p67–87.

Gass, I.G. & Masson-Smith, D. (1963) The geology and gravity anomalies of the Troodos massif, Cyprus. *Phil. trans. Royal Soc. London, Series A* , **255**, p417-467.

Gass, I.G. & Masson-Smith, D. (1968) Is the Troodos massif of Cyprus a fragment of Mesozoic ocean floor? *Nature*, **220**, p39-42.

Gass, I.G. (1980) The Troodos massif: Its role in the unravelling of the ophiolite problem and its significance in the understanding of constructive plate margin processes. *In* Ophiolites: Proceedings International Ophiolite Symposium Cyprus (A. Panayiotou, ed.). Ministry of Agriculture and Natural Resources, Geological Survey Department, Nicosia (23-35).

Gass, I.G., Neary, C.R., Prichard, H.M. & Bartholomew, I.D. (1982) The chromite of the Shetland ophiolite. A reappraisal in the light of new theory and techniques. A report for the Comission of European Communities. The Open University, Milton Keynes. 264pp.

Gerivilla, F. & Leblanc, M. (1990) Magmatic Ores in High-temperature Alpine-type Lherzolite Massifs (Ronda, Spain and Beni Bousera, Morocco). *Economic Geology* **85**, p112–132.

Godlevskii, M.N. & Grinenko, L.N. (1963) Some data on the isotopic composition of sulfur in the sulfides of the Noril'sk deposit. *Geochemistry* , **no.1**, p35-41.

Grady, M.M., Wright, I.P., Swart, P.K. & Pillinger, C.T. (1988) The carbon and oxygen composition of meteoritic carbonates. *G.C.A.*, **52**, 2855-2866.

Graterol, M. & Naldrett, A.J., (1971) The mineralogy of the Marbridge No.3 and No.4 nickel-iron sulfide deposits with some comments on low temperature equilibration in the Fe-Ni-S system. *Economic Geology*, **66**, p886–900.

Gregory, R.T. & Taylor, H.P. JR. (1981) An oxygen isotope profile in a section of Cretaceous oceanic crust, Semail ophiolite, Oman: Evidence for $\delta^{18}O$ buffering of the oceans by deep (> 5km) seawater - hydrothermal circulation at MOR's. *J.G.R.*, **86**, No. 84, p2737–2755.

Grinenko, V.A., Dmitriev, L.V., Migdisov, A.A. & Sharaskin, A.Y. (1975) Sulfur contents and isotope compositions for igneous and metamorphic rocks from mid-ocean ridges. *Geochem. Intl.* **12**, p132–137.

Groves, D.I., Hudson, D.R. & Hack, T.B.C. (1974) Modification of Fe-Ni sulphides during Serpentinization and Talc-Carbonate alteration at Black Swan, W.A. *Economic Geology*. **69**, p1265–1281.

Groves, D.I. & Keays, R.R. (1979) Mobilization of ore-forming elements during alteration of dunites, Mt. Keith-Betheno, W.A. *Can. Min.*, **17**, p373–389.

Gunn, A.G., Leake, R.C. Styles, M.T. & Bateson, J.H. (1985) Platinum-group element mineralization in the Unst ophiolite, Shetland. Mineral Reconnaissance Programme Report No. 17, British Geological Survey, Keyworth. 116pp.

Harland, W.B. & Gayer, R.A. (1972) The Arctic Caledonides and earlier Oceans. *Geol. Mag.*, **109**, p289-314.

Harmon, R.S. , Hoefs, J. & Wedepohl, K.H. (1987) Stable isotope (O,H,S) relationships in Tertiary basalts and their mantle xenoliths from the N. Hessian Depression, W. Germany. *Contrib. Min. Pet.*, **95**, p350–359.

Harris, D.C. & Nickel, E.H. (1972) Pentlandite composition and association in some mineral deposits. *Can. Min.*, **11**, p861–878.

Heddle, M.F. (1878) The county geognosy and mineralogy of Scotland, Orkney and Shetland. *Min. Mag.*, **2**, p9-35.

Heydemann, A. (1969) Tables. *In* Handbook of Geochemistry, Wedepohl, K.H, ed.,**12-I**, p376-412, Springer-Verlag, Berlin.

Hoatson, D.M. & Keays, R.R. (1989) Formation of platiniferous sulfide horizons by crystal fractionation and magma mixing in the Munni Munni layered intrusion, West Pilbara Block, W.A.. *Economic Geology*, **84**, p1775–1804.

Hoefs, J. (1986) Stable isotope geochemistry. Springer-Verlag, Berlin.

Holser, W.T. & Kaplan, I.R. (1966) Isotope geochemistry of sedimentary sulfates. *Chem. Geol.*, **1**, p93-135.

Hudson, D.R. & Groves, D.I. (1974) The composition of violarite coexisting with vaesite, pyrite and millerite. *Economic Geology*, **69**, p1335–1340.

Ikin, N.P. & Harmon, R.S. (1983) A stable isotope study of serpentinization in the Highland Border Suite, Scotland, U.K. *G.C.A.*, **47**, p153-167.

Ionov, D.A., Hoefs, J., Wedepohl, K.H. & Wiechert, U., (1992) Content and isotopic composition of sulphur in ultramafic xenoliths from central Asia. *E.P.S.L.*, **111**, p269-286.

Ito, E. & Clayton, R.N. (1983) Submarine metamorphism of gabbros from the Mid-Cayman Rise: an oxygen isotopic study. *G.C.A.*, **47**, p535-546.

Ixer, R.A., Vaughan, D.J., Pattrick, R.A.D. & Alabaster, T. (1986) Mineralogical studies and their bearing on the genesis of massive sulphide deposits from the Semail Ophiolite Complex, Oman. *In* Metallogeny of basic and ultrabasic rocks. Gallagher, M.J., Ixer, R.A., Neary, C.R. & Prichard, H.M. (eds.). p33-48.

Ixer, R.A. & Prichard, H.M. (1989) The mineralogy and paragenesis of Pt, Pd, Au and Ag - bearing assemblages at Cliff, Shetland. *Bulletin of the Geological Society of Finland.*, **61**, p40 (abstract).

Janecky, D.R. & Shanks, W.C. (1988) Computational modellingof chemical and sulfur isotopic reaction processes in seafloor hydrothermal systems: Chimneys, massive sulfides and subjacent alteration zones. *Can. Min.*, **26**, p805-825.

Jaques, A.L. (1981) Petrology and petrogenesis of cumulate peridotites and gabbros from the Marum ophiolite complex, Northern Papua New Guinea. *Jour. Petrol.*, **22**, p1–40.

Jensen, M.L. & Nakai, N. (1962) Sulfur isotope meteorite standards: Results and recommendations, *In* biogeochemistry of sulfur isotopes: Proc. of a Nat'l Sci. Found. Symposium, Yale University, April 12-14.

Jensen, M.L. (1967) Sulphur isotopes and mineral genesis. *In* Geochemistry of Hydrothermal Ore Deposits, Barnes, H.L. (ed.). New York (Wiley), p143–165.

Kajiwara, Y. & Krouse, O. (1971) Sulfur isotope partitioning in metallic sulfide systems. *Can. Jour. Earth Sci.*, **8**, p1397–1408.

Kaneda, H., Takenouchi, S. & Shoji, T. (1986) Stability of pentlandite in the Fe-Ni-Co-S system. *Mineral. Deposita*, **21**, p169–180.

Kaplan, I.R. & Hulston, J.R. (1966) The isotopic abundance and content of sulfur in meteorites. *G.C.A.*, **30**, p479–496.

Kelley, S.P. & Fallick, A.E. (1990) High precision, spatially resolved analysis of $\delta^{34}S$ in sulphides using a laser extraction technique. *G.C.A.*, **54**, p883–888.

Kiba, T., Takagi, T., Yoshimura, Y. & Kishi, I. (1955) Tin (II) - strong phosphoric acid. A new reagent for the determination of sulfate by reduction to hydrogen sulfide. *Bull. Chem. Soc. Japan*, **28**, p641–644.

Kinloch, E.D. (1982) Regional trends in the Platinum Group Mineralogy of the Critical Zone of the Bushveld Complex, South Africa. *Economic Geology*, **77**, p1328–1347.

Knop, O., Huang, C. & Woodhams, F.W.D. (1970) Chalcogenides of the transition elements. VII. A Mossbauer study of pentlandite. *Am. Mineral.*, **55**, p1115–1130.

Kubaschewski, O. (1982) Iron-binary phase diagrams. Springer Verlag, Berlin Heidelberg New York.

Kullerud, G., & Yund, R.A., (1962) The Ni-S system related minerals. *J. Petrology*, **3**, p126–175.

Kullerud, G., & Yund, R.A. & Moh, G.H. (1969) Phase relations in the Cu-Ni-Fe and Fe-Ni-S systems. *In* Magmatic Ore Deposits (H.D.B. Wilson, ed.). *Econ. Geol. Mon.*, **4**, p323–343.

Kyser, K.T. & O'Neil, J.R. (1984) Hydrogen isotope systematics of submarine basalts. *G.C.A.*, **48**, p2123–2133.

Lachize, M., Lorand, J.P. & Juteau, T. (1991) Cu-Ni-PGE Magmatic Sulfide Ores and their Host Layered Gabbros in the Haymiliyah Fossil Magma Chamber (Haylayn Block, Semail Ophiolite Nappe, Oman). *In* Ophiolite Genesis and Evolution of the Oceanic Lithosphere, Tj Peters *et al.* (eds.). Ministry of Petroleum and Minerals, Sultanate of Oman.

Leake, B.E. (1978) Nomenclature of amphiboles. *Miner. Petrogr. Acta* , **22**, p195-224.

Leblanc, M., Ceuleneer, H.A.A, & Jedwab, J. (1991) Hydrothermal concentration of palladium and platinum in mantle peridotites from the Oman ophiolite. *C.R. Acad. Sci. Paris*, t.312, **Série II**, p1007-1012.

Liebenburg, L. (1968) The sulphides in the layered sequence of the Bushveld Igneous Complex. Unpublished Ph.D. Thesis. University of Pretoria.

Lorand, J.P. (1983) Les mineraux opaques des lherzolites a spinelle et des pyroxénites associées: Un étude comparative dans les complexes orogeniques et dans les enclaves des basaltes alcalines. Unpublished Ph.D. thesis, Paris, Univ. Pierre et Marie Curie. 230pp.

Lorand, J.P. & Pinet, M. (1984) L'orcellite des péridotites de Beni Bousera (Maroc), Rhonda (Espagne), Table Mountain et Blow-Me-Down Mountain (Terre-Neuve) et du Pinde septentrional (Grèce). *Can. Min* **22**, p553–560.

Lorand, J.P. (1989) Mineralogy and chemistry of Cu-Fe-Ni sulfides in orogenic-type spinel peridotite bodies from Ariége (N.E. Pyrenees, France). *Cont. Min. Pet.* **103**, p335–345.

Lord, R.A. (1991) Platinum-Group Element Mineralization in the Shetland Ophiolite Complex. Unpublished Ph.D. Thesis. Open University. 422pp.

Lowry, D., Boyce, A.J., Pattrick, R.A.D., Fallick, A.E. & Stanley, C.J. (1991) A sulphur isotopic investigation of the potential sulphur sources for Lower Palaeozoic-hosted vein mineralization in the English Lake District. *Jour.Geol. Soc. Lond.* **148**, part 6 p993–1005.

Lundquvist, D. (1947) X-ray studies on the ternary system Fe-Ni-S. *Ark. Kemi. Mineral. Geol.*, **24A**, No.22, 12pp.

Lydon, J.W. & Richardson, D.G. (1987) Distribution of PGE in Sulphides of the Bay of Islands Ophiolite Complex, Newfoundland. *In* Geo-Platinum 87. Prichard, H.M., Bowles, J.F.W & Cribb, S.J. eds. Elsevier, London, p251.

Lydon, J.W. & Lavigne, J (1990) Magmatic sulphides and gabbro remelting in the Bay of Islands ophiolite, Newfoundland; evidence for seawater penetration of the mantle. *In* Symposium on Ophiolite Genesis and Evolution of the Oceanic Lithosphere. Ministry of Petroleum and Minerals, Sultanate of Oman (abstract).

Mainwaring, P.R. & Naldrett, A.J. (1977) Country rock assimilation and the genesis of Cu-Ni sulphides in the Water Hen intrusion, Duluth Complex, Minnesota. *Economic Geology*. **72**, p1269–1284.

Makovicky, M., Makovicky, E. & Rose-Hansen, J. (1986) Experimental studies on the solubility and distribution of Platinum-Group Elements in base metal sulfides in

platinum deposits. *In Metallogeny of basic and ultrabasic rocks.* Gallagher, M.J., Ixer, R.A., Neary, C.R. and Prichard, H.M. (eds.). The Institute of Mining and Metallurgy, London. p415–425.

Maltman, A.J. (1978) Serpentine textures in Anglesey, North Wales, United Kingdom. *Geol. Soc. Am. Bull.*, **89**, p972–980.

Menzies, M.A. & Allen, C. (1974) Plagioclase lherzolite residual mantle relationships within two eastern Mediterranean Ophiolites. *Cont. Min. Pet.*, **45**, p197–213.

Misra, K.C. & Fleet, M.E. (1973) The chemical compositions of synthetic and natural pentlandite assemblages. *Economic Geology*, **68**, p518–539.

Mottl, M.J., Holland, H.D. & Corr, R.F. (1979) Chemical exchange during hydrothermal alteration of basalt by seawater: II. Experimental results for Fe, Mn and sulfur species. *G.C.A.*, **45**, p869–884.

Naldrett, A.J., Gasparrini, E., Buchan, R., & Muir, J.E. (1972) Godlevskite (β-Ni_7S_6) from the Texmont Mine, Ontario. *Can. Min.*, **11**, p879–885.

Naldrett, A.J. (1973) Nickel Sulphide Deposits - Their classification and genesis, with special emphasis on deposits of volcanic association. *Builletin CIM Trans.* **LXXVI**, p183–201.

Naldrett, A.J., Hoffman, E.L., Green, A.H., Chou, C-L. & Naldrett, S.R. (1979) The composition of Ni-sulfide ores, with particular reference to their content of PGE and Au. *Can. Min.*, **17**, p403-415.

Naldrett, A.J. (1981) Platinum-group element deposits. *In* Platinum-Group Elements; Mineralogy, Geology, Recovery. *Can. Inst. of Min. Metal.* Special Volume **23**, p197-232.

Neary, C.R. Prichard, H.M. & Potts, P.J. (1984) Chromite, platinoids, gold and moly in the Shetlands. *In* Panorama (anon.). *Mining Mag.*, **151**, p559–560.

Neary, C.R. & Prichard, H.M. (1985) Molybdenum mineralization on Unst, Shetland Isles. *Scot. J. Geol.* **21**, p197–204.

Nielsen, H. (1978) Sulphur isotopes in nature. *In* Handbook of Geochemistry. Wedepohl, K.H. ed., **II-2**, p16B1-16B40, Springer-Verlag, Berlin.

Oen, I.S (1973) A peculiar type of Cr-Ni mineralization; cordierite-chromite-niccolite ores of Malaga, Spain, and their possible origin by liquid unmixing. *Economic Geology*, **68**, p831–842.

Ohomoto, H. (1972) Systematics of Sulfur and Carbon Isotopes in Hydrothermal ore deposits. *Economic Geology*, **67**, p551–578.

Ohomoto, H. (1986) Stable isotope geochemistry of ore deposits. *In* Stable isotopes in high temperature geological processes. Valley, J.W., Taylor, H.P. &, O'Neil, J.R. (eds.) *Mineral. Soc. Amer. Rev. in Mineral.*, **16**, p491-559.

Oppenheimer, C. (1992) Sulphur eruptions at Volcan Poas, Costa Rica. *Jour. Volc. Geoth. Res.*, **49**, p1–21.

Orberger, B., Fredrich, G. & Woermann, E. (1988) Platinum-group element mineralization in the ultramafic sequence of the Acoje ophiolite block, Zambales,

Philippines. *In* Geo Platinum Symp. Vol. (H.M. Prichard, P.J. Potts, J.F.W. Bowles & S.J. Cribb eds.) Elsevier London p361–380.

Oudin, E. & Constantinou, G. (1984) Black smoker chimney fragments in Cyprus sulphide deposits. *Nature*, **308**, p349–353.

Panayiotou, A. (1986) Cu-Ni-Co-Fe slphide mineralization, Limassol Forest, Cyprus. *In* Metallogeny of basic and ultrabasic rocks (M.J. Gallagher, R.A. Ixer, C.R. Neary and H.M. Prichard, eds.). Institute of Mining and Metallurgy, London p102-116.

Paringit, R.V. (1975) Nickel sulfide deposits and exploration works at Acoje mine, Zambales province, Philippines. *Geol. Soc. Philippines Jour.*, **29**, p16-27.

Pederson, R. (1993) Stratiform PGE mineralization in the Ultramafic Cumulates of the Leka Ophiolite Complex, Central Norway. *Economic Geology*, **88**, 782-803.

Peter, J.M. & Shanks III, W.C (1992) Sulfur, carbon and oxygen isotope variations in submarine hydrothermal deposits of Guaymas Basin, Gulf of California, USA. *G.C.A.*, **56**, p2025-2040.

Potts, P.J. (1984) Energy dispersive X-ray fluorescence analysis of silicate rocks for major and trace elements. *X-ray Spectrometry*, **13**, p2-15.

Potts, P.J. (1987) A handbook of silicate rock analysis. Blackie & Sons, London, 622pp.

Poulson, S.R., Kubilius, W.P. & Ohomoto, H. (1991) Geochemical behaviour of sulfur in granitoids during the intrusion of the South Mountain Batholith, Nova Scotia, Canada. *G.C.A.* **55**, p3809-3830.

Prichard, H.M. (1979) A petrographic study of the process of serpentinization in ophiolites and the oceanic crust. *Contrib. Miner. Pet..*, **68**, p231-241.

Prichard, H. & Neary, C.R. (1981) Chromite in the Shetland Islands ophiolite complex. *In* An international symposium on metallogeny of mafic and ultramafic complexes (1980). UNESCO, Athens, p343–360.

Prichard, H.M. (1985) The Shetland ophiolite. *In* The Caledonide orogen - Scandinavia and related areas. Gee, D.G. and Sturt, B.A., (eds.) Wiley, New York. p1173–1184.

Prichard, H.M., Neary, C.R & Potts, P.J. (1986) Platinum group minerals in the Shetland ophiolite. *In* Metallogeny of basic and ultrabasic rocks (M.J. Gallagher, R.A. Ixer, C.R. Neary and H.M. Prichard, eds.). Institute of Mining and Metallurgy, London p395-414.

Prichard, H.M. & Lord, R.A. (1988) The Shetland ophiolite: evidence for a supra-subduction zone origin and implications for platinum-group element mineralization. *In* Mineral Deposits within the European Community. Boissonnas, J. and Omenetto, P., (eds.) *Spec. Publ. No.6 of the Society for Geology Applied to Mineral Deposits.* Springer-Verlag, Berlin, p289-302.

Prichard, H.M. & Lord, R.A. (1989) Magmatic and secondary PGM in the Shetland Ophiolite Complex. *Bulletin of the Geological Society of Finland.*, **61**, p39 (abstract).

Prichard, H.M. & Tarkian, M. (1988) Platinum and palladium minerals from two PGE-rich localities in the Shetland ophiolite. *Can. Min.*, **26**, p979-990.

Prichard, H.M. & Lord, R.A. (1990) Platinum mineralization on the Shetland ophiolite complex. Final report for the Minerals Research Organization. Contract RC 48.

Prichard, H.M., Ixer, R.A., Lord, R.A., Maynard, J & Williams, N. (1994) Platinum group mineral assemblages in silicate lithologies and chromite-rich rocks within the Shetland ophiolite sequence. *Can. Min* (in press).

Rafter, T.A. (1959) Sulphur isotopic variations in nature. Part 1-the preparation of sulphur dioxide for mass specrometer examination. *N.Z.J. Sci Tech*, Sec. **B38**, 849-857.

Ramdohr, P. (1969) *The Ore Minerals and their Intergrowths* (English edition). Oxford, Permagon Press.

Read, H.H. (1934) The Metamorphic Geology of Unst in the Shetland Islands. *Q.J.G.S.* **90**, p637–688.

Rees, C.E., Jenkins, W.J. & Monster, J. (1978) The sulphur isotopic composition of ocean water sulphate. *G.C.A.*, **42**, p377–381.

Ripley, E.M. (1981) Sulfur isotopic studies of the Dunka Road Cu-Ni deposit, Duluth Complex, Minnesota, *Economic Geology*, **76**, p610-620.

Ripley, E.M. (1983) Sulfide mineralogy and sulfur isotope geochemistry of layered sills in the Deer Lake Complex, Minnesota. *Mineral. Deposita* , **18**, p3-15.

Ripley, E.M. & Al-Jassar, T.J. (1987) Sulfur and oxygen isotope studies of melt-country rock interaction, Babbitt Cu-Ni deposit, Duluth Complex, Minnesota. *Economic Geology*, **85**, p1935–1940.

Roberts, S. (1986) The role of igneous processes in the formation of ophiolitic chromitite. Unpublished Ph.D. Thesis. Open University.

Robie, R.A., Hemingway, B.S. & Fisher, S.R. (1978) Thermodynamic properties of minerals and related substances at 298.15K and 1bar pressure and higher temperatures. *US Geol. Surv. Bull.* , **1452**, 456 pp.

Robie, R.A., Wiggins, L.B., Barton, P.B. JR & Hemmingway, B.S. (1985) Low temperature heat capacity and entropy of chalcopyrite ($CuFeS_2$): Estimates of the standard molar enthalpy and Gibbs free energy of formation of chalcopyrite and bornite (Cu_5FeS_4). *J. Chem. Thermodynamics*, **17**, p481-488.

Robinson, B.W. & Kusakabe, M. (1975) Quantitative preparation of SO_2, for $^{34/32}$ Analysis, from Sulfides by combustion with Cuprous Oxide. *Anal. Chem.*, **47**, no.7, p1179–1181.

Robinson, B.W. & Brenninkmeijer, C.A.M. (March 1987) Sulphur Isotope Standard NZ1. Final Report Technical Contract No. 4320/TC. 3pp.

Rumble, D., Palin, J.M. & Hoering, T.C. (1991) Laser Fluorination of Sulfide Minerals with F_2 Gas. Ann. Rep. Director Geophys. Lab., Carnegie Inst. Washington 1990-1991. p30-34.

Sakai, H. (1957) Fractionation of Sulphur Isotopes in Nature. *G.C.A.*, **12**, p150–169.

Sakai, H. Des Marais, D.J., Ueda, A. & Moore, J.G. (1984) Concentrations and isotope ratios of carbon, nitrogen and sulphur in ocean floor basalts. *G.C.A.*, **48**, p2433-2441.

Sanford, R.F. (1983) Growth of ultramafic reaction zones in greenschist to amphibolite facies metamorphism. *Am. Journ. Sci*, **282**, p543-616.

Savin, S.M. & Epstein, S. (1970) The oxygen and hydrogen isotope geochemistry of clay minerals. *G.C.A.*, **34**, p25-42.

Shanks, W.C.III, Bischoff, J.L. & Rosenbauer, R.J. (1981) Seawater sulphate reduction and S-isotope fractionation in basaltic systems. Interaction of seawater with fayalite and magnetite at 200–350°C. *G.C.A.*, **45**, p1977–1995.

Shanks, W.C.III, & Seyfried, W.E JR. (1987) Stable isotope studies of vent fluids and chimney minerals, southern Juan de Fuca Ridge: Sodium metasomatism and seawater sulfate reduction. *Jour. Geophys. Res.*, **92**, p11,387–11,399.

Sheppard, S.M.F. (1980) Isotopic evidence for the origins of water during metamorphic processes in oceanic crust and ophiolite complexes. *In* Associations mafiques-ultramafiques dans les orogenes. Allegre, C.J., and Aubouin (eds.). *Colloq. Int. C.N.R.S., Paris*, No. **272**, p135-147.

Shewman, R.W. & Clark, L.A. (1970) Pentlandite phase relations in the Fe-Ni-S system and notes on the monosulfide solid solutions. *Can. Jour. Earth Sci.*, **7**, p67–85.

Shiga, Y. (1987) Behaviour of Fe,Ni,Co and S during serpentinisation, with reference to the Hayachine ultramafic rocks of the Kamaishi mining district, N.E. Japan. *Can. Min*, **25**, p611–624.

Smewing, J.D. (1980) An Upper Cretaceous ridge-transform intersection in the Oman ophiolite. *Proc. Int. Oph. Symp. Cyprus, Geol. Surv. Dept. Cyprus*, p407-413.

Spooner, E.T.C., Beckinale, R.D., Fyfe, W.S. & Smewing, J.D. (1974) O^{18} enriched ophiolitic metabasic rocks from E. Liguria (Italy),Pindos (Greece), and Troodos (Cyprus). *Contrib. Mineral. Petrol.*, **47**, p41–62.

Spray, J.G. (1988) Thrust-related metamorphism beneath the Shetland Islands oceanic fragment, N.E. Scotland. *Can. J. Earth Sci.*, **25**, p1760–1776.

Stakes, D.S., Taylor, H.P, JR., & Fisher, R.L. (1984) Oxygen isotope and geochemical characterization of hydrothermal alteration in ophiolite complexes and modern oceanic crust. *In* Ophiolites and Oceanic Lithosphere. Gass, I.G., Lippard, S.J. and Shelton, A.W. (eds). *Geol. Soc. Lond.* Blackwell, London. p199-214.

Stuart, F., Turner, G. & Maynard, J. (1992) The isotopic composition of helium and sulphur in hydrothermal fluids trapped in ancient and modern sea floor deposits. *In* Proceedings of the 7th international symposium on water-rock interaction-WRI-7, Utah, U.S.A. p1671-1674.

Thode, H.G. Monster, J & Dunford, H.B. (1961) Sulphur isotope geochemistry. *G.C.A.*, **25**, p159-174.

Trahey, N.M. (Ed.) Light Stable Isotopic Materials (gas, liquid and solid forms). (1992) Standard Reference Materials Catalog 1992-93. National Institute of Standards and Technology (NIST). Spec. Publ. **260** Washington. 52pp.

Ueda, A. & Sakai, H. (1983) Simultaneous determinations of the concentration and isotope ratio of sulfate- and sulfide- sulfur and carbonate carbon in geological samples. *Geochem. Jour.*, **17**, p185–196.

Ueda, A. & Sakai, H. (1984) Sulfur isotope study of Quaternary volcanic rocks from the Japanese Islands Arc. *G.C.A.*, **48**, p1837–1848.

Ueda, A. & Krouse, H.R. (1986) Direct conversion of sulphide and sulphate minerals to SO_2 for isotope analysis. *Geochem. Jour.*, **20**, p209–212.

Upadhyay, H.D. & Strong, D.F. (1973) Geological setting of the Betts Cove copper deposits, Newfoundland: An example of ophiolite suite mineralization. *Economic Geology*, **68**, p161-168.

Urey, H.C. (1948) Oxygen isotopes in nature and in the laboratory. *Science*, **108**, p489-496.

Vasjoki, O., Hakli, T.A. & Tontti, M. (1974) The effect of cobalt on the thermal stability of pentlandite. *Economic Geology*, **69**, p549–551.

Vaughan, D.J. & Craig, J.R. (1978) Mineral Chemistry of Metal Sulphides. Cambridge University Press, Cambridge, England.

Viljoen, M.J., Bernasconi, A., van Coller, N, Kinloch, E. & Viljoen, R.P. (1976) The geology of the Shangani nickel deposit, Rhodesia. *Economic Geology*, **71**, p76–95.

Wenner, D.B. & Taylor H.P. Jr. (1973) O & H isotope studies of the serpentinization of ultramafic rocks in the oceanic environment and continental ophiolite complexes. *Am. Journ. of Sci.*, p207–239.

Woodhead, J.D., Harmon, R.S. & Fraser, D.G. (1987) O,Sr,S & Pb isotopic variations in volcanic rocks from the Northern Mariana Islands; implications for crustal recycling in intra-oceanic arcs. *E.P.S.L.*, **83**, p39–52.

Yund, R.A. & Kullerud, G. (1966) Thermal stability of assemblages in the Cu-Fe-S system. *J. Petr.*, **7**, p454–488.

Zientek, M.L. & Ripley, E.M. (1990) Sulfur isotope studies of the Stillwater Complex and associated rocks, Montana. *Economic Geology*, **85**, p376–391.